

---

# **Kinematics Across Bulge Types A Longslit Kinematic Survey and Dedicated Instrumentation**

**Maximilian Hieronymus Fabricius**

---



München 2012



---

# **Kinematics Across Bulge Types A Longslit Kinematic Survey and Dedicated Instrumentation**

---

DISSERTATION

an der Fakultät für Physik  
der Ludwig-Maximilians-Universität München  
zur Erlangung des Grades  
Doktor der Naturwissenschaften  
Dr. rer. nat.

vorgelegt von

Maximilian Hieronymus Fabricius  
aus Freiburg im Breisgau

München, den 14.2.2012

Erstgutachter: Prof. Dr. Ralf Bender

Zweitgutachter: Priv. Doz. Dr. Andreas Glindemann

Tag der mündlichen Prüfung: 16.4.2012

# Zusammenfassung

Der erste Teil dieser Arbeit stellt die Konstruktion, Inbetriebnahme und erste Daten eines neuen optischen, faserbasierten Feldspektrographen namens VIRUS-W vor. Die Entwicklung wurde durch den Bau des neuen 2 m Fraunhofer Teleskops auf dem Berg Wendelstein in den Bayrischen Alpen motiviert. Die besondere Eigenschaft dieses Instruments liegt zum einen in der Fähigkeit, Spektren in einem zweidimensionalen Sichtfeld aufzuzeichnen, und zum anderen in der Kombination eines grossen Sichtfeldes von  $105'' \times 55''$  mit einer relativ grossen instrumentellen Auflösung von  $R = 8700$ . Diese Auflösung erlaubt es, Geschwindigkeitsdispersionen von Sternen und Gas bis hinunter zu  $15 \text{ km s}^{-1}$  aufzulösen. Es wird im Allgemeinen erwartet, dass dies dem Regime entspricht, in dem sich Sterne in Scheiben bilden. Der abgedeckte Spektralbereich dieses Dynamikmodus beträgt  $4850 \text{ \AA}$  bis  $5480 \text{ \AA}$ . Zusätzlich bietet VIRUS-W einen zweiten Modus, welcher der Studie der Zusammensetzung von stellaren Populationen, also z.B. deren Alter und Metallicität, gewidmet ist. Die spektrale Auflösung ist hier geringer ( $R = 3300$ ), aber der abgedeckte Spektralbereich ist weiter und beträgt  $4340 \text{ \AA}$  bis  $6040 \text{ \AA}$ . Dies deckt eine grössere Zahl von Absorptionsbanden im stellaren Spektrum ab. Insbesondere ist hier  $H_\beta$  enthalten, welches eine wichtige Grundlage zur Bestimmung des Alters einer Stellaren Population liefert.

Bis zur Fertigstellung des Wendelstein Teleskops wird sich der Spektrograph an dem 2.7 m Harlan J. Smith Teleskop des McDonald Observatoriums in Texas befinden. Dort nahm er im November 2010 erfolgreich seinen Betrieb auf. Die bei der Inbetriebnahme gewonnenen Daten erlauben uns, die genaue spektrale Auflösung und die Effizienz zu bestimmen. Durch den Vergleich der aufgezeichneten Daten eines spektrophotometrischen Standardsterns mit veröffentlichten Werten errechnen wir für das gesamte Atmosphären-Teleskop-Spektrographen-System eine Effizienz von 37% im hochauflösenden Dynamikmodus und von 40% im niedriger auflösenden Modus.

Wir schliessen diesen Teil mit der Diskussion der Beobachtungen der drei Galaxien NGC2903, NGC205 und NGC3091 aus den November- und Dezember- Kampagnen ab und präsentieren erste Geschwindigkeitsfelder und Messungen von Absorptionen. Der Vergleich mit Literaturdaten für NGC205 zeigt, dass wir in der Lage sind, diese sehr niedrigen Dispersionen von  $\simeq 20 \text{ km s}^{-1}$  zuverlässig wiederzugeben.

Der zweite Teil dieser Arbeit befasst sich mit einer Beobachtungsreihe von Bulgeregionen benachbarter Spiralgalaxien, die wir am Hobby-Eberly-Teleskop des McDonald Observatoriums mit dem LRS Langspaltspektrographen durchgeführt haben. Wir präsentieren kinematische Profile entlang der Hauptachse von 46 Galaxien der Hubbletypen S0 bis Sc. Für 28 dieser Objekte stellen wir ausserdem Profile entlang der kleineren Halbachse vor.

Ein systematischer Vergleich der gewonnenen Daten mit photometrischen Dekompositionen erlaubt es uns zu zeigen, dass die Unterschiede, die verschiedene Bulgetypen in ihrem so genannten Sérsic-Index zeigen, auch in der Kinematik wiederspiegelt werden. Pseudobulges zeigen oft eine scheibenartige Morphologie und haben niedrigere Sérsic-Indizes — also ein Leuchtkraftprofil, das eher demjenigen einer Scheibe entspricht. Klassische Bulges haben im Allgemeinen grössere Sérsic-Indizes ( $n > 2$ ). Wir zeigen, dass Pseudobulges auch schwächere Gradienten der Geschwindigkeitsdispersion als Funktion des Radius aufweisen — ihre Dispersionsprofile sind also vorwiegend flach. Höhere Sérsic-Indizes hingegen treten in Galaxien mit steiler abfallenden Dispersionsprofilen auf. Ausserdem beobachten wir, dass Pseudobulges vorwiegend in Galaxien mit niedrigeren zentralen Geschwindigkeitsdispersionen auftreten und einen grösseren Grad von Rotation im Verhältnis zu ihrer mittleren Geschwindigkeitsdispersion zeigen.



# Contents

<b>Zusammenfassung</b>	<b>v</b>
<b>1 Introduction</b>	<b>1</b>
1.1 The study of Dynamics and Star Formation Histories in Galactic Disks . . .	1
1.2 Integral Field Spectroscopy . . . . .	7
1.3 Outline of this Thesis . . . . .	10
<b>2 VIRUS-W: A new IFU Instrument</b>	<b>11</b>
2.1 Instrument Design . . . . .	12
2.1.1 VIRUS-W's heritage . . . . .	12
2.1.2 Spectrograph Layout . . . . .	13
2.1.3 Individual Elements . . . . .	19
2.1.4 Guider & Focal reducer . . . . .	19
2.1.5 Filters . . . . .	21
2.1.6 Integral Field Unit . . . . .	21
2.1.7 Fiber Bundle . . . . .	26
2.1.8 Slit Unit . . . . .	27
2.1.9 Mirror System . . . . .	31
2.1.10 Dispersive Elements . . . . .	34
2.1.11 Camera Lens . . . . .	39
2.1.12 Detector System . . . . .	39
2.1.13 Optical Performance . . . . .	45
2.1.14 Bench, Dark Box and Temperature Control . . . . .	45
2.2 Control Software & Modes of Observation . . . . .	49
2.2.1 Observing Modes . . . . .	49
2.2.2 Calibration Dataset . . . . .	50
2.2.3 Instrument Setup . . . . .	52
2.2.4 Astrometry . . . . .	53
2.3 Data Reduction . . . . .	56
<b>3 Commissioning</b>	<b>59</b>
3.1 Commissioning Runs . . . . .	59
3.2 Overall Efficiency and Exposure Time Calculations . . . . .	61

3.3	Wavelength Calibration and Spectral Dispersion . . . . .	68
3.4	Spectral Resolution . . . . .	71
3.5	Stray Light and Fiber Separation . . . . .	73
3.6	Stability . . . . .	77
3.7	Kinematic Templates and Lick Standard Stars . . . . .	79
3.8	First VIRUS-W Kinematic Maps . . . . .	85
3.8.1	Target description . . . . .	85
3.8.2	Observations . . . . .	86
3.8.3	Reduction . . . . .	88
3.8.4	Preliminary Results . . . . .	89
<b>4</b>	<b>Correlation of Bulge Kinematics with Morphology, Sérsic Index</b>	<b>99</b>
4.1	Introduction . . . . .	100
4.2	Sample . . . . .	101
4.3	Observations . . . . .	102
4.4	Data Reduction . . . . .	105
4.4.1	Derivation of the Kinematics and Template Library . . . . .	107
4.4.2	Emission Line Subtraction and Gas Kinematics . . . . .	111
4.4.3	Identification of Pseudobulges . . . . .	114
4.4.4	Photometry . . . . .	114
4.4.5	Bulge Radius . . . . .	115
4.5	Results . . . . .	115
4.5.1	Kinematic Profiles and Comparison with Literature . . . . .	115
4.5.2	Signatures of Bars in Velocity Profiles . . . . .	117
4.5.3	Central Velocity Dispersions . . . . .	118
4.5.4	Velocity Dispersion Gradients . . . . .	118
4.5.5	Influence of Seeing on Velocity Dispersion . . . . .	123
4.5.6	Correlation of $h_3$ and $h_4$ Moments . . . . .	123
4.5.7	Extreme Moments and Multiple Kinematic Components . . . . .	128
4.6	Discussion . . . . .	132
4.6.1	Dichotomous Dispersion Profiles of Classical and Pseudobulges . . . . .	132
4.6.2	Rotational Support . . . . .	134
4.6.3	Multiple Kinematic Components . . . . .	138
4.7	Summary . . . . .	138
<b>5</b>	<b>Summary &amp; Conclusions</b>	<b>141</b>
<b>A</b>	<b>Kinematic profiles</b>	<b>145</b>
<b>B</b>	<b>Notes on individual galaxies</b>	<b>165</b>
B.1	Classical Bulges . . . . .	165
B.2	Pseudobulges . . . . .	169
B.3	Bulges Without Classification . . . . .	176

**Contents** **ix**

---

**Bibliography** **179**

**Acknowledgements** **195**

**Curriculum Vitae** **198**



# List of Figures

2.1	Layout of the spectrograph in the high resolution mode . . . . .	14
2.2	VIRUS-W in low resolution configuration . . . . .	14
2.3	Spectral coverage . . . . .	17
2.4	The complete spectrograph assembled . . . . .	18
2.5	Guider unit and focal reducer . . . . .	20
2.6	Focal reducer . . . . .	20
2.7	High resolution mode filters . . . . .	22
2.8	Filter transmission curves . . . . .	23
2.9	Drilled IFU fiber matrix geometry . . . . .	23
2.10	IFU and slit unit . . . . .	24
2.11	IFU head and IFU micrograph . . . . .	25
2.12	Centroid positions of the IFU fibers . . . . .	25
2.13	Fiber transmission curve . . . . .	27
2.14	V-groove plate . . . . .	28
2.15	Slit unit . . . . .	29
2.16	Slit mask . . . . .	30
2.17	IFU lens . . . . .	30
2.18	Collimating and fold mirrors . . . . .	31
2.19	Mirror reflectivity . . . . .	32
2.20	Gratings . . . . .	34
2.21	2D Diffraction efficiency at 5320 Å . . . . .	36
2.22	Predicted diffraction efficiency as function of wavelength . . . . .	37
2.23	Camera lens design . . . . .	39
2.24	Camera lens photograph . . . . .	40
2.25	CCD and detector head . . . . .	41
2.26	CCD quantum efficiency . . . . .	42
2.27	CCD artefacts . . . . .	42
2.28	Tip tilt mount of the camera head . . . . .	44
2.29	Spot diagram for high resolution mode . . . . .	46
2.30	Spot diagram fro low resolution mode . . . . .	46
2.31	Darkbox . . . . .	48
2.32	Dither pattern and sky nods . . . . .	50
2.33	Ne+Hg lamp spectra . . . . .	51

2.34	IFU trailing procedure . . . . .	52
2.35	Resulting spectrum of trailing procedure . . . . .	53
2.36	Focussing scheme . . . . .	54
2.37	Example of an astrometry field . . . . .	56
2.38	Raw twilight flat . . . . .	57
2.39	A VIRUS-W datacube . . . . .	58
3.1	Littrow ghost . . . . .	60
3.2	Theoretical aperture loss and crosstalk as function of trace width . . . . .	64
3.3	Throughput prediction and measurement . . . . .	65
3.4	Efficiency models . . . . .	66
3.5	$S/N$ predictions as function of exposure time for both resolution modes . . . . .	67
3.6	Linear dispersion . . . . .	68
3.7	Instrumental resolution as function of chip position . . . . .	71
3.8	Resolution as function of fiber number measured on a star . . . . .	72
3.9	Fiber separation in high resolution mode . . . . .	74
3.10	Fiber separation in low resolution mode . . . . .	75
3.11	Contrast maps . . . . .	76
3.12	Instrumental stability over three runs . . . . .	78
3.13	Instrumental stability during on runs . . . . .	79
3.14	Lick standards and kinematic templates . . . . .	82
3.15	High resolution mode equivalent widths: VIRUS-W vs. Lick . . . . .	83
3.16	Low resolution mode equivalent widths: VIRUS-W vs. Lick . . . . .	84
3.17	NGC 2903 and NGC 205 FoV . . . . .	87
3.18	NGC 3091 FoV . . . . .	88
3.19	NGC 3091 sky fibers . . . . .	89
3.20	Reconstructed image of NGC 2903 . . . . .	90
3.21	Literature comparison for NGC 2903 . . . . .	90
3.22	Kinematics maps of the central region of NGC 2903 . . . . .	92
3.23	NGC 205 literature comparison . . . . .	93
3.24	Kinematic maps for NGC 205 . . . . .	94
3.25	Kinematic maps for NGC 3091 . . . . .	96
3.26	Lick indices: VIRUS-W vs. literature . . . . .	97
3.27	M/L from Lick indices and dynamical modelling . . . . .	98
4.1	Distribution of Hubble types . . . . .	101
4.2	Comparison of fits with different templates . . . . .	108
4.3	Vazdekis SSP library vs. out library . . . . .	109
4.4	Example of the nebular emission line subtraction . . . . .	113
4.5	Histograms of the central velocity dispersions . . . . .	119
4.6	Example for different slopes of velocity dispersion, NGC3898 and NGC4448 . . . . .	119
4.7	Dispersion slopes . . . . .	121
4.8	Sérsic index $n$ vs. dispersion slopes . . . . .	122

---

4.9	Local correlation between $h_3$ and $v/\sigma$ . . . . .	124
4.10	Correlations of $\langle h_3 \rangle$ and $\langle h_4 \rangle$ , bulge luminosities and $\langle v/\sigma \rangle$ . . . . .	125
4.11	Kinematic decompositions . . . . .	130
4.12	Double-Gaussian decompositions for NGC3521 . . . . .	131
4.13	$\langle v^2 \rangle / \langle \sigma^2 \rangle$ as function of the velocity dispersion slope, $\gamma$ . . . . .	134
4.14	Local $(v_{corr}/\sigma)(r)$ along the major axis . . . . .	136
4.15	Histograms for the averaged values of $\langle v^2 \rangle / \langle \sigma^2 \rangle$ . . . . .	137
A.16	Major and minor axis kinematic profiles . . . . .	145



# List of Tables

2.1	High resolution mode characteristics . . . . .	16
2.2	Low resolution mode characteristics . . . . .	16
2.3	Surface description for the focal reducer . . . . .	21
2.4	Characteristics of the Integral Field Unit . . . . .	26
2.5	Mirror characteristics . . . . .	33
2.6	Characteristics of the dispersive elements . . . . .	38
2.7	Surface description for the camera lens . . . . .	40
2.8	Characteristics of the CCD detector in science mode . . . . .	43
2.9	Encircled energies for both resolution modes . . . . .	47
2.10	High level routines of the control software . . . . .	55
3.1	Observations during the November 2011 run . . . . .	61
3.2	Observations during the December 2011 run . . . . .	62
3.3	High resolution mode calibration line identifications . . . . .	69
3.4	Low resolution mode calibration line identifications . . . . .	70
3.5	RMS variations of the spectral and distortion calibrations . . . . .	79
3.6	Observed kinematic templates . . . . .	80
3.7	Lick indices covered by the spectral range of VIRUS-W at $z = 0$ . . . . .	81
4.1	Sample . . . . .	103
4.2	List of observations . . . . .	104
4.2	List of observations . . . . .	105
4.3	Observed kinematic templates . . . . .	106
4.4	Parameters for the linear bias corrections in velocity dispersion . . . . .	111
4.5	parameters for the linear bias corrections in $h_3$ and $h_4$ . . . . .	112
4.6	New bulge to disk decomposition parameters . . . . .	116
4.7	Format example of the measured stellar kinematics . . . . .	117
4.8	Structural and kinematic parameters . . . . .	127
4.8	Structural and kinematic parameters . . . . .	129
4.9	Light fractions in kinematic subcomponent . . . . .	131



# Chapter 1

## Introduction

### 1.1 The study of Dynamics and Star Formation Histories in Galactic Disks

Disk galaxies belong to the most visually appealing objects in the night sky. Images of spirals such as the mighty Andromeda galaxy have fascinated both people inside and outside of astronomy ever since first photographs of these objects became feasible. The reason for their attractiveness lies of course in the wealth of structure that is found in these objects. Combined multi band images show a multitude of features. Spiral arms — be it in a few high contrast arms or a tightly wound flocculent spiral — give a hint about the dynamic nature of these objects. Often prominent bars reside in the centers and sometimes the surrounding spiral seems to launch at the ends of these bars. Bright knots of star forming regions are distributed along the spiral arms or are arranged in rings which again can coincide with the ends of the bars. High contrast dust features, sometimes forming lanes which are aligned with the spirals or with the bars, sometimes distributed rather chaotically, seem superimposed on the stellar light. Nebular emission spreads throughout the disk and adds a halo-like glow to their appearance.

We know today that all those features are expression of the multitude of underlying physics that is at play in these objects. Star formation processes and nebular emission are driven by the interplay between the baryonic components, the gas and the stellar structure. The dynamical properties, the amount of rotation and the formation of bars and spiral structure are affected by the overall gravitational potential which — as we have very good reason to believe today (Freeman, 1970; Carignan & Freeman, 1985) — is dominated over large radial ranges by the yet so poorly understood dark matter.

The understanding of the complicated interplay between these various components and the relative importance as a function of cosmic time holds not only the key to the understanding of formation of spiral galaxies but also to the formation of all stellar systems.

Early works have seen the monolithic collapse of gas clouds with subsequent dissipative evolution at the forefront of galaxy formation (Eggen et al., 1962; Larson, 1974; Carlberg, 1984; Thomas et al., 1999). In this model protogalaxies collapse initially spherically, first

condensations of gas from, which become globular clusters and low metallicity stars on highly eccentric orbits. Eventually rotation will balance gravitation and the collapse will only continue in parallel to the rotation axis giving rise to a disk. Ongoing star formation in the disk will enrich the interstellar material and increase its metallicity up to solar values. This model successfully explains the rough structure of the Milky Way and is probably correct in its essence, it almost certainly is a too simplistic view of the cosmic evolutionary process however. We know today from large scale simulations of the  $\Lambda$ CDM universe, that hierarchical clustering of galaxies Toomre (1977) — i.e. the merging of smaller galaxies into larger galaxies — represents in important mode for the growth of stellar mass (White & Rees, 1978a; Frenk et al., 1985; Efstathiou et al., 1988; Cole et al., 1994; Thomas et al., 1999; De Lucia et al., 2006).

Nevertheless the build-up of stellar mass in galactic disks is ubiquitous in our universe. Whilst early disks probably looked nothing like the thin and regular disks we observe today, the formation of rotation dominated systems seems to happen early on (Förster Schreiber et al., 2006), while the formation of massive elliptical galaxies represents a later stage of galaxy evolution. In galaxy mergers the disks are destroyed and the stars are flung into random orbits which leave the systems in a stage where they are supported by dispersion rather than rotation. And, while mergers may well trigger immense outbursts of star formation, the amount of star formation in the resulting galaxies is small compared to the total in our today’s universe — most star formation today occurs in quiescent disks.

With the cosmic expansion and the virialization of galaxy clusters, merging events become less and less frequent (Toomre, 1977; Patton et al., 2002; Conselice et al., 2003). In the late stages of cosmic evolution the transformation of disks ought to be determined by the physics within the disk themselves rather than the interaction with outer systems and the outside world — this secular evolution in disks must become the dominant factor of evolution at some point (Kormendy & Kennicutt, 2004).

It is clear that if one wishes to understand the origin of stellar mass and its build-up in the past and in the local universe, one fundamentally has to study galactic disks. Simulations yet have to produce realistic disk galaxies (e.g. Bell et al., 2003; Kaufmann et al., 2007). This is probably less a failure of  $\Lambda$ CDM model than an expression of the complication of the complex large and small scale physics involved in the formation of these systems. The baryonic physics, the hydrodynamical interaction of gas, star formation and AGN feedback have to be taken into account as well as the fast and violent processes of merging events. On the other hand the yet only through its gravitational force detected dark matter sets the stage on which those processes evolve. Simulations need to be put into a cosmological context in order to capture the full history of accretion of dark matter, stars and gas from both other stellar systems and the larger scale filamentary structure (Dekel et al., 2009). At the same time either high resolutions are needed that are able to resolve the complex dynamical structures of disks or detailed analytical prescriptions of the small-scale physics have to be made (e.g. De Lucia et al., 2011). As simulations become increasingly more sophisticated, more detailed observations are necessary to put tight constraints on the models of galaxy evolution.

The two main observational ways to address formation histories in existing objects are

the study of the composition of the stellar populations and the study of its stellar dynamics. Since stars in galaxies are collisionless (Binney & Tremaine, 1987), stellar orbits carry a memory of their formation history. In systems which have not been vastly disturbed through mergers in their past, we can expect that the formation history is reflected in the dynamical structure as well. Naively speaking, if stars form in gaseous disks on circular orbits they should remain in close to circular orbits for a long time, while if they were accreted in a merging event their orbits should have large eccentricities and be aligned rather randomly. Dispersion dominated systems have probably experienced major mergers while low dispersion systems that are mostly dominated by rotation have probably undergone a more quiescent formation history.

The structure of stellar disks — both morphologically as well as dynamically — is in general complex by itself. In addition to the actual, typically exponential disk, many galaxies host additional components. Substructure is very common:

Most notable in many cases is a central bulge component (e.g. de Vaucouleurs et al., 1991). The classical bulge protrudes out spherically above the disk if the system is seen close to edge on. The most prominent example of such bulge is the Sombrero galaxy M104. Here the disk appears merely as a thin dust-disk that surrounds a massive spherical component. In fact if one was to mask the low latitude parts in the images of this galaxy, one would easily mistake this system for a giant elliptical galaxy. Such bulges may be the natural consequence of a merging event that, while not dramatic enough to destroy the disk completely, did add a large amount of random motion to the system. In fact many bulges do show a similarly low amount of rotational support as elliptical galaxies do (Kormendy, 1982b; Kormendy & Kennicutt, 2004). Many galaxies which are not close to edge on still show a central brightening which was originally thought to be essentially the same phenomenon as the spherical bulge (e.g. Renzini, 1999).

There is evidence today however that many of those central light accumulations resemble disks more than elliptical galaxies. They often show disk-like morphology as seen in high spatial resolution studies for example by Carollo et al. (1997, 1998). Also they often host star formation, nuclear bars, nuclear rings, are flattened and do look nothing like elliptical galaxies living at the center of a disk (e.g. Kormendy, 1982b,a see Kormendy & Kennicutt (2004) for a review). Carollo (1999) finds that these systems deviate from the fundamental plane correlations of ellipticals (Saglia et al., 1993) and classical bulges. It is now well established through photometric decompositions that they are different in their structural parameters as well (Fisher & Drory, 2008, 2010). Sérsic fits to the surface brightness profiles show that they have Sérsic indices which are lower than two while classical bulges have Sérsic indices that are larger than two. An exponential disk would correspond to an index of one, saying that this class of bulges has surface brightness profiles that look more similar to disks than spheroids. This class of bulges is referred to as pseudobulges. They tend to fall above the line of the isotropic oblate rotator line (Binney & Tremaine, 1987) in the famous  $v_{max}/\sigma$  diagram (e.g. Illingworth, 1977; Binney & Tremaine, 1987; Kormendy & Kennicutt, 2004) which is taken as indication that they are flattened by rotations rather than by anisotropy. But the number of systems for which this has been shown has been small so far, calling for a larger and systematic survey.

In addition to bulges, more prominent disk features include spiral structure and bars. In the optical half of all spirals appear barred (de Vaucouleurs et al., 1991). From infrared studies we know that about two third of all spiral galaxies hosts bars (Block & Wainscoat, 1991; Mulchaey & Regan, 1997; Mulchaey et al., 1997; Seigar & James, 1998; Knapen et al., 2000; Eskridge et al., 2000, 2002a; Block et al., 2001; Laurikainen & Salo, 2002). Bars well as as spiral structure are fundamental to the secular evolution of a disk as they form a break in the axisymmetric structure and allow for the transport of angular momentum in the disk. Such substructure is a necessary ingredient for the transport of gas from the outer to the inner disk regions which consequently allow for continued star formation. Yet the structure and the dynamics of bar are not yet fully understood. There is strong indication that bars heat disks vertically (Sellwood & Wilkinson, 1993) and give rise to vertically thickened, boxy parts in galactic disks (Combes & Sanders, 1981; Bureau & Freeman, 1999a; Athanassoula & Misiriotis, 2002; Athanassoula, 2003; Bureau & Athanassoula, 2005). Candidate processes for the vertical heating may be resonance phenomena (Pfenniger, 1984, 1985; Pfenniger & Norman, 1990) and the so called buckling instability (Raha et al., 1991; Merrifield, 1996; Martinez-Valpuesta et al., 2006). The radial range over which bars actually increase velocity dispersions, and to what degree, is still unknown (see Shen & Sellwood, 2004). Bars rotate. It is expected from analytical arguments and simulations (Weinberg, 1985; Debattista & Sellwood, 2000; Athanassoula, 2003) that bars will slow down quickly due to the dynamical friction they experience from the dark matter halo. However, the few observations which try to determine bar pattern speeds directly from stellar kinematics (e.g. (Kent, 1987; Gerssen et al., 1999, 2003; Treuhardt et al., 2007)) point to rather large speeds — close to their physically maximally allowed pattern speed. This raised questions regarding the correctness of our understanding of the underlying dark matter halos.

More subtle disk components include inner and outer rings, lenses, additional inner bars (e.g. Erwin & Sparke, 2002), polar rings and nuclear clusters. All of these components will affect the kinematics along any line of sight which intersects them. The wealth of the observed morphological structure naturally raises the question of its connection to the formation history of the whole galaxy. The answers are likely not simple as the different stellar structures interact with each other in multiple ways on the one hand and with the interstellar matter on the other. For instance, breaks in the axisymmetry of disks such as bars and spiral structure create resonances which in turn are probably reason for the occurrence of ring phenomena (Buta & Combes, 1996). The rich amount of star formation that is observed in inner rings will add greatly to the formation of central light concentrations. But those again will act back on the bar and may even fundamentally destroy it (Hasan & Norman, 1990; Norman et al., 1996; Shen & Sellwood, 2004).

A different perspective is given by the study of star formations histories. Through the advance of stellar population synthesis codes (Vazdekis, 1999; Bruzual & Charlot, 2003; Thomas et al., 2003; Le Borgne et al., 2004; Maraston, 1998, 2005; Schiavon, 2007; Vazdekis et al., 2010) we are now able to infer the ages and chemical compositions of a stellar population. This is done through the measurement of either colours or the strengths of certain spectral features and the comparison with the model spectra or even the direct

fitting of the full spectrum. Derived parameters are typically the age, the metallicity and the alpha element over-abundance.

The alpha element ( $Mg$ ,  $O$ , etc) enhancement with respect to iron is thought to trace the mode of star formation history. As alpha elements are the product of type II supernovae, they trace rapid and short lived formation histories. Once type Ia supernovae — which result from lower mass and hence longer lived stars — start to add iron to the interstellar medium, the alpha element over-abundance in newly formed stars starts to decrease. Therefore high alpha element over abundances point to short lived star formation histories or star bursts (Worthey et al., 1992; Weiss et al., 1995; Terndrup, 1993; Thomas et al., 1999, 2002). It is seen that many bulges of lenticular galaxies show alpha element over-abundances (Bender & Paquet, 1995; Fisher et al., 1996; Kuntschner et al., 2006), while later type galaxies show alpha to iron ratios which are typically more similar to the solar value (Jablonka et al., 1996, see also Peletier et al., 2007 for a review and recent results).

In the recent years attempts have been made to replace single stellar population fits by the fitting of more complex formation histories (e.g. (MacArthur et al., 2009)). In it's easiest form the single burst history is replaced by multiple bursts or an exponentially declining star formation history. If the signal to noise of the data is large enough and the understanding of the stellar evolution is detailed enough then this technique promises to be extremely powerful as it probes the formation history directly. However, once the assumption of a single star formation burst is dropped, the number of the fitted parameters and their uncertainty increase. Further, we begin to understand that the assumption of a fixed radial locus of a population may be invalid. Simulations indicate that spiral structure drives radial migration of stars (Sellwood & Binney, 2002; Roškar et al., 2008). Therefore the composition of stars at a given location in a disk is not only a function of the formation history but also of the migration of stars into and out of that region. Work by Yoachim et al. (2010) recently delivered observational support for this theoretical concept.

As mentioned before, secular evolution — driven by bars and spiral structure — seems responsible for the building of pseudobulges. Naively one could expect that these systems then ought to be young and should show signs of recent star formation. However, Kormendy & Kennicutt (2004) argue from the abundances of cold gas in these systems and the star formation rates that are implied by the Schmitt-Kennicutt law (Kennicutt, 1998) that formation time scales are short. Then, as galactic bars were already abundant 5 *Gyrs* ago (Abraham et al., 1999; van den Bergh et al., 2002), pseudobulges could have any age between 5 and zero Gyrs. The search for ongoing star formation therefore will only detect systems which are currently being built. For a complete picture however, we need to study the complex star formation history in the central regions of spiral galaxies. Kormendy & Kennicutt (2004) state that such studies of stellar populations seem to be at odds with the picture of secular growth of pseudobulges as they mostly find old and quickly evolved populations, but then argue that these studies have been focussed on early type spirals, calling for additional studies like MacArthur et al. (2009) of larger samples including more equal numbers of different hubble types.

The progress of the understanding of disk formation histories and dynamical properties has in the recent years lacked behind the understanding of elliptical galaxies. The complex

physics in disk galaxies explains this partly. But part of the explanation lies simply in the difficulty of the observation of these objects. Typical central surface brightnesses lie significantly below those of bright elliptical galaxies (e.g. Lauer, 1985; Bender et al., 1988; Kormendy et al., 2008). A typical bright disk has a central surface brightness of  $\mu_B = 21.7 \text{ mag/''}^2$  (Freeman, 1970; see e.g. Fisher & Drory, 2010 for more recent data), but central surface brightnesses as low as  $\mu_B = 24 \text{ mag/''}^2$  and beyond are observed in low surface brightness galaxies (LSBs) (e.g. de Blok et al., 1995). Studies addressing these objects require highly efficient spectroscopic instruments and large aperture telescopes.

On the other hand, at the same time relatively large instrumental resolutions are needed. Experience shows that the instrumental dispersion should at least be of the same order as the objects that are observed if one wishes to recover the stellar velocity dispersion. In addition to the dispersion even the recovery of higher moments of the line of sight velocity distributions (LOSVDs) may be desired (Bender et al., 1994; Mehlert et al., 2000). The symmetric and asymmetric deviations of purely gaussian distributions allow to break the degeneracy between different orbital structures. This further pushes the need for high instrumental resolutions. In addition, the measurement of the depth of spectral features in disk galaxies is often hindered by the presence of nebular emissions which fill in the absorption feature. This situation is especially severe for the hydrogen lines which are important tracers of the stellar age. For an accurate measurement of those absorptions one needs to accurately model and subtract the nebular emission which again becomes only possible through high instrumental dispersions.

Typical velocity dispersions of stellar disks lie in the order of a few tens of  $\text{kms}^{-1}$  (e.g. Bottema, 1993). Observations of stars in the solar neighbourhood (Edvardsson et al., 1993; Soubiran et al., 2008) and of cold gas in other disk galaxies (Tamburro et al., 2009) suggest that stars in disks form with  $\simeq 10 \text{ kms}^{-1}$ . This corresponds to an instrumental resolution of  $R \simeq 10000$  which is rarely found in instruments suitable for spatially resolved extragalactic astronomy. The reason is simple: The higher the resolution, the larger the number of spectral resolution elements into which the light is divided and hence the lower the number of photons that end up in the elements. This means that the low signal that corresponds to the lower surface brightness objects is diminished even further by the high resolution.

In summary, not only are the dynamics of disk systems difficult to understand, also are they difficult to measure. But, the knowledge gained from such endeavours is well worth the effort.

For instance, we begin to understand that pseudobulges form the majority of central stellar mass concentrations, and consequently the majority of the stellar mass in our local universe is located in disks (Kormendy & Kennicutt, 2004; Kormendy et al., 2010; Fisher & Drory, 2011). Cosmological simulations just start to produce realistic disk galaxies, whilst typically with too large bulge to total ratios. Highly resolved observations of disk systems will establish important constraints on the coming generations of simulations.

The study of bars and the resonances they create will further strengthen our understanding of the process of secular evolution. Suitable instrumentation will allow us to make precise measurements of pattern speeds in larger samples of galaxies. We will learn about

the state of their evolution, be able to test analytical predictions concerning the radial location of resonances and may be able to make a stronger case for or against a potential clash between n-body simulations and observations.

Low surface brightness galaxies give further access to the direct study of the shape of gravitational potentials. While cosmological simulations suggest cuspy central dark matter halo slopes (Navarro et al., 1996, 2010), observations keep disagreeing and favour flat central density slopes (Burkert, 1995; Kuzio de Naray et al., 2008; de Blok et al., 2008; Oh et al., 2011; see de Blok, 2010 for a review). Observations which are sufficient to resolve their low velocity dispersions will enable us to derive central density slopes.

The low surface brightnesses of disk systems may be addressed with large telescopes. In the second part of this thesis we present results from a longslit survey that we carried out at the 9.1 m Hobby-Eberly Telescope of the McDonald Observatory in Texas. Here we systematically investigate if morphological and structural differences between bulge types are reflected in the dynamics as well. We will see that there is evidence that the morphological and structural differences of classical bulges and pseudobulges are reflected in the radial variation of their velocity dispersions.

But, if one is willing to sacrifice spatial resolution, then also the size of the spatial resolution elements may be increased in order to integrate over larger amounts of signal. In the first part of this thesis we will describe an integral field spectrograph that we build specifically for the study of the dynamics of local disk galaxies at 2 m class telescopes.

## 1.2 Integral Field Spectroscopy

The most common type of spectrograph in astronomy — the slit spectrograph — places a slit-like aperture in the focal plane of the telescope. The light that is admitted through the slit is then collimated through a system of either mirrors or lenses and is then split into its individual wavelength components by a dispersive element. The dispersive element is typically a prism or a grating, sometimes also a combination of both. Placed at an appropriate location within the optical light path where the light is collimated or at least close-to collimated, the disperser splits the light into its colour components either by means of differential refraction (in the case of a prism) or by means of interference (in the case of a grating). A camera subsequently records the spectra.

Newton himself experimented with the combination of prisms and lenses in the 16-th century which subsequently led to his *New Theory about Light and Color* published by the Royal Society in 1672 (Newton, 1672). Since it's application to the study of the solar spectrum by Joseph von Fraunhofer, spectroscopy has had immense impact on our understanding of nature. Most important achievements in astronomy include — but are by far not limited to — the discovery of absorption lines in the solar and stellar spectra (William Hyde Wollaston 1802, Fraunhofer 1814) and the subsequent realization that stars are made out of the same elements that we find on earth. Spectrographs allowed us to study the abundances of elements in stars and galaxies. Their application led to the discovery of the flatness of rotation curves in disk galaxies (Rubin et al., 1985) which gave first

indication — while not proof — for the existence of dark matter Freeman (1970). The discovery of the expansion of the universe and Hubble’s law became only possible through spectrographs (Hubble, 1929), and it is of course again spectrographs which through the application of Hubble’s law enable us to measure distances on largest scales and allow us to study the structure of the universe itself.

The reduction of spatial dimension in a slit spectrograph is necessary due to the fact that our detectors are yet only two-dimensional. The second dimension is needed for the dispersion of the light, i.e. the wavelength dimension. However, many science cases make it desirable, to be able to obtain spectra for every point in a two-dimensional field of view. Techniques that do allow to record spectra in two spatial dimensions are referred to as Integral Field Spectroscopy, spatially resolved spectroscopy, or 3D spectroscopy.

Several technical aspects make a Integral Field Spectroscopy beneficial for the observing procedure: All spectroscopy that targets point-like sources, e.g. stars or Active Galactic Nuclei suffers from *slit losses*. If the slit width is in the order of the seeing disk then instances of poor seeing will lead to light loss at the slit aperture. This may in principle be mitigated through the widening of the slit, but this then decreases the spectral resolution which, depending on the science case, may not be desirable. Of course the same problem applies to other apertures such as circular holes or the light admitting core of an optical fiber. Errors or glitches in the guiding will generally cause similar effects. Further, differential atmospheric refraction causes a wavelength dependent position of the object in the focal plane and hence to wavelength dependent slit losses. These effects make flux calibration of long slit spectra inherently difficult.

Further, in many situations the exact position of the target of interest is not known precisely. In that case slits may miss the target and hence fail to record the desired data. This situation is particularly problematic in the case of transient phenomena such as supernova or gamma ray bursts.

But the technique of Integral Field Spectroscopy is also scientifically very attractive. Galaxies are not one dimensional objects. Therefore almost every spectroscopic study of galaxies profits from data in two spatial dimensions. For instance kinematic studies that are limited to one or two position angles of the slit aperture will necessarily miss the signature of non-axis symmetric structures that fall between the observed position angles. Work on the composition of stellar populations and the composition of the inter-stellar material will miss out on the dependence of the exact location of the intersection of the line of sight with the observed system. Effects of stellar subcomponents such as bars or spiral structure on the line of sight velocity distributions will not be recovered through a single one-dimensional observation.

Another example for the usefulness of Integral Field Spectroscopy are low surface brightness situations such as the outskirts of disk or elliptical galaxies. While this seems to misuse the *spatially resolved aspect* of such data, spatially resolved spectroscopy offers the possibility of spatial binning. The spatial resolution elements are combined in order to improve the signal to noise. This of course sacrifices the spatial information for the sake of signal strength, however the spectral resolution remains unchanged. This is different from the situation of slit spectroscopy where the widening of the slit always results in the loss of

spectral resolution.

Two classes of instruments exist which realize Integral Field Spectroscopy:

Scanning spectrometers use the time domain to record the spectrum. The scanning can occur either in wavelength dimension as in the case of Fabry-Perot spectrometers (Taylor & Atherton, 1980; Boulesteix et al., 1984) and Fourier-Transform Spectrometers (Maillard, 1995), but also in one spatial direction as in the case of the scanning long slit spectrometer (Wilkinson et al., 1986).

Integral Field Spectrographs, on the other hand, record all the information in a single exposure. In all cases these instruments are basically composed of two parts. The Integral Field Unit (IFU) is located in the focal plane of the telescope. It splits the two-dimensional field of view into subapertures and rearranges them into a format that can be fed into the spectrograph. The spectrograph then records the spectra.

Various techniques exist for the realization of IFUs. The first such instrument used optical fibers to split the light into sub apertures (Vanderriest, 1980). The fibers were arranged into a two-dimensional array of hexagonal shape in the focal plane and connected to a — in principle a usual — slit spectrograph.

The so-called Tiger spectrograph (Bacon et al., 1995) used a lenslet array to split the light into sub apertures. More recently this Tiger principle has been implemented in the SAURON spectrograph (Copin et al., 2000) where it has proven — and continues to do so — to be a vastly successful tool to study the stellar populations and stellar and gaseous dynamics in nearby galaxies.

Finally, image slicers use mirrors to split the field of view into a number of parallel slit-apertures — the slices — and then recombine those into a single long slit. A well know example is the IFU of the SINFONI spectrograph (Eisenhauer et al., 2003a,b) which is operated at the Very Large Telescope (VLT) of the European Southern Observatory (ESO) in Chile. SINFONI combines the IFS with an Adaptive Optics module into a powerful instrument for high spatial resolution spectroscopy.

Integral Field Spectroscopy has developed quickly over the past years and is now one of the major workhorses of modern astronomy. Instruments exist at all major optical Observatories in the world and essentially all future facilities including the James Web Space Telescope will be equipped with IFUs.

Along with the development of IFS — but driven mostly by the needs of telecommunication — the field of optical fibers developed dramatically. They can be produced to a wide range of specifications at low cost, and with high and stable quality. Extremely pure materials yield very low absorption losses. The knowledge of the handling and treatment of fibers has progressed equally fast allowing for very high coupling efficiencies and little losses of beam quality within the fibers. The realisation of an IFU with optical fibers is conceptionally trivial: A bundle of fibers is arranged into a two dimensional array of arbitrary shape within the focal plane. At the spectrograph side the bundle is then fanned out into a slit which is then coupled to a more-or-less normal spectrograph. The simplicity of their construction and yet high optical performance make fiber based IFUs a very attractive technology for the design of new spectrographs. In this thesis we will discuss the construction of such an instrument for 2 m class telescopes and present first results from

the commissioning runs.

### 1.3 Outline of this Thesis

This thesis is divided into two main parts. We first describe the construction and the commissioning of the new IFU spectrograph VIRUS-W. The construction of the new 2m Fraunhofer telescope of the University Observatory on the mountain Wendelstein in the Bavarian Alps sparked the development of such an instrument for extragalactic studies at 2m class telescopes. In the next chapter we will briefly motivate this instrumentation effort and then discuss the instrument design in §2.1. We will give an overview over the control software, the observation strategies and the data reduction in §2.2. In chapter 3 we then present first results from the commissioning and discuss the achieved instrumental resolution and throughput, the collection of kinematic and spectrophotometric template stars. In chapter 3.8 we report on the observations of three of the galaxies from the commissioning run and present preliminary kinematic maps and measurements of Lick indices. In chapter 4 we will then present the longslit survey of bulges that we conducted with the LRS spectrograph at the HET telescope. We conclude in chapter 5 and give an overview on the ongoing projects with VIRUS-W and the next steps for the longslit survey data.

## Chapter 2

# VIRUS-W: The Construction of a new Wide Field of View and Large Spectral Resolution Integral Field Unit Spectrograph <sup>1</sup>

The University Observatory in Munich about to complete a new 2 m telescope on top of the mountain Wendelstein in Bavaria, Germany (Hopp et al., 2008). In parallel to the construction of the telescope a number of instrumentation projects have been initiated (Grupp et al., 2008). In this thesis we develop the IFU spectrograph VIRUS-W. While being developed as part of the Wendelstein 2 m instrumentation efforts, this spectrograph is designed for flexible use at different telescopes as well. The design is heavily based on the VIRUS spectrograph that is proposed for the HETDEX experiment (Hill et al., 2006, 2010). A prototype of this instrument is already in operation (Hill et al., 2008b) and has successfully demonstrated its science capability in several published studies (Blanc et al., 2009, 2010a; Yoachim et al., 2010; Adams et al., 2011; Murphy et al., 2011).

The spectrograph has two different modes of spectral resolution: A  $R \simeq 3300$  mode for stellar populations studies of nearby galaxies, and a  $R \simeq 8700$  mode to resolve the velocity dispersions which are expected in kinematically cold systems like disks and pseudobulges of spiral galaxies. A large angular field of view of  $150'' \times 75''$  will give full coverage of the bulge regions of most local late type galaxies in one or two pointings with a fill factor of 1/3. Alternatively a dithering mode will give close to 100% spatial coverage in three pointings per field.

The combination of a relatively high spectral resolution and large field coverage places it into a yet very sparsely populated region in the resolution vs. field coverage plane of already existing IFUs. Given an about eight times larger spatial coverage and a spectral resolution which is higher by a factor of two, VIRUS-W will allow the extension of studies of – for example – the SAURON spectrograph (Bacon et al., 2001; de Zeeuw et al., 2002)

---

<sup>1</sup>Parts of this chapter have been published as Fabricius et al. (2008)

into the direction local late type and lower mass galaxies.

## 2.1 Instrument Design

### 2.1.1 VIRUS-W's heritage

The design of VIRUS-W is derived from, and closely related to the VIRUS spectrograph (Hill et al., 2010) for the Hobby-Eberly Telescope Dark Energy Experiment (HETDEX; Hill et al., 2004, 2008a). HETDEX will use 150 of these instruments at the upgraded Hobby-Eberly Telescope (HET; Ramsey et al., 1998a; Savage et al., 2010) of the McDonald Observatory in Texas and operate them simultaneously for a blind spectroscopic survey that will search for Lyman-Alpha emitting Galaxies in the high-redshift universe. The VIRUS design was first realized in a prototype instrument VIRUS-P (Hill et al., 2008b), which has been tested on multiple occasions at the HET and is now a facility instrument of the 2.7 m Harlan J. Smith Telescope also at McDonald. At the 2.7 m, VIRUS-P has already successfully completed the HETDEX pilot survey (Blanc et al., 2010a; Adams et al., 2011; Finkelstein et al., 2011) and continues to be a highly requested instrument that contributes to large programs such as the VIRUS-P Exploration of Nearby Galaxies (VENGA; Blanc et al., 2010b) and VIRUS-P Investigation of the Extreme Environments of Starbursts (VIXENS; PI Amanda Heiderman).

VIRUS-P's IFU is fiber based. On the telescope side the fibers are arranged into a square array with a physical size of about  $5\text{ mm} \times 5\text{ mm}$ , corresponding to a FoV of  $102'' \times 102''$  on sky. A focal reducer transforms the  $f/8.8$  beam at the Ritchey-Chrétien focus of the 2.7 m telescope into a  $f/3.65$  beam. The shutter and an order separating filter are placed in front of the focal reducer. On the spectrograph side the fibers are arranged into a  $\simeq 80\text{ mm}$  long pseudoslit. They face a spherical collimating mirror. The collimated light is reflected back into the direction of the slit. The slit is actually located within a slot in a flat folding mirror that then reflects the light to the dispersing element — an 831  $\text{ll/mm}$  Volume-Phase-Holographic grating (VPH). A Schmidt camera then records the spectra. The Schmidt plate of the camera corrects spherical aberrations that are introduced by both the spherical collimator on the entrance side and the spherical condenser in the camera. This double-Schmidt design allows for small  $f$ -numbers while keeping the number of optical elements needed for the correction of aberrations small. For its spectral range of  $3400\text{ \AA}$  to  $5700\text{ \AA}$  in a single arm, VIRUS-P only uses four optically active elements: Two lenses – the Schmidt-Plate and a spherical field flattener in front of the detector– and two spherical mirrors. This makes the VIRUS design very efficient both in terms of throughput and cost.

The success of the prototype and our group's access to the details of the design made it a natural choice as a basis for the VIRUS-W instrument.

### 2.1.2 Spectrograph Layout

The requirement of a larger spectral resolution, differences in the telescope optics, and the ease of the production lead to several modifications from the prototype design:

As in all on-axis Schmidt designs, the VIRUS-P detector is located in the beam path which leads to a central obscuration. In its HETDEX application this obscuration is matched to the one that is caused by the prime focus assembly of the telescope itself, and hence causes no additional loss of light as long as the fibers maintain the focal ratio of the light which they are fed with. But the situation is different for VIRUS-W, which will be operated at various telescopes. Smaller central obstructions in other telescopes would lead to light loss and an increase of stray light in a Schmidt type design.

Secondly, the location of the liquid nitrogen cooled detector within the Schmidt camera couples the optics, cryogenics and electronics to each other intimately. The introduction of a refractive camera lens in VIRUS-W allowed us to separate the lens from the detector head which hosts the electronics and the cryogenics. Both parts could then be given to different manufacturers and only the final alignment of camera lens to camera head has to be done during the integration. The final design uses a 200 mm aperture  $f/1.4$  lens consisting of five lenses in four groups. The separate closed-cycle cooled camera head houses a  $2\text{ k} \times 4\text{ k}$   $15\ \mu\text{m}$  pixel backside illuminated CCD detector.

Finally, while VIRUS-P is mounted in a gimbal that is attached to the telescope flange, VIRUS-W is bench-mounted. The fiber bundle is 25 m long which allows us to place the instrument in a separate, temperature controlled room.

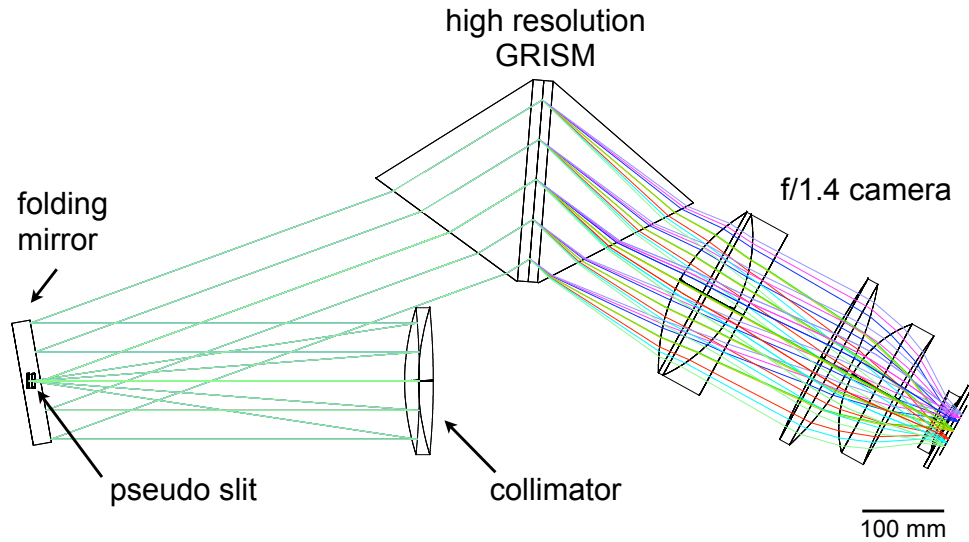


Figure 2.1 Layout of the spectrograph in the high resolution mode. The light enters the spectrograph on the left hand side through the pseudoslit which is located in a slot within a flat folding mirror. The slit is oriented perpendicular to the image plane in this figure. In the high resolution mode a combination of two large prisms and a 3300 l/mm VPH grating — a GRISM — act as dispersive element. Note, the prisms add little to the dispersive power of the grating. Their primary function is to couple the light into, and out of the grating. Further, their geometry is chosen such that the camera location stays fixed between the two resolution modes. The 200 mm aperture,  $f/1.4$  camera on the right-hand side records the spectra.

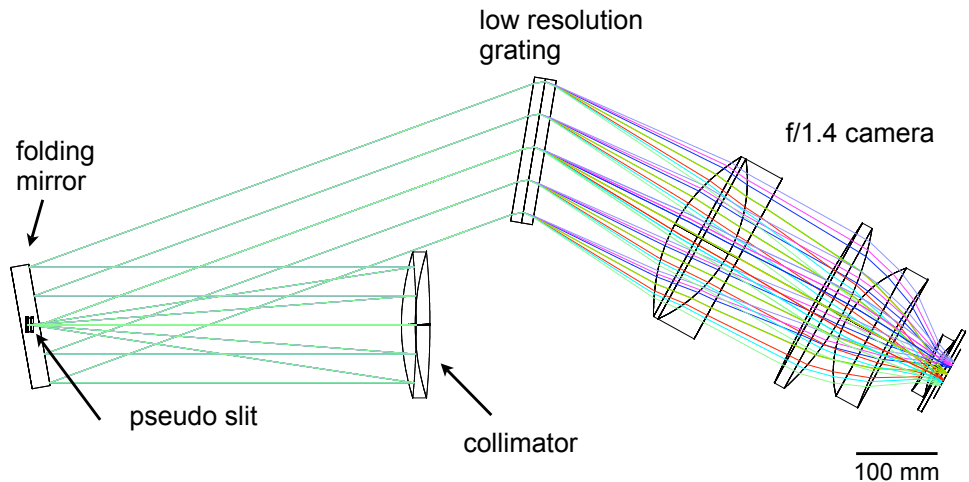


Figure 2.2 As Fig. 2.1 but low resolution configuration. In this mode, the dispersive element is a 1900 l/mm 160 mm  $\times$  170 mm large VPH grating. The camera position stays fixed between the two different resolutions modes.

The spectrograph now offers two different modes of spectral resolution: A  $R \simeq 3300$  mode mainly dedicated to stellar populations studies, and a  $R \simeq 8700$  mode to resolve the small velocity dispersions which are expected in kinematically cold systems. The increase of resolution with respect to the original design is achieved by a higher fringe-frequency grating and a decrease of fiber size — and hence a decrease of spot size on the detector. The smaller fibers also allow for a slight increase of the total number of fibers in the IFU. The input focal ratio of the spectrograph is  $f/3.35$  and is matched to the output numerical aperture of the optical fibers.

On the spectrograph side, the fibers are arrayed in a pseudoslit that is fed into the actual spectrograph. On the telescope side the fibers are arranged into a rectangular IFU with a fill factor of  $1/3$ . The IFU offers a large angular field of view of  $150'' \times 75''$  at a 2 m telescope and  $105'' \times 55''$  at a 2.7 m telescope.

In Fig. 2.1 and 2.2 we show the schematic layout of the instrument in the high and the low resolution mode. The figure shows the perspective from the top facing the optical bench. The light enters the spectrograph through the pseudoslit on the left hand side of the image. The 200 mm aperture camera is located on the right hand side of the image. The respective grating is located in the center of the image. Both gratings are mounted on a sliding stage which allows for automated exchange. There is also a *free* position which we introduced to allow for a flat fielding source that faces the camera directly. At the time of writing this has not been implemented.

The high resolution mode with  $R \simeq 8700$  (see Fig. 2.1) enables the investigator to study velocity dispersions down to 15 km/s. The designed wavelength range is 515 Å wide and reaches from 4930 Å to 5445 Å. This covers the [O III] lines at 4959 Å and 5007 Å and the Mg lines at 5167 Å, 5172 Å and 5183 Å up to a redshift of 0.03 (see Fig. 2.3).

VIRUS-W uses one of the OmegaCam (Deul et al., 2002) spare CCDs. This CCD is larger than accounted for in the original design. Hence the actual covered wavelength range is larger (4850 Å– 5475 Å) but there is a significant decrease of resolution and throughput at the spectral ends.

The grating is a 3300 l/mm VPH grating *blazed* (see 2.1.10) at  $35.9^\circ$  (inside fused silica). Prisms are attached to the VPH surfaces to avoid internal reflection and to keep the camera location fixed during the exchange of the two resolution modes. Due to the larger angle of incidence this grating is larger than in the low resolution case, and is 170 mm  $\times$  220 mm in size.

The low resolution mode with  $R \simeq 3300$  (see Fig. 2.2) has a nominal wavelength range of 4750 Å to 5600 Å. In addition to the already mentioned spectral features this enables the observation of  $H_\beta$  and the iron features Fe5015, Fe5270, Fe5335 and Fe5406 and their corresponding Lick pseudo-continua (Trager et al., 1998; Worthey et al., 1994) up to  $z \simeq 0.03$  (see Fig. 2.3 and §3.7). Again, the actual covered wavelength range is larger due to the larger detector and now covers 4340 Å - 6042 Å. This adds further Lick indices, namely Fe4383, Ca4531, Fe4668, Fe5709, Fe5782, and Na D.

The dispersive element is again a VPH grating with 1900 l/mm blazed at  $38^\circ$ . The size of this grating is 145 mm  $\times$  165 mm. Since here the diffraction angle is smaller, additional prisms are not required.

---

<b>spectral coverage, nominal</b>	4930 Å– 5445 Å
<b>spectral coverage, actual</b>	4850 Å– 5475 Å
<b>resolution (<math>\Delta\lambda/\lambda</math>)</b>	7040 to 9270 (depending on wavelength); mean: 8660
<b>resolution (<math>\sigma</math>)</b>	14 kms <sup>-1</sup> to 18 kms <sup>-1</sup> ; mean: 15 kms <sup>-1</sup>
<b>linear dispersion</b>	0.19 Å/px
<b>grating</b>	3300 ll/mm VPH grating sandwiched between two prisms

---

Table 2.1 High resolution mode characteristics.

In Fig. 2.4 we show a photograph of the fully assembled instrument shortly before shipping to the McDonald Observatory.

---

<b>spectral coverage, nominal</b>	4750 Å - 5600 Å
<b>spectral coverage, actual</b>	4340 Å - 6042 Å
<b>resolution (<math>\Delta\lambda/\lambda</math>)</b>	2890 to 4450 (depending on wavelength); mean: 3270
<b>resolution (<math>\sigma</math>)</b>	28 kms <sup>-1</sup> to 44 kms <sup>-1</sup> ; mean: 39 kms <sup>-1</sup>
<b>linear dispersion</b>	0.52 Å/px
<b>grating</b>	1900 ll/mm VPH grating

---

Table 2.2 Low resolution mode characteristics.

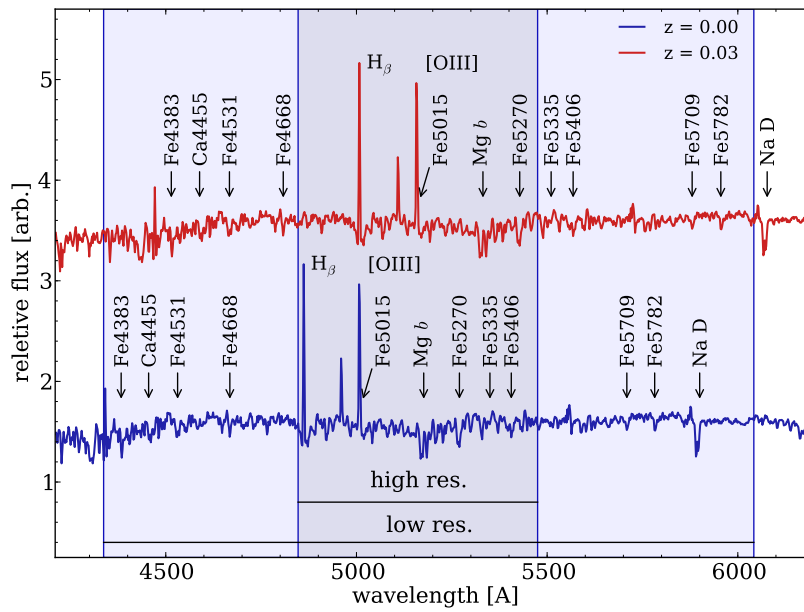


Figure 2.3 Averaged spectrum of 29 SDSS local spiral galaxies at rest frame and  $z=0.03$ . The shaded areas correspond to the spectral coverage of the spectrograph. In the high resolution mode the covered wavelength range reaches from  $4930 \text{ \AA}$  to  $5445 \text{ \AA}$ . This covers the for example [O III] lines at  $4959 \text{ \AA}$  and  $5007 \text{ \AA}$  and the Mg lines at  $5167 \text{ \AA}$ ,  $5172 \text{ \AA}$  and  $5183 \text{ \AA}$  up to a redshift of 0.03. The low resolution mode covers the wavelength range from  $4750 \text{ \AA}$  to  $5600 \text{ \AA}$ . This enables the observation of  $H_\beta$  and the iron lines at  $5270 \text{ \AA}$ ,  $5335 \text{ \AA}$  and  $5406 \text{ \AA}$  and their corresponding pseudo-continua up to  $z \simeq 0.03$ .

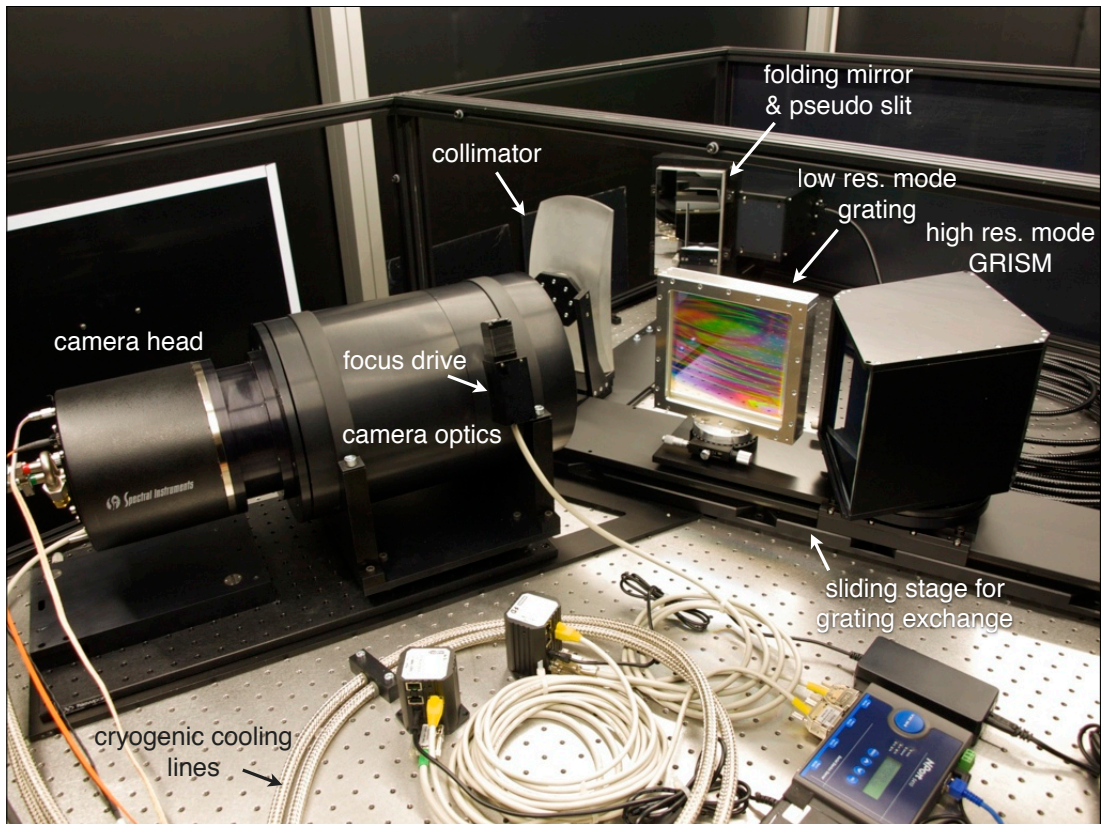


Figure 2.4 The complete spectrograph assembled. The image was taken in the optical laboratory in Munich shortly before the instrument was packed and shipped to the McDonald Observatory. The devices seen in the bottom half are the motor controllers for the grating exchange and the camera focus drive, the ethernet to RS232 converter, and power supplies.

### 2.1.3 Individual Elements

In the following we will describe the individual elements of VIRUS-W and discuss their throughput where possible. The throughput measurements are subsequently used in §3.2 where we compare the overall throughput to actual measurements. We follow the light, starting with the telescope interface and ending with the detector.

### 2.1.4 Guider & Focal reducer

VIRUS-W currently uses the guiding unit of its sister instrument VIRUS-P at the 2.7 m telescope<sup>2</sup>. The guiding unit offers offset auto-guiding through an off-the-shelf Apogee Alta camera, a focal reducer and a shutter. The mechanical design of the VIRUS-W IFU head replicates that of VIRUS-P in order to ensure easy exchange between the two instruments. The unit is mounted at the bend Cassegrain  $f/8.8$  focus.

The guide field is coupled into the guide camera with a flat pickoff mirror that is located right next the aperture of the focal reducer. The guide camera is located on the other side of that aperture (see Fig. 2.5). This creates a guide field that is located about 9' north of the center of the IFU. The guider is equipped with a  $B + V$  filter and its field has a size of  $4.4' \times 4.4'$  with a pixel size of  $\simeq 0.53''$ . After the astrometric calibration this setup proved to allow the IFU to be positioned with  $\simeq 0.5''$  accuracy through exact sub-pixel positioning of the guide stars into the guide field (see §2.2.4).

The 2.7 m telescope delivers a  $f/8.8$  beam. A telecentric, dioptric, two-group focal reducer (see Fig. 2.6) transforms this beam to  $f/3.65$  before feeding it to the IFU. The iris shutter and the filter are located in front of the focal reducer, the IFU directly behind. The focal reduction increases the FoV but also mitigates the effect of focal ratio degradation.

The latter is an important aspect of the instrumental design and consequence of a learning process that occurred in the field of astronomical instrumentation over the past decades. Slow (large focal ratio) beams do not fill the numerical aperture of optical fibers. Bending and stresses in the fiber material tend to degrade the focal ratio of such slow beams more strongly than for beams which fill the fiber's numerical aperture (Grupp, 2006). Hence, if a fiber instrument was built to be fed with a large focal ratio beam, and the optics after the fibers would also only accept such a beam then the light of a degraded beam would be lost. But even if the instrument was able to accept all the degraded light, then the variability of the output focal ratio would cause a change of the instrumental PSF as a function of the amount of stress in the fibers, leading to generally poor instrumental stability. Spectrographs need to be specifically designed to accept all the light exiting the fibers. Consequently fibers are preferably fed with low focal ratio beams and the optics of fiber spectrographs are fast.

The detailed surface prescription of the focal reducer optics is given in Table 2.3.

---

<sup>2</sup>Note: Neither the guide unit nor the focal reducer were developed as part of this thesis. They are included in the description by courtesy of Phillip MacQueen for completeness as at the time of writing no publication describes their design.

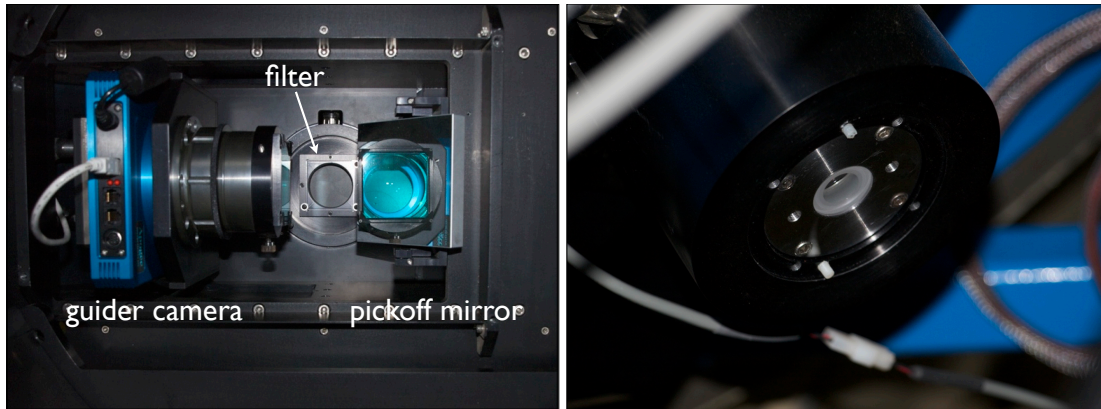


Figure 2.5 VIRUS-W uses the offset guider and focal reducer of its sister instrument VIRUS-P. The left photograph was taken from the inside of the telescope tube. The guider camera can be seen on the left. The pickoff mirror on the right side reflects a guide field to the camera that is offset by about  $9'$  from the center of the IFU. The mount for the filter can be seen in the center of the image. When this picture was taken, a different filter — clear to the eye — was mounted. The shutter blades can be seen behind the filter. The right picture shows the backside of the focal reducer to which the IFU head attaches directly.

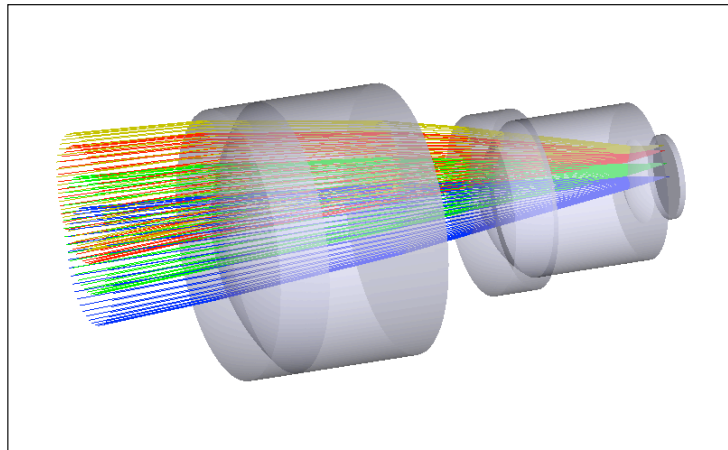


Figure 2.6 The focal reducer converts the  $f/8.8$  beam which is delivered by the 2.7 m into an  $f/3.65$  beam.

Grp.	Surf.	Glass	R of curv. (mm)	Diam. (mm)	thickness (mm)	Notes
1	1	PBL6Y	60.8677	45	4	front surface
1	2	S-FSL5Y	32.74381	45	30	
1	3	-	$\infty$	45	11.81	
2	1	PBL6Y	37.02207	30	4	IFU normalizing plate
2	2	S-FSL5Y	15.98734	26	25	
2	3		13.37092	14	6.478566	
		silica	$\infty$	14	1	

Table 2.3 Surface description for the VIRUS-P focal reducer that is also used by VIRUS-W (courtesy Phillip MacQueen).

### 2.1.5 Filters

Filters are often a necessity in spectrographs to reject higher order refractions that would otherwise interfere with the wavelength range of interest. Also, light outside of the spectral range can scatter uncontrolled within the instrument and create large stray light levels. Lab tests showed that the high resolution mode suffers severely from contamination of red light that is scattered onto the detector. We purchased a filter that is specifically designed to reject light outside of the nominally covered wavelength range. The FWHM wavelength range of this filter is 4917 Å– 5474 Å with a mean transmission of 98.6% in the pass band. The filter blocks 99.999% outside of 4827 Å– 5548 Å.

However, as explained above, the usable wavelength range of VIRUS-W is somewhat larger (4850 Å– 5480 Å) and does give access to the astrophysically very important  $H_{\beta}$  line at 4861 Å, if one is willing to accept the lower throughput in this region. It is possible to use a SDSS  $g$  filter in this case. It does not block the light beyond the blue end of the nominal range but tests showed that this introduces no additional stray light. The caveat of the SDSS  $g$  filter however, is its 11% lower throughput of (87.4% compared to 98.6%, see Fig. 2.8).

The filter — either the SDSS  $g$  or the specialized VIRUS-W filter — is placed in front of the IFU focal reducer. A compensator plate, that is placed in front of the guider, assures that guider and IFU remain confocal. The low resolution mode does not have a dedicated filter at the time of the writing. Tests showed that the level of stray light in this mode is acceptable.

### 2.1.6 Integral Field Unit

The 267 fibers of VIRUS-W’s IFU are arranged in a *densepack* geometry (Barden et al., 1998) with a fill-factor of 1/3. The rectangular field consists of 13 rows of alternating length of 20 and 21 fibers. The pitch between the fibers in one row is 260  $\mu\text{m}$  while the pitch between the rows is 225  $\mu\text{m}$ . The resulting array has outer dimensions of 5.46 mm  $\times$  2.96 mm. The core size of the fibers is 150  $\mu\text{m}$  while their outer diameter is 195  $\mu\text{m}$  in size (see Fig. 2.9). This translates to a fiber diameter of 3.1" and a FoV of 105"  $\times$  55" on sky at a

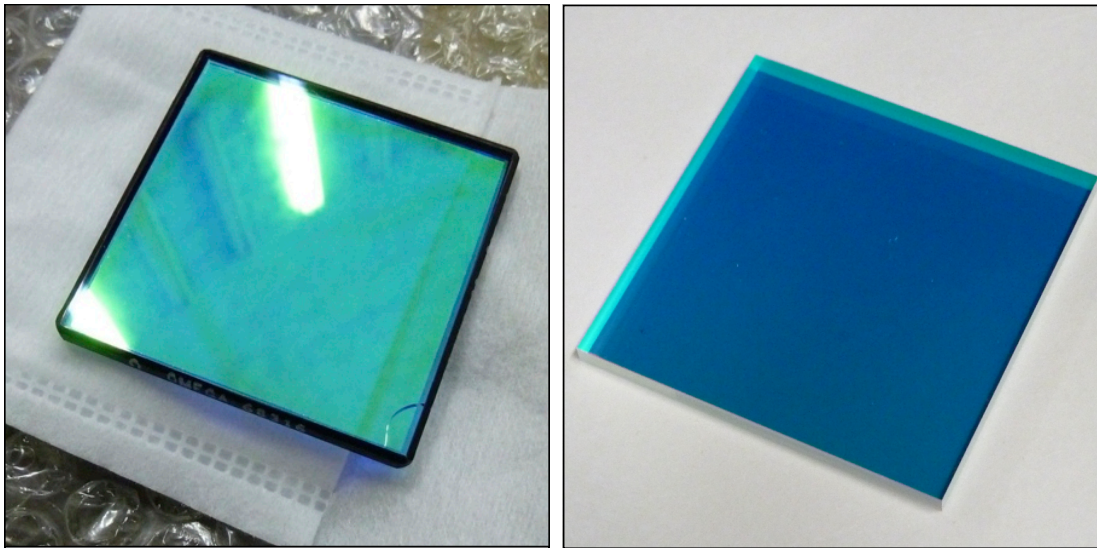


Figure 2.7 The  $50\text{ mm} \times 50\text{ mm}$  filters that are used to block light beyond the red end ( $5475\text{ \AA}$ ) of the nominal spectral range of the high resolution mode. Depending on the science case, one of these filters is used. The left picture shows the SDSS  $g$  filter. It gives access to  $H_\beta$  (whilst at low throughput). The right panel shows a picture of the dedicated filter that we purchased for the high resolution mode. It blocks light blue wards of  $4827\text{ \AA}$  and hence does not transmit light in the  $H_\beta$  regions, but it does on average give an 11% higher throughput. Note: The SDSS  $g$  filter has a little fracture in the lower right hand corner that occurred during the transport. The damage is a result of tensions in the filter material that also affected other filters that we purchased previously. However, the fracture is outside the beam path and has no negative impact on the optical quality.

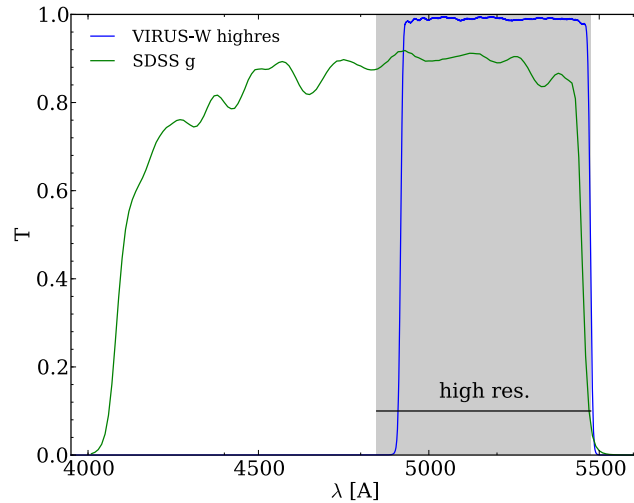


Figure 2.8 Transmission curves for the dedicated high resolution mode filter and the SDSS  $g$  band filter. Both filters block light redwards of the red end of the covered wavelength range. The SDSS  $g$  filter does however not block light beyond the blue end and allows us to study – for instance –  $H_{\beta}$ . The average throughput of the dedicated filter within the nominal range is with 98.6%, considerably higher than the SDSS  $g$  throughput (87.4%).

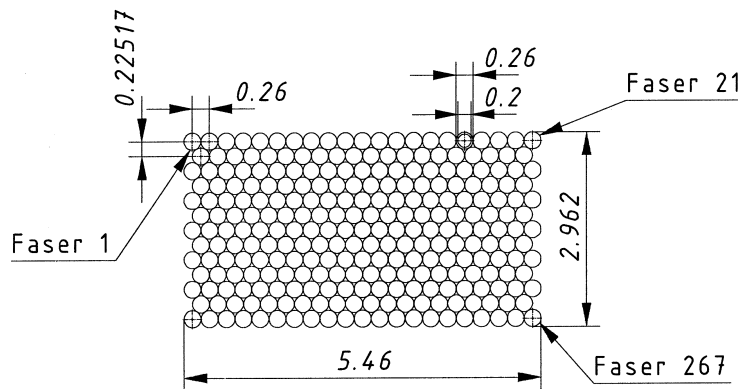


Figure 2.9 A mechanical drawing of the drilled-matrix array that is used to hold the fibers. It shows the mechanical dimensions of the IFU and the hexagonal densepack packing scheme of the fibers within the IFU. The mechanical dimensions are small but with a pixel scale of  $48 \mu\text{m}/''$  at the 2.7 m, the FoV becomes  $\approx 105'' \times 55''$  making this one of the largest IFUs on sky.

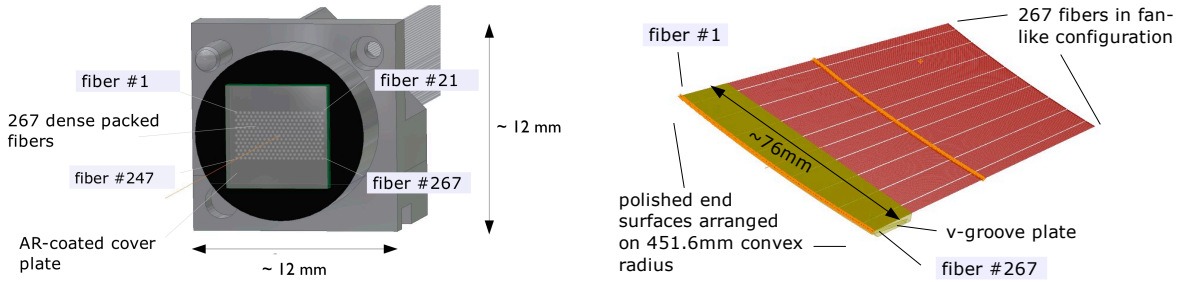


Figure 2.10 This rendered image of the IFU and slit was part of the specification document that was given to the manufacturer. It shows the anti-reflective coated cover plate in front of the IFU that is used to *heal* residual imperfections in the fiber end surfaces. Also, this image shows the mapping of the fibers from the IFU to the slit. The fibers are arranged by IFU rows within the slit. The upper left hand IFU corner is mapped to one end of the slit, the lower right hand IFU corner to the other end. The central IFU fiber is also located in the center of the slit.

2.7 m telescope and a  $f/3.65$  beam or a fiber diameter of 4.2" and a FoV of 144" x 75" at a 2.0 m telescope with the same beam (e.g. the Wendelstein Fraunhofer). The fill factor of the active fiber cores — i.e. the actual light accepting area with respect to the total IFU area — is 1/3. Therefore, in order to achieve a 100% coverage, three *dithered* exposures are needed. In §2.2.1 we discuss routines which facilitate dithered observations.

The fibers are arranged in IFU rows along the slit (see Fig. 2.10), the fiber in the upper left corner of the IFU is mapped to one end of the slit and the fiber in the lower right corner of the IFU is located at the other end of the slit. Sorting the fibers obviously facilitates the interpretation of the data during the observations and data reduction and reconstruction of the on-sky image. It has the additional advantage that fibers of similar signal level are located close to each other on the detector.

The fibers are held in place by a drilled stainless steel matrix. The holes were machined using a mechanical 200  $\mu\text{m}$  drill. Once the fibers were put in place, they were fixated with glue and the package was polished. A 1 mm thick, anti-reflective coated cover plate that is placed on top of the IFU, corrects for residual imperfections from the polishing process. An index matching gel, that is applied between the fiber-end surface and the glass plate, eliminates the air gap and the corresponding change of refractive index.

The usage of a drilled-matrix is a novel approach and different from the original design (Kelz et al., 2006), which used fused silica ferrules to create a hole matrix. The advantage of the drilled hole matrix lies in the very precise positioning of the fibers (typically  $\pm 6 \mu\text{m}$ ), which results from the accuracy of the drilling process and the small size of the gap between the outer fiber surface and the inner hole surface. A disadvantage of this approach is the blank, polished steel surface of the hole matrix, which will contribute to stray light and ghosts. We mitigated this effect through the application of a low-reflectivity chrome-oxide mask to the cover plate (see Fig. 2.10). The mask covers the matrix's steel surface outside of the actual fiber area.

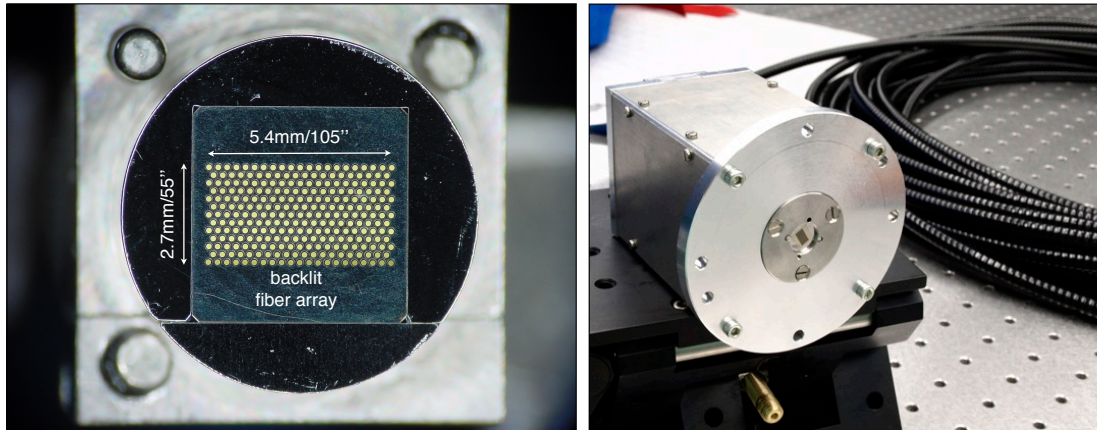


Figure 2.11 The Integral Field Unit (IFU) of the spectrograph. *Right panel:* The complete mechanical package that is attached to the telescope. The aluminium parts were coated black after this image was taken. The 25 m long fiber cable can be seen in the background. *Left panel:* Micrograph of the IFU. The 267 fibers are arranged in a hexagonal densepack scheme. The total fill factor is  $1/3$ . The fiber slit was illuminated while this image was taken.

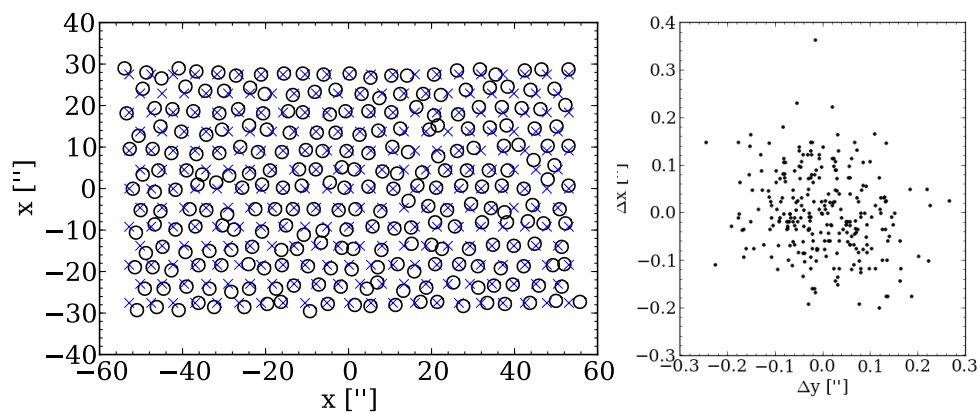


Figure 2.12 *Left panel:* The measured fiber centroid positions (circles) compared to the specified positions (crosses). The actual offsets are exaggerated by a factor of 10 for visibility. *Right panel:* The distribution of offsets in the x and y directions from the specified position. In the x direction we measure an RMS deviation of  $4.31 \mu\text{m}$  and in the y direction we find similarly  $4.15 \mu\text{m}$  corresponding to  $0.09''$  at the 2.7 m.

Table 2.4. Characteristics of the Integral Field Unit

<b>Physical</b>	
Fiber core size	150 $\mu\text{m}$
packing	hexagonal densepack
number of rows	13 $\mu\text{m}$
number of fibers within one row	21/20, alternating
fill factor	1/3
physical dimension of IFU	5.46 mm $\times$ 2.96 mm
positional accuracy of fibers	$RMS = 4.3 \mu\text{m}$
<b>At 2.7 m and <math>f/\# 3.65</math></b>	
fiber core diameter	3.14''
IFU field of view	105'' $\times$ 55''
positional accuracy of fibers	$RMS = 0.09''$
<b>At 2.0 m and <math>f/\# 3.65</math></b>	
fiber core diameter	4.2''
field of view	144'' $\times$ 75''
positional accuracy of fibers	$RMS = 0.12''$

Fig. 2.11 shows an image of the IFU through a microscope before the cover plate was applied. This image was used to measure the exact positions of the fiber centroids. The resulting data are later used for the astrometric solution and flux calibration of the obtained astronomical data. The offsets of the fiber centroids with respect to their specified positions are small. In the x direction we measure a RMS deviation of  $4.31 \mu\text{m}$  corresponding to  $0.09''$ , and in the y direction we find  $4.15 \mu\text{m}$  also corresponding to  $0.09''$  at the 2.7 m (see Fig. 2.12).

### 2.1.7 Fiber Bundle

The bundle consists of a total of 267 fibers and is 25 m long. Its length allows us to mount the spectrograph on a separate optical bench rather than having it attached to the telescope tube. While increasing the length of the bundle does increase the loss due to absorption in the fibers, this long bundle offers two key advantages: First, the instrument does not suffer flexure due to a change of the direction of gravity, and secondly the instrument can be moved from the telescope dome into a separate temperature controlled room. At Wendelstein there will be a dedicated spectrograph room. At the 2.7 m telescope the spectrograph

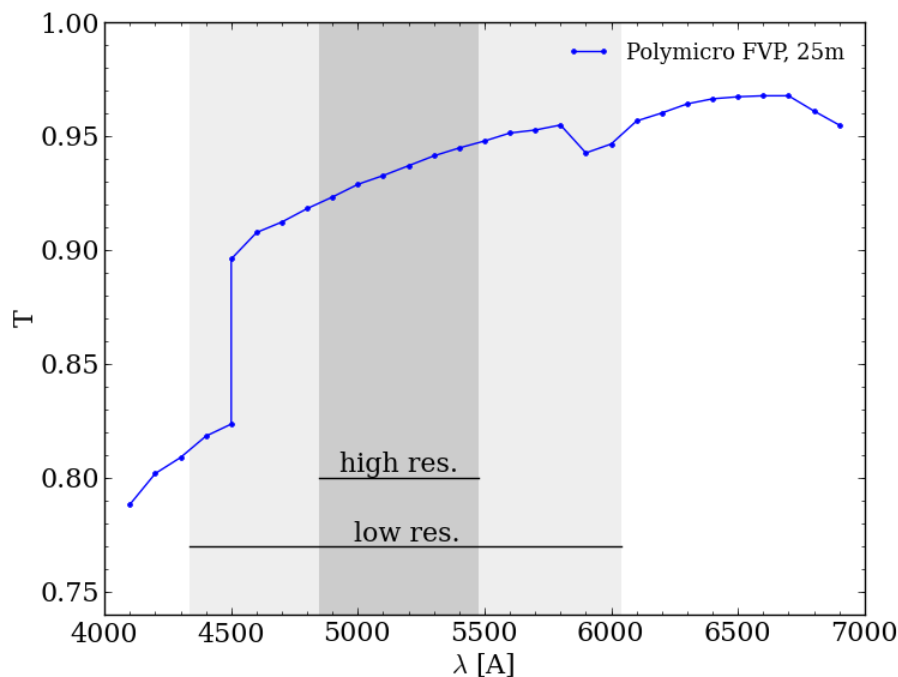


Figure 2.13 Transmission of the 25 m long FVP fibers. Courtesy: Polymicro Technologies

is located in the control room. This results in significantly smaller temperature swings as compared to the telescope dome and hence higher stability of the instrument.

Based on tests of similar bundles (Murphy et al., 2008) we chose Polymicro FVP (FVP150165195) fibers for the bundle as they were found to have the largest throughput in the VIRUS-W spectral range and cause little focal degradation. Due to the resolution goal (see §2.1.3) we chose a core size of  $150\ \mu\text{m}$ . The outer diameter is  $195\ \mu\text{m}$ , which is small enough to allow for the desired packing schemes, both on the IFU and on the slit side.

The manufacturer provides transmission data for the fibers. The mean transmission in the covered wavelength range for 25 m long fibers is 92% (see Fig. 2.13).

### 2.1.8 Slit Unit

The light enters the spectrograph through the 76 mm long pseudoslit that is located within a slot in the flat folding mirror (see Fig. 2.15 and 2.15). The slit has a radius of curvature ( $R = 415.5\ \text{mm}$ ) that is matched to the radius of the collimating mirror. The pitch of the fibers is  $286\ \mu\text{m}$  and was chosen based on ray tracing simulation results to minimize crosstalk whilst keeping the total number of fibers as large as possible. The slit unit consists of a v-groove plate and a cover plate that hold the fibers in place. The fibers are

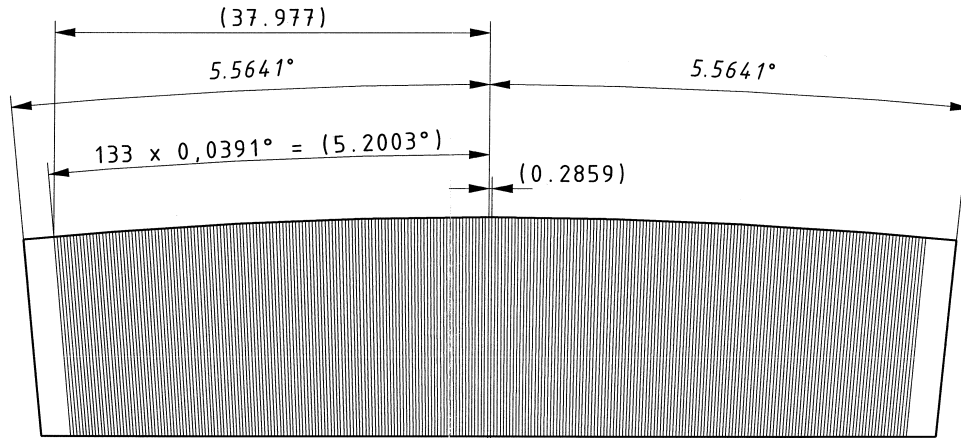


Figure 2.14 Geometrical layout of the v-groove plate that forms the pseudoslit. The fibers are sandwiched and glued between this plate and a cover plate. The package is subsequently polished. Courtesy: Frank Optic Products

sandwiched and glued between those two plates and the package is subsequently polished. An anti-reflective coated cylindrical normalizing lens is attached to the fiber ends. The lens serves to *heal* residual imperfections from the polishing process in the fiber end surfaces. The gap between the fibers and the normalizing lens is filled with an index matching gel. The surface reflectivity after the anti-reflection coating is shown in Fig. 2.17 and is of the order of two tenths of a percent. A laser cut mask that is placed behind the lens. It serves to reject light that exits the fibers in lateral direction at  $f/\# < 3.32$ . (see Fig. 2.16). This suppresses possible stray light passing directly from the slit to the grating.



Figure 2.15 The fiber slit unit. *Upper left panel:* The view onto the fiber plane. The yellow/brown colour of the fibers is a consequence of their polyamide coating. The aluminium has not yet been anodized in this picture. *Lower left panel:* The slit seen from the spectrograph side. The IFU is illuminated with a flash light in this photograph. *Right panel:* The anti-reflective coated IFU normalizing lens is mounted in front of the fiber slit. The slit mask is missing in this picture.

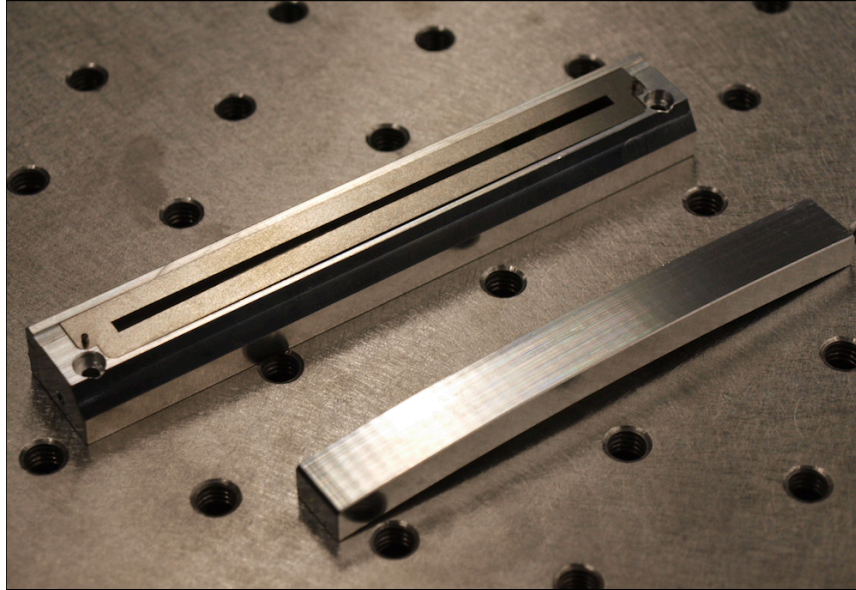


Figure 2.16 The laser cut mask seen on the upper part rejects stray light that leaves the fibers outside of the acceptance  $f$ -ratio of the collimator in lateral direction. The part on the lower right is a dummy for the slit lens that was used during assembly tests.

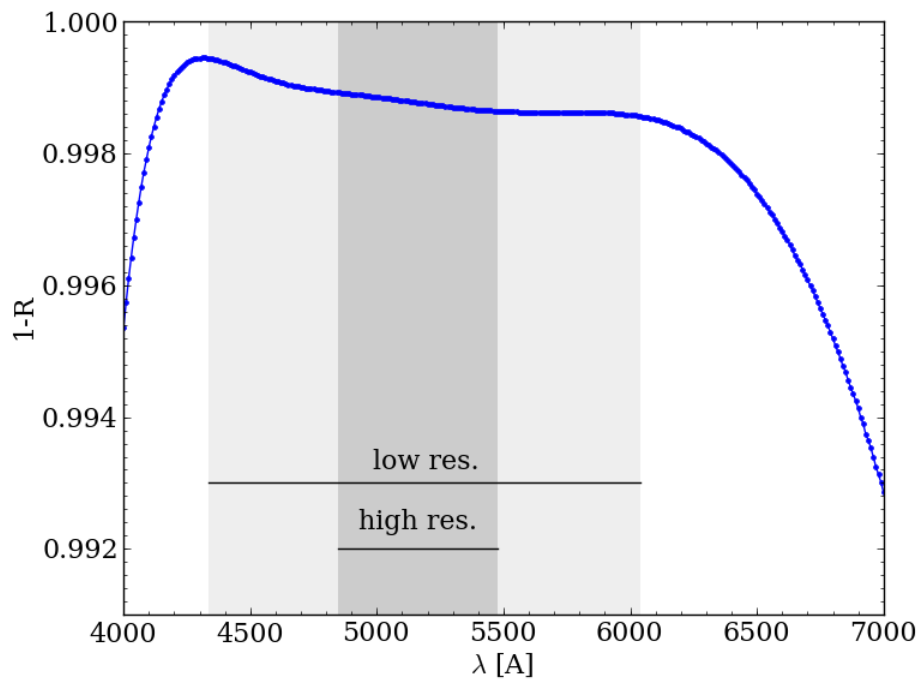


Figure 2.17 Throughput of the normalizing lens after coating. Courtesy: Tafelmaier

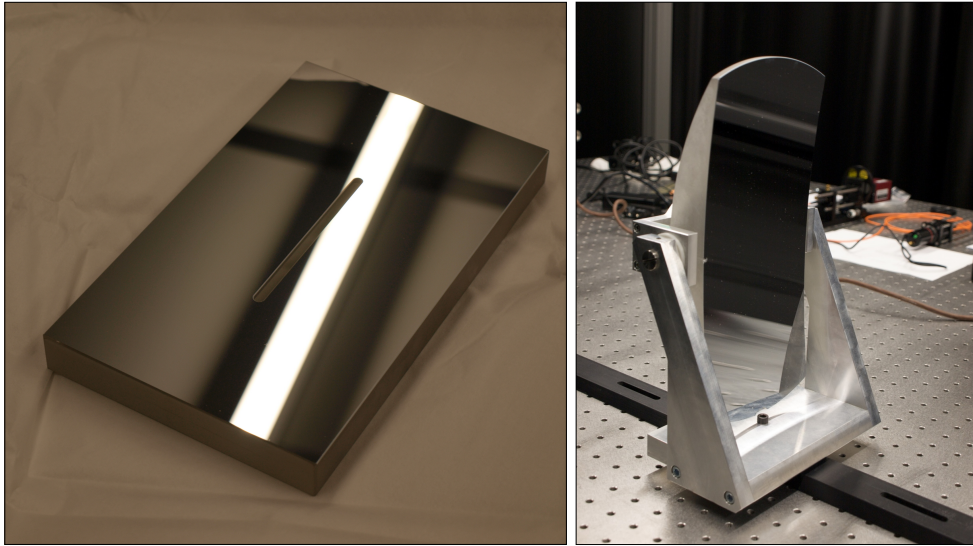


Figure 2.18 The mirrors of VIRUS-W. *Left panel:* The flat folding mirror with the slot for the fiber slit. *Right panel:* The collimator mirror mounted in a test structure.

### 2.1.9 Mirror System

The mirrors (see Fig.2.18) are essentially the only part of spectrograph that we copy directly from the original VIRUS-P design. The collimator's radius of curvature is 848.6 mm, it is 130 mm wide and 295 mm long. The active area is 5 mm smaller at all edges to allow for inhomogeneities of the coating at the edges and for misalignment. Its elongated shape captures all light leaving the fiber slit at  $f/3.32$ . The flat folding mirror has a size of 130 mm  $\times$  215 mm. The slot that houses the fiber slit is 90 mm in length and 4.6 mm wide. We chose an enhanced and protected aluminium coating over a silver coating. This coating offers a higher efficiency in the covered wavelength range and a longer lifetime. The mean reflectivity of the enhanced coating over the covered spectral range is 95 % (see Fig. 2.19).

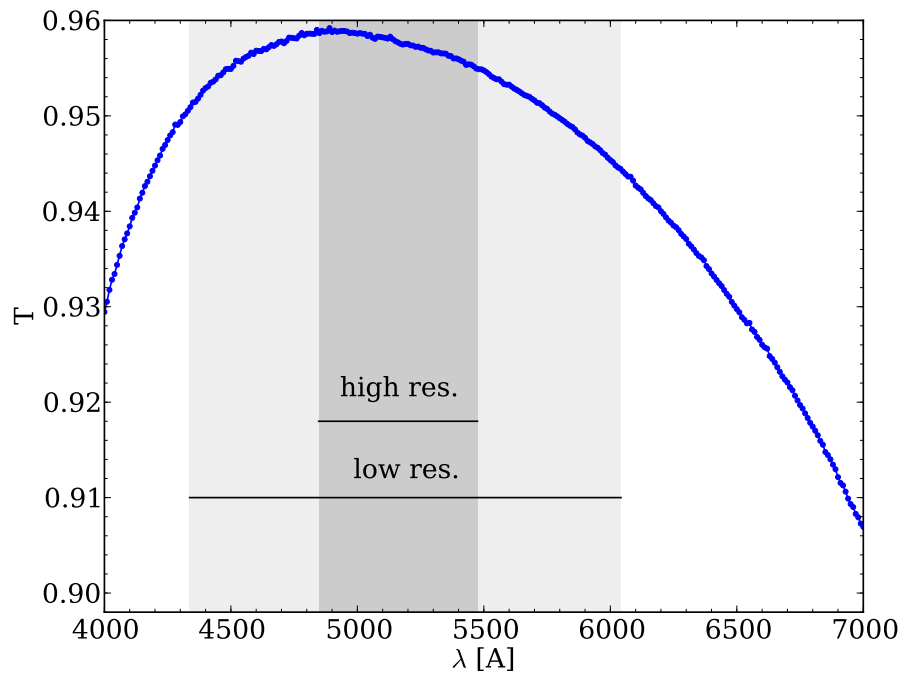


Figure 2.19 Reflectivity of the protected aluminium coating of the collimating mirror and the flat folding mirror. Courtesy: Tafelmaier

Table 2.5. Mirror characteristics

---

---

<b>Spherical collimator</b>	
Grating physical dimensions	130 mm × 295 mm
Radius of curvature	848.6 mm
Coating	enhanced aluminium
Mean reflectivity	95 %
Substrate material	fused silica
Residual surface sphericity	$1/8 \lambda$
<b>Flat folding</b>	
Physical dimensions	130 mm × 215 mm
Radius of curvature	$\infty$
Coating	enhanced aluminium
Mean reflectivity	95 %
Substrate material	fused silica
Residual surface sphericity	$1/8 \lambda$

---

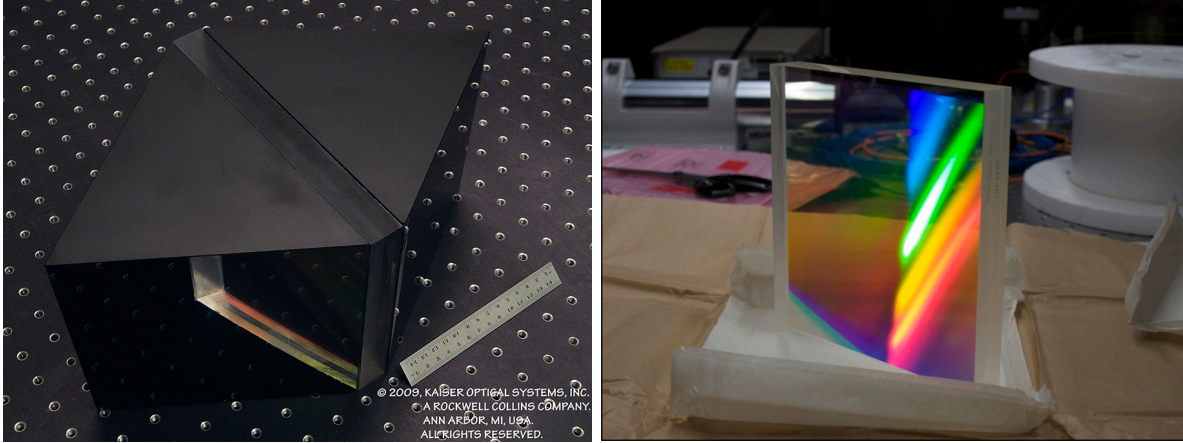


Figure 2.20 The heart of the spectrograph, the VPH gratings. *Left panel:* The high resolution grating with the two prisms attached. (Courtesy: Jim Arns, Kaiser Optical Systems Inc.) *Right panel:* The low resolution mode grating.

### 2.1.10 Dispersive Elements

Two dispersive elements realize the two modes of spectral resolution. The high resolution mode ( $R = 8700$ ,  $\sigma_{inst} \simeq 15 \text{ km s}^{-1}$ ) uses a combination of two large prisms and a VPH grating. The grating's line frequency is 3300  $\text{ll/mm}$  and it has a size of 170 mm  $\times$  220 mm. It is sandwiched between two 12 mm plane parallel substrate plates.

While a VPH grating has no blaze angle in the traditional sense, the incident angle and wavelength of maximum diffraction efficiency can be controlled through the thickness of the grating layer, the amplitude of the refractive index modulation, and the angle of the fringes in the 3-dimensional VPH grating layer (Baldry et al., 2004). VPH gratings where the fringe planes are not aligned perpendicular to the grating plane are referred to as *slanted* gratings. The corresponding effect is the Bragg reflection. Through the choice of the slant angle, the angle at which the Bragg condition is fulfilled can be controlled.

The grating is optimized for throughput at a wavelength of 5193  $\text{\AA}$  and non-polarized light. The prisms match the grating aperture in size, have a prism angle of 58.3 $^\circ$ , and the entrance and exit surfaces have anti-reflective coatings applied to them. The fringes of the high resolution mode grating are not slanted.

The prisms do not serve the purpose of diffraction primarily, their diffractive power is small compared to the grating. However, the diffraction angle of the grating is large enough such that part of the exiting light would suffer total internal reflection at the exit surface of the grating substrate. The prisms decrease the angle of incidence on the exiting glass/air surface. Secondly the prisms serve the purpose of beam steering. Through the choice of the particular prism angle of 58.3 $^\circ$ , the camera position can remain fixed during the exchange of the gratings, which simplifies the mechanical design significantly.

The geometry of the low resolution mode grating is similar to the high resolution mode, but it has a line frequency of 1600  $\text{ll/mm}$  and is optimized for 5170  $\text{\AA}$ . Its geometrical size is

170 mm  $\times$  180 mm. Since no prisms are attached to the low resolution mode grating, both the entrance and exit surfaces are equipped with anti reflective coatings. All materials — the prisms and the grating substrates — are fused silica. The low resolution mode grating does use slanted fringes.

We did not obtain detailed wavelength dependant throughput measurements of the gratings. We determined the monochromatic throughput at  $\simeq 5320 \text{ \AA}$  with a simple setup: A green laser pointer in conjunction with a  $1 \text{ cm}^2$  photo diode and a Keitley microampere meter allowed to measure the intensity of the light that was refracted into the first order. A comparison of that intensity to the direct beam intensity gives the diffraction efficiency at that wavelength. We repeated this measurement on multiple locations over the grating aperture. The results are shown in Fig. 2.21. In this plot we also outline the actual beam footprint. The beam is round and therefore the lower efficiency in the grating corners does not affect the overall instrumental throughput. The efficiencies of the higher dispersion grating vary between 50% and 75% (average over the beam footprint: 69.8%) and the ones of the lower dispersion grating between 80% and 90% (average over the beam footprint: 87.5%). For this crude measurement we adjusted the grating angle in this measurement for maximum throughput by monitoring the photo current while changing the angle. Since the grating was optimized for a different angle of incidence and a different wavelength this procedure will likely give a pessimistic estimate of the true throughput.

For the throughput prediction we use the theoretical diffraction efficiency from the manufacturer that was determined through a rigorous coupled wave analysis and scale it such that its maximum matched the footprint averaged values that we obtained at  $5320 \text{ \AA}$ . The curves are shown in Fig. 2.22. However, we need to point out that the theoretical maximum is located at  $5160 \text{ \AA}$  and not at  $5320 \text{ \AA}$ . Hence the scaling will only give a rough estimate of the true throughput.

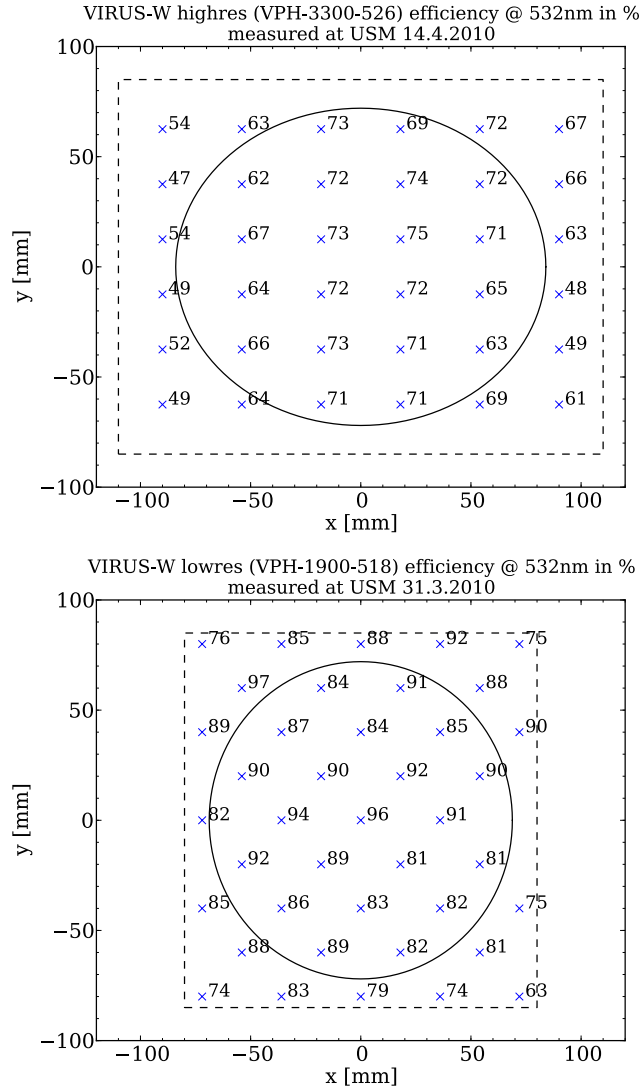


Figure 2.21 The grating diffraction efficiency tested at  $\simeq 5320 \text{ \AA}$ . The upper panel shows the efficiency of the high resolution mode GRISM while the lower panel shows the low resolution mode grating. We use a green laser pointer to determine the efficiency at the indicated locations. The beam diameter of the laser pointer is about 3 mm. The dashed lines outline the physical dimensions of the grating, while the ellipses outline the actual beam footprint.

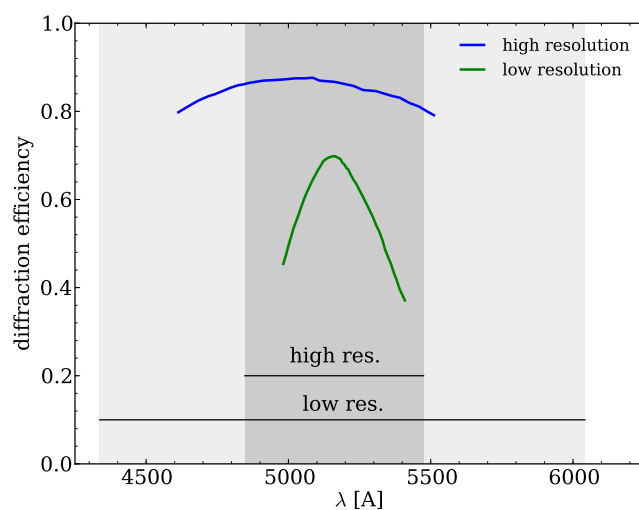


Figure 2.22 The predicted diffraction efficiency of the two gratings (Courtesy Jim Arns, Kaiser Optical Systems Inc.). For this plot and the later throughput prediction we scale the predictions from the manufacturer such that their maxima match the value that we measure at  $5320 \text{ \AA}$ . We use a beam footprint averaged value for the scaling. The extent of the curves corresponds to the nominal wavelength ranges that were built into the design. The grey areas indicate the finally adopted spectral ranges.

Table 2.6. Characteristics of the dispersive elements

---



---

<b>High resolution mode</b>	
Grating physical dimensions	170 mm × 220 mm × 24 mm with two prisms attached
Line frequency	3300 l/mm
Blaze wavelength	5193 Å
Angle of incidence	35.9° in fused silica.
Angle of diffraction	-35.9° in fused silica.
Substrate material	fused silica
Mean diffraction efficiency	58 %
<b>Low resolution mode</b>	
Physical dimensions	170 mm × 180 mm × 24 mm
Line frequency	1600 l/mm
Blaze wavelength	5170 Å
Angle of incidence	19.7° in fused silica, 24.4° in air.
Angle of diffraction	-13.3° in fused silica, -19.6° in air.
Substrate material	fused silica
Mean diffraction efficiency	86 %

---

### 2.1.11 Camera Lens

The dispersed light is captured by a 200 mm aperture,  $f/1.4$  refractive camera lens (see Fig. 2.23 and 2.24). The design is based on the SALT telescope High Resolution Spectrograph red arm (Barnes et al., 2008; Buckley et al., 2004) and incorporates mostly spherical components in 4 groups and five lenses. The only aspheric surfaces are the entrance surface and the last field flattener surface (see Table 2.7).

Besides avoiding the central obscuration, a refractive design has the advantage of simplifying the dewar design for the detector. Even though a close proximity of the detector to the field flattener is generally favourable, we decided to place a dewar window between the field lens and the detector. This allows us to mechanically decouple the camera head from the lens housing. The whole head — including cryostat and camera housing — is then aligned relative to the camera lens rather than having to align the detector inside the vacuum.

The camera lens focus is adjustable (realized through the first group), and compensates for the change of focus that results from exchanges of the grating, and instrument deformations due to temperature changes.

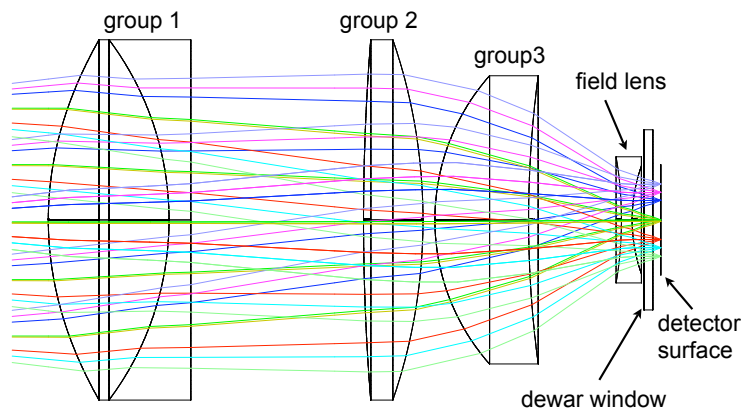
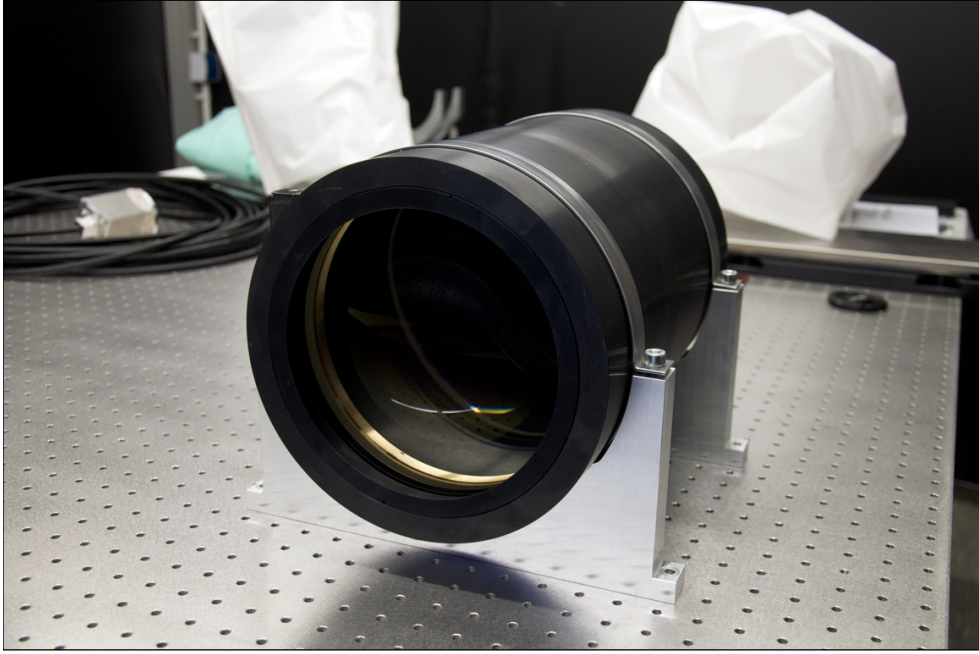


Figure 2.23 The VIRUS-W 200 mm aperture  $f/1.4$  camera. Surface data are given in Table 2.7. The window between the field flattener and the detector allows us to mechanically decouple the cryostat from the optics housing. Otherwise the fast optical beam would have resulted in either exceedingly tight tolerances for the detector position or the necessity to implement in-vacuum alignment capabilities.

### 2.1.12 Detector System

We use a Marconi (today e2v) CCD44-82 back side illuminated CCD. The CCD has  $2048 \times 4096$   $15 \mu\text{m}$  square pixels. The full well capacity is  $200 \text{ ke}^-/\text{pixel}$ . The detector is actually one of the spare CCDs of the recently commissioned OmegaCam (Deul et al., 2002) (ESO ID: *Indus II*) and has undergone extensive testing. In Fig. 2.26 we

Figure 2.24 The 200 mm aperture  $f/1.4$  camera lens.

Grp.	Surf.	Glass	R of curv. (mm)	Diam. (mm)	thickness (mm)	Notes
1	1	S-FSL5	179.4796	200	67.0000	asph. $c = -4.4296$ , $a_4 = 7.7344 \times 10^{-8}$ , $a_6 = -3.7140 \times 10^{-12}$ , $a_8 = 1.7621 \times 10^{-16}$ , $a_{10} = -5.3331 \times 10^{-21}$
1	2	S-TIH1	-166.2436	200	12.0000	
1	3		$\infty$	200	96.2878	
2	1	S-BAH11	1280.2371	200	33.0000	
2	2		-305.1473	200	5.3918	
3	1	N-LAK7	121.2324	160	52.0000	
3	2		593.2538	160	52.3159	
4	1	Lithosil	-233.3127	70	6.0000	field lens, asph. $c = 0.0$ , $a_4 = -4.9830 \times 10^{-7}$ , $a_6 = 3.1592 \times 10^{-10}$ , $a_8 = -6.9386 \times 10^{-14}$
4	2		91.5383	60	7.5556	
5	1	silica	$\infty$	100	4.7630	dewar window
	2	vacuum	$\infty$	100	3.5000	
	1		$\infty$			e2v CCD44-82 2k x 4k 15 $\mu$ m pixel CCD

Table 2.7 Surface description for the VIRUS-W camera design. The entrance surface and the first field lens' surface are aspheres.

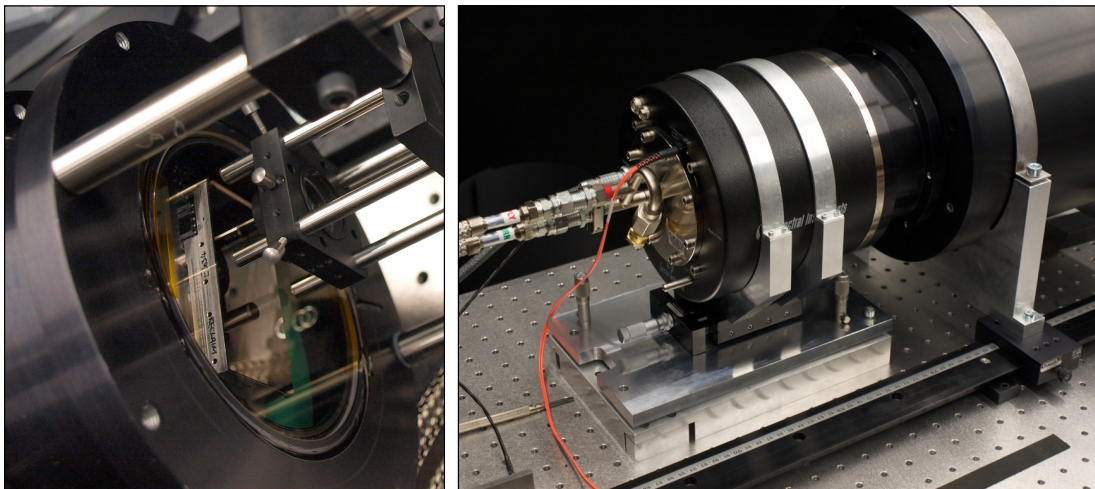


Figure 2.25 *Left panel:* The CCD detector, here placed behind a spot projector that we used for testing. *Right panel:* The camera head integrates cryostat and readout electronics. Here the head is mounted on a test stage behind the camera lens.

plot the quantum efficiency curve that was obtained at by Fabrice Christen of the Optical Detector Department at ESO. The mean efficiency in the covered range is 83 %. With an imaging area of  $30.7 \text{ mm} \times 61.4 \text{ mm}$  the detector is somewhat larger than needed for our application which results in larger covered spectral ranges than nominally built into the design.

Spectral Instruments Inc. integrated the detector into their SI1100 camera head (see Fig 2.25). The head includes 16bit readout electronics, a shutter driver, and a Polycold Systems (Cryotiger) based closed-cycle cryogenic cooling system.

We operate the detector at  $-130^\circ\text{C}$ . At larger temperatures the detector starts showing artefacts like a few hot columns and vertical striping — rows, vertical to the CCD column structure, a few tens of pixels in length, that show increased dark current up to few hundred counts per pixel per hour, see left panel in Fig. 2.27. However, at  $-130^\circ\text{C}$ . those artefacts disappear completely and the mean dark current averaged over the whole detector area is  $4.1 \text{ e}^- \text{ pixel}^{-1} \text{ h}^{-1}$ .

The CCD shows one obvious surface contamination that resembles a speck of dust towards one of its longer edges (see right panel of Fig. 2.27). The affected area measures about 75 pixel in length and is 10 pixels wide.

The SI1100 allows for multiple readout modes which can — within certain limits — be adjusted by the user. In our adopted *science mode* the camera system reads out at 100 kHz over two amplifiers with a gain of  $1.61 \text{ ADU}/\text{e}^-$  and a read noise of  $2.55 \text{ e}^-$  on both amplifiers <sup>3</sup>.

<sup>3</sup>The gain and read noise were measured by Spectral Instruments Inc.

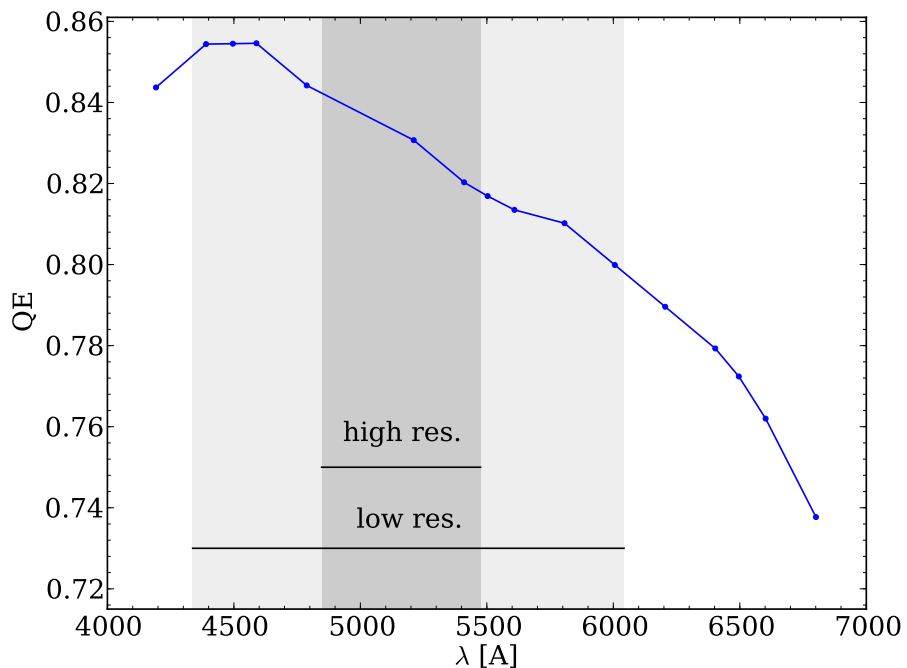


Figure 2.26 The quantum efficiency of the Indus II detector. Measurement by Fabrice Christen, ESO, Optical Detector Department

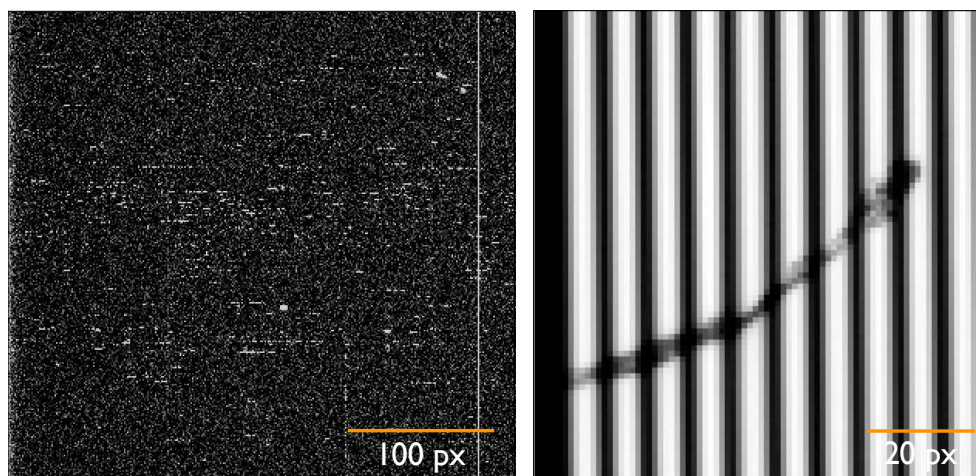


Figure 2.27 Artefacts of the CCD detector. The left image shows the vertical striping feature in a 60s dark image. These stripes run vertically to the CCD columns and become apparent through an increased dark current of up to a few hundred counts per pixel per hour. At an operating temperature of  $-130^{\circ}\text{C}$  these stripes disappear completely. The right panel shows the dust speck contamination in a fiber-flat image.

Table 2.8. Characteristics of the CCD detector in science mode

Property	Values
type	Marconi (today e2v) CCD44-82 back side illuminated (ESO ID: Indus II)
number of pixels	$2048 \times 4096$
pixel size	$15 \mu\text{m}$ square
physical dimensions	$30.7 \text{ mm} \times 61.4 \text{ mm}$
number of amplifiers	2 (serial split read)
quantum efficiency	mean= 83%, $QE(4337 \text{ \AA}) = 85\%$ , $QE(6042 \text{ \AA}) = 80\%$ <sup>(2)</sup>
dark current	$4.1 e^-$ at $-130^\circ \text{ C}$
read noise	$2.55 e^-$ <sup>(1)</sup>
gain	$1.61 \text{ ADU}/e^-$ on both ampl. <sup>(1)</sup>
full well capacity	$200 \text{ ke}$ <sup>(1)</sup>
readout out speed	100 kHz, serial split
CTE	$> 0.99999$ (serial & parallel) <sup>(1)</sup>

Notes: 1) Measured by Spectral Instruments. 2) Measured by ESO.

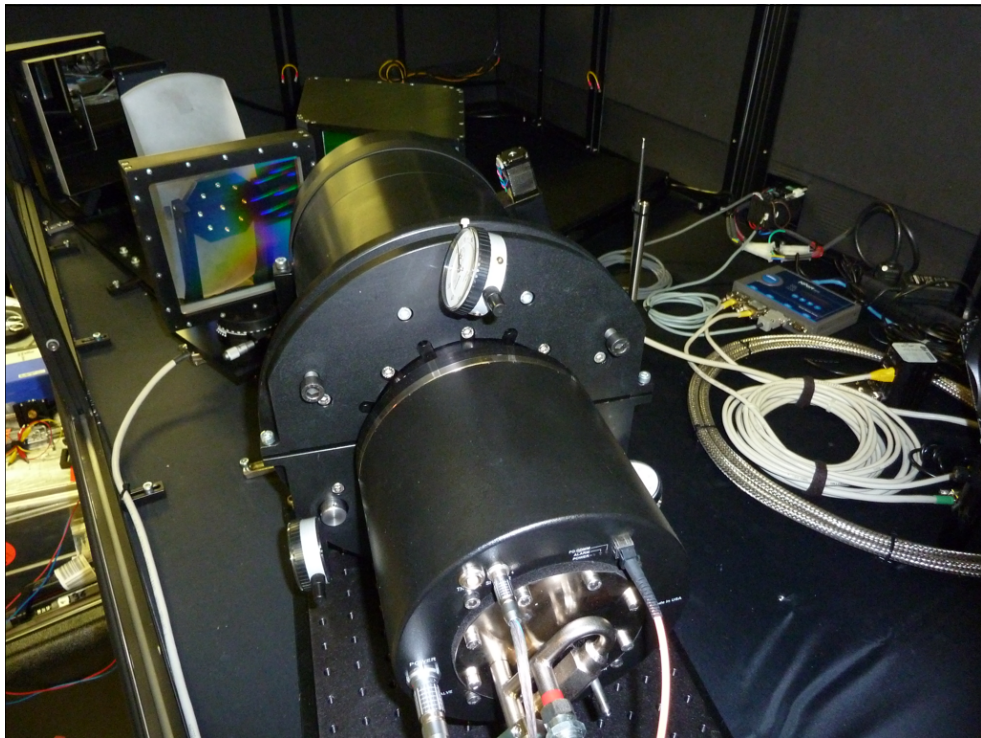


Figure 2.28 The camera head mount. Three fine-adjustment screws allow to adjust for tip, tilt and piston of the detector head with respect to the camera lens.

The camera head is attached through a 3-point mount to the lens housing. Fine adjustment screws allow the user to adjust for tip, tilt and piston of the detector (see Fig. 2.28). The rotation is controlled by rotating the whole camera lens around its optical axis.

### 2.1.13 Optical Performance

The spectral resolution is limited by the spot size. The light exits the fiber with  $f/3.65$  the camera has an  $f$ -ratio of 1.4. Therefore the fiber diameter of  $150\ \mu\text{m}$  in the silt plane is imaged to  $57.5\ \mu\text{m}$  in the focal plane of the spectrograph. In Fig. 2.29 and 2.30 we show the spot diagrams from the optical ray tracing software. Except for the outermost end of the covered spectral range the spots are well contained within the  $30\ \mu\text{m} \times 30\ \mu\text{m}$  box. Hence, the image size will dominate the final spot size in most cases. Table 2.9 lists the 50 % and 90 % encircled energy distances from the spot centers. Only at the blue end of the spectral range we do expect a significant broadening due to the spectrograph's point spread function. A circle-like image will have a FWHM of  $\sqrt{3} \cdot r$  after projection onto one dimension. Given the linear dispersion of  $0.19\ \text{\AA}/\text{px}$  in the high resolution mode and  $0.52\ \text{\AA}/\text{px}$  in the low resolution mode we can expect to get a resolution of  $R = 8230$  in the former and  $R = 3005$  in the latter for the corresponding central wavelengths.

In §3.4 we investigate actual measured resolution as a function of slit position and wavelength and in §3.5 we discuss the fiber separation. We will show that the achieved resolution is actually slightly larger than predicted here. The reason probably lies in the fact that circles are not a perfect approximation of the light exit surfaces of the fibers; if more light is emitted close to the fiber centers then the FWHM would effectively become smaller and the resolution will increase.

### 2.1.14 Bench, Dark Box and Temperature Control

VIRUS-W is built on a standard optical bench: a 58 mm thick, 1.25 m wide, and 1.8 m long breadboard equipped with M6 mounting holes in a standard 25 mm pattern (Newport M-IG-46-2). The breadboard is placed on top of the bench that was originally used for the laser of the lunar laser ranging program at the 2.7 m after the installation of the back reflector by the Apollo 11 landing (Bender et al., 1973).

The dark box enclosure is constructed out of 25 mm aluminium rails and 6 mm PVC panels (see Fig. 2.31). It is 506 mm high and encloses the full optical bench. The top and front panels are attached with magnetic tape and can be taken off for alignment and maintenance.

Since VIRUS-W was designed to be located inside a temperature controlled room, no specific measures were taken in the mechanical design to assure temperature stability. Indeed, lab tests revealed that temperature changes cause significant flexure of the instrument. The spectra move by up to one pixel per degree C in cross dispersion direction. Since the temperature in the control room of the 2.7 m is not perfectly stable — air conditioning assures stability only within a few degree C — we integrate an active temperature control

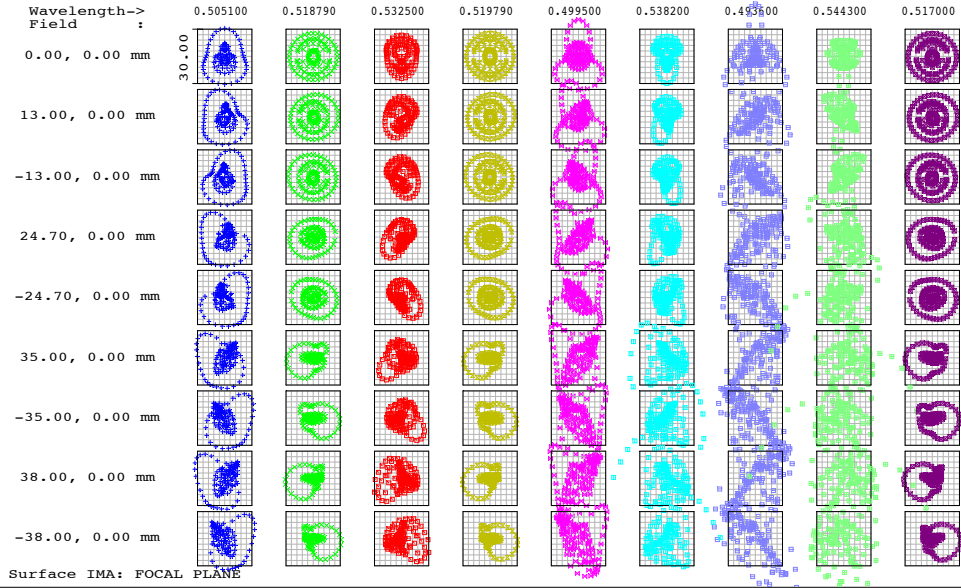


Figure 2.29 Spot diagrams for the high resolution mode. The fiber number varies vertically where 0 mm in the top row corresponds to the slit center and  $\pm 38$  mm in the bottom two rows correspond the fibers at the slit-ends. The wavelength varies horizontally with central wavelength at the left and wavelengths at the two ends of the spectral range on the right. The box edge length is  $30 \mu\text{m}$  and corresponds to 2 pixels. The most significant degradation is seen in the blue at the wavelengths  $4995 \text{ \AA}$  and  $4936 \text{ \AA}$ . The fiber diameter of  $150 \mu\text{m}$  is imaged to  $57.5 \mu\text{m}$  the focal plane.

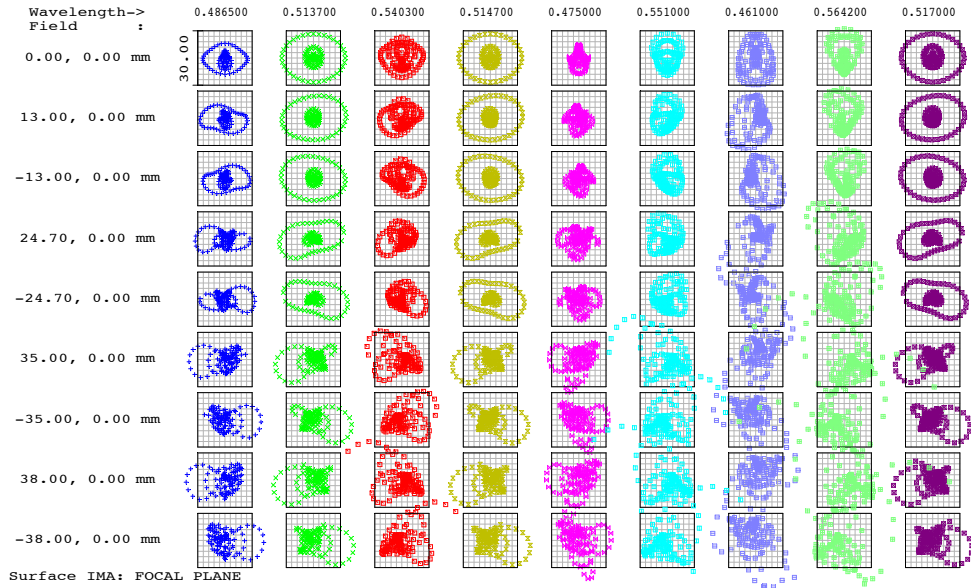


Figure 2.30 As Fig. 2.29. Spot diagrams for the low resolution mode.

Table 2.9. Encircled energies for both resolution modes

<b>high resolution mode</b>					
wavelength [ $\text{\AA}$ ]	50% E.E.		90% E.E.		
	slit center	slit end	slit center	slit end	
4847	15 $\mu\text{m}$	16.5 $\mu\text{m}$	25 $\mu\text{m}$	36 $\mu\text{m}$	
5051	5 $\mu\text{m}$	6 $\mu\text{m}$	9 $\mu\text{m}$	11 $\mu\text{m}$	
5188	7.5 $\mu\text{m}$	3.5 $\mu\text{m}$	10 $\mu\text{m}$	6 $\mu\text{m}$	
5443	7.5 $\mu\text{m}$	3.5 $\mu\text{m}$	10 $\mu\text{m}$	6.5 $\mu\text{m}$	
5475	7.5 $\mu\text{m}$	16 $\mu\text{m}$	12 $\mu\text{m}$	33 $\mu\text{m}$	
5936	6.5 $\mu\text{m}$	13 $\mu\text{m}$	9 $\mu\text{m}$	26 $\mu\text{m}$	
<b>low resolution mode</b>					
wavelength [ $\text{\AA}$ ]	50% E.E.		90% E.E.		
	slit center	slit end	slit center	slit end	
4337	31 $\mu\text{m}$	26.5 $\mu\text{m}$	>40 $\mu\text{m}$	>40 $\mu\text{m}$	
4610	8.5 $\mu\text{m}$	8.5 $\mu\text{m}$	13.5 $\mu\text{m}$	19 $\mu\text{m}$	
4865	2.5 $\mu\text{m}$	6 $\mu\text{m}$	6.5 $\mu\text{m}$	11 $\mu\text{m}$	
5137	6 $\mu\text{m}$	7.5 $\mu\text{m}$	10.5 $\mu\text{m}$	10.5 $\mu\text{m}$	
5642	7.5 $\mu\text{m}$	11.5 $\mu\text{m}$	13.5 $\mu\text{m}$	30 $\mu\text{m}$	
6042	25 $\mu\text{m}$	21 $\mu\text{m}$	>40 $\mu\text{m}$	>40 $\mu\text{m}$	

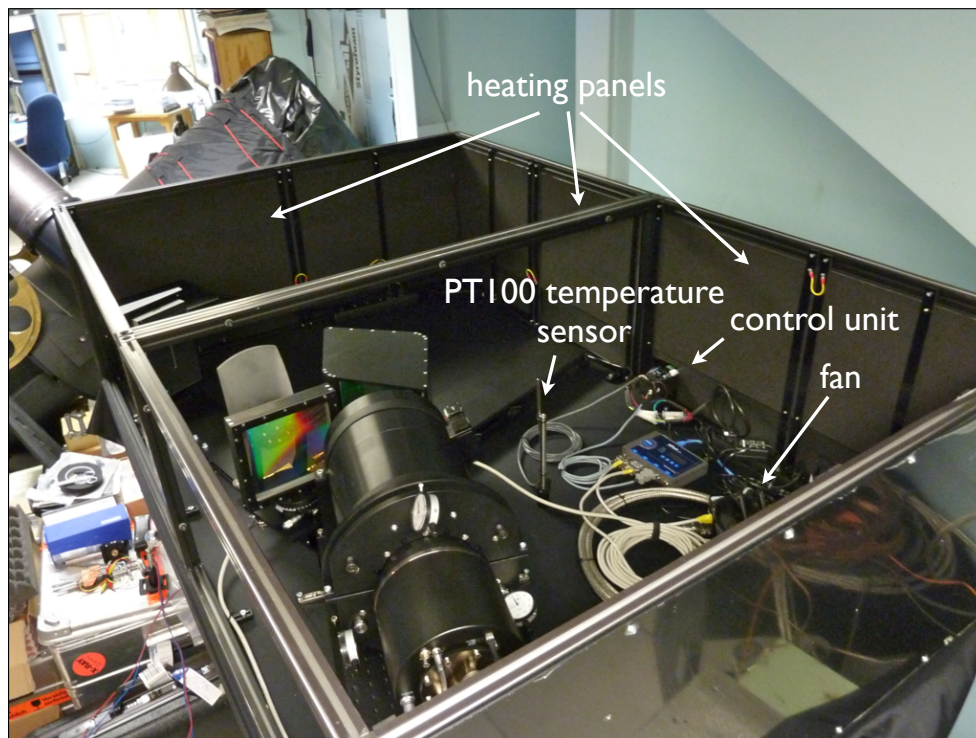


Figure 2.31 The spectrograph, fully assembled in the control room of the 2.7 m. The enclosure is seen surrounding the instrument. Heating elements are attached to the inside of the side panels of the dark box.

system into the dark box. We adopt the design for the heating panels of the FOCES spectrograph (Frank Grupp, private communication). Four 220 V driven, adhesive heating foils were attached to 2 mm thick aluminium plates and deliver up to 200 W of heating power. The foils are covered with a layer of 1 mm thick black neoprene. A 1 cm layer of fire proof Armaflex foam attached to the inside of the PVC panels serves as thermal insulation layer. The heating elements are mounted on the inside of the insulation layer. A standard temperature controller (EMKO ESM-XX50) with 0.1° C resolution and a RS232 interface in conjunction with a PT100 temperature sensor controls the heat input through adjustment of the length of the duty cycle for the heating foils. A fan is used to circulate the air continuously in the dark box. This enhances the thermalisation between parts and was found to improve the system’s stability. This temperature control increases the system’s stability sufficiently for operation in the control room. We will address the stability in §3.6.

## 2.2 Control Software & Modes of Observation

VIRUS-W is controlled through a python command line with a collection of routines that tie together the functionality of the camera software (provided by Spectral Instruments), the control of the various focussing and GRISM drives, the interface of the Telescope Control System (TCS) for automated execution of nodding and dithering schemes, and the temperature control system.

In this section we will first describe the observation modes that we have implemented and then describe typical calibration sets, and the instrumental setup.

### 2.2.1 Observing Modes

The IFU has a fill factor of 1/3 (see §2.1.6). Three pointings are necessary to reach 100% coverage. The technique of these few-arcsecond offset observations is referred to as *dithering*. Sometimes — in situations where a higher spatial resolution is desired — the dither pattern is modified to smaller step widths and a larger number of exposures. This is referred to as *sub-dithering* (see Fig. 2.32).

The IFU is not equipped with dedicated sky fibers. If the object is of comparable size to the IFU’s FoV, or larger, and no fibers can be expected to contain non-object-contaminated sky signal, the sky has to be observed in separate offset pointings. The actual science observations are interleaved with offset sky positions — this is referred to as *nodding*. The bracketing sky observations are then typically averaged together, scaled for exposure time and subtracted from the object signal.

Both, the nodding and dithering schemes are adopted from VIRUS-P observations from VENGA (Adams et al., 2011; Blanc et al., 2010a) and were modified in step widths and exposure times to match the IFU geometry and typical signal levels of VIRUS-W. The control routine `dither_on.off()` implements this observation mode. It accesses a TCP/IP interface to the TCS to execute offset pointings, and automatically triggers the spectro-

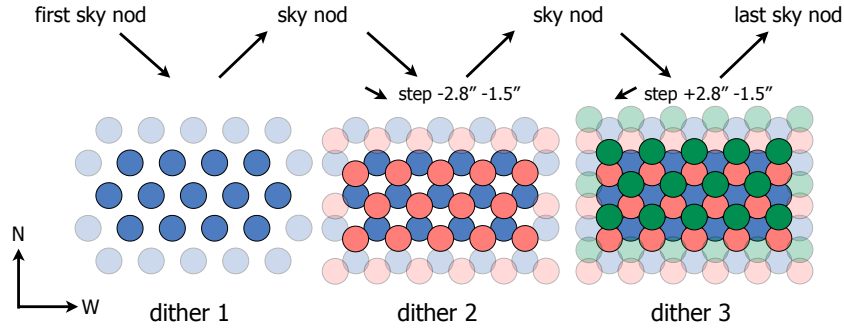


Figure 2.32 In the dithered observing mode three exposures fill the field of view to reach 100% coverage. The subdithered mode repeats the same pattern, offset by  $0.8''$  to the east. The dithered mode typically brackets and interleaves the actual science exposures with sky offsets. Depending on the desired total integration time the sequence may be repeated.

graph camera and shutter. The observer typically places a previously chosen guide star on a specific pixel position in the guider camera that is determined during the preparation of the observation such as to place the science target exactly at the desired position within the IFU.

The script then moves the telescope to the sky position (currently  $540''$  north) and starts the sky exposure. The script carries out the sky nods and dither offsets with little manual interaction. Currently only the recapturing of the guide star after a sky nod needs interaction since the  $2.7\text{ m}$  offsets are sometimes inaccurate.

The current standard science mode assumes alternating sky and object exposures with always one sky exposure at the beginning and at the end of each sequence. The sky exposures are 10 to 20 minutes in length and typical exposure times for local galaxies are 30 minutes.

If the observer wishes to take multiple exposures in one dither position then the typical mode would be a Round-Robin scheme, which repeats the dither and nodding pattern until the desired total integration time is reached. However, the number of exposures per dither position, the exposure times on object and on sky, and the optional number of cosmic ray splits in one dither position (without a sky nod in between), are passed as parameters and can be modified according to needs.

A second dither routine called `subdither()` performs the automatic subdithering that is typically used for calibrations and astrometry (s.b.). It executes two dither patterns with no sky nods. The second dither-set is offset by  $0.8''$  from the first one.

### 2.2.2 Calibration Dataset

During the commissioning phase we experimented with a number of available calibration lamps. Based on the actual line density and the flux level in those lines we finally chose mercury and neon lamps for the wavelength calibration of both, the high and the low

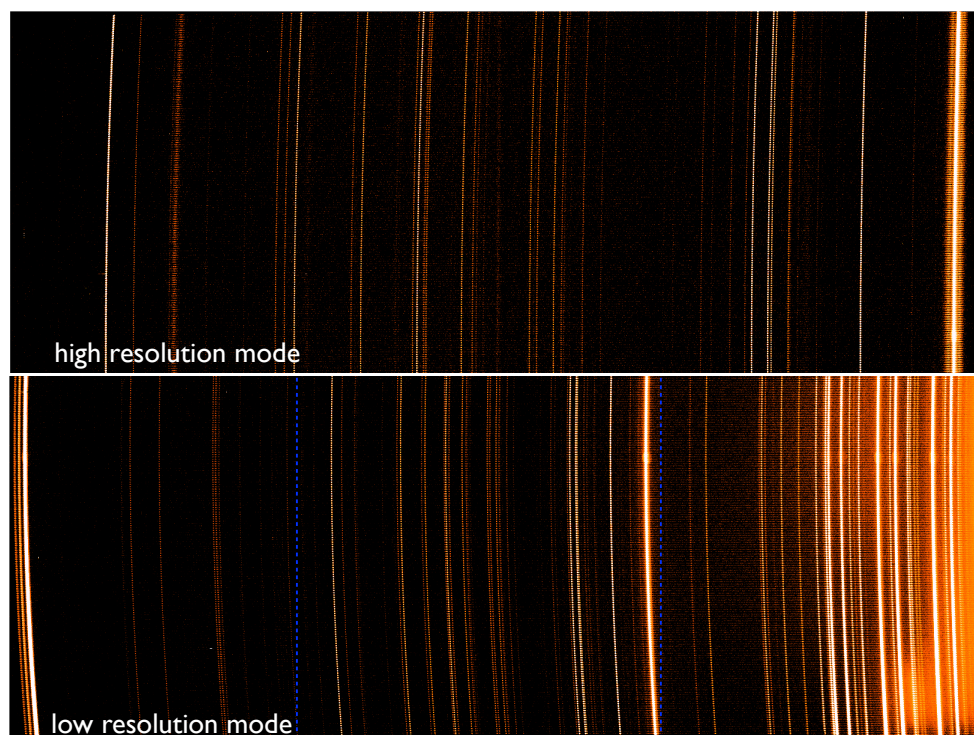


Figure 2.33 Examples for the raw arc  $Ne + Hg$  lamp spectra. *Upper panel:* High resolution mode. *Lower panel:* Low resolution mode. The blue lines in the lower panel indicate the spectral coverage of the high resolution mode.

resolution mode. The spectra are recorded with both lamps switched on simultaneously. The total number of lines that we use for wavelength calibration is 19 in the high resolution mode and 34 in the low resolution mode. The density of lines at the blue end of the spectrum is somewhat lower than we would wish for (see Fig. 2.33). However, the flux of the available higher line density lamps such as iron proved to be insufficient to reach sufficient signal levels in reasonable exposure times ( $< 20$  min). This is a consequence of the setup at the 2.7 m. The lamps are placed manually on the south pier of the dome. One then *observes* the reflection of the arc lamp light off the dome wall or the wind screen that is made out of a white plastic material.

At the Wendelstein 2 m we plan to have a dedicated telescope simulator that directly feeds the spectrograph with calibration light. This should allow us to use lower luminosity but larger line density lamps such as iron or argon.

The basic set of calibrations includes bias frames, arc-line lamps for spectral calibration, and twilight or dome flat frames for flat fielding and mapping of the fiber positions on the detector. All calibration frames are typically taken in the evening before the start of the observations and in the morning after the observations. The routines `arcs()`, `biases()`, and `flats()` support this standard set of calibrations, will assure that the correct readout

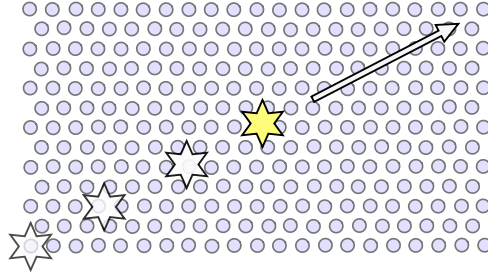


Figure 2.34 During the IFU trailing procedure the telescope is slewed while the spectrograph integrates. The telescope movement is such that the star moves diagonally from one to the opposite corner of the IFU. During this procedure each fiber row gets illuminated once which allows to test for possible variations of resolution as a function of fiber number and chip position.

mode is used, and add corresponding header information to the image frames. On top of this basic set of calibrations astrometry fields (mostly open clusters), spectrophotometric standard stars, radial velocity standards, and kinematic templates may be observed.

One will typically observe at least one spectrophotometric standard star per night and instrumental mode. These stars — with publicly available spectrophotometry (e.g. Stone, 1977; Massey et al., 1988; Oke, 1990) and with few spectral features, such as white dwarfs or A-type stars — are also typically observed in subdithered mode to mitigate aperture effects.

Finally — depending on the science case — a set of kinematic templates may be needed for the extraction of the kinematic information. These are typically G or K giant stars as their spectra most closely resemble the integrated spectra of elliptical galaxies or early type spiral galaxy bulges. The stars are *trailed* across the IFU, i.e. the shutter is left open and the detector keeps integrating while the telescope is slewed such that the star moves from one corner of the IFU to the opposite corner (see Fig. 2.34). In this way each row of fibers in the IFU is illuminated at least once and the spectra spread across the whole CCD (see Fig. 2.35). In this way one can account for the variation of the resolution across the detector which is a consequence of the image quality degradation toward the edges of the camera's field of view (see however §3.4). The procedure `trailIFU()` executes the telescope slew such as to illuminate each fiber row once and controls the camera/shutter accordingly.

### 2.2.3 Instrument Setup

Before the start of the observations the instrument has to be set up. The spectrograph camera is with  $f/1.4$  relatively fast. Therefore the depth of focus is very shallow and the CCD easily drifts out of focus. It proved necessary but sufficient to focus the camera each evening before the start of the observations.

A focus series is taken with `focusSeries()`, typically with dome lights. The focus



Figure 2.35 This raw spectrum is the result of a trailing procedure. As each row of fibers got illuminated once, the spectra spread out over the whole chip. The dispersion direction runs from the left to the right. The fiber number increases from the bottom to the top.

drive — somewhat arbitrarily — maps the lens focus range onto the numerical interval [0–30], which roughly corresponds to the change of the position of focal plane along the optical axis in  $\mu\text{m}$ . `determineFocus()` then reads the images of the series and calculates the image variance within given windows in the detector area. The variance reaches a maximum at the optimum focus position (e.g. Subbarao et al., 1993). A parabola is fitted to the variance as function of focus position and the result is returned (see Fig. 2.36). The focus drive must then be instructed accordingly through the command `focusDrive()`.

An operating temperature must be chosen. The enclosure of the spectrograph — the *dark box* — is equipped with heating elements and a temperature control unit (see §2.1.14). The procedures `getBoxTemp()`, `setBoxTargetTemp()`, `getBoxTargetTemp()` allow to read the spectrograph’s temperature, and to read and to modify the set point of the control unit. The box is typically kept at  $1^\circ\text{C}$  above its thermalized temperature.

The procedure `grismDrive()` chooses the actual grating that should be used during an observation. The change of gratings is in principle a fast procedure  $\simeq 20\text{s}$ . However at the 2.7 m the filter in front of the IFU needs manual exchange.

## 2.2.4 Astrometry

The procedure for the astrometric calibration has been largely adopted from the HETDEX pilot survey (Adams et al., 2011). Observations of open clusters serve to calculate the exact position of the IFU relative to the guider camera and to allow for later reconstruction of the source position on the sky. One typically tries to target at least four stars that are equally distributed over the FoV of the IFU (see Fig. 2.37). For increased resolution —

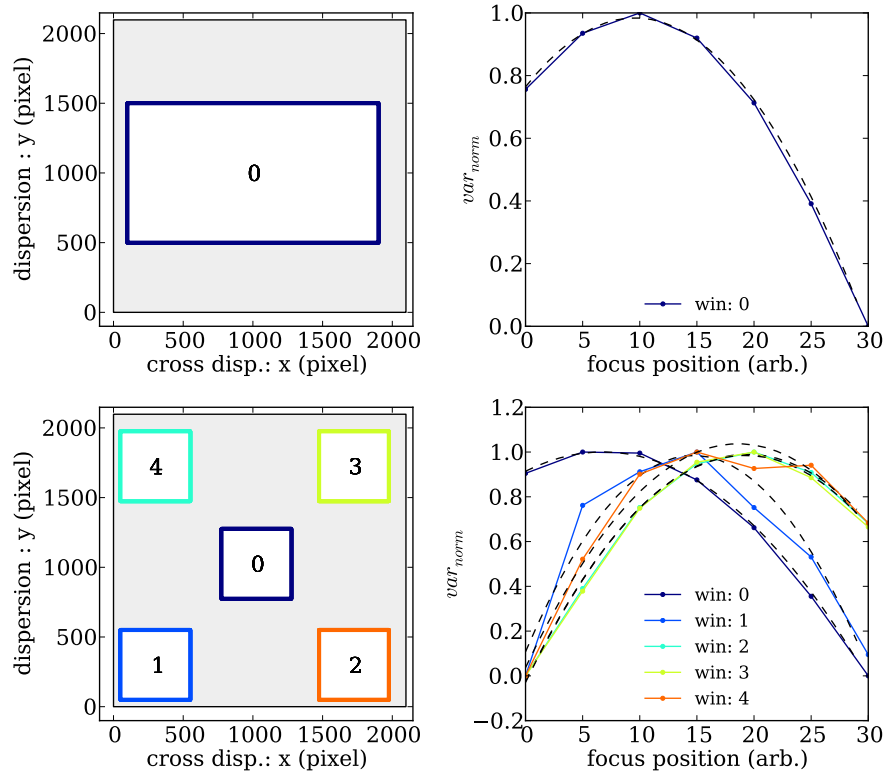


Figure 2.36 Example output of the spectrograph camera focussing routine. The `focusSeries()` command takes a series of dome flat images (typically seven) at different positions of the lens' focus drive. The images are then given to `determineFocus()` which calculates the image variance in a given window. A parabola-fit then determines the optimum focus position. Here the data were binned  $2 \times 1$  (as we usually do for higher speed). The grey area in the left panels outlines the detector. *Upper row:* The standard mode determines the focus in a single, large, pre-defined area (indicated in the left panel). The right panel shows the normalized variance (minimum variance subtracted) and the fitted parabola. The fit gave an optimum focus of 9.6 in this case. *Bottom row:* Multiple windows can be defined within which the focus should be determined. This is used for instance in the tip tilt alignment procedure for the detector. The central field has a optimal focus that is offset from the other fields which indicates that the focal plane has a residual curvature.

Table 2.10. High level routines of the control software

Routine	function
<code>arcs()</code>	records a given number calibration lamp series
<code>darks()</code>	takes a dark series with given number of frames and <i>exposure</i> time
<code>biases()</code>	takes a bias series
<code>flats()</code>	takes a flat series
<code>science()</code>	standard routing for single science exposures, takes series of science frames, usually one or two
<code>testImage()</code>	takes a test image
<code>focusSeries()</code>	takes a focus series, a given number of images — typically dome flats — which are equally spaced in the setting of the lens' focus drive
<code>determineFocus()</code>	takes output of <code>focusSeries()</code> and determines focus position
<code>focusDrive()</code>	instructs the focus drive to move to a specified position
<code>autoFocus()</code>	automated combination of the three previous routines
<code>trailIFU()</code>	trails object (e.g. star) across IFU while exposing
<code>image_on_off()</code>	object/sky nodding in sky -object -sky -... -sky sequence
<code>dither_on_off()</code>	like <code>image_on_off()</code> but also does IFU dithering, this is the main routine for dithered science observations
<code>subdither()</code>	for subdithered observations for astrometry and standard stars
<code>grismDriveCal()</code>	calibrate grism drive (needs to be executed at start of obs.)
<code>focusDriveCal()</code>	calibrate focus drive (needs to be executed at start of obs.)
<code>grismDrive()</code>	positions GRISM, used for change of resolution mode
<code>getBoxTemp()</code>	read dark box temperature
<code>setBoxTargetTemp()</code>	sets dark box temperature set-point
<code>getBoxTargetTemp()</code>	reads dark box temperature set-point

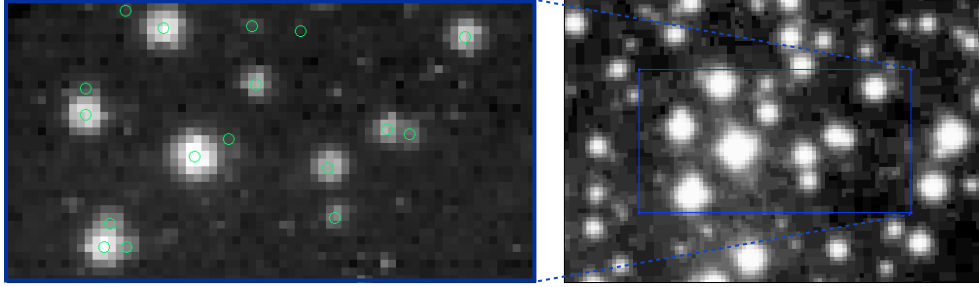


Figure 2.37 Example of an astrometry field. The depicted region lies in the open cluster M37. A Digital Sky Survey image is shown on the right. The FoV of VIRUS-W is outlined in blue. The left panel shows an actual reconstructed image from the subdithered observation. Green circles indicate sources from the 2MASS Point Source Catalogue which are used to derive the precise relative location of the IFU with respect to the guider.

note that the fiber size on sky is  $3.2''$  — the observation is carried out in the subdithered mode using the routine `subdither()` (see Fig. 2.32).

The pixel positions of stars in guide field are obtained through SExtractor (Bertin & Arnouts, 1996). Those are then matched against United States Naval Observatory’s (USNO) NOMAD catalogue (Zacharias et al., 2005). The IFU data are collapsed along the spectral direction over the full bandpass in the respective resolution mode. We then generate images through bicubic interpolation between the fiber fluxes. The centroids of star positions in the IFU can then also be compared the Nomad catalogue.

The obtained positions allow to fit for plate scales, relative offsets and positions angles of the IFU and the guider. As discussed in §2.1.6 the RMS deviation of the individual fiber positions is small with  $0.09''$  and is expected to contribute little to the overall error budget of the astrometric solution. (Adams et al., 2011) compare their recovered positions of emission line sources to high confidence counterparts and find a typical uncertainty of  $\simeq 0.5''$  for the astrometric solution.

## 2.3 Data Reduction

We are using a slightly adjusted version of the HETDEX data reduction pipeline `cure`. This pipeline was developed by Ralf Koehler, Niv Drory and Jan Snigula and offers basic image reduction, wavelength and spatial distortion correction, spectral extraction and various data monitoring and visualisation routines. `cure` will be described in detail elsewhere. We focus here on the aspects relevant to the VIRUS-W data reduction.

The basic image reduction uses the `fitstools` package (Gössl & Riffeser, 2002) and follows standard recipes of creation and subtraction of master bias frames and the averaging of flat fields and calibration lamp frames. The `fitstools` create error frames based on shot noise and read noise and gain. Those frames are properly propagated through the reduction process.

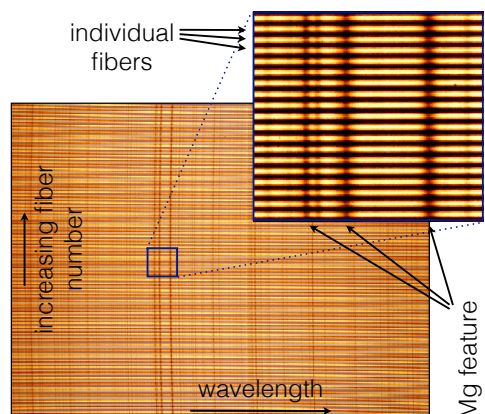


Figure 2.38 A raw twilight flat spectrum recorded in the high resolution mode. The dispersion direction runs horizontally, the fiber number varies vertically. The magnified region shows the Mg triplet feature in the solar spectrum.

`cure` traces the positions of the fiber spectra on the chip using the twilight or dome flat frames. The spectra of individual fibers in a twilight or dome flat exposure will be referred to as *traces* from here on (see Fig. 2.38). `cure` then searches for the calibration lamp line positions along those traces. It fits a two-dimensional Gauss Hermite model (Gerhard, 1993; van der Marel & Franx, 1993) to the light spots that correspond to the calibration lines. The shape of the light spot will be referred to as PSF from here on <sup>4</sup>. Finally, the cross section of a fiber spectrum is fitted again by a one-dimensional Gauss Hermite expansion which includes the parameters  $h_2$  and  $h_3$  <sup>5</sup>.

`cure` then models the trace and wavelength positions, the PSF shape and the trace cross-sectional shape as a two-dimensional Chebyshev polynomial of 7-th degree across the CCD surface. It calculates transformations between fiber number/wavelength and x/y positions and corresponding inverse and cross transformations.

`cure` offers a routine to extract spectra on a fiber basis. Given the previously determined models for fiber position and wavelength calibrations, the fiber extraction *walks* along the trace positions across the CCD and extracts the spectra through bicubic interpolation at given wavelength steps. The algorithm integrates the fluxes within a user-defined aperture around the trace centroid. The result is a wavelength calibrated frame with 267 rows corresponding to the 267 fibers of VIRUS-W. Here we typically extract spectra binned linearly in wavelength space.

Further routines allow to construct data cubes or reconstruct images by collapsing the data along the spectral direction (see Fig. 2.39).

<sup>4</sup>This is not strictly correct, as the shape really is a convolution of the spectrograph's point spread function (PSF), and the fiber core geometry and light emission characteristics.

<sup>5</sup>The detailed modelling of the instrumental PSF and the trace cross section are a consequence of `cure`'s original purpose to detect faint  $\text{L}\alpha$  emitters in a blind spectroscopic survey. The exact knowledge of the PSF shape enables the detection algorithm to use a Bayesian approach for line source detections.

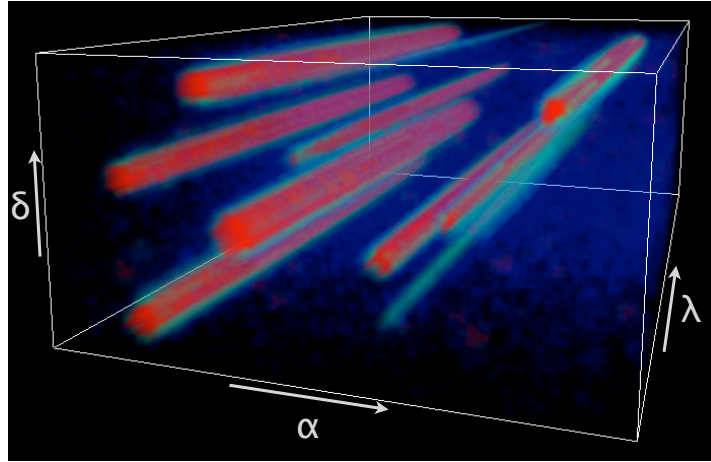


Figure 2.39 Example for a reconstructed cube using the subdithered M37 observations. The cube was rendered using `cure`'s `volviz` routine.

Finally, there are multiple options for the sky subtraction. The sky subtraction can use the bracketing sky nods or fibers that do not contain object signal. As the exact method of sky subtraction depends on the science case, this has to be handled by subsequent steps that are not part of the automatic `cure` pipeline.

However, `cure` does offer a routine to assist the sky subtraction called `skysubtract`. Fibers that do contain continuum sources such as stars are first rejected based on a medium filtering technique. Then the sky signal is determined in a window of adjustable width in cross dispersion direction (typically 100 px). The purpose of the window is to increase the sky signal to noise while being small enough to avoid mixing of regions with significant differences in spectral resolution. The sky subtraction routine then fits a spline to the window-averaged sky signal to remove high frequency noise and maps the resulting noise-free spectrum back into the CCD pixel space using the previously determined models for distortion and trace shape. The resulting noise and object-free frame is then subtracted from the original frame. The sky subtracted frame can then be given to the fiber spectra extraction. For extended sources `skysubtract` offers the ability to determine the sky signal from a separate frame, which for instance could be the exposure time scaled average of the bracketing sky nods.

# Chapter 3

## Commissioning

VIRUS-W was commissioned in November and December 2010. The commissioning went rather smoothly and involved the assembly of the instrument, the implementation of the interface to the telescope control system and the control algorithms, the choice of calibration lamps and strategies, the collections of various calibration standards, and of course first science observations. In this chapter we discuss results from these commissioning runs. We determine the actual instrumental throughput and the spectral resolution — both from lamps and from standard stars. We take a look at stray light, crosstalk, the instrumental stability and discuss the sample of kinematic and spectrophotometric standard stars that we obtained, and compare measurements of Lick indices to published values (Worthey et al., 1994). We will conclude with the presentation of first kinematic maps that we derived for three of the galaxies that we observed.

### 3.1 Commissioning Runs

VIRUS-W celebrated first light at the 2.7 m telescope at the McDonald Observatory in Texas on the 11-th of November 2010. This very first run borrowed time from the VENGA (Blanc et al., 2010b) survey. We observed spectrophotometric standards, astrometry fields, four kinematic templates and three spiral galaxies – all in the high resolution mode.

We assembled and aligned the instrument during the 10 days prior the November run and implemented interfaces to the telescope control system. We used daytime to adjust the tip-tilt of the spectrograph’s camera detector and to focus the camera. At midnight of the 11-th to the 12-th we exchanged the VIRUS-P IFU for the VIRUS-W IFU. The similarity of the mechanical interface and observing modes of VIRUS-P and VIRUS-W resulted in a very smooth deployment of the new instrument. We took a set of standard calibrations (dome flats, Ne and Hg arc lamps and bias frames) and continued with a first pointing to a bright star to verify the centring of the IFU. We then continued with an area in the outskirts of the open cluster M37 to establish an astrometric solution. The first actual galaxy was then the barred spiral galaxy NGC 2903. During the first night we observed two 1800 s pointings centred on the galaxy together with three 1200 s sky nods before, in between,

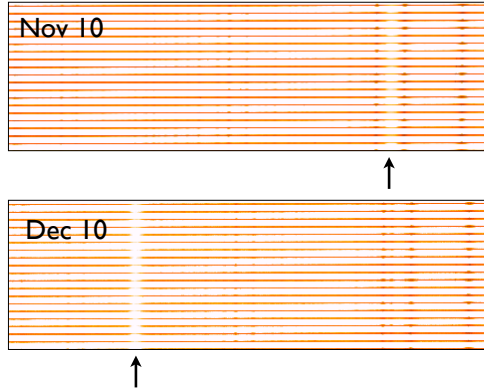


Figure 3.1 The original setup after the assembly in November 2010 created a Littrow ghost that fell right into the  $Mg\ b$  feature here seen in a twilight flat image. This situation was corrected in the December 2010 run. A few degree turn of the high resolution grating shifted the ghost towards bluer wavelengths.

and after the actual science exposures. We continued to observe the spectrophotometric standard star Feige 34 and concluded the night with another set of standard calibrations.

In the following four nights we also observed central pointings on the two late type spirals NGC 1042 and NGC 7479, the spectrophotometric standards Feige 34 and Feige 110, and five kinematic template stars (see Table 3.1) in the high resolution mode. The data that we obtained in the very first minutes after the installation are already of science quality rendering this first run a full success.

The time allocation committee awarded us with five further nights of actual commissioning time in December 2010. During this time we improved the alignment of the high resolution grating, extended the library of kinematic templates and observed five additional galaxies (see Table 3.2). We observed the dwarf elliptical galaxy NGC 205 — a satellite of M31 — which has a very low central velocity dispersion ( $\simeq 20 \text{ kms}^{-1}$ ) and hence tests the high dispersion mode at its extreme. We used for the first time the low resolution mode to observe the elliptical galaxies NGC 3091 and NGC 307. The data will accompany high spatial resolution adaptive optics assisted data that our group obtained as part of a black hole mass survey with the SINFONI spectrograph at the ESO Very Large Telescope. The VIRUS-W data will specifically help us to constrain the dynamical mass to light ratio.

The data from the first run showed that the Littrow ghost — a consequence of the instrument design (Burgh et al., 2007) — fell right into the  $Mg\ b$  region for objects with zero redshift. Since this would have created complications in the extraction of kinematics we decided to change the grating angle slightly to move the Littrow ghost towards the blue end of the spectrum (see Fig. 3.1). This modification does affect the throughput of the spectrograph and shift its maximum to the blue.

We observed a field in the disk region of M31. The region is located  $1000''$  away from the galaxy’s center along the major axis. These data test our ability to recover LOSVDs in low

Table 3.1. Observations during the November 2011 run

Target	type	date	resolution	exposure time & mode	seeing
<b>Galaxies</b>					
NGC 2903	SABbc <sup>(1)</sup>	11/11/2011	HR	2 × 1800 s + 3 × 1200 s sky	2.5''
		11/13/2010	HR	2 × 1800 s + 3 × 1200 s sky	2.5''
		11/14/2010	HR	3 × 1800 s + 4 × 1200 s sky	2.2''
NGC 7479	SBc <sup>(1)</sup>	11/14/2010	HR	3 × 1800 s + 4 × 1200 s sky	2.3''
		11/14/2010	HR	3 × 1800 s + 4 × 1200 s sky	2.3''
		11/15/2010	HR	2 × 1800 s + 3 × 1200 s sky	1.8''
NGC 1042	SABcd <sup>(1)</sup>	11/13/2010	HR	4 × 1800 s + 5 × 1200 s sky	2.0''
		11/14/2010	HR	3 × 1800 s + 4 × 1200 s sky	2.0''
		11/15/2010	HR	3 × 1800 s + 4 × 1200 s sky	2.0''
<b>Astrometry field</b>					
M37	open cluster	11/11/2010	HR	6 × 120 s subdithered	2.0''
<b>Spectrophotometric standards</b>					
Feige 34	sdO	11/11/2010	HR	6 × 180 s subdithered	2.2''
Feige 110	D0p	11/13/2010	HR	6 × 120 s subdithered	?
<b>Kinematic templates and Lick standards</b>					
HR2600	K2III	11/12/2010	HR	260 s	2.2''
HD74377	K3V	11/14/2010	HR	trailed 20 s/step	2.0''
HR4435	G9IV	11/14/2010	HR	trailed 20 s/step	2.0''
HR3428	K0III	11/15/2010	HR	trailed 20 s/step	?
HR3369	G9III	11/15/2010	HR	trailed 20 s/step	2.5''

Notes: 1) from de Vaucouleurs et al. (1991)

surface brightness situations through binning over many fibers in the IFU, and to prepare a future program to study the large scale kinematic structure of M31 with VIRUS-W.

The final dataset (see Table 3.1 & 3.2) from the two commissioning runs includes data of 8 galaxies and 18 Lick/IDS standard stars out of which 12 are G or K-type giants and are suitable kinematic templates stars. During all nights we observed spectrophotometric standards which allow us to determine the instrumental throughput of both the high and the low resolution mode.

## 3.2 Overall Efficiency and Exposure Time Calculations

It is instructive to compare the actual to the expected throughput. This exercise will tell us whether the alignment of the instrument is done sufficiently to avoid light loss. In §2.1 we took a look at the transmission and the reflectivity of all parts of the spectrograph. A straightforward multiplication of the transmission curves and incorporation of the atmospheric extinction allows us to predict the photon flux on the detector. We then compare the prediction to the actual observed fluxes of the standards.

Table 3.2. Observations during the December 2011 run

Target	type	date	resolution	exposure time & mode	seeing
<b>Galaxies</b>					
NGC 205	E5 pec <sup>(1)</sup>	12/02/2010	HR	6 × 1800 s dithered + 7 × 1200 s sky	1.5–1.7''
NGC 3091	E3 <sup>(1)</sup>	12/05/2010	LR	12 × 600 s + 13 × 300 s sky, dithered	2.0–2.2''
M 31	SAb <sup>(1)</sup> (disk)	12/03/2010	HR	4 × 1800 s + 5 × 1200 s sky	2.0''
NGC 307	S0 <sup>(1)</sup>	12/05/2010	LR	9 × 1200 s + 10 × 600 s sky dithered	2.5–3.0''
		12/06/2010	HR	6 × 1800 s + 7 × 1200 s sky dithered	2.0–2.2''
NGC 2841	SAb <sup>(1)</sup>	12/03/2010	HR	3 × 1600 s + 4 × 1000 s sky, dithered cosmic ray split	2.2''
<b>Astrometry field</b>					
M 37	astrometry field	12/02/2010	HR	6 × 120 s subdithered	2.0''
<b>Spectrophotometric standards</b>					
Feige 110	sd0	12/02/2010	HR	60 s subdithered	1.5''
		12/03/2010	HR	300 s subdithered	1.5''
		12/05/2010	LR	120 s subdithered	1.7''
		12/06/2010	HR	120 s subdithered	2.0''
<b>Kinematic templates</b>					
HD101501	G8V	12/03/2010	HR	trailed 5 s/step	2.0''
HD101501	G8V	12/05/2010	LR	trailed 5 s/step	2.2''
HD161817	A2IV	12/03/2010	HR	60 s three IFU positions	2.5''
HD64606	G8V	12/03/2010	HR	60 s three IFU positions	2.5''
HD64606	G8V	12/05/2010	LR	trailed 10 s/step	2.0''
HD74377	K3V	12/05/2010	LR	trailed 10 s/step	2.0''
HD74377	K3V	12/03/2010	HR	trailed 60 s/step	2.0''
HR2600	K2III	12/02/2010	HR	trailed 20 s/step	2.0''
HR2600	K2III	12/05/2010	LR	trailed 20 s/step	2.5''
HR3369	G9III	12/05/2010	LR	trailed 10 s/step	2.5''
HR3418	K2III	12/02/2010	HR	trailed 5 s/step	1.9''
HR3418	K2III	12/05/2010	LR	trailed 5 s/step	2.0''
HR3422	G8IV	12/02/2010	HR	trailed 5 s/step	2.0''
HR3422	G8IV	12/05/2010	LR	trailed 5 s/step	2.0''
HR3427	K0III	12/02/2010	HR	trailed 20 s/step	1.9''
HR3427	K0III	12/05/2010	LR	trailed 5 s/step	2.0''
HR3428	K0III	12/05/2010	LR	trailed 10 s/step	2.0''
HR3905	K2IIIb	12/02/2010	HR	trailed 5 s/step	2.0''
HR3905	K2IIIb	12/05/2010	LR	trailed 5 s/step	2.0''
HR4435	G9IV	12/05/2010	LR	trailed 5 s/step	2.2''
HR6770	G8III	12/03/2010	HR	15 s three IFU positions	2.5''
HR6817	K1III	12/03/2010	HR	trailed 10 s/step	2.0''
HR6817	K1III	12/05/2010	LR	15 s three IFU positions	2.0''
HR7576	K3III	12/04/2010	HR	trailed 60 s/step	3.0''
HR7576	K3III	12/05/2010	LR	15 s three IFU positions	2.0''

Notes: 1) from de Vaucouleurs et al. (1991)

We use the subdithered spectra of the spectrophotometric standard star Feige 110 that we observed during the December commissioning run. The spectra are reduced using the `cure` pipeline and procedures described in §2.3. The task `fiberextract` extracts the flux in a given aperture around the center of the fiber spectra (traces) on the chip. The larger the extraction aperture, the smaller the aperture loss. But with increasing aperture the crosstalk between neighbouring fibers increases. We use a simple model to determine a suitable aperture for the throughput calculation. We assume a purely gaussian trace profile and calculate the overlap and the aperture loss as a function of aperture size and fiber separation. The FWHM of the trace in cross dispersion direction varies from 2.3–3 pixel. The separation of the fibers on the chip varies from 7.7 pixels in the center to 7.5 pixels at the ends of the spectral range. Through integration of the gaussian models, we determine that a 7 pixel wide extraction aperture results in less than 1% aperture losses and less than 0.1% crosstalk between the fibers (see Fig. 3.2). For the throughput measurement we choose an extraction aperture of 7 pixels around the trace center.

The result of the extraction is a wavelength calibrated frame with 267 rows — one row for each fiber — in each dither position. We sum the signal of all fibers for which the center position lies within a  $r = 10''$  wide aperture of the star center position. We use a  $7''$  wide annulus around the central aperture to subtract the sky signal. A further increase of the aperture sizes showed to have little effect on the result. The subdithered observation results in two effective observations of the star <sup>1</sup>. We average the summed fluxes of the first three dithers together with the ones from the last three dithers.

We have detailed measurements of the throughput of the filter, the reflectivity measurements of the mirrors, the transmission of the slit lens and the fibers, and the quantum efficiency of the CCD detector at hand. For the gratings we use the theoretical throughput estimate from the vendor that we scale to match the monochromatic measurement that we have conducted in our lab (see §2.1.10). For the camera lens we assume identical reflection losses at all air/glass surfaces and use the slit lens measurement to model those. We do not have a detailed measurement for the telescope and the focal reducer throughput at hand. The telescope mirrors are coated with aluminium. The SOPRA<sup>2</sup> database lists values for the real and the complex part of the refractive index of aluminium. We calculate the reflectivity according to

$$R = \frac{(n - 1)^2 + k^2}{(n + 1)^2 + k^2} \quad (3.1)$$

(e.g. Pedrotti & Pedrotti, 1993). We model the telescope losses by three consecutive reflections at the mirrors M1-M3 which assumes a new coating. We use a 2.7 m aperture and a 43 cm wide central obscuration from the secondary mirror<sup>3</sup>. The focal reducer has four anti-reflective coated air-glass surfaces. We assume a 99% throughput, following

<sup>1</sup>The fill factor of the IFU is 1/3. The first three dithers are arranged such that 100% coverage is reached. Dithers number 4 to 6 again give additional 100% coverage.

<sup>2</sup><http://www.sopra-sa.com/>

<sup>3</sup>see: <http://www.as.utexas.edu/mcdonald/facilities/2.7m/2.7.html>

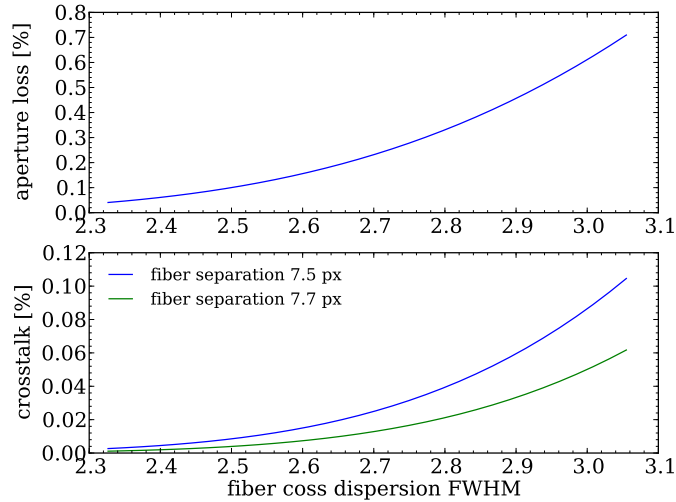


Figure 3.2 Theoretical aperture loss and cross talk for a fixed 7 pixel wide extraction aperture as a function of the FWHM width of the trace. *upper panel:* A 7 pixel wide extraction aperture results in less than 1% aperture losses and less than 0.1% crosstalk between the fibers.

the suggestion by the designer Phillip MacQueen (private communication). We calculate atmospheric extinction losses using the IRAF ONEDSPEC extinction law for the Kitt Peak Observatory (altitude 2096 m, McDonald 2070 m).

In the upper panels Fig. 3.3 we show the calculated cumulative throughput curve for the respective effective airmass of the standard star observations for the high and the low resolution mode. In the middle panels we further plot the expected electron counts based on the literature values (Oke, 1990) and compare them to our actual measurements. The bottom panels show the ratio of predicted to measured counts and hence the measured throughput of the whole system of atmosphere, telescope, and spectrograph. We also plot the expected throughput curves in red for comparison.

We find that both the high and the low resolution mode throughput curves deviate from the predictions. With a maximum throughput of 37%, the high resolution mode curve peaks at a value that lies about 7% higher than the predicted throughput. Also, the peak occurs at a different wavelength of about 5100 Å as compared to the peak of the prediction which lies at 5150 Å. The shift of the peak is expected. It is a consequence of the adjustment of the grating angle that we applied during the December commissioning run in order to move the Littrow ghost away from the Mg *b* feature. The overall larger throughput is surprising and hints at the possibility that some of the values that we use for the prediction are too pessimistic.

On the other hand the low resolution mode efficiency is systematically smaller than the prediction. It peaks at about 5140 Å with a value of about 40% while we expected

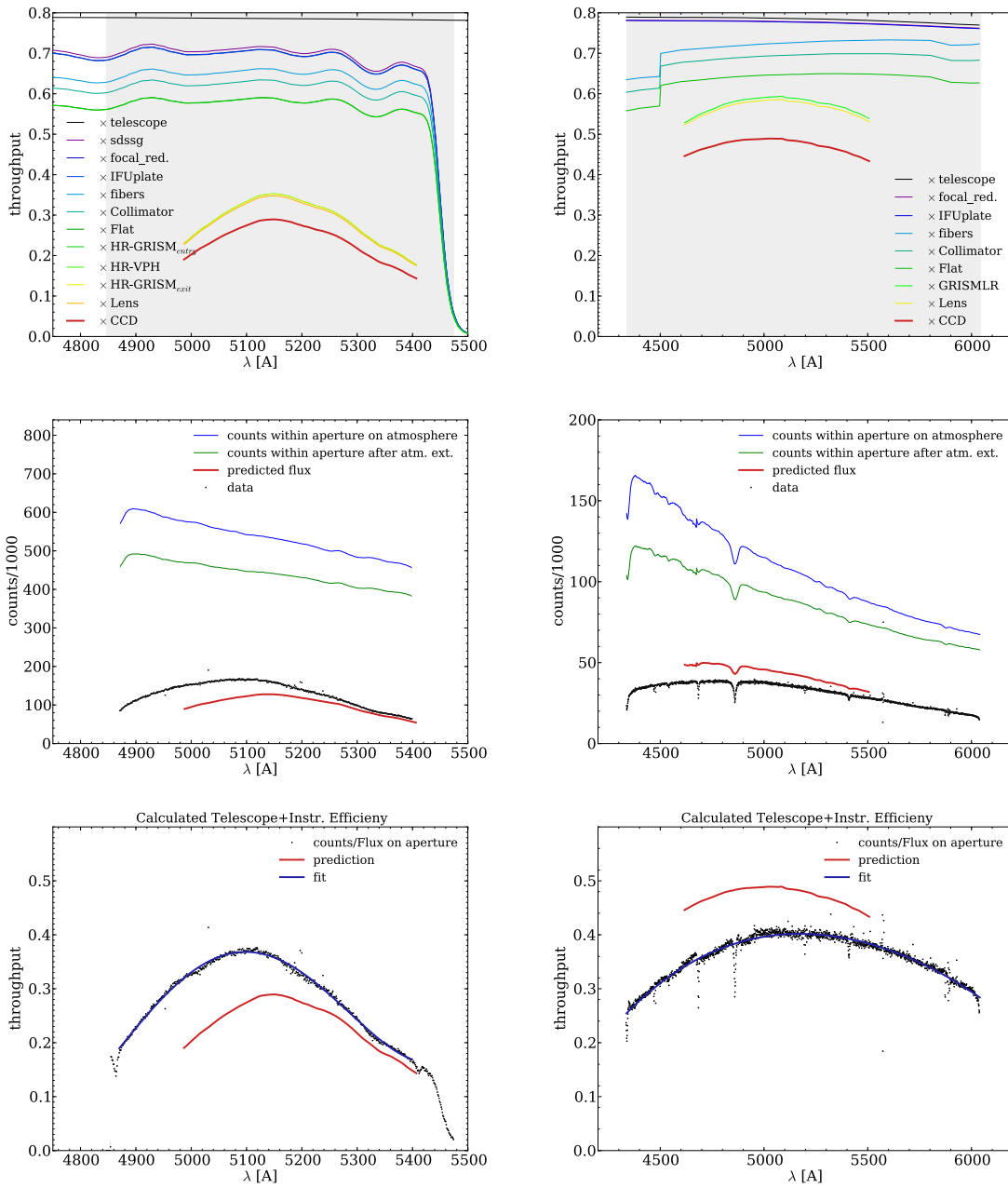


Figure 3.3 Predictions of the throughput and comparison to measurements. *Top panels:* We plot the cumulative throughput as function of wavelength for the high resolution mode left and for the low resolution mode right. The plotted curves represent the respective throughput after the corresponding element listed in the legend. The curves are based on the measurements and prediction of the individual optical elements discussed in §2.1.3. The atmospheric extinction is not included in these plots. *Middle panels:* Compares the predicted flux of the spectrophotometric standard Feige 110 based on the data of Oke (1990) to the reconstructed fluxes (see text). The predicted fluxes are corrected to the effective airmass of the observation. *Bottom panels:* The throughput as calculated from the ratio of recovered counts and the incident flux. The fitted throughput model that is used in the exposure time calculations is plotted in blue.

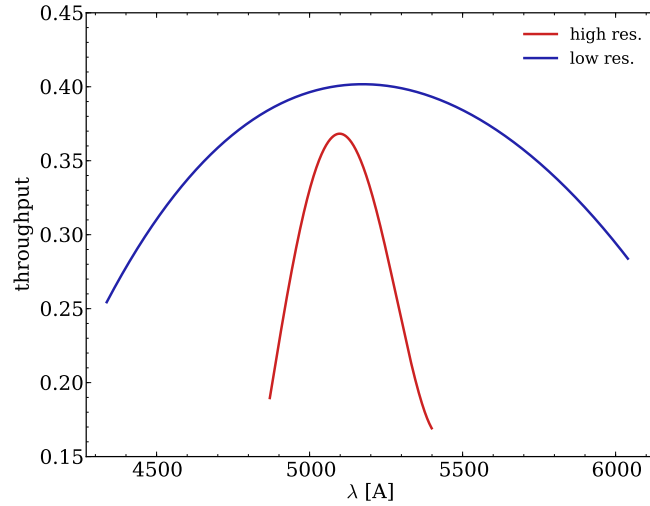


Figure 3.4 Adopted throughput models for both resolution modes for airmass one. The throughput includes atmospheric loss, telescope, all optical elements between the telescope and the CCD detector, and the detector’s quantum efficiency. Since VIRUS-W will observe mostly extended sources we do not include any aperture effects.

a peak of 49% at 5040 Å. We confirmed the low values by using a further standard star observation that was conducted in May 2011 under excellent conditions and found good agreement with the shown values. The shift of the throughput maximum is again explained by a slight angular offset of the low resolution mode grating with respect to the nominal angle. During the assembly the grating angle was set by hand and no attempt was made to adjust it precisely. An incorrect setting of the grating angle also likely explains the overall decrease 9% efficiency<sup>4</sup>.

The measured throughput is affected by noise and spectral features that cause obvious artefacts in the lower panels of Fig. 3.3. To eliminate those, we model the throughput curve by fitting a fourth order polynomial to the measurements. The high resolution mode curve shows an extended tail at the red end (5300 Å – 5400 Å) that we model separately by a linear function. The blue curves in Fig. 3.3 and both curves in Fig. 3.4 show the fits.

The models allow us to predict signal to noise values (as function of wavelength) for a given surface brightness, sky brightness and exposure time. We assume a readout noise of  $1.36 e^-$  which is the value for the 100 kHz readout speed that we typically use for science observations. In Fig. 3.5 we show monochromatic  $S/N$  estimates at a wavelength of 5160 Å (the position of the for kinematics important Mg *b* feature). For a typical McDonald

<sup>4</sup> During a regular science run in October and November 2011 we were able to confirm incorrect grating angle setting by taking dome flats at various grating angles. Unfortunately the transparency still suffered from the severe forest fires in West Texas in the spring of the same year, leaving us unable to remeasure the actual throughput on a star.

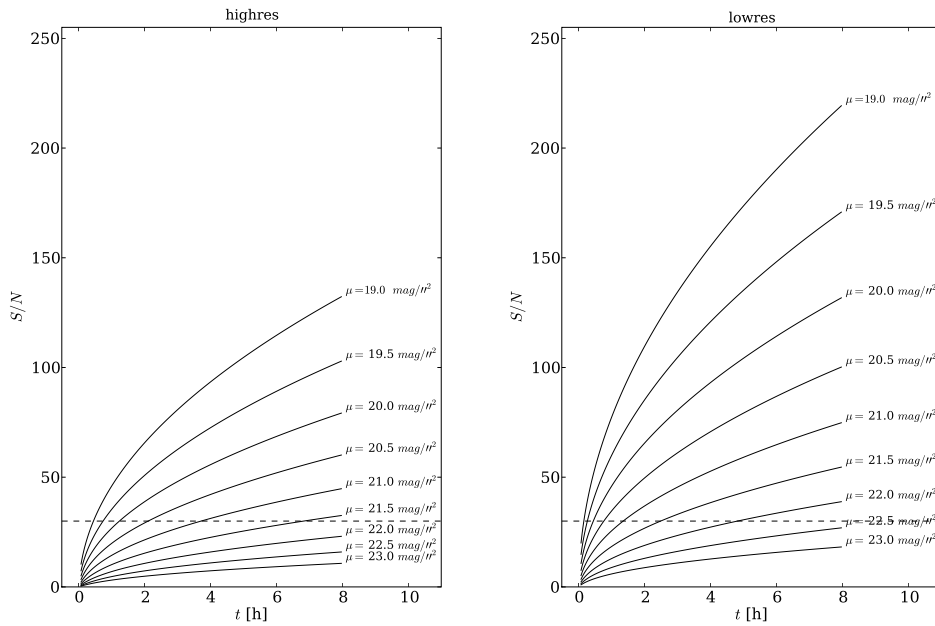


Figure 3.5 Signal to noise estimates based on the determined throughput. We plot the  $S/N$  build-up as a function of integration time. The different curves correspond to different surface brightnesses in V band. The left panel shows the  $S/N$  estimates for the high resolution mode, while the right panel shows the low resolution mode. In both panels the horizontal dashed line corresponds to a  $S/N$  of 30 per pixel, a value that we consider appropriate to derive higher moments of the LOSVDs reliably. The  $S/N$  predictions here assume a night sky brightness on  $22 \text{ mag}/\mu^2$  in V-band and are calculated for a single dither.

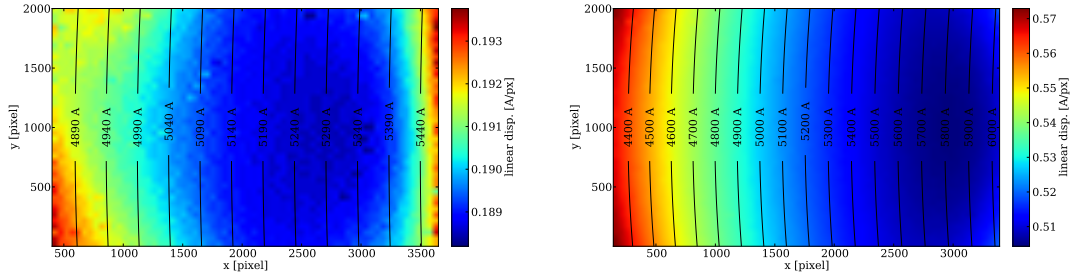


Figure 3.6 The linear spectral dispersion as function of position on the CCD. The left panel plots the dispersion for the high resolution mode, the right panel plots the dispersion for the low resolution mode. The corresponding wavelengths are overplotted.

dark-time sky brightness of  $22.0 \text{ mag}/''^2$  (AB) we expect to reach a signal to noise of 30 per spectral pixel ( $\approx 0.19 \text{ \AA}$  wide) for a surface brightness of a  $21.7 \text{ mag}/''^2$  (AB) within 8 hours of integration and 16 readouts of the detector (to allow for sky nods). With overhead, and sky observations this results in about two nights of observation. Actual exposure times will differ depending on the dither strategy, the maximum amount of acceptable binning and transparency. For the same conditions the low resolution mode will reach a  $S/N$  of 30 per spectral pixel in 2 h.

### 3.3 Wavelength Calibration and Spectral Dispersion

In §2.2.2 we show images of a typical set of calibration lamp frames. We use the wavelength calibration routine of `cure` to determine a wavelength and distortion solution. The line lists that we use for calibration are given in Table 3.3 and 3.4. In Fig. 3.6 we plot the linear spectral dispersion as function of the position on the chip. In good agreement with the expectations from the optical design we get values of  $0.19 \text{ \AA}/\text{px}$  ( $0.52 \text{ \AA}/\text{px}$ ) in the high (low) resolution mode in the chip center. The typical standard deviation of the wavelength calibration is 0.2 pixel or  $0.04 \text{ \AA}$  in the high resolution mode and  $0.1 \text{ \AA}$  in the low resolution mode. The adopted ends of the usable wavelength range are determined by the availability of calibration lines. The high resolution mode covers  $4300 \text{ \AA}$ –  $6030 \text{ \AA}$  and the low resolution mode covers  $4847 \text{ \AA}$ –  $5470 \text{ \AA}$ .

Table 3.3. High resolution mode calibration line identifications

$\lambda$ [Å]	approx. CCD row [px]	Ion
4916.33	360	Hg II
5025.61	930	Hg II
5037.75	996	Ne I
5080.38	1218	Ne I
5113.67	1395	Ne I
5116.50	1410	Ne I
5122.26	1440	Ne I
5144.94	1560	Ne I
5151.96	1595	Ne I
5188.61	1790	Ne I
5193.13	1815	Ne I
5203.90	1871	Ne I
5208.87	1898	Ne I
5330.78	2542	Ne I
5341.09	2595	Ne I
5343.28	2608	Ne I
5354.03	2666	Hg I
5400.56	2910	Ne I
5460.75	3225	Hg I

*Notes:* From the NIST Atomic Spectra Database  
[http://physics.nist.gov/PhysRefData/ASD/lines\\_form.html](http://physics.nist.gov/PhysRefData/ASD/lines_form.html).

Table 3.4. Low resolution mode calibration line identifications

$\lambda$ [Å]	approx. CCD row [px]	Ion
4339.22	65.	Hg I
4347.49	79.	Hg I
4358.34	98.	Hg I
4704.39	723.5	Ne I
4708.85	732.3	Ne I
4715.34	744.	Ne I
4916.07	1118	Hg II
5031.35	1336	Ne I
5037.75	1348	Ne I
5074.20	1417.4	Ne I
5080.38	1429.4	Ne I
5116.50	1498.3	Ne I
5144.94	1553	Ne I
5151.96	1566	Ne I
5188.61	1637	Ne I
5193.13	1645	Ne I
5330.78	1911	Ne I
5341.09	1931	Ne I
5400.56	2047	Ne I
5460.75	2164	Hg I
5562.77	2364	Ne I
5656.66	2548.5	Ne I
5689.82	2614	Ne I
5719.22	2672	Ne I
5748.30	2729	Ne I
5764.41	2761	Ne I
5769.61	2771	Ne I
5804.45	2840	Ne I
5820.16	2870.5	Ne I
5852.49	2934.5	Ne I
5881.90	2992.5	Ne I
5944.83	3114.4	Ne I
5975.53	3174.5	Ne I
6023.00	3279.5	Ne I

*Notes:* From the NIST Atomic Spectra Database  
[http://physics.nist.gov/PhysRefData/ASD/lines\\_form.html](http://physics.nist.gov/PhysRefData/ASD/lines_form.html).

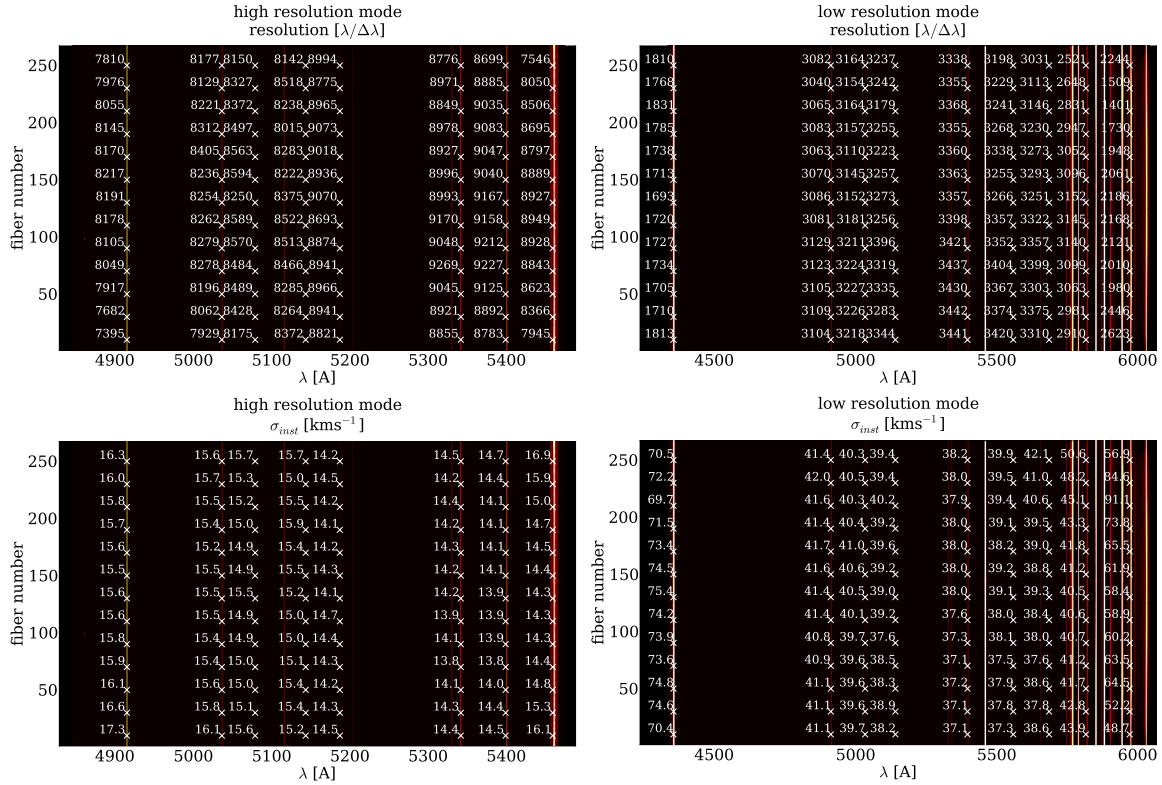


Figure 3.7 The resolution as calculated from the calibration lamp frames (see text). We plot the wavelength calibrated and fiber extracted spectra in the background and indicate the lines and positions that were used to calculate the resolution  $R = \lambda/\Delta\lambda$ . The labelled values are the median of a measurement on 20 neighbouring fibers. The lower panels plot the corresponding instrumental resolution in  $\text{kms}^{-1}$  as given by  $\sigma_{inst} = c \cdot R^{-1} \cdot 2.35^{-1}$ .

### 3.4 Spectral Resolution in Dispersion and Cross-Dispersion Direction

As VIRUS-W's niche is the combination of a large field of view with a high spectral resolution, this thesis would be incomplete without a test of the actual resolution that the instrument reaches. This test is also crucial in order to access whether we need to correct for a potential change in resolution as function of fiber number. If we did find such a variation then this would need to be taken into account during the reduction of actual science observations.

For the measurement we extract wavelength calibrated spectra (see §2.3) from two of the combined calibration lamp frames. We then fit Gaussians to a subset of lines using a standard least squares algorithm. The lines are selected to reject obvious asymmetric line profiles and blends. Next to the dispersion  $\sigma$ , we fit for the mean wavelength  $\mu$ , the amplitude  $A$ , and a constant offset to account for a potential continuum or stray light.

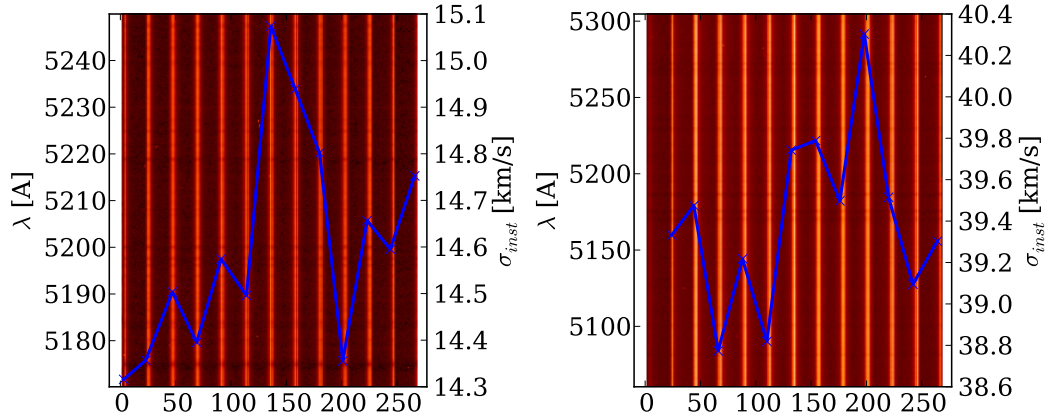


Figure 3.8 Resolution as function of fiber number measured on a stellar spectrum. The blue line shows the resolution as function of fiber number. We use a spectrum of the star HR3369 which has the spectral type G9 III. The plotted values are derived by fitting a Gaussian to the width of the autocorrelation function of the data. The background image shows the actual extracted data that the resolution was measured on. The image is the result of a IFU-trailing procedure as described in the text. *Left panel:* High resolution mode mean  $14.6 \text{ km s}^{-1}$ ,  $RMS = 0.2 \text{ km s}^{-1}$ . *Right panel:* Low resolution mode, mean  $39.4 \text{ km s}^{-1}$ ,  $RMS = 0.4 \text{ km s}^{-1}$ .

In Fig. 3.7 we report the resulting resolutions as  $R = \lambda/\Delta\lambda$  where  $\Delta\lambda(\lambda) = 2.35 \cdot \sigma_{fit}(\lambda)$ . We also show the corresponding instrumental dispersion in  $\text{km s}^{-1}$  as  $\sigma_{inst} = c \cdot \sigma_{fit}(\lambda)/\lambda$ . We find that the resolution varies from  $R = 2890$  ( $\sigma_{inst} = 44.1 \text{ km s}^{-1}$ ) to  $R = 4550$  ( $\sigma_{inst} = 28.0 \text{ km s}^{-1}$ ) with a mean value of  $R = 3274$  ( $\sigma_{inst} = 39.0 \text{ km s}^{-1}$ ) in the low resolution mode. In the high resolution mode it varies from  $R = 7039$  ( $\sigma_{inst} = 18.1 \text{ km s}^{-1}$ ) to  $R = 9270$  ( $\sigma_{inst} = 13.8 \text{ km s}^{-1}$ ) with a mean value of  $R = 8660$  ( $\sigma_{inst} = 14.7 \text{ km s}^{-1}$ ). The central values are slightly larger than the ones one would expect from the naive model of §2.1.13. As mentioned therein, this may have to do with the subtleties of the exact form of the surface luminance of the fiber ends. A detailed discussion leaves the scope of this thesis, we content ourselves with the finding that the optical performance meets our goals.

We complete the assessment of the spectral resolution through a measurement on an actual star. Basis for this measurement is one of the kinematic template spectra that we obtained during the commissioning runs in November and December 2010. We use the spectrum of the G9 giant star HR3369. The star was observed in both resolution modes and trailed across the IFU as we explain in §3.7. The trailing results in the illumination of one or a few fibers in each row of the IFU. Since the fibers are arranged in the slit by their respective IFU-row, the trailing results in spectra that are distributed across the whole CCD. We pick one spectrum per row that is reasonably high in signal but is still not saturated or close to the non-linear regime of the output amplifiers. Typical accepted

counts lie between 5000 and 40000.

We again reduce and extract the spectra using the `cure` routines described in §2.3. The selected spectra are then log-wavelength rebinned in a subsequent step. We calculate the resolution by measuring the width of the peak of the autocorrelation function of the individual spectra. We fit a Gaussian using a standard least squares algorithm and do not fit to values that lie lower than 15% of the peak maximum. The actual resolution is given by the width of the peak divided by the square root of two. In the high resolution mode we estimate the resolution in the wavelength region 5170 Å – 5250 Å and in the low resolution mode in the region 5060 Å – 5300 Å corresponding to approximately equally large physical regions on the detector.

In Fig. 3.8 we plot the variation of the spectral resolution across the CCD. The variation of the resolution is small, and the shape of the curve suggests that our measurement is dominated by noise. The mean resolution in the high resolution mode is  $\langle \sigma_{inst} \rangle = 14.6 \text{ km s}^{-1}$  with a standard deviation of  $0.2 \text{ km s}^{-1}$ . The low resolution mode has a mean resolution of  $\langle \sigma_{inst} \rangle = 39.4 \text{ km s}^{-1}$ , standard deviation  $0.4 \text{ km s}^{-1}$ .

Both the measurement on calibration lines and on the stellar features are in good agreement. However we do find that the method of the width of the autocorrelation is affected by the exact choice of the spectral window. In the high resolution mode we find that including the *Mgb* feature results in a lower resolution  $\simeq 18 \text{ km}^{-1}$  than what we determine when we exclude them. This may be due to the inset of blending of various lines in that region even at resolutions of  $\simeq 8000$ . However both methods show little variation as function of fiber number. We conclude that for most applications we probably will not have to apply corrections to the derived dispersions as function of fiber.

## 3.5 Stray Light and Fiber Separation

The ability to cleanly separate spectra belonging to different fibers is critical for the derivation of accurate kinematics. If the signal of a bright fiber *bleeds* into a fiber that receives significantly less light, then the derived broadening function for the latter will be distorted by the one of the former.

The effect is somewhat mitigated by the fact that the fibers in the IFU are sorted and at least for the center of the IFU it is true that neighbouring fibers belong to spatially adjacent regions on sky. This assures that not regions of very different surface brightness and kinematics are mixed together. However, the centers of galaxies tend to show pronounced peaks in the local surface brightness and strong gradient in surface brightness tends to coincide with strong gradients of the shape of the LOSVDs.

As proxy for the separation of the fiber signal we test at what signal levels the fiber spectra cross. In Fig. 3.9 and 3.10 we plot cuts along the cross-dispersion dimension of dome flats. The panels correspond to different locations on the CCD, showing a central region as well as regions close to the edge of the detector. In order to suppress noise, the signal was averaged over 30 neighbouring columns. As the separation is determined by the image quality, and the image quality varies over the CCD, the separation will degrade at

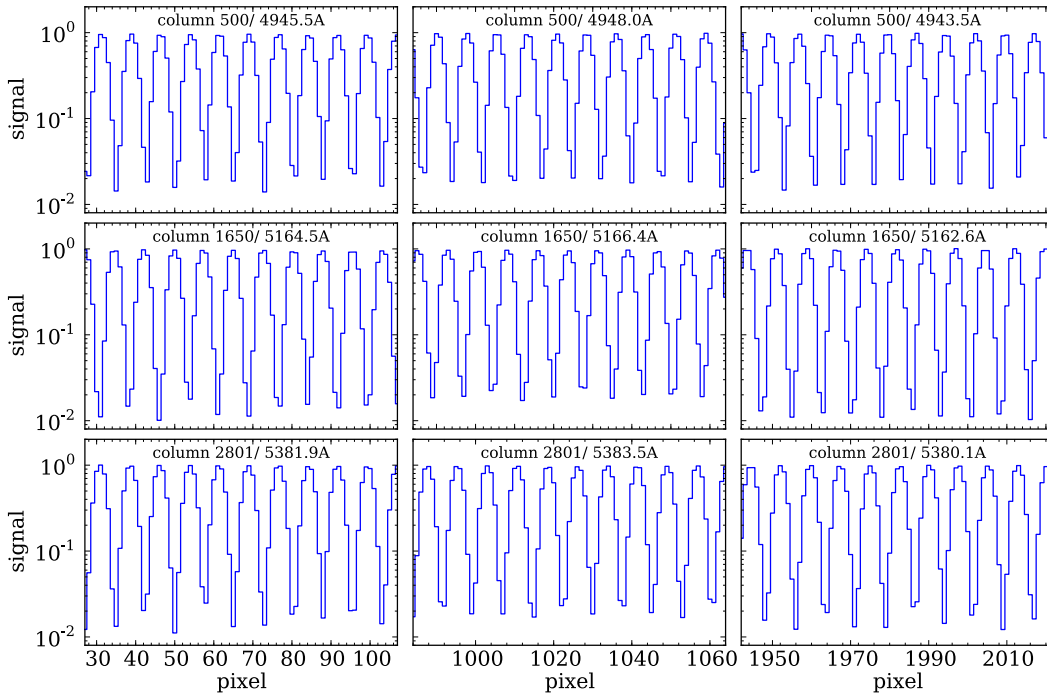


Figure 3.9 Cross cuts in spatial dimension (along CCD columns) for a dome flat taken in high resolution mode. We average the signal over 30 columns. The different panels correspond to different positions on the detector with the blue end of the spectral range shown in the top panels and the red end shown in the bottom panels. The separation of the spectra is somewhat degraded and the ends of the spectral range — due to the loss of image quality — and in the center of the detector possibly due to stray light. Spectra cross at 2% – 3% of the peak intensity in all plots.

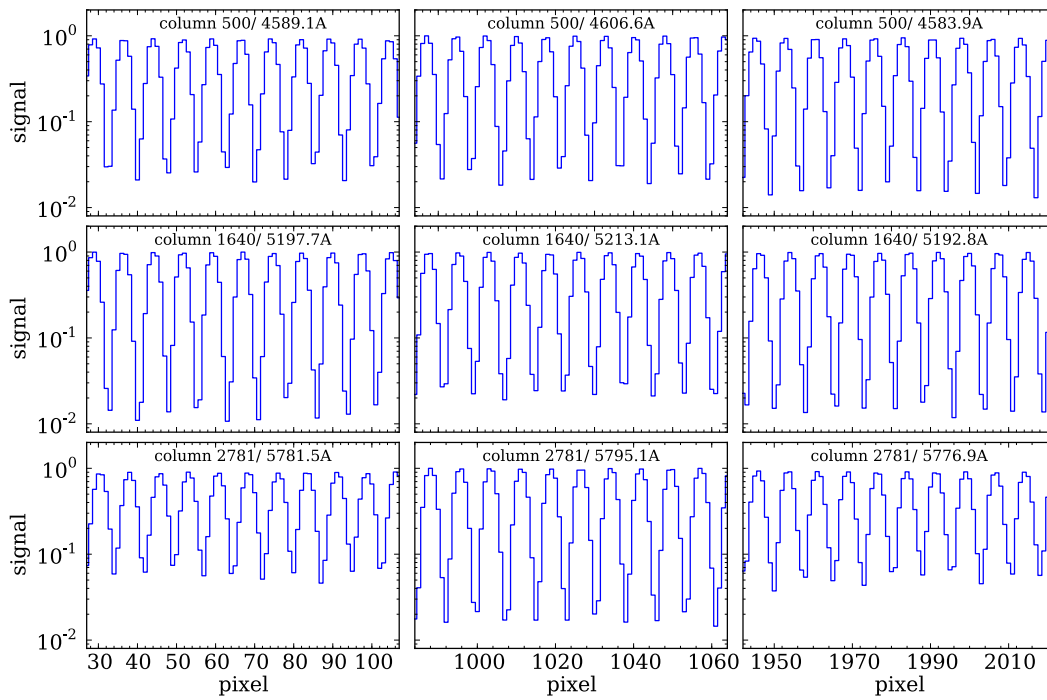


Figure 3.10 Like Fig. 3.9 but for the low resolution mode. Especially at the red end the degradation of image quality is notable with spectra crossing at about 7% of the peak values.

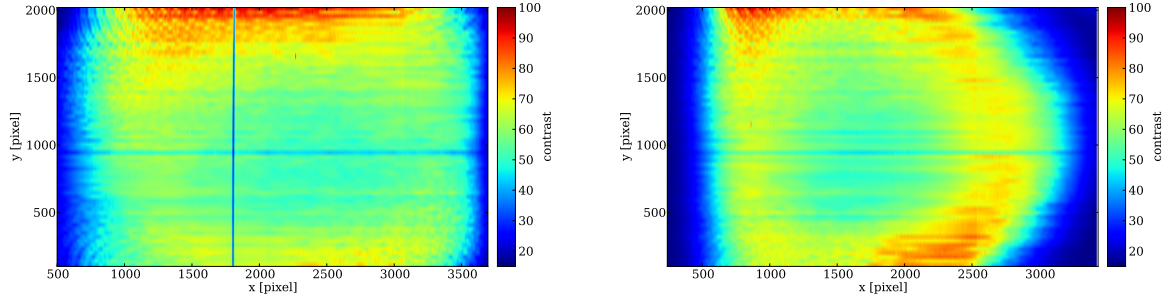


Figure 3.11 Maps of the fiber peak to gap contrast as a function of the chip position. In the left panel we plot the contrast map for the high resolution mode and in the right panel we plot the contrast map for the low resolution mode. The vertical feature in the high resolution map corresponds to the Littrow ghost described in §3.1. Note that the chip is larger than the depicted area. The rest of the chip area is discarded.

the ends of the spectral range. This is readily seen in the upper and the bottom rows of the figure. But also the central panel shows larger crossing values. The reason probably lies in scattered light that falls mostly into the central area of the CCD. Typical signal levels in the crossings lie at 2% – 3% of the peak intensity. A more concise view is given in Fig. 3.11. We plot the local contrast — i.e. the ratio of peak values to crossing signal values — as function of detector position. We measure the contrast in a given region by determining the fiber peak signal values and dividing it by the minimum values found between two fibers. We average measurements in windows that are 5 pixel wide in dispersion and 30 pixel wide in cross-dispersion direction. The contrast takes values between 10 and 100 across the CCD but the low values are only seen at the ends of the spectral range. Over most of the actual spectral range the contrast remains above 50.

In the high resolution mode contrast map a vertical feature is seen around column 1700. This feature corresponds to the Littrow ghost discussed in §3.1. The location of this ghost can be modified by turning the grating by a small angle. The current position is chosen such that the ghost does not contaminate any features that are important for the derivation of stellar or gaseous kinematics.

Again, in both modes the contrast in the chip center is somewhat decreased, probably due to residual stray light. The horizontal feature around the CCD row 950 is not understood. The falloff of the contrast at the red end of the low resolution mode map is partly a consequence of the fact that we actually use a larger spectral range than the instrument was designed for but also in this mode we do not employ a filter to reject light that falls out of the spectral range of this mode. This is different to the high resolution mode where we do use a SDSS  $g$  filter.

## 3.6 Stability

As the instrument is bench-mounted the stability is virtually only affected by thermal expansions. We briefly addressed the issue of temperature stability in §2.1.14. We explain therein that we integrated a temperature control into the enclosure to prevent thermal drifts.

Drifts in dispersion direction will create systematic offsets in the derived velocities and — if they occur on short time scales — decrease the effective spectral resolution. Also drifts in cross dispersion direction need to be considered. In classical slit spectrographs they create systematic uncertainties in the astrometry and decrease the effective spatial resolution. In fiber spectrographs such drifts would cause the spectral extraction apertures not to be centred on the fiber centroids which then leads to losses and/or increased crosstalk between neighbouring fibers.

We are mostly interested in short term drifts since we typically calibrate once in the evening before the observations, and once in the morning after. We like to determine whether this scheme is sufficient or if calibrations need to be done more frequently. As loss of resolution is also mostly a concern for the high resolution mode, we restrict the analysis to this mode.

In order to assess the magnitude of drifts we investigate the spectral and distortion calibrations that we obtained over three observing runs. We exclude the November commissioning run because we readjusted the grating afterwards. We do however include data from observing runs in May 2012 and August 2012 that were not part of the commissioning.

The calibration data allow to determine to which x and y pixel coordinates a specific fiber centroid and wavelength combination mapped. In Fig. 3.12 we pick three different such combinations. One corresponds to a central chip position and consequently to the central slit fiber and a central wavelength (middle row). The other two (top and bottom rows in the figure) correspond to the outermost fibers and wavelengths close to the ends of the spectral range. They are mapped to diagonally opposite corners on the detector. We plot the variation of the corresponding pixel coordinates with respect to the mean position over all three runs. The x-direction corresponds to the dispersion direction, while the y-coordinate varies along the cross-dispersion direction.

As can be seen from the plots there is significant variation with time. Especially the difference in y-position (the cross dispersion direction) of the fibers between the December 2010 and the August 2011 runs amounts to about  $\pm 2$  pixel. We suspect the reason lies in different relative dark box temperature with respect to the ambient temperatures of the control room between these three runs. The spectra are aligned in parallel with the table surface and therefore flexure of the table will move them along the y-direction. Relative differences between ambient and dark box temperatures will create such table flexure.

However, we do calibrate on a nightly basis and hence these long term variations are corrected for. More relevant are variations on shorter time scales. In Fig. 3.13 we subtract the mean positions of the respective runs rather than the overall mean. The plotted differences give indication for how much drift we typically have to account for during one run. These plots reflect also upper limits on the variation during a night and hence the

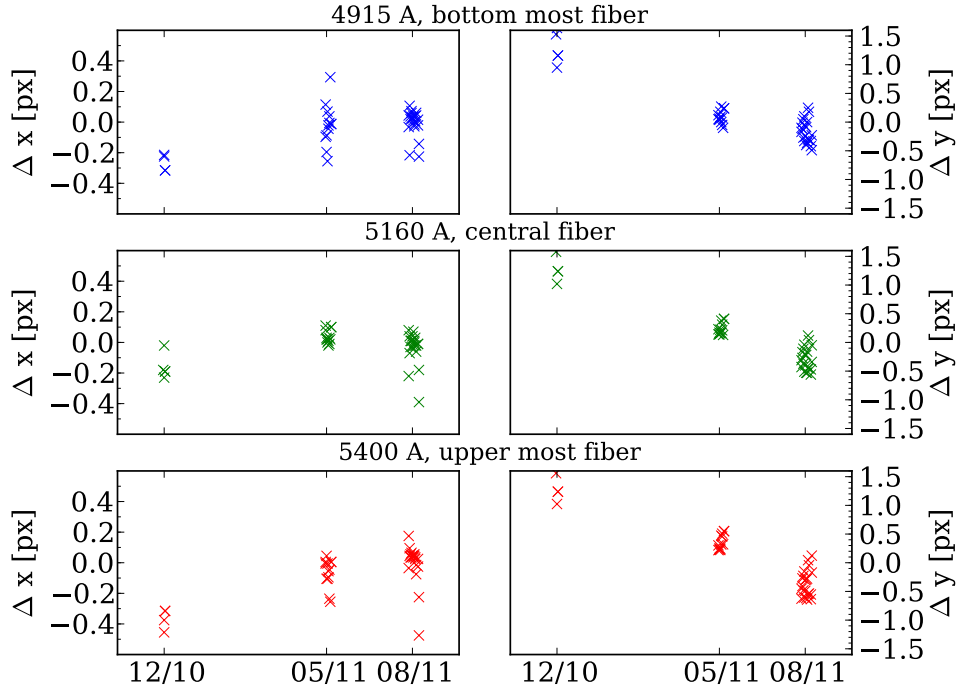


Figure 3.12 The high resolution mode stability. We pick three fibers and three wavelengths corresponding to

*upper row:* the blue spectral end and the centroid position of the bottom most fiber

*middle row:* a central wavelength and the central fiber

*bottom row:* the red end and the upper most fiber

and plot the difference in corresponding pixel position with respect to the mean value. The bottom and the upper fibers are also the fibers at the slit ends. The x direction corresponds to the cross dispersion direction while y corresponds to the dispersion direction. The three groups of data points correspond to three different observing runs.

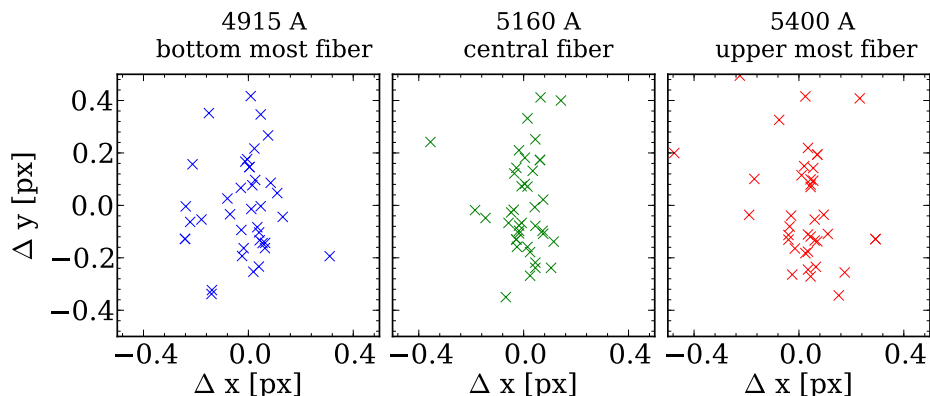


Figure 3.13 This plot is similar to Fig. 3.12, but here we subtract the corresponding mean values for the three runs respectively. The scatter of the points reflects the variations that are typical during one observing run.

Table 3.5. RMS variations of the spectral and distortion calibrations

	$RMS_x$ [px]	$RMS_x$ [Å]	$RMS_x$ [kms <sup>-1</sup> ]	$RMS_y$
4915 Å, bottom most fiber	0.17	0.03	2.06	0.18
5160 Å, central fiber	0.08	0.02	0.98	0.18
5400 Å, upper most fiber	0.20	0.04	2.25	0.20

quality of the evening/morning calibration scheme.

From the figure it can be seen that the variations in y-direction are again larger than in x-direction. Again the explanation probably lies in the flexure of the optical bench itself. For the central fiber and central wavelength it is close to a tenth of a pixel and probably dominated by measurement errors. The RMS variations are given in Table 3.5. For the central wavelength the RMS drift in dispersion direction is 0.08 px which corresponds to 0.02 Å at the linear dispersion of 0.19 Å/px and to 1.2 kms<sup>-1</sup> in velocity offset. In cross dispersion direction the typical variations are in the order of 0.2 pixel which is probably negligible for most applications.

### 3.7 Kinematic Templates and Lick Standard Stars

For the extraction of the LOSVDs with multiple template fitting algorithms, we collected a set of K and G giant stars as kinematic templates. All stars that we observed are part of the Lick/IDS database (Worthey et al., 1994). This allows us to compare published data to

Table 3.6. Observed kinematic templates

Identifier (1)	type (2)	[Fe/H] (3)	date of HR obs. (4)	date of HR obs.
HD161817	A2VI	-1.71	12/03/2010	-
HR6770	G8III	-0.05	12/03/2010	-
HR3422	G8IV	-0.12	12/02/2010	12/05/2010
HD101501	G8V	-0.27	12/03/2010	12/05/2010
HD64606	G8V	-0.92	12/03/2010	12/05/2010
HR3369	G9III	0.17	11/15/2010	12/05/2010
HR4435	G9IV	-0.40	12/03/2010	12/05/2010
HR3427	K0III	0.16	12/02/2010	-
HR3428	K0III	0.24	11/15/2010	12/05/2010
HR6817	K1III	-0.06	12/03/2010	12/05/2010
HR8165	K1III	-0.09	05/25/2011	05/24/2011
HR7148	K1III	-0.09	05/26/2011	05/24/2011
HR7176	K1III	0.17	05/27/2011	-
HR2600	K2III	-0.35	12/02/2010	12/05/2010
HR3418	K2III	0.09	12/02/2010	12/05/2010
HR3905	K2IIIb	0.46	12/02/2010	12/05/2010
HR7576	K3III	0.42	12/04/2010	12/05/2010
HD74377	K3V	-0.37	12/03/2010	12/05/2010

*Notes:* 1) Identifier, 2) type, 3) metallicity (SIMBAD), 4) date of observation

our measurements. We further augment the giants stars by dwarfs from the Lick database. This gives us a sufficient number of index measurements to calculate corresponding linear corrections and to map our future data to the Lick system — a necessary step towards the derivation of stellar population parameters.

In Table 3.6 we list all stars that we observed during the commissioning runs. We add three additional stars that were observed in May 2011 during a regular science run. All observations were either trailed see §2.2.2 or the star was placed at three different locations within the IFU (central, and to opposite corners). The complete sample consists of 18 stellar spectra in the high resolution mode out of which 12 are giants, and 14 spectra in the low resolution mode out of which 9 are giant stars. Fig. 3.14 shows the reduced and continuum removed spectra.

The primary mode for the stellar population analysis is the low resolution mode. It gives access to 13 out of the 21 indices in the Lick system including  $H_\beta$  that is an important tracer of the age of a stellar population. The full list of covered indices at redshift zero is given in Table 3.7. 7 indices are also covered in the high resolution mode.

The trailing results in a number of spectra across the detector — one spectrum for each position where the star crossed one of the fiber rows of the IFU. For each star we pick the spectrum with the largest flux that is not yet endangered of reaching the non-linear regime of the output amplifiers ( $< 40,000$  counts). In the high resolution mode we find that the very peaked instrumental throughput leads to significant offsets ( $> 1 \text{ \AA}$ ) between our measurements and the Lick values for the  $Mg_1$  and  $Mg_2$  indices. Therefore we divide the spectra by the instrumental throughput that we determine in §3.2. We correct for redshift

Table 3.7. Lick indices covered by the spectral range of VIRUS-W at  $z = 0$ 

Identifier (1)	mode availability (2)
Fe4383	low res.
Ca4455	low res.
Fe4531	low res.
Fe4668	low res.
H $\beta$	low res.
Fe5015	high res. & low res.
Mg $_1$	high res. & low res.
Mg $_2$	high res. & low res.
Mg $_b$	high res. & low res.
Fe5270	high res. & low res.
Fe5335	high res. & low res.
Fe5406	high res. & low res.
Fe5709	low res.
Fe5782	low res.
NaD	low res.

using the location of the lines in the Mg  $b$  and measure the equivalent width following the same procedure as (Mehlert et al., 2000).

In Fig. 3.15 and 3.16 we compare our measurements to those of the Lick database. Typical RMS values lie below 0.2 Å with the notable exception of Fe4258, Fe4531, Fe4668, Fe5015, and Fe5406 which show RMS values of up to 0.64 Å. In the case of Fe4531 the slope of the best fit linear correction is also quite different from one with a value of 0.72.

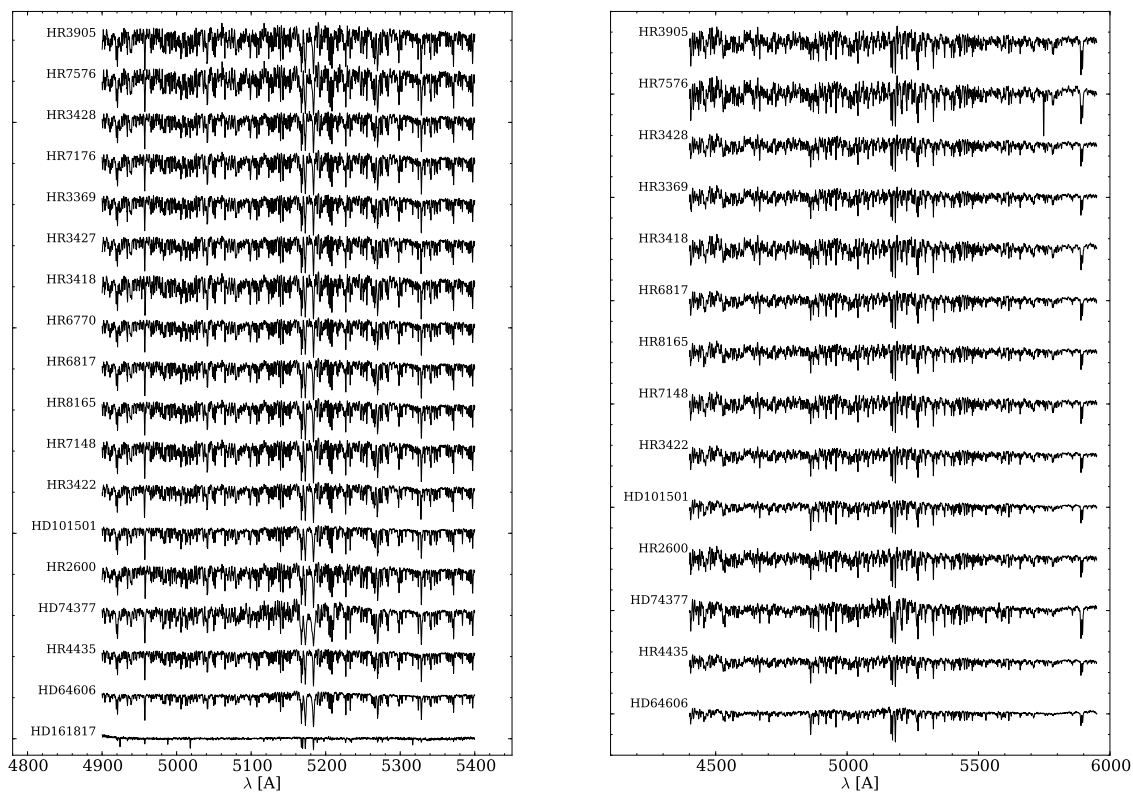


Figure 3.14 Collection of Lick standards and kinematic templates observed during the commissioning run and the May 2011 run. The high resolution spectra are plotted in the left and the low resolution mode spectra are plotted in the right panel. The continua have been removed.

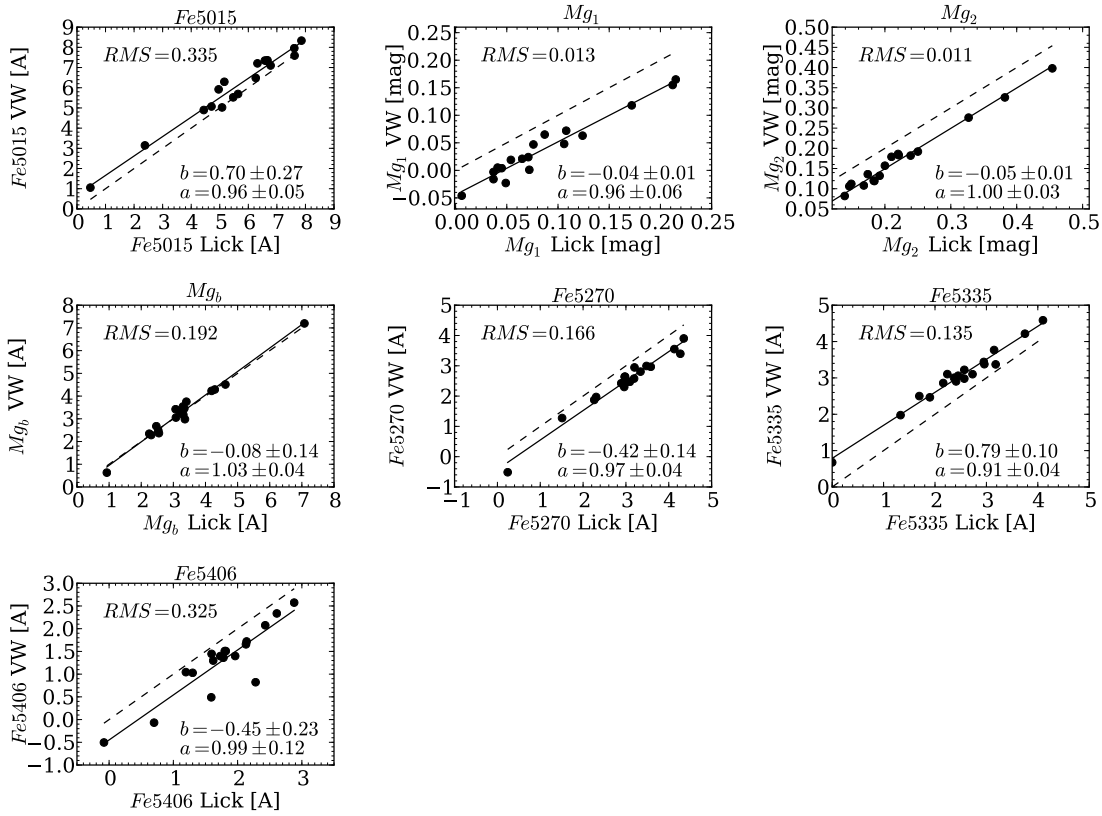


Figure 3.15 Comparison of the index values measured in the high resolution mode with the Lick/IDS data (Worthey et al., 1994). The dashed lines show the one-to-one correlation while the solid line is a linear fit with slope  $a$  and offset  $b$ .

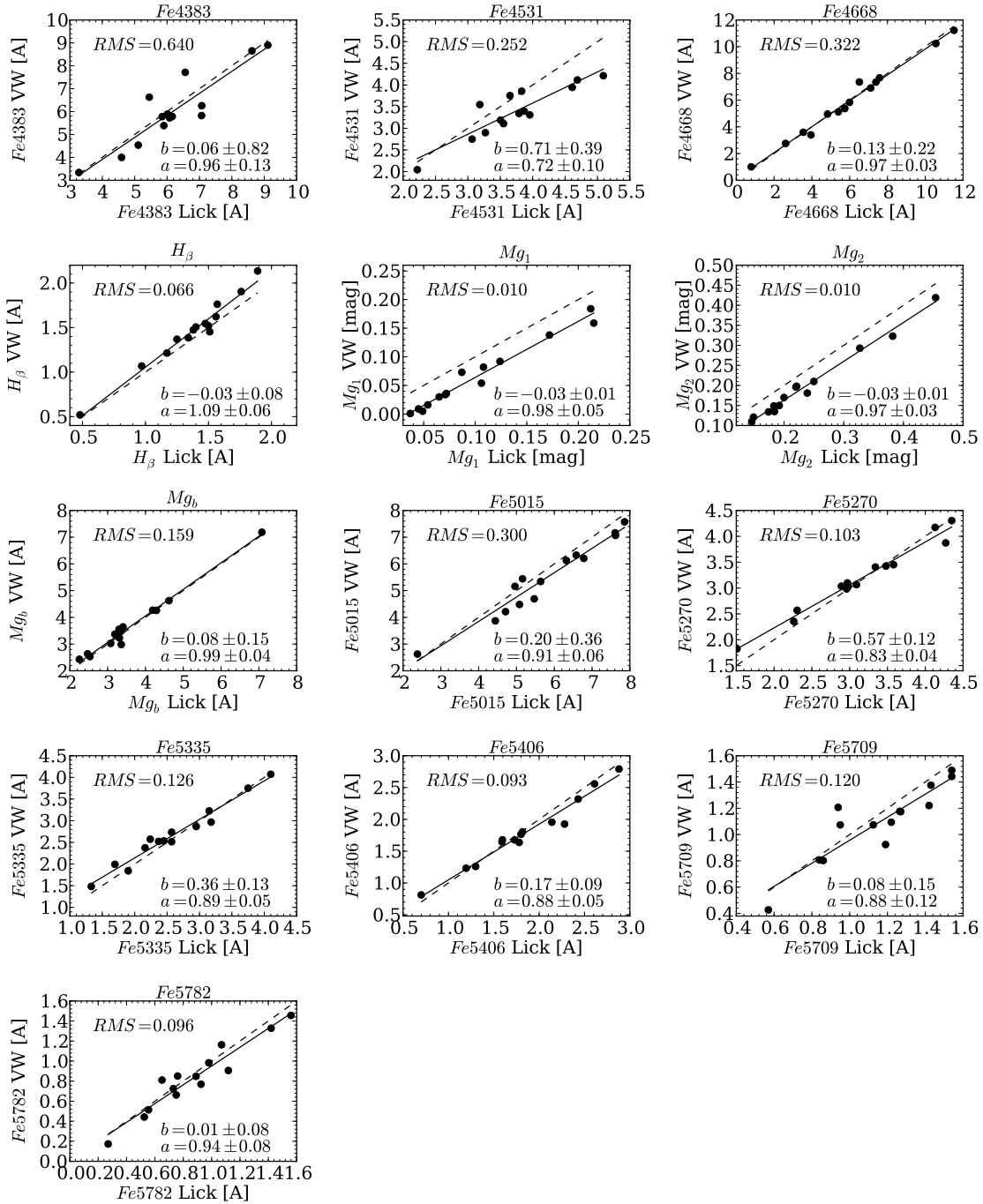


Figure 3.16 Like Fig. 3.15 but for the low resolution mode.

## 3.8 First VIRUS-W Kinematic Maps

In the following we will briefly describe observations of the three galaxies NGC 2903, NGC 205, and NGC 3091 that we carried out during the commissioning runs of VIRUS-W. A detailed analysis and interpretation of the obtained data leaves the scope of this thesis. We show that the instrument, the software and the data reduction are in a state that fully enables the investigators to obtain, absorption line stellar kinematics and emission line gas kinematics. With NGC 205 we will demonstrate VIRUS-W's ability to resolve stellar dispersions at the order of  $20 \text{ km s}^{-1}$ .

### 3.8.1 Target description

NGC 2903 is a nearby, prominently barred galaxy (Hubble type SAB(rs)bc, de Vaucouleurs et al., 1991). With a moderate inclination of  $56^\circ$  (Hyperleda) it offers a relatively unperturbed view into its bulge region. NGC 2903 is located at a distance of 8.9 Mpc (Drozdovsky & Karachentsev, 2000) at which the fiber diameter corresponds to about 130 pc. Its bulge effective radius (Fisher & Drory, 2008) is  $8.3''$ . The bulge is therefore resolved by the  $3.2''$  diameter fibers of VIRUS-W at the 2.7 m. The relatively high surface brightness of  $\mu_V = 20 \text{ mag}/''^2$  for the outermost fibers at  $r \simeq 60''$  (Fisher & Drory, 2008) promises high signal to noise with short integration times. All these features — plus of course its visibility in the November period — made NGC 2903 an ideal target for a first-light observation.

NGC 3091 is an elliptical galaxy (E3, de Vaucouleurs et al., 1991) that was previously observed as part of the SINFONI black hole program by our group (Nowak et al., 2007, 2008, 2010; Rusli et al., 2011) in April 2009 with the adaptive optics assisted (AO) SINFONI spectrograph (Eisenhauer et al., 2003a; Bonnet et al., 2004) at the VLT. One of the aims of this program is to study the scaling relations between the mass of the central super massive black hole and its host galaxy at the high mass end. Black hole masses are obtained through Schwarzschild modelling (Schwarzschild, 1979) of the stellar systems using the axisymmetric, three-integral code by Gebhardt et al. (2000, 2003) and Siopis et al. (2009). With a central velocity dispersion of  $\simeq 320 \text{ km s}^{-1}$  (Hyperleda), NGC 3091 is a candidate for a high mass black hole host. The central velocity dispersion – black hole mass scaling relation with parameters by Gültekin et al. (2009) suggests an impressive mass of  $1.09 \times 10^9 M_\odot$ .

In the recent years it has been established that larger scale ground based observations are an important ingredient towards establishing a tight constraint on the black hole mass. While the AO assisted high spatial resolution observations allow to study the stellar motions in the vicinity of the black hole, these data typically do not allow constrain the mass to light ( $M/L$ ) ratio in the systems under investigation. But in maximum likelihood methods, the mass of the central black hole tends to be degenerate with  $M/L$ . With the aid of larger scale kinematic information this degeneracy can be broken and a tighter constraint on the black hole mass can be obtained (Gebhardt & Thomas, 2009; Krajnović et al., 2009; Schulze & Gebhardt, 2011).

Since NGC 3091 had no suitable ground-based kinematic data from the literature avail-

able we took the chance to observe this galaxy during our second commissioning run in December 2010. Due to the large velocity dispersion of this object we could observe in the low resolution mode which yields also information on the stellar populations.

The dwarf elliptical galaxy NGC 205 is one of the three only known galaxies of this type in our local group. It is a close satellite to M31 with a projected angular distance of  $40'$  corresponding to 8 kpc (Geha et al., 2006), but is likely to be located  $48 \pm 30$  kpc behind the disk of M31 (De Rijcke et al., 2006). Its proximity, brightness and large angular size let it to become arguably the best studied galaxy of its type.

NGC 205 has been known for a long time to host a blue nucleus (Baade, 1944; Peletier, 1993). Numerous works concern themselves with the young stellar populations that are the source of the blue colour (e.g. Lee, 1996; Cappellari et al., 1999) and find that the dominant population formed 50-500 Myr ago. Davidge (2003) sees signs of multiple epochs of star formation which seem connected to the orbital periods of NGC 205 around M31.

There is evidence for interaction between the two galaxies, both from photometry — the isophotes are found to twist beyond radii of  $300''$  (Hodge, 1973; Kormendy, 1982a; Choi et al., 2002) — and from kinematics (De Rijcke et al., 2006). Indeed while counter rotation was already observed in high resolution long slit data by Bender et al. (1991); Simien & Prugniel (2002). Geha et al. (2006) show an impressive turn in the rotation curve at about  $4'$  from measurements on individual stars.

The J-band magnitude rises by  $2 \text{ mag}/''^2$  within  $3''$  of the center (De Rijcke et al., 2006). This sudden increase of luminosity is found to correspond to drop in dispersion of about  $10 \text{ kms}^{-1}$  from  $30 \text{ kms}^{-1}$  down to  $20 \text{ kms}^{-1}$ .

Its central brightness and low velocity dispersion, the availability of detailed literature data for comparison based both on long slit observations and individual star measurements, and its visibility in the December time frame made NGC 205 a very interesting target for the commissioning run. It allows us to test VIRUS-W's ability to recover LOSVDs close to the instrumental resolution limit.

Given the low central velocity dispersion, endeavours to recover a mass for a potential central black hole may be hopeless given the current availability of instrumentation (Valluri et al., 2005). However, these data will likely allow future modelling attempts to form an even tighter constraint on the upper limit for the black hole mass than currently available.

### 3.8.2 Observations

The observations of NGC 2903 were carried out in the nights from the 11-th to the 14-th of November 2010. We used the high resolution mode GRISM in conjunction with the SDSS  $g$  filter. We obtained 7 on-object pointings — centred on the galaxy — with individual integration times of 1800s resulting in a total of 3.5h. The on-object pointings were interleaved and bracketed with 1200s sky nods for sky subtraction. Fig. 3.17 outlines the FoV of our observation. Due to the experimental state of the observation, the pointings were not dithered but rather all centred on the same position. Consequently the fill-factor of our data is  $1/3$ .

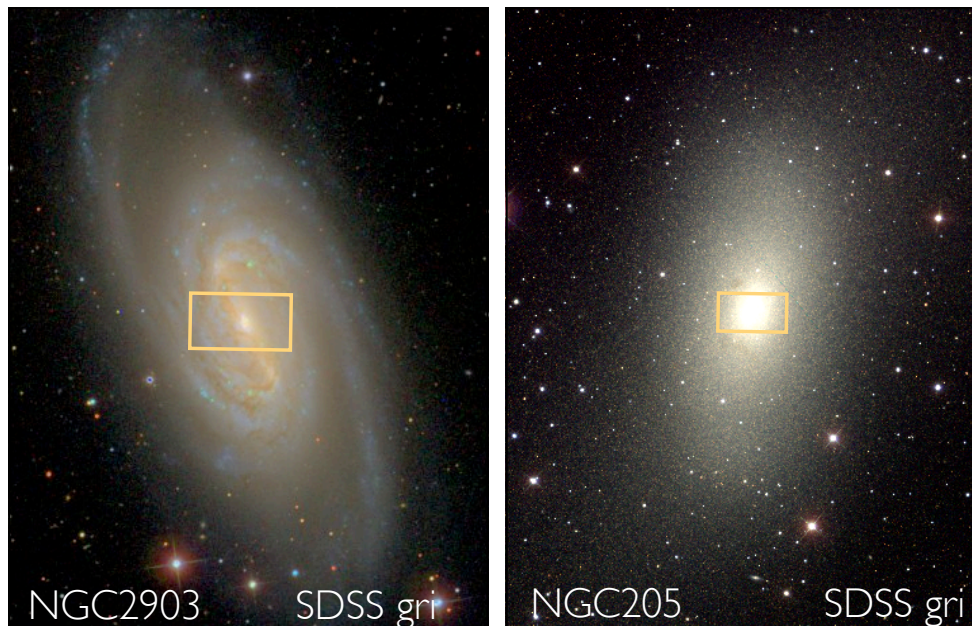


Figure 3.17 *Left panel*: SDSS *gri* composite image of NGC 2903. The  $105'' \times 55''$  FoV of the VIRUS-W IFU is outlined. Note that the FoV is sparsely sampled due to the non-dithered observations. *Right panel*: SDSS *gri* composite and VIRUS-W FoV for NGC 205.

We observed NGC 205 during the night of the 2-nd of December 2010, the first night of the second commissioning run. We used the same instrumental setup as for NGC 2903 with the only exception of the slight turn that we applied to the GRISM in order to move the Littrow ghost away from the  $Mgb$  feature (see §3.1). The observations were centred on the nucleus. Given the then implemented routines, we observed in the dithered mode to achieve 100% coverage. We obtained two on-objects exposures in each dither position with an individual integration time of 1800 s resulting in a total on-object integration time of 3 h. The on-object observations were interleaved and bracketed with 1200 s observations of blank sky for sky subtraction.

In the night of the 5-th of December we observed two off-centred and slightly overlapping regions (see Fig. 3.18) of NGC 3091. These observations made use of the low resolution mode grating. Here no filter was placed in front of the IFU. The pointings were dithered to obtain a 100% fill factor. We repeated each dither position once for cosmic ray rejection. The exposure time of the individual pointing was 600 s resulting in a total on-object integration time of 2 h. All science observations were interleaved and bracketed with 300 s sky nods.

The science observations of all galaxies were accompanied by a standard set of flat fields, Ne+Hg calibration lamps, and bias frames as described in §2.2.2.

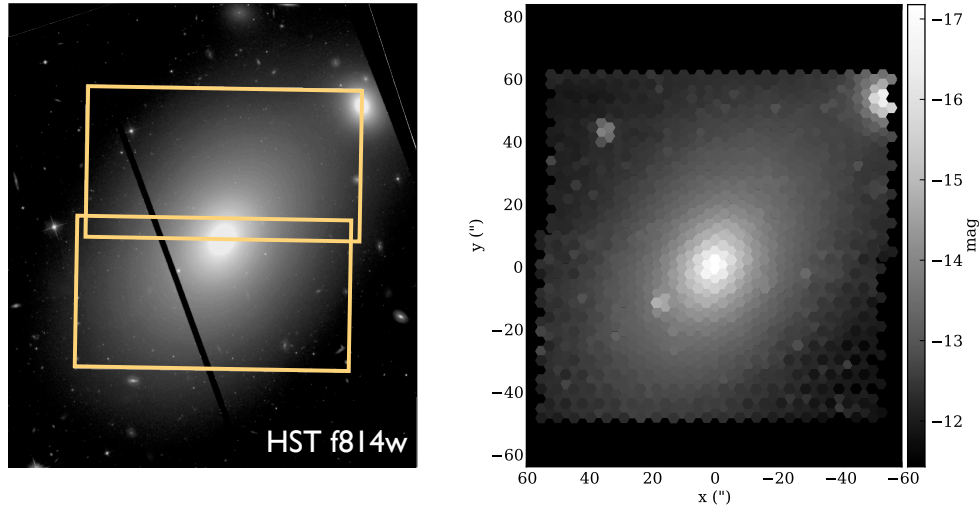


Figure 3.18 *left panel*: HST I-band image. The boxes outline the FoV of our two different fields. *right panel*: Reconstructed image.

### 3.8.3 Reduction

We follow the reduction procedure described in §2.3. Standard bias subtraction, and frame cropping is carried out using the `fitstools` package (Gössl & Riffeser, 2002) and the wavelength calibration and distortion model is obtained through the `cure` pipeline. We average the bracketing sky frames of a science observation while rejecting cosmic rays and scale the result to the relative exposure time of the on-object integrations. The sky-subtraction is then carried out using the cross sky-subtraction feature of `cure`'s `subtractsky` routine (see §2.3).

We extract the kinematics using the Fourier Correlation Quotient (FCQ) method of Bender (1990); Bender et al. (1994). The procedure of iterative template fitting and emission line subtraction follows closely the recipe described in §4.4 of this work. However here we do not yet apply the multiple template fitting but rather use the single stellar template HR2600. We fit the wavelength range  $5019.1 \text{ \AA} - 5297.5 \text{ \AA}$  which includes the Mg *b* and the Fe5270 features.

Given the relatively high  $S/N$  of the data for NGC 2903 we do not bin these data spatially. For NGC 205 we do sum the three dithers together in order to increase the  $S/N$  on the cost of the lost of spatial resolution. This effectively bins the data by integrating over every three neighbouring fibers.

We reject the last science observation of NGC 3091 as it showed already an increased background due to the inset of twilight. We find that the use of the sky nods for sky subtraction results in an unrealistic gradient of the velocity dispersion over the observed field. We therefore determine the sky signal from the outermost  $\simeq 20\%$  fibers of the two fields (see Fig. 3.19). We bin the data spatially following the radial binning scheme of the

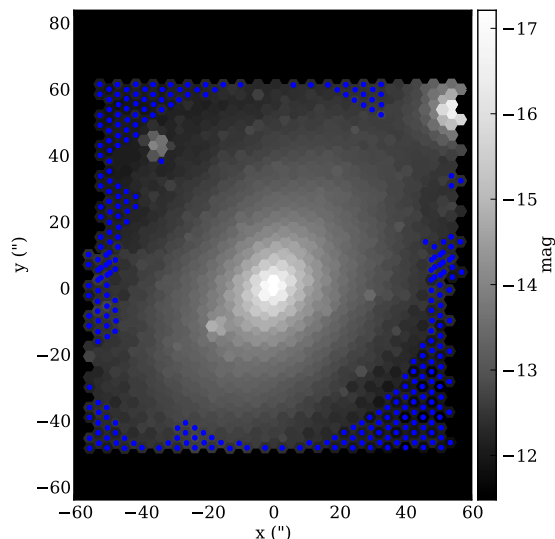


Figure 3.19 Same image as right panel of Fig. 3.18. The fibers that are marked blue were used for sky subtraction.

SINFONI black hole program (see Fig.3.25). The mean binned  $S/N$  per  $\text{\AA}$  is 22 with a minimum of 10 in the outermost bins. The kinematics are again extracted using the FCQ algorithm. We do not apply any gas removal or multiple template fitting as we do not see signs of any emission in our data. We measure the line strengths in the Lick/IDS system as defined in Worthey et al. (1994) following the procedure in (Mehlert et al., 2000). This includes broadening our spectra to the typical instrumental dispersion of the Lick data of  $\sigma = 220 \text{ km s}^{-1}$ . We finally apply the linear corrections obtained in §3.7 (see Fig. 3.16).

### 3.8.4 Preliminary Results

#### NGC 2903

In Fig. 3.20 we compare a reconstructed image of NGC 2903 to the actual SDSS  $g$  band image. The central elongated light structure is well reproduced in the reconstructed image and suggests that the positioning of individual fibers agrees with our expectations.

Héraudeau & Simien (1998) and publish velocities and velocity dispersions along the major and the minor axis. For comparison we generate pseudo longslit data from our kinematic maps through nearest neighbour interpolation along a straight line with the same position angle as the observations from Héraudeau & Simien (1998). They seem to find lower velocity dispersions along the major axis, but this disagreement is only borderline significant. On the minor axis they find somewhat larger velocity dispersions which are in good agreement with our measurements.

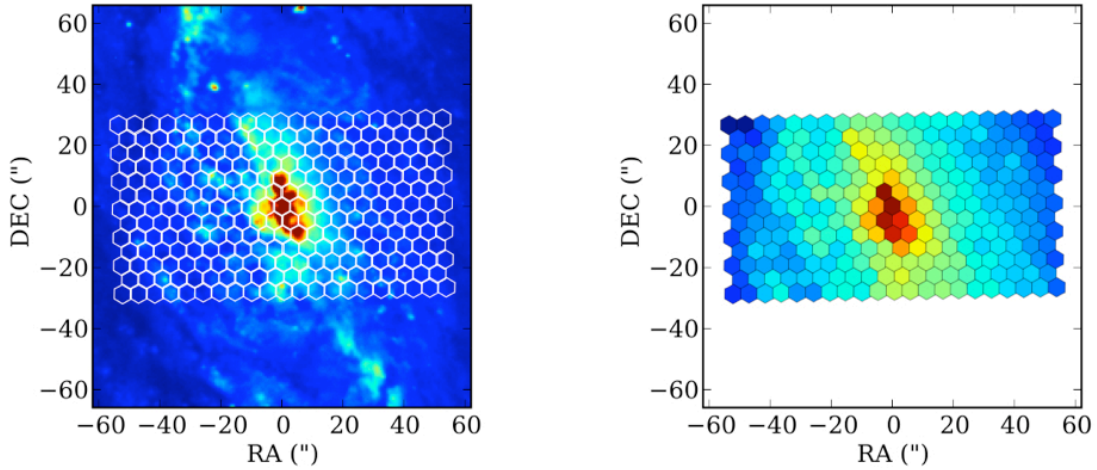


Figure 3.20 The left panel shows a SDSS  $g$  false colour image of the central region of NGC 2903. The positions of the fibers are outlines as white hexagons. Note though, that the fill factor of the IFU is only 1/3. In the right panel we show a reconstructed image from the obtained data. The fiber fluxes are integrated over in the SDSS  $g$  bandpass.

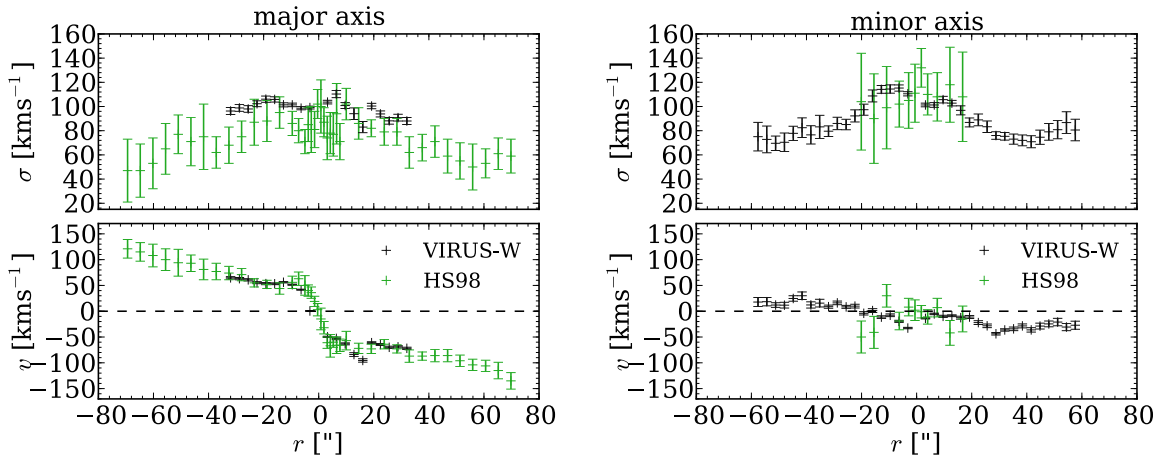


Figure 3.21 Comparison of our velocities and velocity dispersions to the values from (Héraudeau & Simien, 1998). The pseudo-longslit data for VIRUS-W are generated through nearest neighbour interpolation along a straight line with the same position angle as the literature data (major axis =  $17^\circ$ , minor axis =  $107^\circ$ ).

In Fig. 3.22 we show the full kinematic maps that we obtain from FCQ. The panels **a** through **h** show the velocity field, the velocity dispersion, the Gauss-Hermite  $h_3$  moments and  $h_4$  moments, the line strength, the gas velocity as measured from the brighter [O III] line, the velocity dispersion of the gas and the flux of the [O III] line in arbitrary units.

The velocity field shows irregularities in the form of an s-shape and a faster rotating central component. The velocity dispersion reaches values of up to  $120 \text{ km s}^{-1}$  in the innermost region, the shape of the dispersion field is round and does not seem to follow elongation of the bar.

The  $h_3$  moments are anti-correlated with velocity. The  $h_4$  moments are mostly dominated by noise. An interesting feature is a colder, stronger rotating, central component in the gas. It is roughly aligned with the North-South axis and remains distinctly visible throughout the extent of the FoV in that direction. The spatial scale of this feature seems to correspond with the increase of rotation that is seen in the central regions of the stellar velocity map.

NGC 2903 is known to contain a nuclear *hot spot* of star formation (e.g. Bonatto et al., 1989; Kinney et al., 1993). It is therefore tempting to interpret this as a situation where cold gas — possibly brought into the center with the aid of the bar — settles into a disk leading to active star formation. We do see a central decrease in the line-strength map as well, which itself is an indication of either a lower metallicity or a young stellar population. However, due to the low throughput in the  $H_\beta$  region, we do lack a tracer of stellar age in the high resolution spectral coverage and hence can not break this degeneracy between metallicity and age given our data alone. Indeed though, (Song, in prep 2012) uses data from the VENGA survey that were obtained with the sister instrument VIRUS-P to study the stellar populations in NGC 2903. She finds a young population and a prominent increase of star formation that coincides well spatially with the depression in lines strength. Hence we think that NGC 2903 is a prototypic example of ongoing secular evolution (Kormendy & Kennicutt, 2004) driven by a bar.

### NGC 205

In Fig. 3.23 we compare our obtained velocities and velocity dispersions to the values given in (Simien & Prugniel, 2002). We again create pseudo longslit data through nearest neighbour interpolation along a straight line with the position angle of  $165^\circ (75^\circ)$  for the major (minor) axis. We find excellent agreement between our data and the published values.

In Fig. 3.24 we show the set of derived kinematic maps. The lower panels show the FCQ-computed  $S/N$  per Å (**panel a**) and a reconstructed image that we obtain by collapsing the spectra along the dispersion direction (**panel b**). In the middle row we show the velocity (**panel c**) and the velocity dispersion (**panel d**). The velocity map shows rotation along the major axis at the level of  $2\text{-}3 \text{ km s}^{-1}$ . The dispersion map reproduces the central drop in dispersion that has been described in previous works (Bender et al., 1991; Simien & Prugniel, 2002). The line strength map in the upper panel shows a clear and elongated depression from  $\gamma \simeq 0.55$  down to  $\gamma \simeq 0.45$  within the central  $\pm 25''$ . The spatial shape

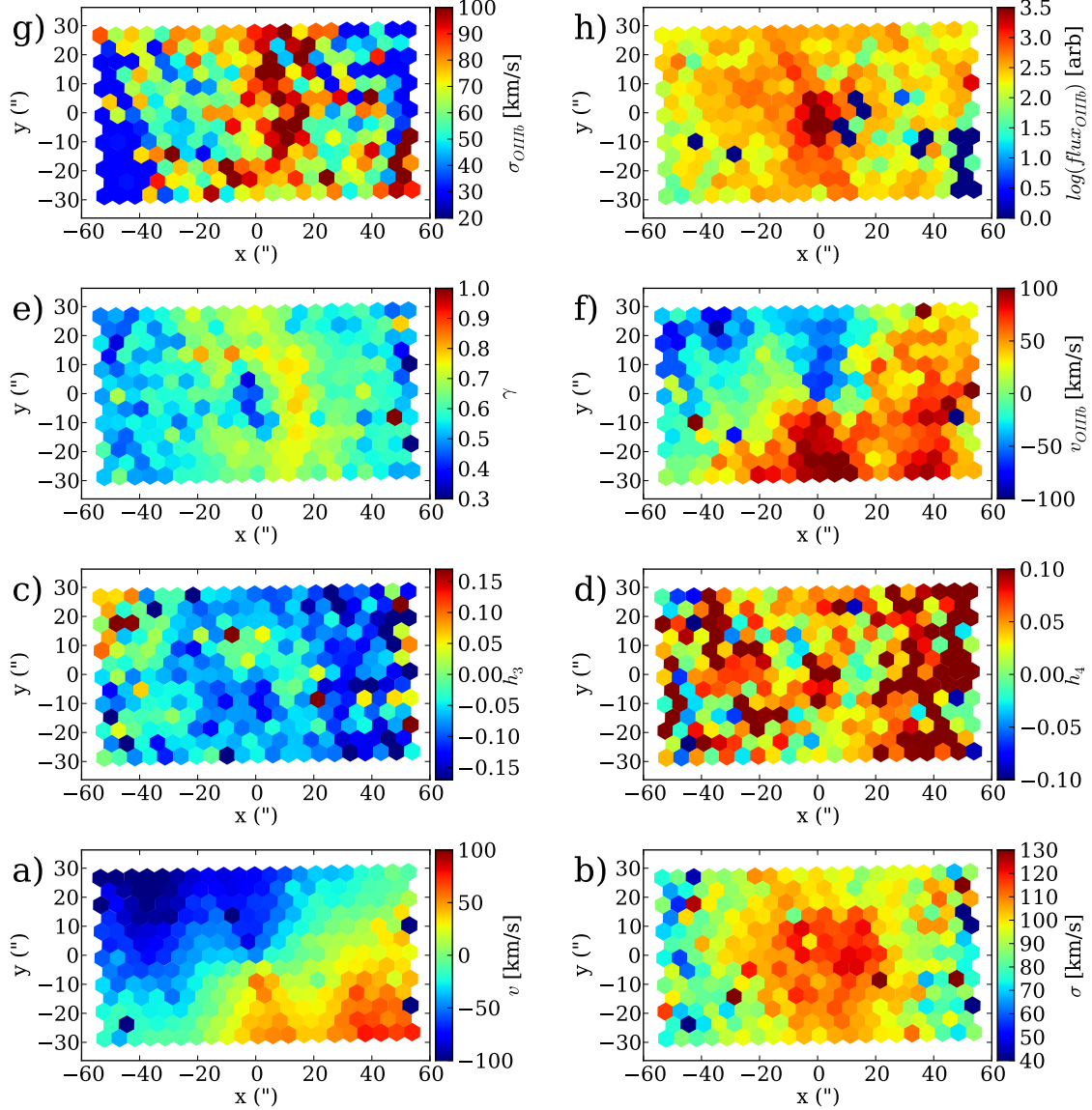


Figure 3.22 Kinematics maps of the central region of NGC 2903. Positive  $y$ -values point to north. Negative  $x$  correspond to the east direction. *Panel a*: FCQ derived mean stellar velocity. *Panel b*: Stellar velocity dispersion. *Panel c*: Gauss-Hermite  $h_3$  moments of the stellar LOSVDs. *Panel d*:  $h_4$  moments. *Panel e*: Line-strength. *Panel f*: Gas mean velocity as measured from the [O III] line. *Panel g*: Gas velocity dispersion. *Panel h*: [O III] line flux (arbitrary zeropoint).

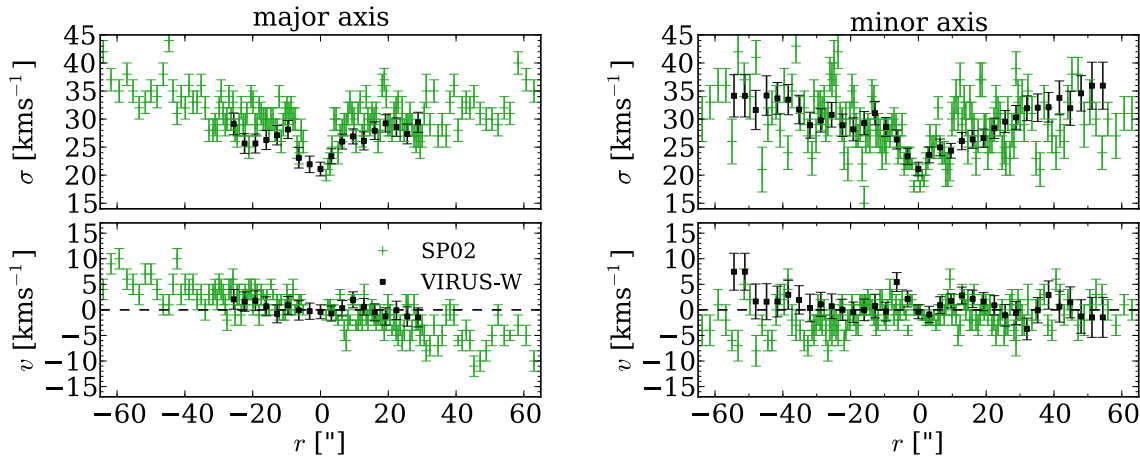


Figure 3.23 Comparison of our velocities and velocity dispersions to the values from (Simien & Prugniel, 2002). The pseudo-longslit data for VIRUS-W are generated through nearest neighbour interpolation along a straight line with the same position angle as the literature data (major axis =  $165^\circ$ , minor axis =  $75^\circ$ ).

of this depression correlates well with the area of increased luminosity that is seen in the reconstructed image. The lower line strength and the increase in luminosity stem from the young population studied by other authors (Peletier, 1993; Lee, 1996; Cappellari et al., 1999; Davidge, 2003). The elongation suggest that the young population is not distributed spherically.

This analysis is clearly preliminary. NGC 205 is known to contain gas and our spectra do show signs of nebular emission, however we have not yet attempted to remove the emission before the recovery of the LOSVD. Also the central young population leaves room for doubt whether a single template fit can truly recover the central dispersions. Hence a more detailed study that is aimed towards a dynamical model of NGC 205, should include emission line removal, multiple template fits — preferably including earlier type templates than we have collected so far — and an optimized binning scheme. However, the ability to recover rotation already within the central  $\pm 30''$  and the recovery of the dispersion drop that — whilst with some noise, but clearly — distinguishes different radial regions at the  $\simeq 5 \text{ km s}^{-1}$  level, beautifully demonstrates the ability of VIRUS-W to resolve LOSVDs at these very low dispersions close to the instrumental resolution limit.

### NGC 3091

We plot the maps of the kinematic moments  $v$ ,  $\sigma$ ,  $h_3$  and  $h_4$  in Fig. 3.18. We reject bins outside of  $47''$  as there the signal to noise becomes too low for a reliable measurement. We also do not include bins at radii smaller than  $10''$  since the fiber diameters start exceeding the bin size in the radial binning scheme.

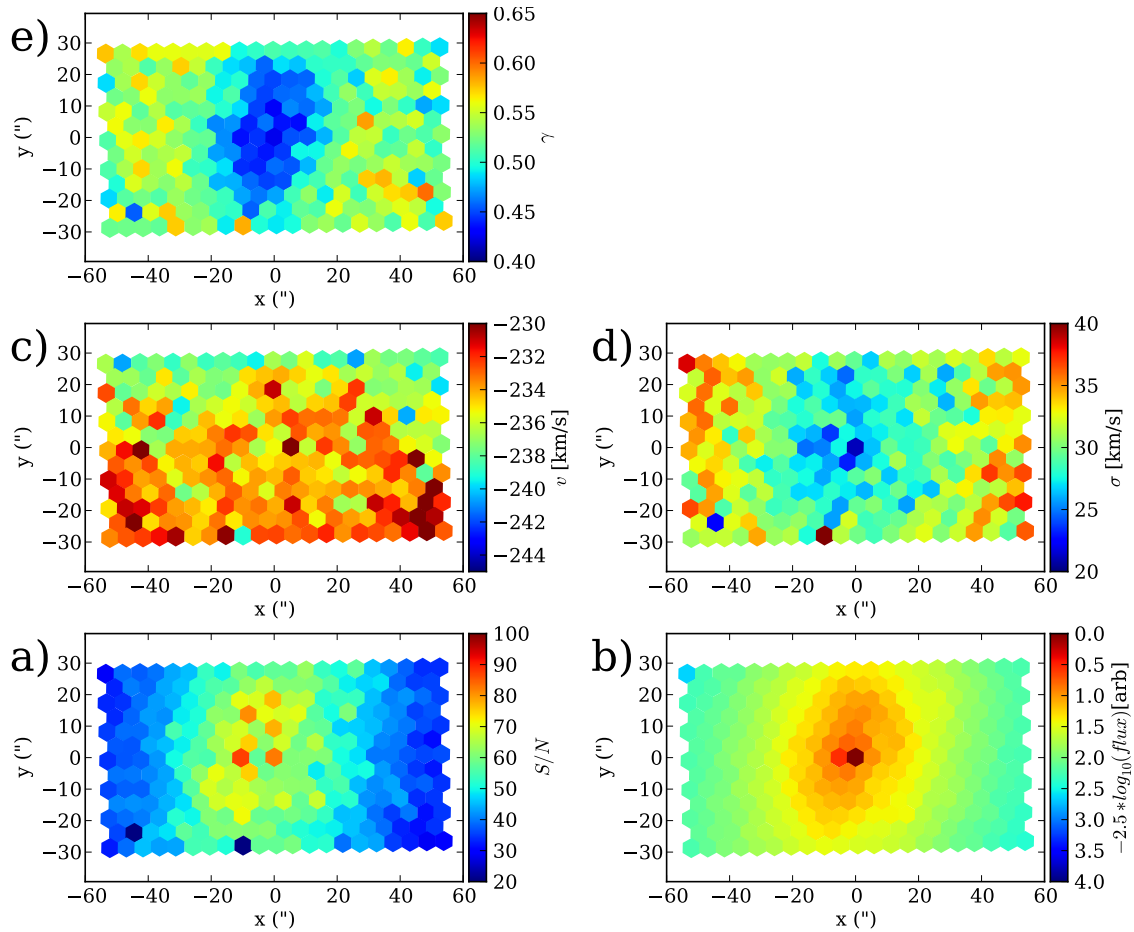


Figure 3.24 Kinematic maps for NGC 205. Positive  $y$  point to north. Negative  $x$  to east. *Panel a:*  $S/N$  per Å as computed by FCQ. *Panel b:* Reconstructed image with arbitrary zeropoint. *Panel c:* Mean velocity. *Panel d:* Velocity dispersion. *Panel e:* Line strength.

Within the field of view the rotation reaches an amplitude of about  $\pm 150 \text{ kms}^{-1}$ . There is no obvious radial gradient in the dispersion map, the mean value of all plotted bins is  $285 \text{ kms}^{-1}$  with a considerable standard deviation of  $45 \text{ kms}^{-1}$ . The  $h_3$  map shows a mild anti-correlation with velocity and the  $h_4$  map shows no obvious structure or gradients.

Beuing et al. (2002) publish Lick index measurements for NGC 3091. We compare their data to our measurements in Fig. 3.26. We plot histograms for the values that we obtain in individual bins and overplot the data of Beuing et al. (2002) with a blue bar where the width of the bar corresponds to their error estimate. We find a reasonable agreement between their and our measurements with a possible bias towards smaller values in our data. However, they measure the line strength within a  $5.2''$  wide central aperture of. This is significantly closer to the center than the radial range that our data stem from which may explain the observed deviation.

We fit the index measurements with predictions from models of simple stellar populations (SSP) by Maraston (1998, 2005) with a Kroupa (2001) initial mass function (IMF) and  $\alpha$ -element over abundances from Thomas et al. (2003). The method is adopted from Saglia et al. (2010) and operates on a grid of models that cover ages of up to 15 Gyr, metallicities  $[Z/H]$  from -2.25 to +0.67 and  $[\alpha/Fe]$  over abundances from -0.3 to +0.5. The models are fit by minimizing the  $\chi^2$  between our index measurement and the predicted values and take the indices  $H_\beta$ ,  $Mgb$ ,  $Fe5015$ ,  $Fe5270$ ,  $Fe5335$ ,  $Fe5406$ ,  $Fe5709$ , and  $Fe5782$  into account (for details see Saglia et al., 2010).

We compare the mass to light ratio obtained from these SSP fits to the result of a preliminary dynamical model. The dynamical model of NGC 3091 was constructed by Stephanie Rusli and will be subject to a future publication (Rusli, 2012) and details will be discussed therein. The model used here includes an additional dark matter halo component, assumes a constant mass to light ratio, and inclination of  $90^\circ$ .

In Fig. 3.27 we show histograms of the predicted mass to light ratios from the SSP analysis for the individual bins. The blue curve shows the  $\Delta\chi^2$  as a function of  $M/L$  from the dynamical modelling. By fitting a 3-rd order polynomial to the function  $\Delta\chi^2(M/L)$  we obtain the preferred value from the modelling as  $M/L_I^{dyn} = 4.37_{-0.27}^{+0.27}$  (one-sigma errors) and the SSP analysis yields  $M/L_I^{SSP} = 3.38_{-0.42}^{+0.42}$ .

Actual dark matter fractions shall be discussed in the light of a less preliminary analysis elsewhere but we find that the  $M/L$  values obtained from dynamical models that are based on VIRUS-W data and  $M/L$  values that are based on a stellar population analysis — again based on VIRUS-W data — give comparable results.

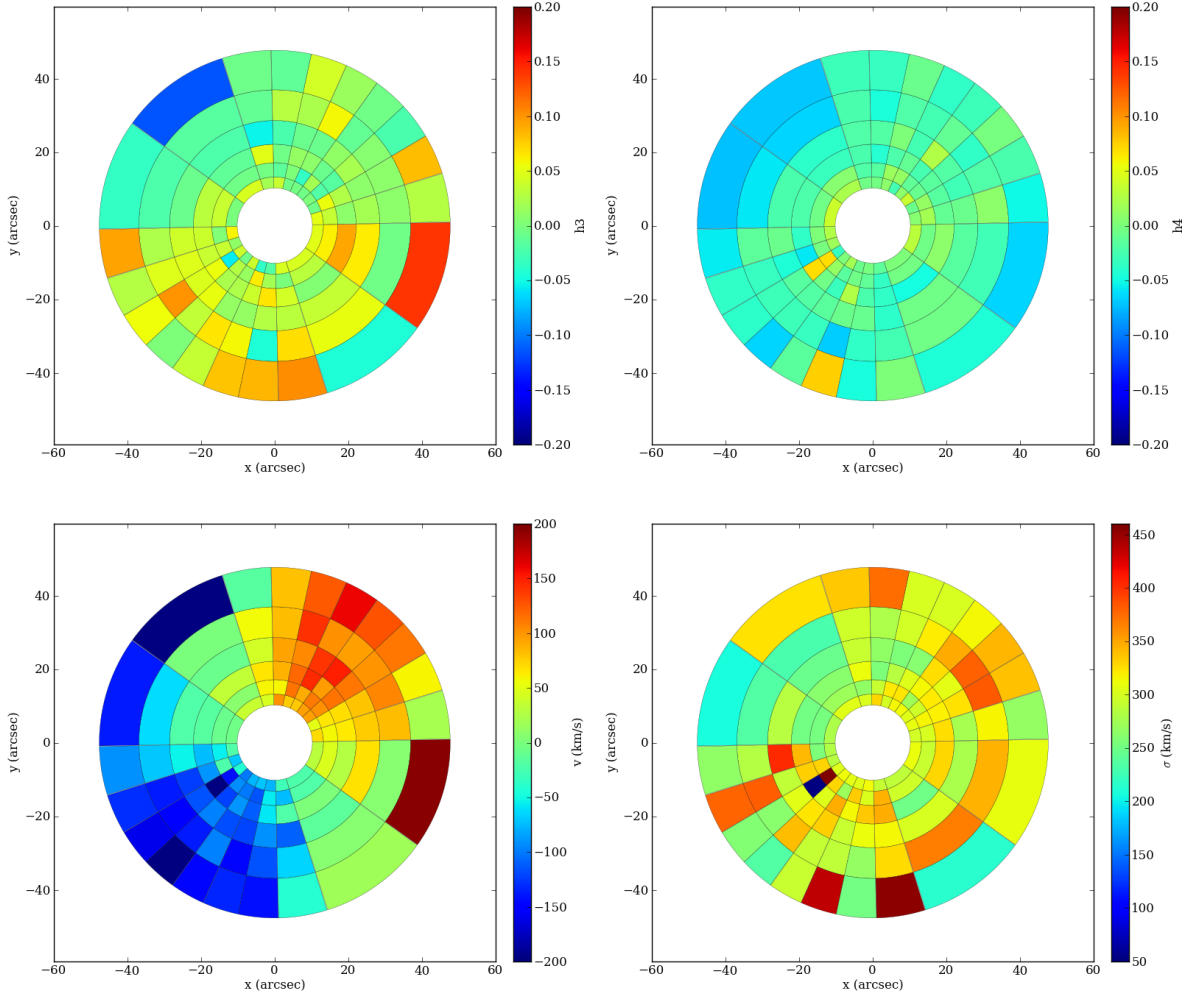


Figure 3.25 Kinematic maps for NGC 3091 observed in the low resolution mode. Differently than in Fig. 3.22 and 3.24 we do not plot individual fibers but bin them using the radial binning scheme that is adopted in the dynamical modelling. The panels show velocity (lower left), velocity dispersion (lower right),  $h_3$  (upper left), and  $h_4$  moments (upper right). We only show bins out to about  $47''$  as the  $S/N$  is too low at larger radii to recover the LOSVDs. Bins inside of  $10''$  are rejected as well because the fiber size exceeds the bin size of the radial binning scheme. Positive  $y$ -values correspond to north, negative  $x$ -values correspond to east. Two bins to the lower left of the center — easily visible in the  $\sigma$ -map — are affected by a foreground star (comp. Fig. 3.18).

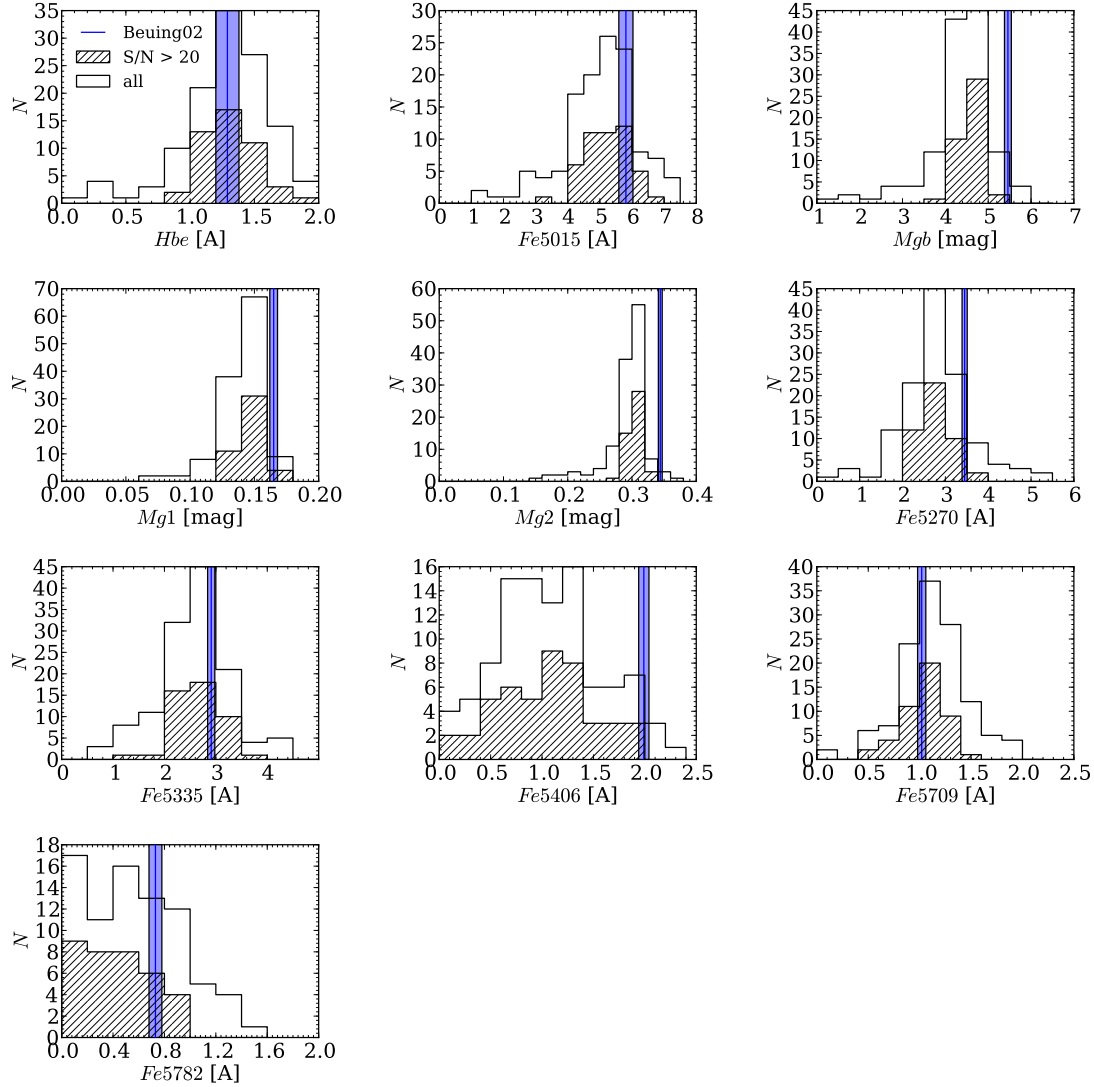


Figure 3.26 Comparison of our index measurements to the values from the literature. The histograms show the values that we calculate for individual bins. The hatched histograms take only those bins into account where the  $S/N$  per pixel exceeds 20. The blue bar corresponds to the values of (Beuing et al., 2002), the width of the blue bar shows their one-sigma errors. We apply the linear corrections from Fig. 3.16.

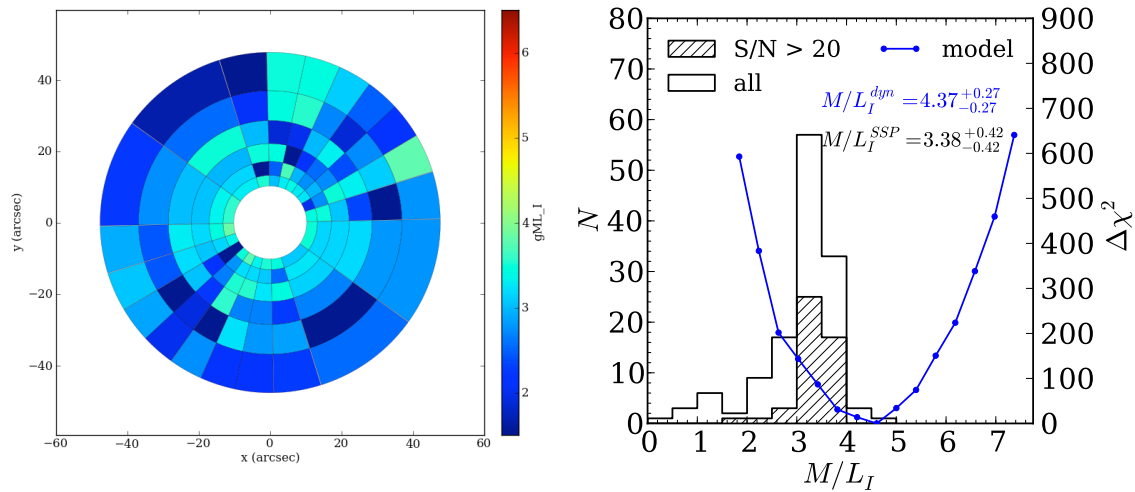


Figure 3.27 *Left panel:* Map of the I-band mass to light ratio as obtained from the single stellar population analysis. Positive  $y$ -values point to north, negative  $x$ -values to east. *Right panel:* Histogram of the I-band mass to light ratios that we determined in individual bins. The shaded bins count only those bins which have a  $S/N$  per  $\text{\AA}$  that is larger than 20. The blue line shows the result from the dynamical modelling of NGC 3091.

# Chapter 4

## Kinematic Signatures of Bulges Correlate with Bulge Morphologies and Sérsic Index <sup>1</sup>

**Abstract** We use the Marcario Low Resolution Spectrograph (LRS) at the Hobby-Eberly Telescope (HET) to study the kinematic behaviour of pseudobulges and classical bulges in the nearby universe. We present major axis rotational velocities, velocity dispersions,  $h_3$  and  $h_4$  moments that we derive from our high resolution ( $\sigma_{inst} \simeq 39 \text{ km s}^{-1}$ ) spectra for 46 S0 to Sc type galaxies — for 28 of the galaxies we also present minor axis data. These results are combined with bulge-to-disk decompositions. We show agreement between purely kinematic diagnostics of the bulge dichotomy with structural and morphological indicators of bulge types. We find that pseudobulges — as indicated both by Sérsic index and by morphology — have both increased rotational support (higher  $v/\sigma$  values) and on average lower central velocity dispersions. We also find that the shape of the velocity dispersion profiles correlates well with bulge type. Classical bulges have centrally peaked velocity dispersion profiles, pseudobulges have flat velocity dispersion profiles. We present evidence for previously undetected counter rotation in the two systems NGC3945 and NGC4736. The correlation between  $h_3$  and  $v/\sigma$ , that is observed in elliptical galaxies, is also observed in intermediate type galaxies, irrespective of bulge type.

---

<sup>1</sup>This chapter has been submitted as Fabricius et al. (2011)

## 4.1 Introduction

There is ample observational evidence that bulges in early type spiral galaxies come in different varieties. They are not all just like small elliptical galaxies which happen to live in the centre of a spiral disk (Kormendy, 1993; Kormendy & Kennicutt, 2004).

While classical bulges seem to lie on the fundamental plane of elliptical galaxies (Fisher & Drory, 2010) pseudobulges resemble disks more than little ellipticals. They are still photometrically distinct from the outer disk as they appear as a central brightening above the inwards extrapolation of the outer exponential disk profile. Though, other than in the case classical bulges, their Sérsic indices fall close to or below two. Other groups have shown that a large fraction of galaxies with boxy or peanut shaped bulges do show signs of inner disks (Bureau & Freeman, 1999b; Chung & Bureau, 2004; Kormendy & Barentine, 2010).

These inner disk-like structures are believed to have formed from secular evolution processes rather than violent mergers (Kormendy & Kennicutt, 2004; Athanassoula, 2005). Asymmetries such as spiral structures and bars may support the angular momentum transfer of disk material and thereby the transport of gas into the inner bulge regions. In their recent study of bulges within the local 11 Mpc volume Fisher & Drory (2011) show that a majority of bulges in the local universe are pseudobulges. Their existence in large quantities in our local low density environment may pose a problem for the understanding of the baryonic physics of galaxy formation (Kormendy et al., 2010) as we do not yet understand how these central disks would survive low redshift ( $z < \simeq 1$ ) mergers typical of  $\Lambda$ CDM simulations (White & Rees, 1978b; White & Frenk, 1991). Recent progress has been made by Fontanot et al. (2011) who show that the existence of the majority of the galaxies with no significant bulge component can be understood in the context of semi-analytical models for hierarchical growth.

Kormendy & Kennicutt (2004) identify a number of criteria to differentiate between classical and pseudobulges such as the bulge vs. the disk ellipticity, their location in the  $v_{max}/\sigma$  diagram and the bulge morphology. Fisher & Drory (2008, 2010) show that the bulge Sérsic Index is successful in differentiating bulge types — pseudobulges have Sérsic indices that fall near or below  $n = 2$ , unlike classical bulges and elliptical galaxies which have higher Sérsic indices.

The identification of the bulge morphology as well as the accurate derivation of photometric structural parameters heavily relies on high spatial resolution imaging. Now a large number of bulges have such data available and — with the supplement of sufficiently high resolution spectroscopic data — allow us to ask the question whether all morphologically disk-like bulges also show kinematic disk-like behaviour such as high  $v/\sigma$  values, flattening or drops in the sigma profile and whether differences seen in structural parameters — namely the Sérsic index — are reflected in the kinematic structure as well.

In §4.2 we describe the sample selection and characteristics, in §4.3 we describe the long slit observations, in §4.4 we give account on the details of the data reduction, especially the removal of emission features and the kinematic extraction. Our results are presented in §4.5, in §4.6 we discuss correlations between kinematic parameters and morphological

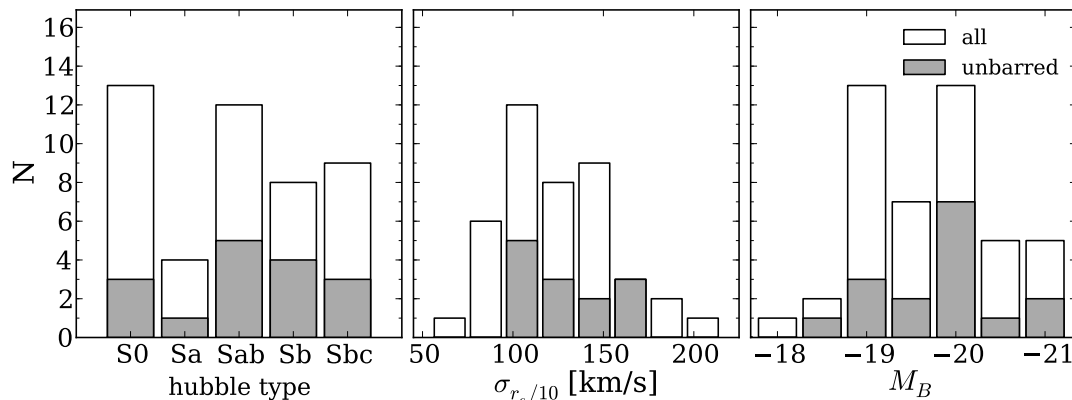


Figure 4.1 Distribution of Hubble types, central velocity dispersions and total magnitudes in the sample.

parameters and indications for an increased rotational support of pseudobulges. We finally summarize our findings in §4.7.

## 4.2 Sample

As we aim to study the kinematics of bulges, our sample consists of 46 galaxies spanning from S0 to Sbc type galaxies and hence the full range of Hubble types that do contain bulges. Further, it contains roughly two-thirds barred galaxies — similar to the total fraction of bars observed in the local universe (see Fig. 4.1). For signal-to-noise ( $S/N$ ) reasons we are biased towards high luminosity objects. Absolute B-Band magnitudes span the range from  $M_B = -17.3$  to  $M_B = -21.3$ . Central velocity dispersions lie between  $60 \text{ km s}^{-1}$  and  $220 \text{ km s}^{-1}$ . We select our targets to be located close enough in distance to properly resolve the bulge regions at typical seeing conditions. With the exception of NGC2964 all galaxies have bulge radii larger than 5 arcseconds and are typically located at distances closer than 25 Mpc. Only NGC4030, NG4260, and NGC4772 are located at significantly larger distances of 29.3 Mpc, 48.4 Mpc and 40.9 Mpc respectively but their relatively large bulge radii of 8.4 arcseconds, 17.5 arcseconds and 16.9 arcseconds leave us confident that we are able to resolve the bulge sufficiently. NGC2964 has a bulge radius of 3.4 arcseconds and is excluded from all structural analysis concerning its bulge, we only present the kinematic data here. In order to break the known degeneracy between the bulge effective radius and Sérsic index in 1D surface brightness decompositions (Graham & Colless, 1997) we require all our targets to have HST imaging in a band similar to V — or preferably in a redder band — and ground based or Spitzer  $3.6 \mu\text{m}$  data available. Most of the objects are found in Fisher & Drory (2008) and/or Fisher & Drory (2010) and have extensive HST and ground based multi-wavelength coverage. To allow for a visual inspection and morphological classification of the bulge region we do not observe

edge-on or close-to edge-on objects ( $i > 70^\circ$ ). Four objects in our sample do have a larger inclination. NGC1023 and NGC4371 are S0-types and contain very little dust and allow an undisturbed view into the bulge region. The situation is different for NGC3593 and NGC7331, where the inclination and — in the case of NGC3593 — the unavailability of an optical HST image inhibits a morphological classification. We present the kinematic data for those objects but do not classify them as classical or pseudobulges.

### 4.3 Observations

We obtain major axis spectra for all and minor axis spectra for about half of the galaxies in our sample. In some cases the observed position angle is not identical to the one published in Hyperleda<sup>2</sup> (Paturel et al., 2003). Also, in a few cases the *minor axis* position angle is not orthogonal to the major axis position angle. We label observations accordingly in Tab. 4.2.

Observations were carried out in service mode during the period from April 2005 to April 2010 (see Tab. 4.2) at the Hobby-Eberly Telescope (HET; Ramsey et al., 1998b) at the McDonald Observatory. We use the Marcario Low Resolution Spectrograph (LRS; Hill et al., 1998) with a one arcsecond wide and 3.5 arcminute long slit, the E2 phase volume holographic GRISM, and a Ford Aerospace 3072×1024 15  $\mu\text{m}$  pixel (usable range 2750×900 pixel) CCD detector yielding a spatial scale of 0.235 arcseconds per pixel. The spectra cover the wavelength range from 4790 Å to 5850 Å with 0.38 Å per pixel and a median instrumental resolution of  $\sigma_{inst} = 39.3 \text{ kms}^{-1}$  (as measured on the 5577 Å night skyline). The seeing varies from 1.2 to 4 arcseconds with a median value of 2.2 arcseconds. Integration times vary from 1.800 s to 3.800 s and on-object exposures are typically split into two for cosmic rejection. For large galaxies (the DSS image of the galaxy exceeded the slit length) we obtain separate exposures of empty sky with an exposure time of 420 s at the end of the actual observation. In order to avoid the azimuth move of the telescope main mirror, the sky exposures are typically obtained one hour in RA after the object but at similar DEC.

Furthermore we observe a collection of kinematic template stars (G and K giants, see Tab. 4.3, metallicity:  $[\text{Fe}/\text{H}] = -0.35 - 0.01$ ) at the beginning and spectroscopic standards throughout the duration of this campaign. The stars are wiggled and trailed along the slit such that a spectrum is recorded as each position where the star crosses the slit. This is used to map out the anamorphic distortion of the spectrograph.

---

<sup>2</sup><http://leda.univ-lyon1.fr>

Table 4.1. Sample

Galaxy	<i>htype</i>	D [Mpc]	<i>srcD</i>	$M_B$ mag	$i$ [°]
(1)	(2)	(3)	(4)	(5)	(6)
NGC 1023	.LBT-..	11.5	2	-20.0	77
NGC 2460	.SAS1..	23.6	1	-19.1	44
NGC 2681	PSXT0..	17.2	2	-20.1	0
NGC 2775	.SAR2..	14.4	1	-19.8	41
NGC 2841	.SAR3*	9.0	1	-19.7	68
NGC 2859	RLBR+..	25.4	1	-20.2	33
NGC 2880	.LB.-..	21.9	2	-19.2	68
NGC 2964	.SXR4*	19.9	1	-19.1	58
NGC 3031	.SAS2..	3.9	2	-20.1	59
NGC 3166	.SXT0..	22.0	1	-20.4	56
NGC 3245	.LAR0*	20.9	2	-19.9	67
NGC 3351	.SBR3..	8.6	1	-19.1	42
NGC 3368	.SXT2..	8.6	1	-19.6	55
NGC 3384	.LBS-*	8.6	1	-18.8	62 <sup>a</sup>
NGC 3521	.SXT4..	8.1	1	-19.7	42
NGC 3593	.SAS0*	8.8	1	-17.9	75
NGC 3627	.SXS3..	12.6	4	-20.9	57
NGC 3675	.SAS3..	10.7	1	-19.1	60
NGC 3898	.SAS2..	21.9	1	-20.1	57
NGC 3945	RLBT+..	19.0	1	-19.6	63
NGC 3953	.SBR4..	13.2	1	-19.8	62
NGC 3992	.SBT4..	22.9	5	-21.2	47
NGC 4030	.SAS4..	29.3	6	-21.1	40
NGC 4203	.LX.-*	15.1	2	-19.1	27
NGC 4260	.SBS1..	48.4	7	-20.7	70
NGC 4274	RSBR2..	12.5	1	-19.1	66
NGC 4314	.SBT1..	12.5	1	-19.1	16
NGC 4321	.SXS4..	14.3	1	-20.7	30
NGC 4371	.LBR+..	14.3	1	-19.0	79
NGC 4379	.L.-P*	15.9	8	-18.4	42
NGC 4394	RSBR3..	14.3	1	-19.0	20
NGC 4448	.SBR2..	12.5	1	-18.5	52
NGC 4501	.SAT3..	14.3	1	-20.4	61
NGC 4536	.SXT4..	12.2	9	-19.3	59
NGC 4569	.SXT2..	14.3	1	-20.5	66
NGC 4698	.SAS2..	14.3	1	-19.3	51
NGC 4736	RSAR2..	4.2	1	-19.1	35
NGC 4772	.SAS1..	40.9	5	-21.1	68
NGC 4826	RSAT2..	7.5	2	-20.0	60
NGC 5055	.SAT4..	7.8	1	-20.2	56
NGC 5248	.SXT4..	14.8	1	-19.9	56
NGC 5566	.SBR2..	20.1	5	-20.1	61
NGC 7177	.SXR3..	19.8	1	-19.5	42
NGC 7217	RSAR2..	16.6	1	-19.8	36
NGC 7331	.SAS3..	15.5	1	-20.8	75
NGC 7743	RLBS+..	19.2	10	-19.0	40

*Notes:* 1) Galaxy name 2) Hubble type (RC3) 3) distance 4) source for distance: 1= Tully & Fisher (1988) 2= Tonry et al. (2001) 3= de Vaucouleurs et al. (1991) 4= Saha et al. (2006) 5= Tully et al. (2009) 6= Springob et al. (2009) 7= Ekholm et al. (2000) 8= Blakeslee et al. (2009) 9= Riess et al. (2009) 10= Jensen et al. (2003) 5) total  $B$ -band magnitude (Hyperleda) 6) inclination (Hyperleda) *Comments:* a) no values in Hyperleda, from Peter Erwin (private communication)

Table 4.2. List of observations

Galaxy	axis	date	seeing ["']	exp.-time [s]	angle [°]	sky
(1)	(2)	(3)	(4)	(5)	(6)	(7)
NGC 1023	MJ	2009-10-24	1.9	2,400	87	yes
NGC 1023	MN	2009-10-23	2.2	2,400	177	yes
NGC 2460	MJ	2005-11-08	2.0	1,800	30	no
NGC 2460	MN	2005-11-08	2.0	1,800	120	no
NGC 2681	MJ	2007-10-21	2.0	2,700	114	yes
NGC 2775	MJ	2008-03-05	2.6	2,700	156	no
NGC 2775	MN	2008-12-24	3.4	2,400	66	no
NGC 2841	MJ	2007-11-08	1.6	1,800	152	no
NGC 2841	MN <sup>c</sup>	2008-12-23	3.2	2,280	58	no
NGC 2859	MJ	2005-11-09	1.6	3,000	80	no
NGC 2859	MN	2006-05-25	2.5	1,800	170	no
NGC 2880	MJ	2009-11-16	3.4	2,200	142	no
NGC 2880	MN	2009-12-18	2.2	2,400	52	no
NGC 2964	MJ	2010-02-18	1.9	2,400	96	yes
NGC 2964	MN	2010-03-21	2.2	2,400	7	yes
NGC 3031	MJ <sup>b</sup>	2007-02-22	2.2	2,700	137	yes
NGC 3031	MN <sup>c</sup>	2005-12-28	3.1	1,800	67	no
NGC 3166	MJ	2008-02-06	2.0	2,454	85	yes
NGC 3166	MN	2008-12-25	2.4	2,400	175	no
NGC 3245	MJ	2008-02-06	1.7	2,700	174	yes
NGC 3245	MN	2008-12-25	2.5	2,400	84	no
NGC 3351	MJ <sup>b</sup>	2008-02-09	1.5	2,550	165	yes
NGC 3351	MN	2008-12-27	5.0	2,400	75	yes
NGC 3368	MJ <sup>b</sup>	2007-02-26	3.1	2,420	153	yes
NGC 3368	MN <sup>c</sup>	2008-12-09	2.6	2,400	87	yes
NGC 3384	MJ	2009-12-13	1.7	2,400	53	yes
NGC 3384	MN	2010-02-19	1.8	2,400	143	yes
NGC 3521	MJ	2007-04-18	1.6	2,700	161	yes
NGC 3521	MN	2009-01-03	2.3	2,528	74	yes
NGC 3593	MJ	2010-02-17	1.2	2,400	84	yes
NGC 3627	MJ <sup>b</sup>	2006-12-27	2.3	1,800	10	no
NGC 3627	MN	2007-02-23	2.2	1,800	100	no
NGC 3675	MJ	2008-03-05	2.6	2,700	178	yes
NGC 3898	MJ	2007-04-19	1.6	2,700	108	no
NGC 3945	MJ <sup>b</sup>	2009-12-17	2.1	2,400	154	yes
NGC 3945	MN	2010-04-12	1.6	4,200	64	yes
NGC 3953	MJ <sup>b</sup>	2008-02-06	2.0	2,700	32	yes
NGC 3992	MJ <sup>b</sup>	2008-12-28	2.7	2,700	66	yes
NGC 4030	MJ	2005-04-05	2.3	1,800	27	no
NGC 4203	MJ	2007-04-12	1.3	2,520	7	yes
NGC 4260	MJ	2008-12-29	2.7	2,700	62	no
NGC 4274	MJ	2007-04-19	1.7	2,623	99	yes
NGC 4314	MJ	2007-02-20	2.3	2,700	127	no
NGC 4321	MJ	2005-06-11	3.6	1,800	100	no
NGC 4321	MN	2006-05-24	2.4	3,000	10	no
NGC 4371	MJ <sup>b</sup>	2006-12-27	2.4	1,800	85	no
NGC 4371	MN	2006-06-19	1.8	1,800	175	no
NGC 4379	MJ	2007-02-21	2.7	1,800	97	yes
NGC 4394	MJ	2007-05-11	1.5	2,556	123	yes
NGC 4448	MJ <sup>b</sup>	2007-04-16	2.3	2,700	85	yes
NGC 4501	MJ	2010-04-06	2.0	3,340	140	yes
NGC 4501	MN	2010-04-08	2.1	2,505	50	yes
NGC 4536	MJ	2010-04-08	3.6	2,385	120	yes

Table 4.2 (cont'd)

Galaxy	axis	date	seeing ["]	exp.-time [s]	angle [°]	sky
(1)	(2)	(3)	(4)	(5)	(6)	(7)
NGC 4536	MN	2010-04-10	2.1	2,500	30	yes
NGC 4569	MJ	2007-06-15	2.1	2,700	14	yes
NGC 4569	MN	2010-04-12	- <sup>a</sup>	2,880	115	yes
NGC 4698	MJ	2008-12-28	2.4	2,700	166	no
NGC 4736	MJ	2009-12-12	1.9	2,400	105	yes
NGC 4736	MN <sup>c</sup>	2008-04-01	2.2	2,700	30	yes
NGC 4772	MJ <sup>b</sup>	2008-12-29	2.5	2,700	145	no
NGC 4826	MJ <sup>b</sup>	2008-01-09	2.0	2,187	96	yes
NGC 4826	MN <sup>c</sup>	2009-06-25	1.5	2,122	25	yes
NGC 5055	MJ	2008-03-05	4.0	2,700	103	yes
NGC 5055	MN	2009-06-26	2.2	2,400	13	yes
NGC 5248	MJ <sup>b</sup>	2007-04-18	1.6	2,700	109	yes
NGC 5566	MJ	2005-07-07	2.5	1,800	30	no
NGC 5566	MN	2006-05-24	2.0	1,750	120	no
NGC 7177	MJ <sup>b</sup>	2007-08-11	2.3	2,700	60	yes
NGC 7177	MN <sup>c</sup>	2009-11-12	1.9	2,600	173	yes
NGC 7217	MJ	2007-08-12	1.7	2,700	81	yes
NGC 7217	MN <sup>c</sup>	2008-12-29	1.4	2,400	178	no
NGC 7331	MJ	2007-08-11	1.7	2,700	171	yes
NGC 7743	MJ <sup>b</sup>	2008-12-28	2.3	2,400	100	no
NGC 7743	MN <sup>c</sup>	2009-10-17	2.3	2,400	167	no

*Notes:* List of observations. 1) Galaxy name 2) MJ=major axis, MN=minor axis, 3) date of observation 4) seeing FWHM 5) total exposure time 6) slit position angle east of north 7) dedicated sky frame was taken *Comments:* a) No seeing information available, b) the position angle differs by more than 10° from the Hyperleda published value, c) MN axis PA not orthogonal to MJ axis PA.

## 4.4 Data Reduction

We reduce the long-slit spectra following standard procedures of bias subtraction, cosmic ray rejection and flat fielding under MIDAS described in Mehlert et al. (2000) with additional steps needed to correct for spectral alignment and anamorphism. We correct a two degree tilt between the spectra and the CCD rows by appropriate sub-pixel shifting of the CCD columns. Two bad columns at positions corresponding to  $\lambda = 4850 \text{ \AA}$  are corrected through interpolation. The wavelength calibration is performed on neon and cadmium arc frames with typically ten lines. Where the line signal is low we bin over a few rows along the spatial direction but never over more than five pixels corresponding to 1.2 arcseconds. After the original line identification we first fit a polynomial of degree four to the line positions along the spatial direction in order to remove noise-induced row to row jitter, and then fit a polynomial of degree three along the spectral direction. The remaining RMS scatter in line position is smaller than one pixel. The spectra are then rebinned in log-wavelength and corrected for anamorphic distortion. The distortion of the LRS spectrograph is measured using stellar spectra. Stars are trailed along the slit in order to generate several spectra or *traces* along the whole length of the slit. The centroids

Table 4.3. Observed kinematic templates

Identifier (1)	type (2)	[Fe/H] (3)	date of obs. (4)
HR2600	K2III	-0.35	04/03/2005
HR6159	K4III	-0.13	04/02/2005
HR6817	K1III	-0.06	04/02/2005
HR6770	G8III	-0.05	04/02/2005
HR6018	K1III	0.01	04/02/2005
HR3418	K1III	0.09	04/02/2005
HR3427	G8III	0.16	04/02/2005
HR3369	G9III	0.17	04/02/2005
HR6136	K4III	0.20	04/02/2005
HR3428	G9III	0.24	04/02/2005
HR7576	K3III	0.42	04/02/2005
HR3905	K2III	0.46	04/02/2005

*Notes:* (1) Identifier (2) type (3) metallicity (SIMBAD), (4) date of observation

of the traces are found by calculating the first moment for the pixel counts in a 10 pixel wide window around the trace. We then first fit a third order polynomial to describe the trace position as function of wavelength and then fit a second third order polynomial to the trace positions in each column to model the distortion. We find a distortion of up to ten pixel in the corners of the CCD with respect to the centre of the detector (see also Fig 2. in Saglia et al. 2010). We correct for the distortion by means of sub-pixel shifting. Counts of individual pixel are distributed into pixel of the target frame according the their overlapping surface area. We measure the distortion on several stellar spectra which are taken in similar manner at different nights. We find that the residual distortion at the edges of the chip — after correcting one stellar spectra with the distortion information of a different night — is never larger than 1.5 arcseconds. This is below the typical FWHM of the PSF of our observations and — more importantly — well below the typical spatial bin sizes that we use at the ends of the slit. To correct for flexure of the instrument during the night we measure the wavelength position of the 5577 Å skyline at the slit ends and correct the wavelength calibration to zeroth order by adding a constant offset. The median absolute offset of all observations is 17 kms<sup>-1</sup>. Where dedicated sky spectra are available we collapse them along the spatial direction in order to obtain a single maximum signal to noise sky spectrum. This spectrum is then scaled according to the exposure time of the object and subtracted from the full frame. In cases where no sky frame is available, the sky signal is determined from the slit ends. One advantage of long-slit spectroscopy is that often the slit ends do contain sufficient non-object contaminated sky. However, the differential slit illumination is subject to change with time because the HET prime focus assembly moves across the telescope pupil during the duration of an observation. We test the effect of this differential illumination on 44 blank sky spectra that were obtained over the course of this survey. We use the slit ends to determine the sky signal in the same way as we do for the galaxy spectra. We then determine the differences between those and the

sky signal that we measure from the slit centre. We find that the residuals amount to no more than 5% of the sky signal in all cases. We then derive kinematics using 5% higher and 5% lower sky values. The resulting errors are significantly smaller than the reported error bars in all cases. In the case of the major axis observation of NGC3368, NGC4569, and the minor axis observation of NGC4569 the use of the dedicated sky frame results in an over-subtraction of the sky — i.e. clearly negative residuals — possibly because of stray light or an increased level of sky background at the time the sky frame was taken. In those cases we use the sky from the slit ends instead. In the cases of large galaxies such as NGC3031 we test the effect of object contamination by using different window sizes at the slit ends for the sky extraction. We find the effect of object contamination to be negligible in all cases. Finally all frames go through an extensive visual inspection. Artifacts like residuals of comic ray removal are corrected through interpolation of the neighbouring pixel.

#### 4.4.1 Derivation of the Kinematics and Template Library

We derive stellar kinematics using the Fourier Correlation Quotient (FCQ) method of Bender (1990); Bender et al. (1994). The log-wavelength calibrated and sky subtracted spectra are spatially binned to reach signal to noise values of at least 30 per pixel. An 8-th order polynomial is then fitted to the continuum and the first and last three channels in Fourier space are filtered out to remove low and high frequency variations in the continuum level.

FCQ measures the full line of sight velocity distribution (LOSVD). By means of deconvolving the autocorrelation function, the FCQ method is more robust against template mismatches than other Fourier or pixel-space based methods. Nevertheless, nebular emission lines can significantly affect the derived higher moments of the LOSVDs and therefore need to be taken into account for the derivation of the kinematics. This introduces the necessity of a very accurate model spectrum because otherwise residual mismatches between the observed galaxy spectrum and the broadened model spectrum will mimic emission signatures which are then incorrectly removed. We therefore form a pool of template spectra by combining actual observed stellar spectra (see Tab. 4.3) with synthetic simple stellar population templates (SSP) from Vazdekis (1999). Those include varying metallicities and ages. We use a sub-sample of the published spectra with Salpeter IMF (Salpeter, 1955), and all combinations of ages of 1, 2, 5, 10, 17.78 Gyr and metallicities of  $[\text{Fe}/\text{H}] = -1.68, -1.28, -0.68, -0.38, +0.00, +0.20$ . The published SEDs have a nominal resolution of  $1.8 \text{ \AA}$  (FWHM) which corresponds to  $\sigma^* = 45 \text{ kms}^{-1}$  and is therefore slightly lower than the spectral resolution of  $\sigma_{inst} = 39.3 \text{ kms}^{-1}$ .

We run FCQ with the collection of all velocity templates. Then we choose the single best-fitting template based on the minimum *RMS* between the broadened template and the galaxy spectrum

$$RMS = \int_{\lambda_1}^{\lambda_2} (G(\lambda) - B(\lambda) \otimes S_i(\lambda))^2 d\lambda, \quad (4.1)$$

where  $\lambda_1 = 4817 \text{ \AA}$  to  $\lambda_2 = 5443 \text{ \AA}$  is the fitted wavelength range,  $G(x)$  is the galaxy

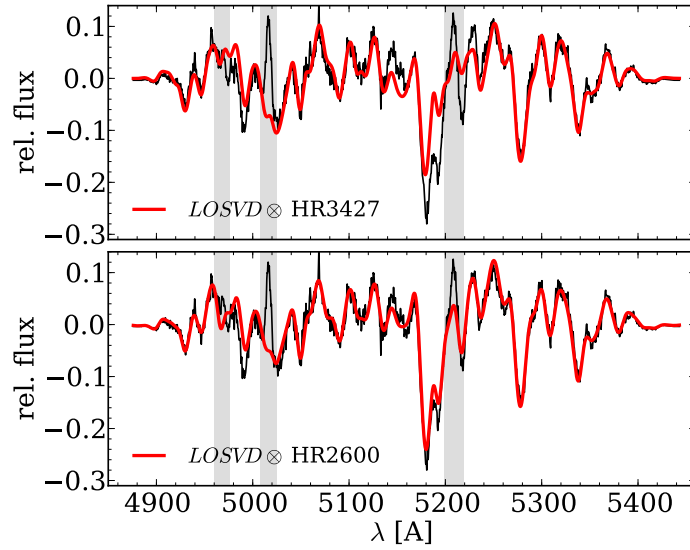


Figure 4.2 Continuum removed spectrum in the central radial bin of NGC2841 (black) and the broadened template spectrum (red). Grey bars mark the positions of the [OIII] and [NII] emission lines. *upper panel:* Choosing the G8III,  $[Fe/H] = 0.16$  star HR3427 results in a notable mismatch around the Mg triplet region. Best fit parameters are  $\sigma = 235.1 \pm 3.0 \text{ km s}^{-1}$ ,  $h_3 = 0.037 \pm 0.009$ ,  $h_4 = 0.041 \pm 0.009$ ,  $RMS = 0.034$ . *lower panel:* using HR2600 (K2III,  $[Fe/H] = -0.35$ ) results in a much better match with  $\sigma = 241.2 \pm 3.2 \text{ km s}^{-1}$ ,  $h_3 = 0.022 \pm 0.009$ ,  $h_4 = 0.048 \pm 0.009$ ,  $RMS = 0.024$ . While FCQ finds values for the LOSVD moments that fully agree within the errors, the residual spectrum will look very different for those two cases and render the detection of weak emission lines impossible in the case of HR3427.

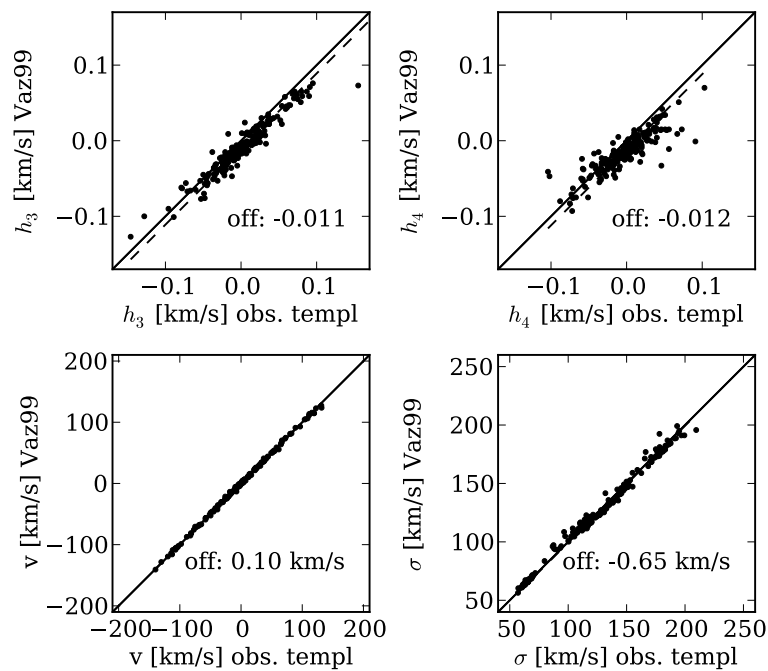


Figure 4.3 Moments of the of the LOSVD that we obtain from the kinematic extraction using the Vazdekis SSP library vs. the values that we obtain for the observed templates. The solid lines correspond to a one-to-one correlation, the dashed lines are actual fits to the data. Note: We only compare galaxies with no obvious sign of emission.

spectrum,  $S_i(x)$  is the  $i$ -th template spectrum, and  $B(x)$  is the broadening function derived from FCQ. Note that this is different from other algorithms such as the Maximum Penalized Likelihood (MPL) technique of Gebhardt et al. (2000) or the Penalized Pixel-Fitting method (pPXF) of Cappellari & Emsellem (2004) which fit a linear combination of their templates. FCQ subsequently fits Gaussians with Hermite expansions ( $h_3$  and  $h_4$  moments) (Gerhard, 1993; van der Marel & Franx, 1993) to the derived LOSVDs. In Fig. 4.2 we show examples of fits with two different broadened templates. While FCQ indeed finds very similar values for the moments of the LOSVD, the quality of the template match differs significantly in the two cases.

In Fig. 4.3 we compare the impact of the usage of either just our observed templates or just the SSP library. We compare only a subset of galaxies (NGC2775, NGC2880, NGC3675, NGC4030, NGC4371, NGC4379, NGC7457) for which we detect no significant emission in order to assure that the derived moments are not affected by emission. The biases that we introduce by adding the SSP templates to our library are generally small ( $\Delta\sigma = -0.65 \text{ kms}^{-1}$ ,  $\Delta h_3 = -0.011$ ,  $\Delta h_4 = -0.012$  and much smaller than our median errors on the respective moments).

As our spectra often reach into the disk regions we deal with relatively low velocity dispersions. In a few cases the derived dispersions are in the order of the instrumental resolution. The matter gets complicated by the fact that the disk regions are also the regions of lowest surface brightness and therefore the regions with poorest  $S/N$ . It is important to understand how reliable the derived moments are under these circumstances.

A caveat of the deconvolution in Fourier space is the amplification of high frequency noise. Fourier based algorithms therefore filter the signal before the actual deconvolution step. FCQ uses the optimal Wiener filter (Braut & White, 1971; Simkin, 1974). The basic idea is to decompose the Fourier transform of the input data into a Gaussian contribution — the data part — and an exponential function — the noise part. The *optimal* Wiener filter then weighs the various signal channels according to their relative contribution to the data part of the input signal (for details see Bender 1990). While a purely Gaussian LOSVDs ought to be well modelled by a Gaussian in Fourier space, the Gauss-Hermite moments cause higher frequency shoulders, that are easily *swallowed* by the noise. Adjusting the filter width may recover characteristics of the LOSVD (Bender et al., 1994) at the cost of increased statistical uncertainty.

Here we choose not to broaden the Wiener Filter as this yields better stability against statistical deviations. But this causes biases especially at low velocity dispersions. To correct for these biases we carry out extensive Monte Carlo simulations on a regular parameter grid of velocity dispersion,  $h_3$ ,  $h_4$ ,  $S/N$  and template. We generate artificially broadened spectra at each grid point with 30 different noise realisations according to the input signal to noise. We find that the necessary corrections to  $\sigma$ ,  $h_3$  and  $h_4$  are well behaved and linear functions between input and retrieved values and independent of input template if the velocity dispersion is larger than  $75 \text{ kms}^{-1}$ , the signal to noise is larger than 30 per pixel and a stellar template is used. The SSP templates cause non-linear behaviour at small velocity dispersions. While we still use the SSP templates to generate broadened model spectra during the emission line fitting, the reported kinematic values are exclusively based

Table 4.4. Parameters for the linear bias corrections in velocity dispersion

	<i>S/N per pixel</i>			
	22.5	40.0	37.5	75.0
$a_\sigma$	1.06	1.06	1.06	1.07
$b_\sigma$	-11.04	-10.89	-10.80	-10.70

on stellar templates, and corrected for biases using

$$\begin{aligned}\sigma(r) &= a_\sigma \cdot \sigma^{\text{FCQ}}(r) + b_\sigma \\ h_3(r) &= a_{h_3} \cdot h_3^{\text{FCQ}}(r) + b_{h_3} \\ h_4(r) &= a_{h_4} \cdot h_4^{\text{FCQ}}(r) + b_{h_4}.\end{aligned}$$

Tab. 4.4 and 4.5 list the corresponding parameters that we obtain from the simulations. For velocity dispersions below  $75 \text{ km s}^{-1}$  and  $S/N < 30$  per pixel, we do not report values for  $h_3$  and  $h_4$ . Further we report values of  $v$  and  $\sigma$  only for  $S/N > 20$ .

We estimate statistical errors in the derived moments through Monte Carlo simulation as described in Mehlert et al. (2000). Once the optimum LOSVD is derived by FCQ we generate the synthetic spectra using the fitted  $v$ ,  $\sigma$ ,  $h_3$  and  $h_4$ -parameters and the best fitting stellar template. In a similar manner as for the bias correction, 100 different realisations of artificial noise are then added to the spectra to reach the same signal to noise values as in the original spectra. We then use FCQ again to derive the kinematics on those spectra. The reported errors correspond to the statistical one-sigma deviations from the mean.

#### 4.4.2 Emission Line Subtraction and Gas Kinematics

A significant fraction of the objects in our sample show emission in  $H_\beta$  ( $4861.32 \text{ \AA}$ ),  $[OIII]$  ( $4958.83 \text{ \AA}$  &  $5006.77 \text{ \AA}$ ) and  $[NI]$  ( $5197.90 \text{ \AA}$  &  $5200.39 \text{ \AA}$ ). The nitrogen emission line lies on the red flank of the Mg triplet feature – the most important kinematic feature in our spectral range. While typically weak, the nitrogen emission often significantly affects the derivation of  $h_3$ -moments.  $h_3$ -moments measure the asymmetric deviation from a Gaussian and are expected to behave antisymmetrically with respect to the galaxy centre in the case of axisymmetric systems. Deviations from this antisymmetry may hint at contamination by nitrogen emission lines. We therefore decided to remove nebular emission following a similar procedure as the GANDALF routine (Sarzi et al., 2006): We perform a first fit to the galaxy spectrum over a larger spectral range reaching from  $4820 \text{ \AA}$  to  $5440 \text{ \AA}$  using the FCQ algorithm. We then subtract the best fitting broadened stellar spectrum from the galaxy spectrum and fit Gaussian functions — using a standard least squares algorithm — to the residual emission. The algorithm first searches for emission in a  $500 \text{ km s}^{-1}$  window around the brighter oxygen line at  $5007 \text{ \AA}$  (the oxygen doublet is well resolved

Table 4.5. parameters for the linear bias corrections in  $h_3$  and  $h_4$ 

	$\sigma[\text{kms}^{-1}]$	$S/N$ per pixel		
		30.3	37.5	75.0
$a_{h_3}$	75.0	1.3084	1.2947	1.2734
	100.0	1.1281	1.1142	1.0874
	150.0	1.0182	1.0104	1.0000
	200.0	1.0103	1.0059	0.9988
	250.0	1.0037	1.0008	0.9945
$b_{h_3}$	75.0	0.0002	0.0001	0.0001
	100.0	0.0003	0.0003	0.0002
	150.0	0.0003	0.0003	0.0003
	200.0	0.0009	0.0008	0.0006
	250.0	0.0010	0.0010	0.0009
$a_{h_4}$	75.0	1.8521	1.8088	1.7277
	100.0	1.4994	1.4500	1.3555
	150.0	1.0857	1.0655	1.0307
	200.0	1.0407	1.0275	1.0045
	250.0	1.1503	1.1371	1.1089
$b_{h_4}$	75.0	0.0864	0.0814	0.0738
	100.0	0.0280	0.0240	0.0160
	150.0	0.0165	0.0148	0.0127
	200.0	0.0105	0.0104	0.0104
	250.0	-0.0027	-0.0015	0.0006

at our instrumental resolution) red-shifted to the systemic velocity. It fits for the three parameters of amplitude, central velocity, and the velocity dispersion. It then goes on to the other and generally weaker emission lines and performs a fit to their amplitude while assuming the same central velocity and velocity dispersion as the oxygen line. In principle the ratio of the two oxygen emission lines is given by atomic physics and constant at 0.33. Rather than fixing these values during the fit we also fitted the lower amplitude line as this provided another handle on the reliability of our method. We then subtract the best fitting emission lines from the original galaxy spectrum and repeat the FCQ multiple-template fit. The best fitting broadened template is again subtracted from the input spectrum and the gas fit is repeated on the improved difference spectrum. This — in principle iterative — approach was found to converge very quickly. A fourth FCQ fit typically yields no significant change in the derived kinematics any more. Our reported stellar kinematics went through three subsequent iterations of template fitting with two interleaved gas removal steps. The gas removal routine gives access to the study of line ratios (Sarzi et al., 2006) and is also a necessary step before the calculation of absorption line indices and subsequent stellar population analysis. Both of which will be subject to a forthcoming publication.

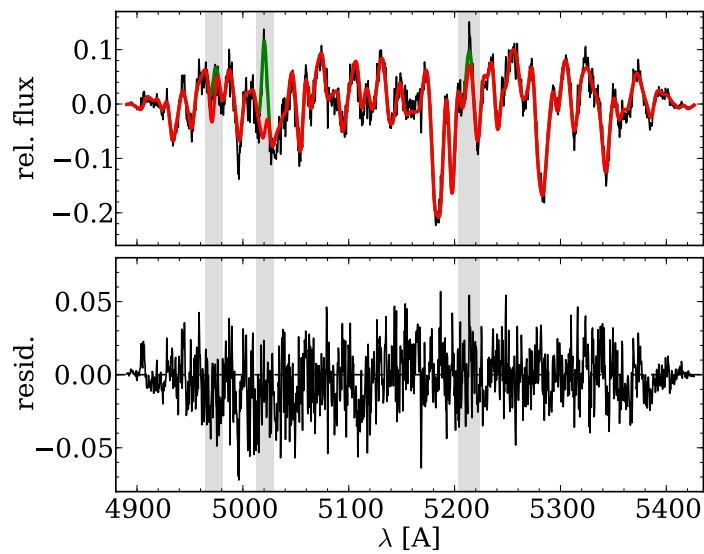


Figure 4.4 Example of the nebular emission line subtraction. Here the gas emission was removed from one of the central spectra of NGC3368. *upper panel:* After subtraction of the best fitting broadened stellar template (red) the algorithm finds a significant emission signal in the OIII lines and the nitrogen doublet (green). The vertical bars mark the search range for emission. *lower panel:* Residuals between observed and model spectrum after removal of the emission.

### 4.4.3 Identification of Pseudobulges

If no classification is available already from Fisher & Drory (2008) or Fisher & Drory (2010) we follow the same procedure for the identification of pseudobulges. We define a bulge photometrically as the excess light over the inwards extrapolation of the outer disk exponential luminosity profile. The bulge to disk decompositions that we adopt in §4.4.4 allow us to determine the bulge region of an object. Here we classify bulges using close-to V-band HST images (*F547M*, *F555W* & *F606W*). While these bands are subject to dust obscuration they are also sensitive to an enhancement in star formation rate, a feature commonly observed in pseudobulges (Fisher, 2006). We visually inspected the HST images to see whether the bulge regions contain disk-like structures such as nuclear spirals, nuclear bars and/or nuclear rings. If such structure is present we call the photometric bulge a pseudo-bulge. If there is no structure — the bulge resembles an elliptical galaxy with a smooth light distribution — we call this bulge a classical bulge.

Weak central dust spirals, that also occur frequently in elliptical galaxies (e.g. Storchi-Bergmann et al. 2007) — often distinguishable from the outer disk because they are inclined differently — are no reason for us to call a bulge a pseudobulge. NGC2841 poses an example for this situation. A dust spiral can easily be identified in HST F438W, but it is misaligned with the outer disk also seen only in vicinity of the nucleus.

Yet, a few objects remain for which we do not feel confident to assign a classification based on their HST morphology: NGC2460 and NGC3953. We treat them as unclassified throughout this work. As mentioned in §4.2, we also do not classify the bulges of the galaxies NGC3593 and NGC7331 due to their high inclination. In Appendix B we give a detailed explanation for the bulge classification for each individual object.

### 4.4.4 Photometry

We use the results from surface brightness decompositions to study possible correlations between photometric parameters and kinematic structure and to identify the actual bulge region of a particular galaxy.

Many of our objects already have decompositions available in Fisher & Drory (2008) and Fisher & Drory (2010). For those galaxies where this is not the case we obtain archival data and perform a bulge to disk decomposition following the same prescription.

We generally give preference to Spitzer 3.6  $\mu\text{m}$  data for the large scale coverage. In cases where no 3.6  $\mu\text{m}$  data could be obtained we use *I* or *H* band data instead. Similar preference is given to the IR HST data. If *NIC160W* data could be obtained we use those and otherwise *I* or *R* band data instead.

We fit ellipses to the isophotes of the large scale data and HST images. Isophotal fitting is carried out using the code of Bender & Moellenhoff (1987). See Fisher & Drory (2008) for a brief summary of the procedure.

The major axis luminosity profiles of the deeper large scale data and the higher spatial resolution HST data are combined by matching the zero point of the large scale data to the HST profiles. Points in the overlapping regions are averaged.

Intermediate type galaxies are known to contain many components that are not well described by the decomposition into a Sérsic bulge and exponential disk (e.g. bars, rings, nuclear star clusters). We frequently exclude the very inner regions of the surface brightness profiles (typically  $r < 1''$ ) when they show an excess of light. We also excluded regions affected by bars and background affected points. The parameters from those new decompositions are presented in Tab. 4.6.

In a few cases we use the V-band decompositions from Fisher & Drory (2008) because no redder data could be obtained or because their V-band decompositions yield results which we deem more trustworthy in the light of the kinematic information at hand. Such cases are discussed in Appendix B.

#### 4.4.5 Bulge Radius

Here we are particularly interested in the kinematic properties of the bulge regions of our observed galaxies. Of course the derived LOSVDs will always be the light weighted average of all components (bulge, disk, bar) along a particular line of sight through the galaxy. But the photometric bulge to disk decompositions allow us to determine within which radius the bulge should dominate. We define the *bulge radius*  $r_b$  along the major axis as the radius where the light contribution of the photometric bulge component exceeds the light contribution of the disk component by 25%:

$$I_0^{bulge} \exp\left(-\left(\frac{r_b}{r_0}\right)^{\frac{1}{n}}\right) = 1.25 \cdot I_0^{disk} \exp\left(-\frac{r_b}{h}\right) \quad (4.2)$$

where  $I_0^{bulge}$  is the central surface brightness of the bulge component,  $I_0^{disk}$  is the central surface brightness of the disk component,  $r_0$  and  $h$  are the scale lengths of the bulge and disk components and  $n$  is the Sérsic index (see Caon et al. (1993) for the relation between  $r_0$  and  $r_e$ ). One might argue that the bulge effective radius  $r_e$  is a more natural choice as  $r_b$  of course is dependent on the disk parameters. But we find that in a number of galaxies  $r_e$  actually lies in a region that is dominated by disk light. The choice of 25% is a compromise between the desire to be reasonably dominated by the bulge component on the one hand and still wanting to maintain a sufficient number of resolution elements within the bulge radius on the other. The values for the bulge radius are listed in Tab. 4.8.

## 4.5 Results

### 4.5.1 Kinematic Profiles and Comparison with Literature

Tab. 4.7 gives an example of the format of the measured stellar kinematic moments as function of the distance from the center of the galaxy. The full listing is available electronically<sup>3</sup>. In the Appendix A we plot the kinematic profiles. When available, we also plot

<sup>3</sup><http://cds.u-strasbg.fr/>

Table 4.6. New bulge to disk decomposition parameters

Galaxy (1)	Bulge morph. (2)	Band (3)	$n$ (4)	$\mu_e$ mag arcsec <sup>-2</sup> (5)	$r_e$ arcsec (6)	$m^{Sérsic}$ mag (7)	$\mu_0^{disk}$ mag arcsec <sup>-2</sup> (8)	$h$ arcsec (9)	$m^{disk}$ mag (10)
NGC 2460	?	3.6 $\mu$ m	3.70 $\pm$ 0.36	18.53 $\pm$ 0.28	11.13 $\pm$ 3.78	9.95 $\pm$ 0.28	17.31 $\pm$ 0.26	11.90 $\pm$ 1.00	9.94 $\pm$ 0.29
NGC 2681	p	3.6 $\mu$ m	3.39 $\pm$ 0.43	15.55 $\pm$ 0.77	3.59 $\pm$ 2.81	9.47 $\pm$ 0.77	18.39 $\pm$ 0.38	34.69 $\pm$ 5.71	8.70 $\pm$ 0.45
NGC 2859	c	I	2.84 $\pm$ 0.28	18.85 $\pm$ 0.34	8.76 $\pm$ 9.10	10.92 $\pm$ 0.34	19.83 $\pm$ 1.46	18.76 $\pm$ 7.97	11.47 $\pm$ 1.59
NGC 2880	c	I	3.14 $\pm$ 0.15	19.54 $\pm$ 0.19	10.32 $\pm$ 4.08	11.20 $\pm$ 0.19	20.46 $\pm$ 0.27	25.81 $\pm$ 1.22	11.41 $\pm$ 0.28
NGC 3166	c	3.6 $\mu$ m	2.89 $\pm$ 0.26	16.86 $\pm$ 0.44	12.20 $\pm$ 5.75	8.21 $\pm$ 0.44	20.09 $\pm$ 0.62	85.35 $\pm$ 21.82	8.44 $\pm$ 0.73
NGC 3627	p	3.6 $\mu$ m	1.37 $\pm$ 0.32	16.61 $\pm$ 0.34	4.21 $\pm$ 1.48	10.64 $\pm$ 0.34	18.56 $\pm$ 0.33	60.52 $\pm$ 4.44	7.65 $\pm$ 0.35
NGC 3898	c	3.6 $\mu$ m	3.41 $\pm$ 0.55	16.93 $\pm$ 0.84	8.22 $\pm$ 4.48	9.05 $\pm$ 0.84	18.13 $\pm$ 0.60	29.05 $\pm$ 4.26	8.82 $\pm$ 0.64
NGC 3992	c	H	3.49 $\pm$ 0.44	17.75 $\pm$ 0.55	14.65 $\pm$ 4.13	8.60 $\pm$ 0.56	17.71 $\pm$ 0.40	79.22 $\pm$ 15.15	6.22 $\pm$ 0.49
NGC 4260	c	I	3.84 $\pm$ 0.28	21.86 $\pm$ 0.20	36.81 $\pm$ 8.48	10.67 $\pm$ 0.20	19.95 $\pm$ 0.22	25.15 $\pm$ 1.81	10.95 $\pm$ 0.24
NGC 4379	c	I	2.17 $\pm$ 0.32	18.66 $\pm$ 0.43	5.54 $\pm$ 1.58	11.87 $\pm$ 0.44	18.98 $\pm$ 0.45	13.42 $\pm$ 1.57	11.35 $\pm$ 0.48
NGC 4527	?	3.6 $\mu$ m	1.64 $\pm$ 0.27	15.31 $\pm$ 0.13	4.87 $\pm$ 0.83	8.93 $\pm$ 0.14	16.66 $\pm$ 0.09	40.08 $\pm$ 1.38	6.65 $\pm$ 0.10
NGC 4536	p	3.6 $\mu$ m	2.14 $\pm$ 0.14	15.18 $\pm$ 0.20	4.76 $\pm$ 1.34	8.72 $\pm$ 0.20	17.85 $\pm$ 0.10	46.80 $\pm$ 1.29	7.50 $\pm$ 0.10
NGC 4772	c	H	3.03 $\pm$ 0.44	17.73 $\pm$ 0.60	13.49 $\pm$ 8.24	8.84 $\pm$ 0.60	18.87 $\pm$ 0.28	71.96 $\pm$ 8.02	7.59 $\pm$ 0.64
NGC 4826	p	3.6 $\mu$ m	3.57 $\pm$ 0.35	18.56 $\pm$ 0.42	19.70 $\pm$ 21.15	18.32 $\pm$ 0.46	18.32 $\pm$ 0.22	58.12 $\pm$ 2.85	7.50 $\pm$ 0.23
NGC 7743	c	3.6 $\mu$ m	3.47 $\pm$ 0.30	15.96 $\pm$ 0.46	2.31 $\pm$ 0.74	10.83 $\pm$ 0.46	17.87 $\pm$ 0.30	21.90 $\pm$ 2.69	9.17 $\pm$ 0.35

Notes: (1) Galaxy name (2) bulge classification (3) photometric band used for decomposition (4) bulge Sérsic index (5) bulge surface brightness at  $r_e$  (6) bulge effective radius along the major axis (7) bulge apparent magnitude (8) disk central surface brightness (9) disk scale length (10) disk apparent magnitude

Table 4.7. Format example of the measured stellar kinematics

Galaxy	PA [deg]	r ["]	v [kms <sup>-1</sup> ]	$\sigma$ [kms <sup>-1</sup> ]	$h_3$	$h_4$
(1)	(2)	(3)	(4)	(5)	(6)	(7)
NGC 1023	87	51.46	186.55 ± 2.71	92.16 ± 2.55	-0.067 ± 0.017	-0.037 ± 0.015

*Notes:* (1) Identifier (2) observed position angle (3) distance from the center (positive: east; negative: west), (4) velocity relative to systemic velocity (5) velocity dispersion (6) Gauss-Hermite  $h_3$  moment (7)  $h_4$  moment. The full listing is available electronically <http://cds.u-strasbg.fr/>.

data from the literature for comparison. Some of the galaxies in our sample have Integral Field Spectroscopic data from SAURON available. In those cases we create pseudo long slit data through interpolation of the SAURON  $v$ ,  $\sigma$ ,  $h_3$  and  $h_4$  maps along a slit aperture with a position angle corresponding to our observation. In general the agreement of our data with the published values is acceptable.

In a few cases such as NGC4203 a difference between the previously published data and ours are explained by the difference in the observed position angle.

Bertola et al. (1995) find somewhat larger velocity dispersions for NGC4379 than we do. Formally their instrumental dispersion should allow to resolve the 80 kms<sup>-1</sup> — 118 kms<sup>-1</sup> that we find for the dispersion in the bulge.

Dumas et al. (2007) finds larger velocity dispersions in the cases of NGC3351 and NGC5248 than we do. The dispersion of those objects is probably too low to be resolved by their instrumental dispersion of  $\simeq 110$ . kms<sup>-1</sup>.

Vega Beltrán et al. (2001) find systematically lower velocity dispersions for NGC2841 than we do. However, we also plot data from Héraudeau & Simien (1998) which are in excellent agreement with ours.

The SAURON data for NGC4698 (Falcón-Barroso et al., 2006) suggest a somewhat larger velocity dispersion over our whole observed range than we find. They also find negative  $h_3$  moments on the east side. The dispersion of this galaxy ( $\simeq 140$  kms<sup>-1</sup>) should be well resolved by SAURON and such the difference remains somewhat mysterious but small.

### 4.5.2 Signatures of Bars in Velocity Profiles

In our sample, 30 out of 46 of the galaxies are classified as barred or as hosting an oval. Bars and ovals will affect the observed kinematics — their presence should be reflected in the moments of the observed LOSVD. Bureau & Athanassoula (2005) use n-body simulations to derive diagnostics for the presence of bars in edge-on disks. They find that *double-hump* rotation curves, plateaus and shoulders in velocity dispersion and correlation of  $h_3$  moments with velocity — in contrast to the usually seen anti-correlation — are indicators for the presence of a bar. The *double-hump* describes a rotation curve that first rises quickly with radius, reaches a local maximum then drops slightly and starts rising again towards

larger radii. We do see similar features in a number of our galaxies even though they are not observed edge-on. Not always is the signature strong enough to form an actual local minimum after the fast inner rise. Instead in some cases we observe shelves — the rise in velocity stagnates for a certain radial range but becomes larger again before finally flattening out.

Out of 30 barred galaxies (including 6 ovals) 20 do show such features. However our data do not extend very far into the disk region in many of the objects in our sample, also the visibility may be inhibited by the coarse spatial binning of some of our spectra. Further, this diagnostic tool was developed for edge-on systems. So it is likely that we miss bar signatures in the velocity profiles. But also 9 of the 16 non-barred galaxies show either shelves or double humps which may be an indication that those systems actually do host a bar that is not readily seen photometrically.

### 4.5.3 Central Velocity Dispersions

We calculate the central velocity dispersion of the galaxies in our sample by averaging the major axis dispersion within a tenth of the effective bulge radius  $r_e$  that we obtain from the photometric decomposition. The values for the central dispersions are given in Tab. 4.8.

In Fig. 4.5 we show corresponding histograms of the central dispersions. In the left panel we discriminate bulge types based on their morphology, in the right panel we discriminate by Sérsic index. There is significant overlap between the distributions of velocity dispersions for the classical and pseudobulges. Nonetheless, it is clear that, in our sample, pseudobulges have on average lower velocity dispersions. We find in our sample that classical bulges become exceedingly rare below central velocity dispersions of  $100 \text{ km s}^{-1}$ . However, we caution that our sample is not volume limited.

### 4.5.4 Velocity Dispersion Gradients

Inspection of the individual rotation curves reveals a wide variety of structures. Though, in particular the shape of the velocity dispersion profile seems to fall into two rough classes. In Fig. 4.6 we show the kinematic profiles for the two galaxies NGC3898 and NGC4448 from our sample. Depicted are the velocity, the velocity dispersion and the  $h_3$  and  $h_4$  moments for the fitted Gauss-Hermite expansion of the LOSVDs. Dashed lines indicate the bulge radius from the photometric decomposition. While in the case of NGC3898 the velocity dispersion rises all the way to the centre, NGC4448 has a relatively flat dispersion profile within the bulge radius. Similar to Fisher (1997) we examine the logarithmic slope of the velocity dispersion within the bulge radius and call it  $\gamma$ . We derive the slope point-wise and then take the average, i.e.

$$\gamma = \left\langle \frac{\Delta \log(\sigma)}{\Delta \log(r)} \right\rangle_{|r_{min} < r < r_b}, \quad (4.3)$$

where  $r_{min}$  always excludes the inner FWHM of the seeing of that particular observation and in some cases is chosen larger to exclude central features like nuclear regions of en-

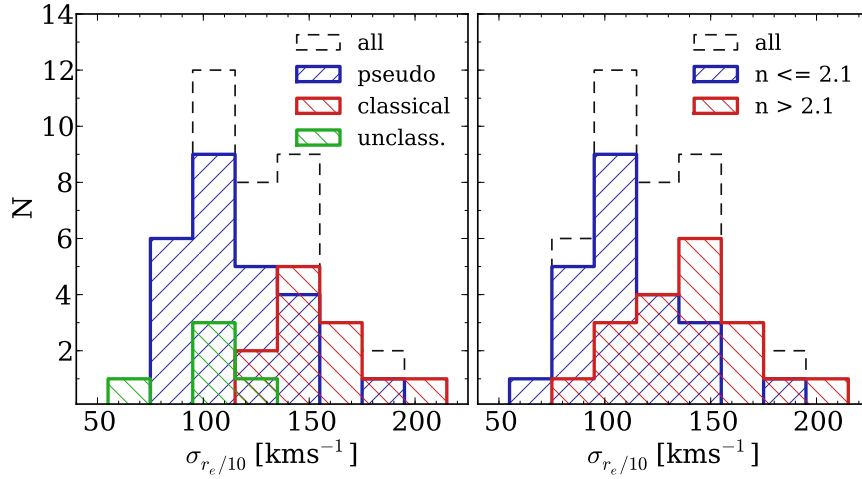


Figure 4.5 Histograms of the central velocity dispersions. The left panel discriminates bulge types by morphology, the right panel discriminates them by their Sérsic index.

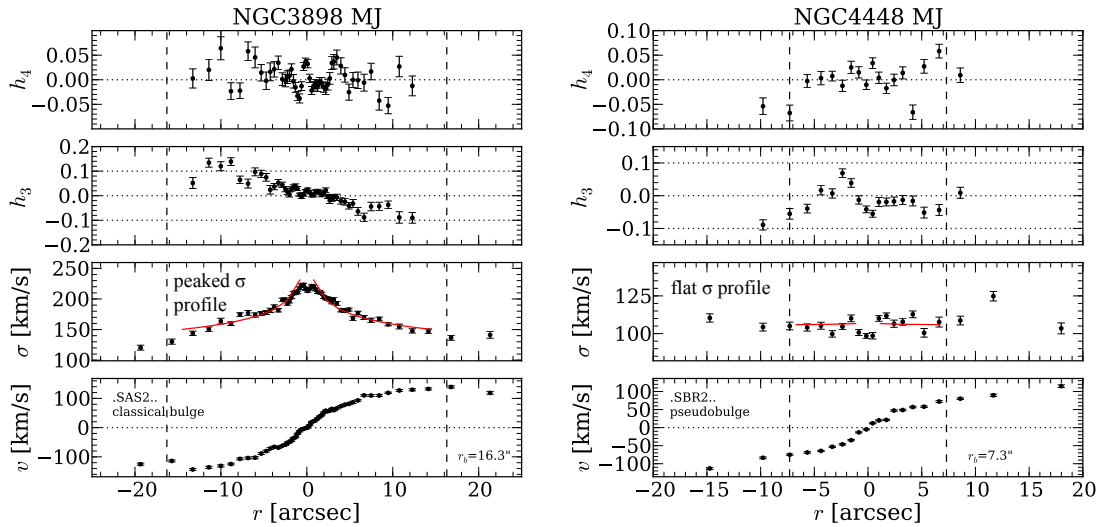


Figure 4.6 Major axis kinematic profiles for NGC3898 and NGC4448. Positive radii are east of the galaxy center. We plot from bottom to top the rotational velocity, velocity dispersion,  $h_3$  and  $h_4$  moments. The curvature of the red lines correspond to the derived logarithmic slope of the dispersion profile, they are scaled to match the depicted profile. Their extend indicates the radial range which is taken into account.

hanced star formation (see Appendix B). In Fig. 4.6 we also overplot lines which correspond to the derived  $\gamma$  values. Further, in order to avoid that the derived slope is a function of the particular binning scheme of our data, we bin the data first radially such that the bins are equally sized in  $\log(r)$ . We create five radial bins. In cases where the resulting bins do not all at least contain one data point, we skip the binning.

Alternatively we test the ratio of the averaged velocity dispersions within two annuli within the bulge radius

$$\delta = \frac{\langle \sigma \rangle|_{r_{min} < r < r_b/3}}{\langle \sigma \rangle|_{r_b/3 < r < r_b}} \quad (4.4)$$

as proxy for the slope. The choice of  $r_b/3$  as cut radius for the two different annuli is somewhat arbitrary, but we do not find a strong dependence of our results on the specific chosen radius. The derived values for the slope — both  $\gamma$  and  $\delta$  are reported together with the bulge structural parameters in Tab. 4.8.

We find that all bulges which are classified as pseudobulges indeed show flattened velocity dispersion profiles or even sigma drops. The dispersion profiles of many pseudobulges are sometimes slightly asymmetric. On the other hand a majority of the classical bulges show centrally peaked velocity dispersion profiles.

Fig. 4.7 summarizes this finding qualitatively. There we plot the velocity dispersion profiles for all our bulges separated by bulge type. These velocity dispersions are normalized by the central dispersion and the radius is normalized by the bulge radius. We do not plot bulges that were left unclassified. We also plot the minor axis dispersion profiles. For this plot we adjust the bulge radius that was obtained from a major axis profile by the mean ellipticity in the bulge region. Whilst not as clear — partly due to the lower number of profiles, but partly probably also due to the subtleties of choosing a correct radius for the normalisation — we again find that classical bulges tend to show centrally rising velocity dispersions.

In Fig. 4.8 we now plot the Sérsic index from the photometric decomposition as a function of both metrics for the slope of the velocity dispersion. Similar to the distributions of central velocity dispersion, there is significant overlap in profile slope. Nonetheless, the bulges with the largest values of Sérsic index all have steeply decaying dispersions profiles. Similarly the bulges with low Sérsic indices more commonly have flat dispersion profiles. This result is true for both the logarithmic slope of dispersion, and the dispersion ratio.

The increasing slope of velocity dispersion with Sérsic index is not fully unexpected. For instance Ciotti (1991) describes a series of models for isotropic and spherical galaxies which have a surface brightness profiles that follow a Sérsic law. He gives projected velocity dispersion profiles for his models and outside of the very central regions ( $r > r_e/10$ ), and for Sérsic indices larger than one, the slope is a monotonically increasing function of  $n$ . We calculate slopes and  $\sigma$  ratios for these profiles in a similar manner as we did for our data. One caveat of this exercise is that our definition of a bulge radius is not applicable in the case of the one-component models. Also, we have to chose an inner cut radius for the fit as the models feature central sigma drops in the case of small  $n$ . Sigma drops are

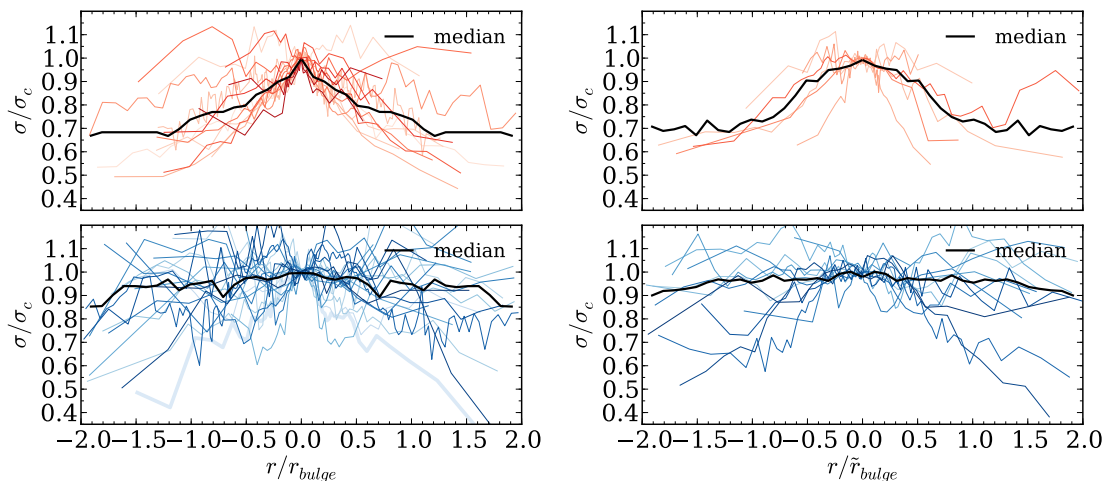


Figure 4.7 Major (upper panel) on minor axis (lower panel) velocity dispersion profiles, normalized by central velocity dispersion and bulge radius. Profiles of classical bulges are plotted in red, those of pseudobulges in blues. Different color shades correspond to different galaxies. The thick black line shows the median profile for all bulges in one panel. The bulge radii for the minor axis profiles have been corrected using the mean bulge ellipticity according to  $\tilde{r}_{bulge} = (1 - \langle \epsilon \rangle) \cdot r_{bulge}$ .

an observed phenomenon (e.g. Falc3n-Barroso et al. 2006), but our spatial resolution is typically not fine enough to resolve those. We somewhat arbitrarily fit for  $\gamma$  in the radial range of  $r_e/10 < r < r_e$  and calculate  $\sigma$  ratios for  $r_e/10 < r < r_e/3$  and  $r_e/3 < r < r_e$ . Note that our effective bulge radii are on average 15% smaller than the definition of the bulge radius that we use throughout the work. In Fig. 4.8 we overplot the obtained values as a black line. The dashed lines show the range of values one would obtain by choosing 50% larger or smaller outer cut radii for the integration. While the spherical and isotropic galaxies are a very simplistic model for the variety of bulges in our sample, one can see that the general trends are reproduced, however a more detailed dynamical modelling is needed to confirm this result.

In the major axis plots all unbarred pseudobulges fall below or very close to  $\gamma = 0.05$  and  $\delta = 1.06$  (the corresponding values of the isotropic models for  $n = 2$ ) and only one unbarred classical bulge falls below  $\gamma = 0.05$ . However 3 out of 8 unbarred classical bulges do fall significantly below  $\delta = 1.09$  suggesting that  $\gamma$  is more successful in discriminating bulge types. Again this picture is complicated further once barred galaxies are taken into account. The additional component of a bar seems to lead towards flatter dispersion profiles.

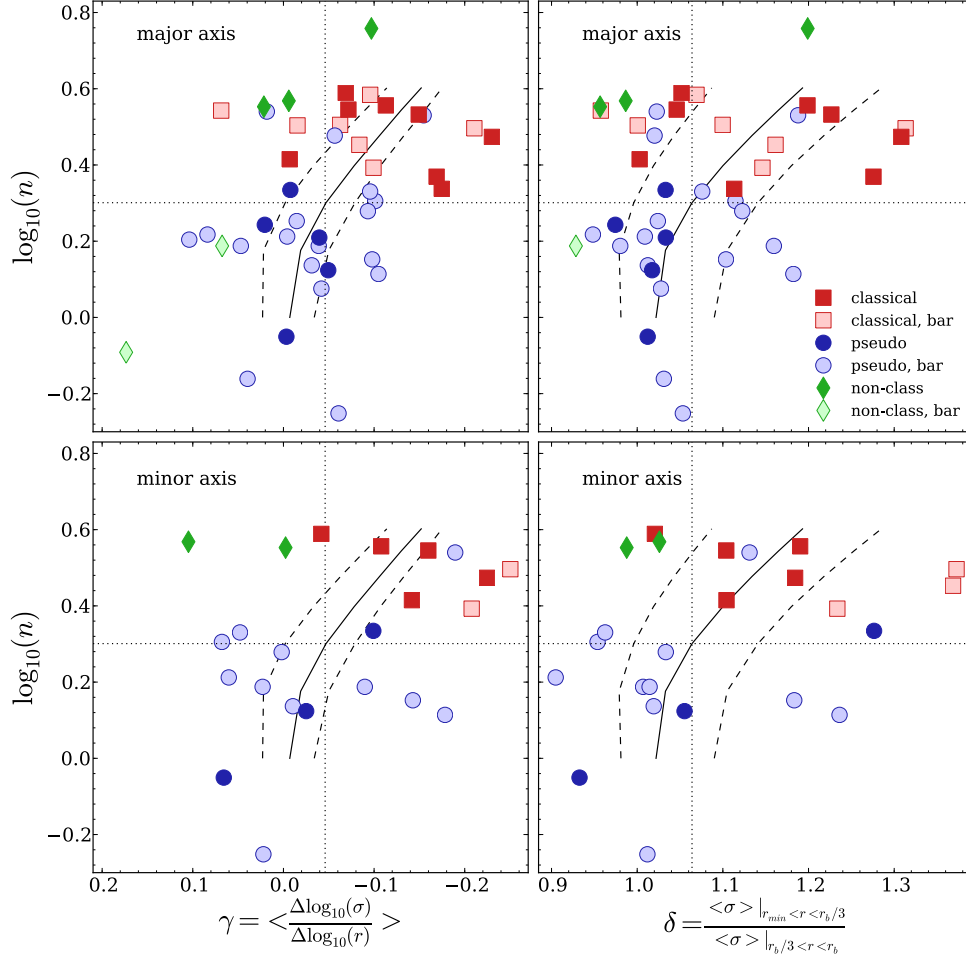


Figure 4.8 Sérsic index  $n$  is shown as a function of both metrics for the flatness of the velocity dispersion profile,  $\gamma$  and  $\delta$ , respectively. *Upper left:* shows the logarithmic slope of the velocity dispersion. Red squares and blue circles correspond to classical and pseudo-bulges respectively. Open symbols label barred galaxies. The green diamonds represent unclassified objects. The black solid line shows the respective behaviour of the isotropic models in Ciotti (1991), here the slopes were calculated in the radial range  $r_e/10 < r < r_e$ . The dashed lines show the  $\gamma$  values one would obtain by choosing the outer integration radius 50% smaller or larger. The horizontal line marks a Sérsic index of two. The vertical dotted lines mark  $\gamma = -0.05$  and  $\delta = 1.06$ , the respective values that the isotropic models take for a Sérsic index of 2. *Upper right:* shows the ratio of the averaged velocity dispersion in two different annuli *lower panels:* Same for the minor axis dispersions. The radii were adjusted according the mean bulge ellipticity  $\tilde{r}_{bulge} = (1 - \langle \epsilon \rangle) \cdot r_{bulge}$ .

### 4.5.5 Influence of Seeing on Velocity Dispersion

The seeing disk and the width of the slit will *smear* the observed velocities and can create increases in the observed line of sight velocity dispersion. This effect is commonly known as *slit smearing*. All data presented here were observed with a slit width of 1 arcsecond. The effect of slit smearing on the velocity dispersion is therefore expected to be negligible compared to the effect caused by the seeing ( $> 1.2$  arcseconds in all cases). At least two galaxies NGC3384 and NGC3528 do show peaks in velocity dispersion in the central arcseconds. In both galaxies the velocity profile also rises rapidly in the centre. We test whether this rapid rise in combination with the seeing may be responsible for the observed dispersion peak. We model the point spread function (PSF) with a Gaussian of the same FWHM. We then calculate the standard deviation of the velocity which is weighted by the PSF amplitude at all radii and subtracted the result from the observed velocity dispersion. In this simple one-dimensional model the PSF smearing does generate a central peak which is of similar size and amplitude as the observed one. We cannot rule out the possibility that the central peaks of NGC3384 and NGC3528 can be explained through PSF-smearing alone. We refrain ourselves from correcting the presented velocity dispersions as an accurate correction has to include the knowledge of a high resolution luminosity profile and a more rigorous, 2-dimensional modelling of the PSF. We rather exclude the central peaks from the further analysis.

### 4.5.6 Correlation of $h_3$ and $h_4$ Moments

As  $h_3$  measures the asymmetric deviation from a purely Gaussian distribution it detects lower velocity tails of the LOSVD along the line of sight. Such tails arise naturally in disks (Binney & Tremaine, 1987). Bender et al. (1994) found that local  $h_3$  and local  $v/\sigma$  are strongly anti-correlated with a slope of  $-0.12$  in their sample of elliptical galaxies. Fisher (1997) finds a similar anti-correlation in the inner regions of his lenticular galaxies but also sees that — for a number of his objects — at values of  $v/\sigma \simeq 1$  the anti-correlation turns — at least briefly but abruptly — into a correlation.

We reproduce the plot for the local correlation of  $h_3$  and  $v/\sigma$  from Bender et al. (1994) for our sample in Fig. 4.9. The  $h_3$  moments are generally anti-correlated with  $v/\sigma$  out to  $v/\sigma \simeq 0.5$ . While a linear fit reveals a different slope for classical bulges ( $h_3 = (-0.127 \pm 0.004) \cdot v/\sigma$ ) and pseudobulges ( $h_3 = (-0.137 \pm 0.003) \cdot v/\sigma$ ), their absolute values are still very similar to  $-0.12$  of Bender et al. (1994). This local correlation is reproduced in the mean values for the bulge region (Fig. 4.10).

We test for a possible correlation with bulge magnitude (see Fig. 4.10) and the bulge averaged value  $\langle h_3 \rangle$ . Because we use decompositions from different bands we derived the bulge luminosity by multiplying the bulge to total ratio from the photometric decomposition with the total B-band magnitude from Hyperleda. We do not see any correlation between bulge luminosity and  $\langle h_3 \rangle$ .

The  $h_4$  moment of the Gauss-Hermite expansion measures the symmetric deviation from a Gaussian distribution. Negative  $h_4$  describe a more boxy, centrally flattened distribution,

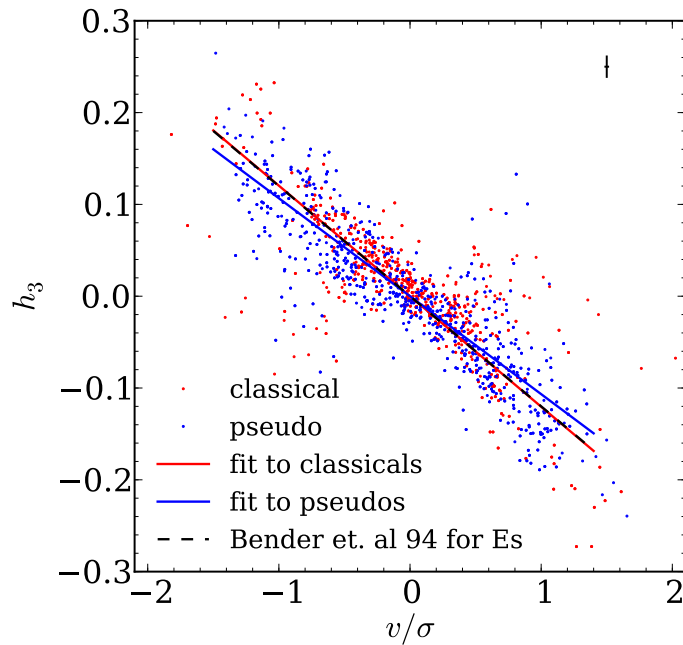


Figure 4.9 Local correlation between  $h_3$  and  $v/\sigma$  along the major axis for the galaxies in our sample. We only plot points for which the error in  $h_3$  is lower than 0.05. Plotted are all galaxies for which the bulge was classified either as classical (red) or a pseudobulge (blue). Typical errorbars are shown in the upper right of the diagram. The red and blue lines correspond to the fitted linear correlations for the classical and pseudobulges respectively. The black line represents the values from Bender et al. (1994).

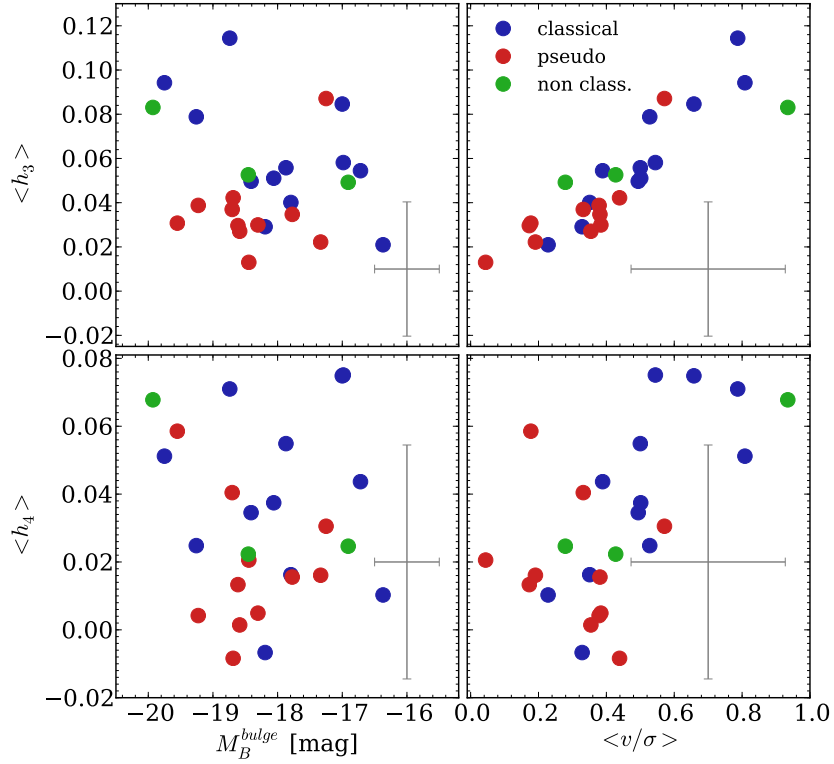


Figure 4.10 Major axis correlations between bulge averaged Gauss-Hermite moments  $\langle h_3 \rangle$  and  $\langle h_4 \rangle$ , bulge luminosities and  $\langle v/\sigma \rangle$ . *upper left*:  $\langle h_3 \rangle$  as function of bulge magnitude (as derived from the bulge to total ratio and the total B-band luminosity). Red circles represent classical bulges, blue circles are pseudobulges, green circles represent unclassified bulges. The typical errors in bulge magnitude from the decomposition and the standard deviation of the  $h_3$  values within the bulge are plotted in the lower right. *upper right*:  $\langle h_3 \rangle$  as function of  $\langle v/\sigma \rangle$ . No inclination corrections were applied. The error bars represent the mean standard deviations of values within the bulge. *lower left*:  $\langle h_4 \rangle$  as function of bulge magnitude. *lower right*:  $\langle h_4 \rangle$  as function of  $\langle v/\sigma \rangle$ .

more positive values describe centrally peaked distributions with extended wings. The averaged  $h_4$  moments in the bulges are generally close to zero, the median for the complete sample of major axis spectra is 0.026 with a standard deviation of 0.048. None of our bulges show obvious dips in the  $h_4$  profile as the ones described by Debattista et al. (2005); Méndez-Abreu et al. (2008). But this diagnostic for boxy-peanut shape bulges only applies to low inclinations ( $i < 30^\circ$ ), given that the inclinations of most of our galaxies is larger than  $30^\circ$  (41 out of 46) this is not further surprising. However, fourteen galaxies show a double peak in the  $h_4$  profile within the bulge region. This is typically seen in combination with a rapid increase of the rotational velocity and relatively strong  $h_3$  moments. From our Monte Carlo simulations described in §4.4.1 we can rule out that the observed peaks are a result of a degeneracy between  $h_3$  and  $h_4$  moments in the fit.

We find no correlation between the averaged moments  $\langle h_4 \rangle$  and the bulge luminosities. However — while the error bars are large — larger  $h_4$  moments seem to be found in bulges with larger averaged  $v/\sigma$  (Fig. 4.10).

Table 4.8. Structural and kinematic parameters

Galaxy (1)	Bulge morph. (2)	Band (3)	$n$ (4)	$r_e$ arcsec (5)	$r_{\mu_b=\mu_d}$ arcsec (6)	$r_b$ arcsec (7)	$\langle \epsilon_b \rangle$ (8)	$\langle \epsilon_d \rangle$ (9)	$\sigma_{r_e/10}$ kms $^{-1}$ (10)	$\gamma_{MJ}$ (11)	$\delta_{MJ}$ (12)	$\gamma_{MN}$ (13)	$\delta_{MN}$ (14)	$\frac{\langle v^2 \rangle}{\langle \sigma^2 \rangle}$ (15)	<i>src</i> (16)
NGC 1023	c	3.6 $\mu\text{m}$	2.5	15.0	25.2	22.4	0.20	0.59	212.9 $\pm$ 5.2	-0.10	1.15	-0.21	1.234	0.178	3
NGC 2460	?	3.6 $\mu\text{m}$	3.7	11.1	9.2	7.5	0.19	0.25	111.4 $\pm$ 3.5	-0.01	0.99	0.10	1.026	...	1
NGC 2681	p	3.6 $\mu\text{m}$	3.4	3.6	13.1	11.9	0.11	0.27	112.5 $\pm$ 1.3	-0.16	1.19	...	...	...	1
NGC 2775	c	3.6 $\mu\text{m}$	3.5	22.4	22.8	19.4	0.11	0.16	173.9 $\pm$ 13.7	-0.07	1.05	-0.16	1.104	0.236	3
NGC 2841	c	3.6 $\mu\text{m}$	3.6	22.2	21.4	18.6	0.24	0.55	222.2 $\pm$ 19.3	-0.11	1.20	-0.11	1.190	0.218	3
NGC 2859	c	I	2.8	8.8	22.5	19.3	0.16	0.25	176.8 $\pm$ 5.4	-0.08	1.16	-2.40	1.369	...	1
NGC 2880	c	I	3.1	10.3	23.2	20.1	0.20	0.34	142.2 $\pm$ 5.3	-0.21	1.31	-0.25	1.373	0.469	1
NGC 2964 <sup>a</sup>	p	3.6 $\mu\text{m}$	1.0	2.0	3.7	3.4	0.19	0.32	88.4 $\pm$ 1.3	...	...	...	...	...	3
NGC 3031	c	3.6 $\mu\text{m}$	3.9	71.8	83.2	72.0	0.29	0.47	157.5 $\pm$ 13.6	-0.07	1.05	-0.04	1.021	0.415	3
NGC 3166	p	V	0.6	3.8	7.1	6.7	0.41	0.27	151.4 $\pm$ 6.1	-0.06	1.05	0.02	1.012	1.342	2
NGC 3245	c	3.6 $\mu\text{m}$	3.0	5.2	10.9	9.7	0.21	0.45	225.2 $\pm$ 8.3	-0.23	1.31	-0.22	1.184	0.315	1
NGC 3351	p	3.6 $\mu\text{m}$	1.5	7.7	14.9	13.6	0.17	0.28	90.0 $\pm$ 4.2	0.05	0.98	0.02	1.007	0.709	3
NGC 3368	p	3.6 $\mu\text{m}$	1.6	8.2	14.4	13.0	0.13	0.34	122.5 $\pm$ 6.6	0.00	1.01	0.06	0.905	0.566	3
NGC 3384	p	3.6 $\mu\text{m}$	1.4	6.2	16.8	15.6	0.19	0.34	150.3 $\pm$ 2.4	-0.10	1.10	-0.14	1.183	...	3
NGC 3521	c	3.6 $\mu\text{m}$	2.6	9.5	11.3	9.9	0.27	0.44	129.5 $\pm$ 2.9	-0.01	1.00	-0.14	1.104	0.849	3
NGC 3593	?	3.6 $\mu\text{m}$	0.8	13.1	31.5	29.8	0.53	0.58	62.3 $\pm$ 3.1	0.17	0.72	...	...	...	3
NGC 3627	p	3.6 $\mu\text{m}$	1.4	4.2	9.5	8.8	0.31	0.55	116.1 $\pm$ 3.9	-0.03	1.01	-0.01	1.019	0.240	1
NGC 3675	p	3.6 $\mu\text{m}$	1.6	9.8	9.7	8.3	0.36	0.48	114.7 $\pm$ 5.3	-0.04	1.03	...	...	0.342	3
NGC 3898	c	3.6 $\mu\text{m}$	3.4	8.2	18.5	16.3	0.25	0.41	219.0 $\pm$ 8.3	-0.15	1.23	...	...	0.307	1
NGC 3945	p	3.6 $\mu\text{m}$	1.5	9.3	28.7	26.7	0.19	0.17	183.1 $\pm$ 5.4	-0.04	1.16	-0.09	1.014	1.043	3
NGC 3953	?	3.6 $\mu\text{m}$	1.5	6.6	8.8	7.8	0.30	0.50	110.6 $\pm$ 3.1	0.07	0.93	...	...	...	3
NGC 3992	c	H	3.5	14.6	16.0	14.0	0.22	0.50	144.2 $\pm$ 9.5	0.07	0.96	...	...	0.388	1
NGC 4030	p	V	1.8	11.3	10.0	8.4	0.13	0.22	102.9 $\pm$ 4.5	0.02	0.97	...	...	0.889	2
NGC 4203	c	V	2.3	7.0	14.9	13.3	0.11	0.11	170.1 $\pm$ 3.6	-0.17	1.28	...	...	0.223	2
NGC 4260	c	I	3.8	36.8	22.9	17.5	0.28	0.59	143.8 $\pm$ 14.3	-0.10	1.07	...	...	0.209	1
NGC 4274	p	3.6 $\mu\text{m}$	1.6	8.0	16.2	14.8	0.30	0.48	106.9 $\pm$ 5.3	0.10	0.84	...	...	0.753	3
NGC 4314	p	3.6 $\mu\text{m}$	3.0	10.8	9.0	7.8	0.11	0.56	123.3 $\pm$ 5.1	-0.06	1.02	...	...	0.578	3
NGC 4321 <sup>b</sup>	p	3.6 $\mu\text{m}$	1.2	9.6	21.8	20.3	0.22	0.30	86.0 $\pm$ 2.0	...	...	...	...	...	3
NGC 4371	p	V	2.0	7.7	17.3	15.7	0.30	0.35	125.8 $\pm$ 5.0	-0.10	1.12	0.07	0.954	0.403	2
NGC 4379	c	I	2.2	5.5	8.8	7.6	0.11	0.21	121.0 $\pm$ 4.6	-0.17	1.11	...	...	0.155	1
NGC 4394	p	V	1.6	5.1	8.0	7.2	0.12	0.33	80.0 $\pm$ 3.1	0.08	0.95	...	...	1.369	2
NGC 4448	p	3.6 $\mu\text{m}$	1.2	6.3	8.3	7.3	0.19	0.59	98.5 $\pm$ 3.7	-0.04	1.03	...	...	0.407	3
NGC 4501	p	3.6 $\mu\text{m}$	0.9	5.7	7.0	6.2	0.25	0.47	144.2 $\pm$ 4.9	0.00	1.01	0.07	0.933	0.377	3
NGC 4536	p	3.6 $\mu\text{m}$	2.1	4.8	14.8	13.7	0.38	0.48	98.1 $\pm$ 3.3	-0.10	1.08	0.05	0.963	0.707	1
NGC 4569	p	V	1.9	1.6	6.4	6.1	0.48	0.56	114.4 $\pm$ 0.9	-0.09	1.12	0.00	1.033	0.505	2
NGC 4698	c	3.6 $\mu\text{m}$	3.2	17.1	30.5	26.5	0.07	0.35	139.3 $\pm$ 10.4	-0.02	1.00	...	...	0.034	3
NGC 4736	p	3.6 $\mu\text{m}$	1.3	8.4	17.1	15.6	0.10	0.18	107.0 $\pm$ 2.3	-0.10	1.18	-0.18	1.236	1.337	3
NGC 4772	c	V	3.2	15.1	19.4	16.9	0.07	0.38	144.5 $\pm$ 8.1	-0.06	1.10	...	...	0.060	2

### 4.5.7 Extreme Moments and Multiple Kinematic Components

Five galaxies show extreme  $h_3$  and  $h_4$  moments. The most extreme case NGC3521 (a classical bulge) exhibits values of  $h_3$  and  $h_4$  as large as 0.24 and 0.35 respectively. NGC3945, NGC4736, NGC7217 (all pseudobulges) NGC7331 (unclassified; note though, the high Sérsic index of  $n = 5.7$ ) show values of  $h_3$  and  $h_4$  of up to 0.2. The LOSVD is poorly reproduced by a Gauss-Hermite expansion at the radii of such extreme higher moment values (see Fig. 4.12). The reason lies in the existence of a secondary kinematic component in all those cases. For NGC3521 this has been reported by Zeilinger et al. (2001) who attributed the counter-rotating stellar component to the presence of a bar. The two component nature of NGC7217 was discovered before by Merrifield & Kuijken (1994). They suggest that the second component is a result of an extended period of accretion with intermittent change of angular momentum of the infalling material. Prada et al. (1996) reported a counter rotating bulge in NGC7331.

Two more systems in our sample — namely NGC2841 (Bertola & Corsini, 1999), NGC3593 (Bertola et al., 1996) — were reported to hosts counter-rotating components and a kinematically decoupled component was found in NGC4698 (Corsini et al., 1999; Bertola et al., 1999) see Pizzella et al. (2004) for a review. However in these cases the secondary component does not result in unusually strong  $h_3$  and  $h_4$  moments in our data.

In an attempt of a fairer treatment of their complexity we decomposed the FCQ-derived LOSVDs into two separate Gaussian components in a similar manner to Scorza & Bender (1995); Zeilinger et al. (2001). We use a Metropolis-Hastings algorithm (Hastings, 1970; Press et al., 2007) to infer the parameters and error bars. Before the fit, the spectra are binned to a minimum  $S/N$  of 75 per pixel. We run four simultaneous chains for each radial bin. The step width is tuned to achieve a 25% acceptance ratio and after convergence the first half of the chain is discarded (clipped). The run was aborted if the chains do not converge after 100.000 steps.

Fig. 4.11 shows the result of this decomposition. The plotted values are the maximum likelihood values, and the end of the error bars mark the 20% and 80% quantiles in all four chains after clipping. Central values with strong degeneracies between the parameter sets are omitted. In all five galaxies we do find significant second components under the assumption that individual components are purely Gaussian. In Tab. 4.9 we list the integrated fractions of light in the two different kinematic components and compare those to the values that one would expect from the photometric decomposition. For NGC3521 we find that 35% of the light is captured in the lower dispersion component which is in reasonable agreement with the value of 20%-30% of Merrifield & Kuijken (1994).

Table 4.8 (cont'd)

Galaxy (1)	Bulge morph. (2)	Band (3)	n (4)	$r_e$ arcsec (5)	$r_{\mu_b=\mu_d}$ arcsec (6)	$r_b$ arcsec (7)	$\langle \epsilon_b \rangle$ (8)	$\langle \epsilon_d \rangle$ (9)	$\sigma_{r_e/10}$ kms $^{-1}$ (10)	$\gamma_{MJ}$ (11)	$\delta_{MJ}$ (12)	$\gamma_{MN}$ (13)	$\delta_{MN}$ (14)	$\frac{\langle v^2 \rangle}{\langle \sigma^2 \rangle}$ (15)	$src$ (16)
NGC 4826	?	3.6 $\mu\text{m}$	3.6	19.7	21.1	18.3	0.23	0.40	$95.7 \pm 6.4$	0.02	0.96	0.00	0.988	0.299	1
NGC 5055	p	3.6 $\mu\text{m}$	1.3	27.2	28.5	24.3	0.22	0.42	$106.1 \pm 8.6$	-0.05	1.02	-0.03	1.055	0.516	3
NGC 5248	p	3.6 $\mu\text{m}$	0.7	8.3	15.5	14.4	0.25	0.37	$78.4 \pm 2.5$	0.04	1.03	...	...	0.547	3
NGC 5566 <sup>c</sup>	p	...	...	...	...	...	...	...	$146.7 \pm 2.7^d$	...	...	...	...	...	...
NGC 7177	p	3.6 $\mu\text{m}$	1.8	6.1	9.3	8.1	0.22	0.30	$115.3 \pm 4.8$	-0.01	1.02	...	...	0.434	3
NGC 7217	p	3.6 $\mu\text{m}$	2.2	25.0	42.3	36.3	0.05	0.10	$141.1 \pm 12.7$	-0.01	1.03	-0.10	1.277	...	3
NGC 7331	?	3.6 $\mu\text{m}$	5.7	77.3	21.2	17.3	0.34	0.60	$123.6 \pm 13.0$	-0.10	1.20	...	...	1.100	3
NGC 7743	p	3.6 $\mu\text{m}$	3.5	2.3	5.8	5.3	0.11	0.31	$84.6 \pm 2.4$	0.02	1.02	-0.19	1.131	...	1

*Notes:* Structural and kinematic parameters for the galaxies in our sample. (1) Target name (2) bulge classification, c = classical, p = pseudobulge, ? = not classified (3) band for decomposition (4) Sérsic index (5) bulge effective radius from decomposition (6) radius of equal bulge and disk surface brightness (7) adopted bulge radius for this study (8) mean apparent bulge ellipticity (9) mean apparent disk ellipticity (10) central velocity dispersion averaged within one-tenth of the bulge effective radius (11) slope of major axis velocity dispersion profile (12) major axis ratio of the averaged velocity dispersion within the annulus  $r < r_b/3$  to averaged dispersion within  $r_b/3 < r < r_b$  (13) slope of minor axis velocity dispersion profile (14) minor axis ratio of velocity dispersion (15)  $\langle v^2 \rangle / \langle \sigma^2 \rangle$  (Binney, 2005) for the inclination corrected velocity (16) source of decomposition. 1 = this work, 2 = Fisher & Drory (2008), 3 = Fisher & Drory (2010) *Comments:* a) The bulge is not sufficiently resolved to calculate the slopes of the velocity dispersion. b) Our datapoints cover only about a third of the bulge region. We do not calculate the slopes of the velocity dispersion. c) Surface brightness does follow a typical bulge/disk profile. We do not decompose the profile and only present the kinematics data here. d) No decomposition, this is the innermost value.

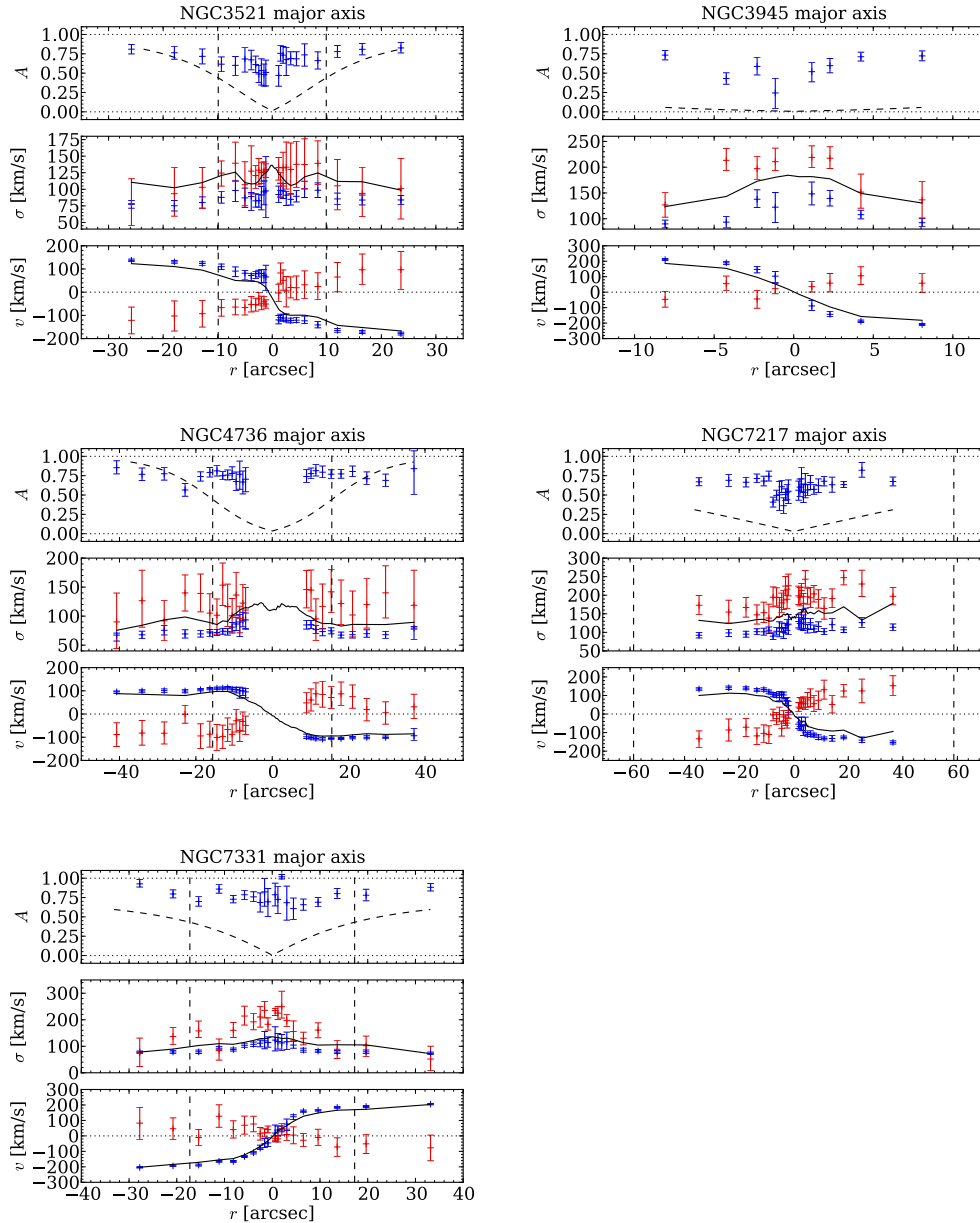


Figure 4.11 Kinematic decompositions of the major axis data of NGC 3521, NGC 3945, NGC 4736, NGC 7217 and NGC 7331. In a procedure similar to Scorza & Bender (1995); Zeilinger et al. (2001) we fit two Gaussians to the FCQ derived kinematics at all radii. Blue and red error bars show mean velocity and dispersion of the two Gaussians where the Metropolis-Hastings algorithm chains achieved convergence. The length of the error bars represent the 20% and 80% quantiles. Black curves indicate the FCQ fitted moments of a single Gauss-Hermite expansion of the LOSVD. Here the error bars are comparable to the thickness of the line. The upper panel shows the relative weight of the fast component with respect to the total light. Here the dashed curve shows the disk to total ratio from the photometric decomposition. Vertical lines indicate the bulge radius.

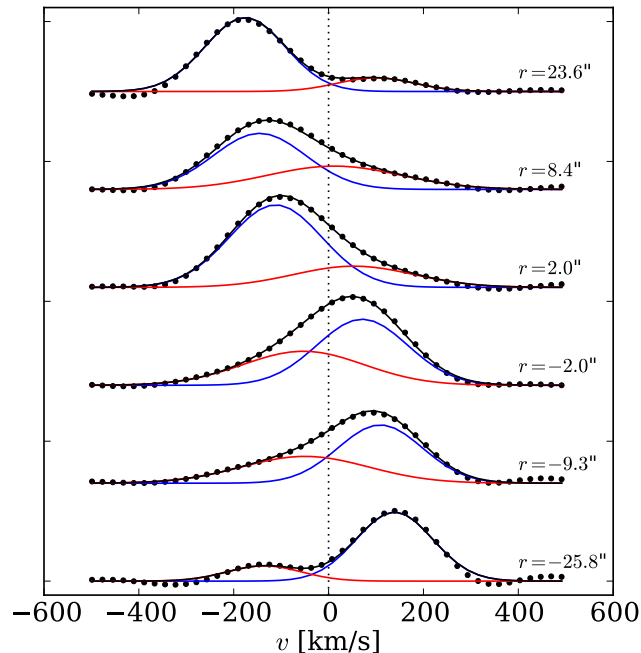


Figure 4.12 Example for the double-Gaussian decompositions for NGC3521. The FCQ derived full line of sight velocity distribution for five selected radii is plotted in black. The two-gaussian kinematic decompositions plotted in red and blue.

Table 4.9. Light fractions in kinematic subcomponent

galaxy	morph.	disk light [%]	light in fast component [%]
(1)	(2)	(3)	(4)
NGC 3521	SAB(rs)bc	26	31
NGC 3945	(R)SB <sup>+</sup> (rs)	2	30
NGC 4736	(R)SA(r)ab	42	32
NGC 7331	SA(s)b	38	40
NGC 7217	(R)SA(r)ab	17	31

*notes:* Comparison of the amount of light in the lower dispersion component to the light that one would expect from the photometric decomposition. We integrated the amplitudes of the Gaussian fits to the two components over all radii shown in Fig. 4.11. (1) Galaxy (2) morphology (RC3) (3) integrated light in disk component from the extrapolation of the outer disk exponential profile (4) integrated light in lower dispersion component.

## 4.6 Discussion

### 4.6.1 Dichotomous Dispersion Profiles of Classical and Pseudobulges

It is commonly assumed that the bulge light — typically determined from a bulge-disk decomposition — represents a dynamically hot component. Yet it has been known for a long time that bulges exist that are supported by rotation (Kormendy, 1982a). Also, many bulges have lower central velocity dispersions than expected from the Faber & Jackson (1976) relation (Kormendy & Kennicutt, 2004). Falcón-Barroso et al. (2006); Ganda et al. (2006) find that several galaxies in the SAURON survey have centers that are dynamically colder than the surrounding disks. Thus, it is now clear that not all galaxies fit the picture that a bulge is a dynamically hot component.

There is an observed dichotomy in bulge properties, including Sérsic index, bulge morphology, star formation & ISM properties, and optical color (Carollo et al., 1997; Gadotti & dos Anjos, 2001; Kormendy & Kennicutt, 2004; Fisher, 2006; Fisher & Drory, 2008, 2010). Recently Fisher & Drory (2010) showed that the dichotomous properties in Sérsic index, morphology, ISM properties are consistent. Furthermore they show that bulges of different type occupy different regions in the projection of fundamental plane properties, thus indicating that there are very likely two physically distinct classes of bulges — are dynamics part of this dichotomy?

The high spectral resolution of ( $39 \text{ kms}^{-1}$ ) our data enables us to recover dispersions out into the disk regions in many of our targets — a feature uncommon to many similar surveys. We extract LOSVDs using the FCQ algorithm with additional procedures to account for nebular emission and template mismatch. We recover  $v$ ,  $\sigma$ ,  $h_3$ , and  $h_4$  moments of a Gauss-Hermite model of the LOSVDs as function of radius.

We observe a great variety of shapes of kinematic profiles. Similar to Falcón-Barroso et al. (2006) and Ganda et al. (2006), we find that it is not necessarily true that the center of a bulge has the highest observed velocity dispersion (e.g. NGC3593). In our sample only  $\sim 1/3$  of the galaxies have centrally peaked velocity dispersion profiles (like NGC3898). Many galaxies have roughly flat velocity dispersion profiles. In these galaxies there is no apparent transition in velocity dispersion from the bulge to the disk region unlike as seen in the stellar surface brightness profile (e.g. NGC4448 and NGC5055).

It is interesting to note that to the radial extent of our data, in many of these cases the disk velocity dispersion is as high as the central velocity dispersion of the galaxy. For example in NGC4448 the disk velocity dispersion remains above  $100 \text{ kms}^{-1}$ . Therefore some disks of spiral galaxies are not necessarily cold stellar systems over the radii that we cover in this study.

We show in Fig. 4.7 that dispersion the profile shape correlates very well with bulge type. Galaxies with classical bulges have centrally peaked profiles. Galaxies with pseudobulges have — on average — flat dispersion profiles. We have attempted to quantify this using the logarithmic derivative of the velocity dispersion as function of radius (Eq. 4.3) and also the ratio of dispersions (Eq. 4.4). We find that pseudobulges and classical bulges occupy

different regions in the parameter space of logarithmic derivative of velocity dispersion and Sérsic index (see Fig. 4.8) — in a way that is not inconsistent with models of dynamically isotropic systems (Ciotti, 1991).

It is important to note that the dynamics of a few galaxies are not well described by a simple monotonic trend of velocity dispersion with radius; we stress that for the purpose of this paper we are interested in the bulk properties of the distribution of stellar dynamics. The great variety of shapes in dispersion profiles that we observe is likely to be a consequence of the fact that there are multiple ways to heat galactic disks, for example through mergers (van Albada, 1982), bars (Saha et al., 2010) and other disk instabilities (Sellwood & Wilkinson, 1993; Combes et al., 1990). Even under the strong assumption that classical and pseudobulges are dynamically distinct it does not seem plausible that any simple description of the kinematic profile cleanly separates classical from pseudobulges.

A few classical bulges such as NGC3992 do not seem to fit this general picture. Though, all those cases are barred and it is conceivable that bars may disturb the kinematic profile of a classical bulge as they vertically heat the disk they reside in (Gadotti & de Souza, 2005; Saha et al., 2010). Central velocity dispersions lie higher by a factor of two than at the bulge radius in the most extreme cases in our sample, e.g. NGC1023, NGC3898, NGC4203. If bars raise velocity dispersions by a factor of up to four as suggested by Saha et al. (2010), the signature of a central dispersion peak can of course easily be washed out.

A few outliers in Fig. 4.8 are worth to be discussed individually here: NGC4826 stands out as it has a relatively high Sérsic index of  $3.57 \pm 0.35$  for a pseudobulge. The V-band value of  $n = 3.94 \pm 0.68$  (Fisher & Drory, 2008) agrees well. The bulge radius of 18.3 arcseconds seems small once the kinematic data are taken into account. The velocity dispersion starts rising already at about 50 arcseconds which corresponds to the radius of the final flattening of the rotation curve. However, this galaxy has extreme amounts of dust in the bulge region — hence also its name *black eye* or *evil eye* galaxy — which is easily visible also in the infrared which may affect the decomposition. If one was to take the value of 50 arcseconds as the bulge radius then the  $\gamma$  value would become -0.33 (at 0.02 before) and the sigma ratio would take a value of 1.29 (at 0.96 before). This would move NGC4826 significantly further to the right in both plots into the region occupied by classical bulges — in much better agreement with the Sérsic index. Further the disk of NGC4826 is relatively free of dust and actually resembles more an S0. We hypothesize that the unusual morphology is a result of a recent merging event. A satellite may have fallen into an S0-like disk brought in dust and triggered star formation. This hypothesis is supported by the existence of two counter rotating gaseous disks observed by Braun et al. (1992, 1994). NGC3593 has a very large value of  $\gamma$  and a very small sigma ratio, i.e. it falls far to the left in both diagrams. This is a result of the strong depression in velocity dispersion in the bulge region. NGC3593 is the only galaxy in the sample where we observe actual counter rotation in the sense of a change of sign of the mean rotational velocity in the bulge region. The small Sérsic index of 0.81 supports the picture that the bulge region is dominated by a kinematically cold and distinct but luminous disk (Bertola et al., 1996). NGC2681 is classified as a pseudobulge by morphology and yet has a relatively large Sérsic index of  $n = 3.4$ . Further it has a centrally peaked dispersion profile with  $\gamma = -0.16$  and

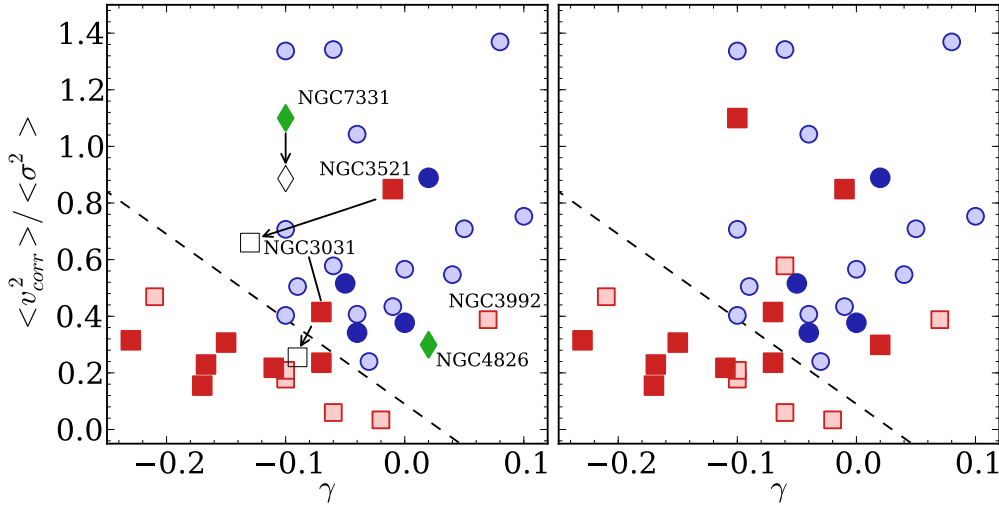


Figure 4.13 The bulge averaged quantity  $\langle v^2 \rangle / \langle \sigma^2 \rangle$  as function of the slope of the velocity dispersion,  $\gamma$ . The meaning of the symbols is the same as in Fig. 4.8. In the left panel we discriminate bulge types based on morphology. In the right panel we discriminate by Sérsic index (blue  $n \leq 2.1$ , red otherwise). For NGC3521, NGC3031, and NGC7331 we remeasure  $\gamma$  changing the outer radius cut to isolate only the central dispersion peak as described in the text. The corresponding new locations are marked as black open symbols.

$\delta = 1.19$ . This agreement of photometric structure and dispersion slope lets us revisit the morphological classification. While the disk shows relatively little amounts of dust a high contrast dust spiral within in the bulge — easily seen in HST F555W — offers a clear sense of rotation. Also the spiral is not obviously misaligned with the outer disk. This galaxy may represent a prototypical case for the breakdown of the morphological classification scheme. However, this galaxy shows multiple bars — possibly three (Erwin & Sparke, 1999) — and hence the central heating may also be a consequence of its complicated dynamical structure.

#### 4.6.2 Rotational Support

In order to study the level of rotational support of a stellar system, it has become common practice to study its location in the  $v_{max} / \langle \sigma \rangle$  vs.  $\epsilon$  diagram (Illingworth, 1977; Binney & Tremaine, 1987; Kormendy, 1993) — where  $v_{max}$  measures the maximum rotational velocity and  $\langle \sigma \rangle$  the averaged velocity dispersion within a certain radius and  $\epsilon$  the system's ellipticity. One can also directly compare  $v_{max} / \langle \sigma \rangle$  to the expected values of an oblate-spheroidal system with isotropic velocity dispersion. For instance, Kormendy (1982b) define the anisotropy parameter  $(v/\sigma)^* = (v_{max} / \langle \sigma \rangle) / \sqrt{\epsilon / (1 - \epsilon)}$  as a measure for the rotational support of a stellar system. Values of  $(v/\sigma)^* \simeq 1$  point towards a support

by rotation whereas values  $< 1$  indicate support by anisotropy. Those measures involve the ellipticity of the system which is typically subject to relatively large uncertainties — especially when measured for galaxies which are dominated by large quantities of dust. Here we decided to rather examine the local  $(v_{corr}/\sigma)(r)$  — i.e. as a function of radius — and the averaged values of  $\langle v_{corr}^2 \rangle / \langle \sigma^2 \rangle$  (Binney, 2005) across the bulge region,  $v_{corr} = v_{obs} / \sin(i)$  is the inclination corrected velocity at a given radius. We use inclinations from Hyperleda (see Tab. 4.1). We apply no further correction to the velocity dispersion.

In Fig. 4.14 we plot  $(v_{corr}/\sigma)(r)$  separately for classical and pseudobulges. We further plot histograms of the bulge-averaged quantities in Fig. 4.15. Again we normalize the radii by the bulge radius and exclude the central seeing FWHM from the analysis. While there is significant overlap between the two sub samples, pseudobulges are biased towards larger  $(v_{corr}/\sigma)(r)$ . This is especially seen in the histograms for the averaged values. A Kolmogorov-Smirnov test (Smirnov, 1939; Press, 2002) yields a probability of 0.2% (0.3%) for the classical and the pseudo bulges in the full (non-barred) sample to stem from the same distribution. A students two-tailed t-test for two independent samples yields a probability of 0.2% (0.4%) for the classical and the pseudo bulges in the full (non-barred) sample. This result supports a picture of increased rotational support of pseudobulges that was originally described by Kormendy (1993) and discussed in detail in Kormendy & Kennicutt (2004), see also Kormendy & Fisher (2008).

While the average values of  $\gamma$  and  $\langle v^2 \rangle / \langle \sigma^2 \rangle$  are different for classical and pseudobulges, neither of the two quantities separates the bulge types. In Fig. 4.13 we combine both and plot  $\langle v^2 \rangle / \langle \sigma^2 \rangle$  against the logarithmic slope of the velocity dispersion,  $\gamma$ , for the bulges in our sample. In the left panel we discriminate bulges morphologically and in the right based on the bulge Sérsic index. The dashed line is drawn to contain all the pseudobulges. Classical bulges both tend to have low  $\langle v^2 \rangle / \langle \sigma^2 \rangle$  and steeper negative slopes than pseudobulges.

There are 3 galaxies with high Sérsic index that fall dynamically into the region of pseudobulges (NGC7331, NGC3521 and NGC3031; the latter two also have classical bulge like morphology). Nonetheless all three of these galaxies, have centrally peaking velocity dispersion profiles but they also have a subsequent rise in velocity dispersion at larger radius (see Appendix A), yet still within the radius of the bulge. This behaviour is not what we observe in pseudobulges, which have flat dispersion profiles. None of these three galaxies violate the general dichotomy observed in Fig. 4.7. Therefore it is likely that their location in the  $v/\sigma$  vs.  $\gamma$  plane is due to a failure in the machinery of measuring dynamical quantities. NGC7331 and NGC3521 both show signs of counter rotating components and NGC3031 is well known to be interacting. It is possible in each of these galaxies that an outside mechanism is superimposing an extra kinematic component that is visible as secondary rise in the velocity dispersion profile of the bulge. In NGC3521 and NGC3031 we remeasure  $\gamma$  changing the outer radius cut isolating only the central dispersion peak. In the case of NGC3031 this moves the measured dynamical quantities into the region of parameter space that is only occupied by classical bulges, NGC3521 moves significantly closer, it makes little difference in the case of NGC7331.

Fig. 4.13 illustrates for the first time agreement between kinematic diagnostics of the

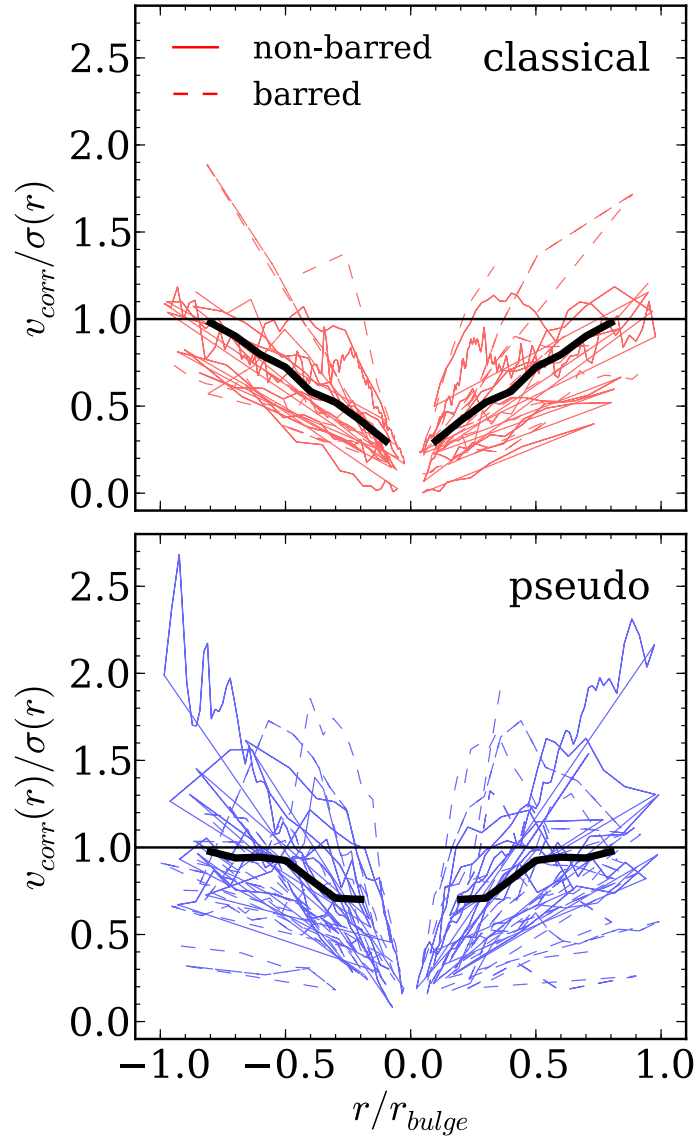


Figure 4.14 Local  $(v_{corr}/\sigma)(r)$  along the major axis, the radii are normalized by bulge radius. The velocities are corrected for inclination through  $1/\sin(i)$ . Classical bulges are plotted in the upper panel, pseudobulges in the lower panel. The solid black line marks the median of all profiles.

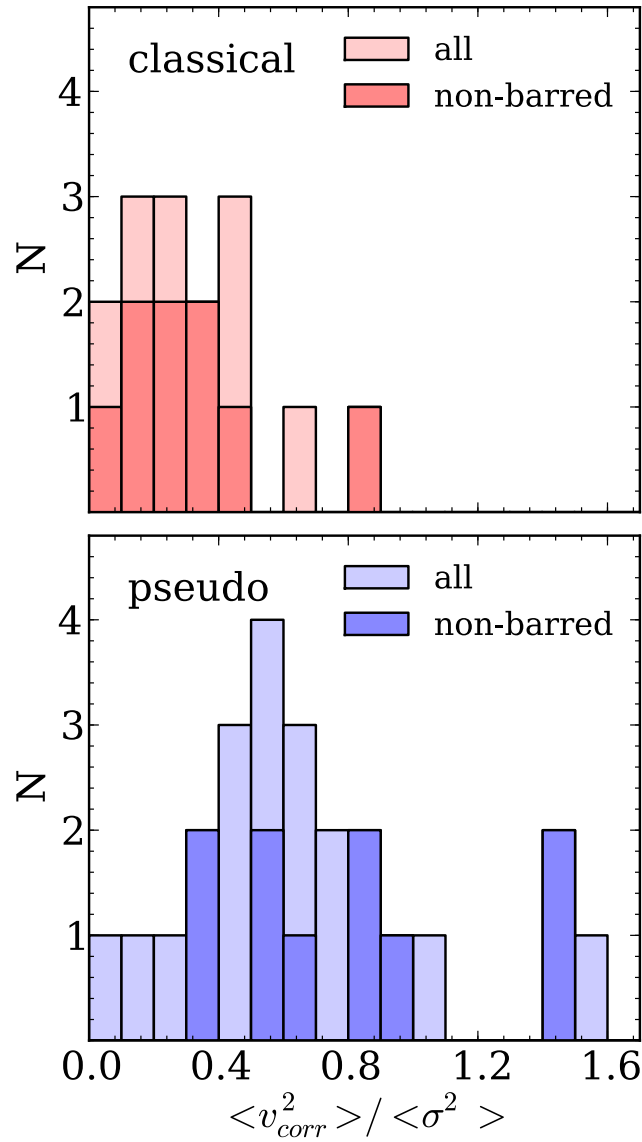


Figure 4.15 Histograms for the averaged values of  $\langle v^2 \rangle / \langle \sigma^2 \rangle$  (Binney, 2005). The velocities are corrected for inclination through  $1/\sin(i)$ . Classical bulges are plotted in the upper panels, pseudobulges in the lower panels.

bulge dichotomy with structural and morphological indicators of bulge types.

### 4.6.3 Multiple Kinematic Components

We observe counter rotation — seen in the full shape of the LOSVD — in five systems. It is striking how clearly the LOSVDs can be decomposed into a small dispersion and a high dispersion component in all cases. It is tempting to interpret the latter as the bulge and the former as the disk. However, if we plot the local disk to total ratios as obtained from the photometric decomposition over the values obtained from the kinematic decomposition (respective upper panels of Fig. 4.11), then we see that the disk contribution from the photometry falls short in all cases. I.e. the observed small dispersion component within the bulge region is not simply the extension of the outer disk as more light contributes to this component as one would expect from the extrapolation of the outer disk exponential profile alone. It is important to point out that a Gauss-Hermite distribution with moderate  $h_3$  moments can be modelled rather well by two individual Gaussians.  $h_3$  moments though, occur for instance naturally in disks (Binney & Tremaine, 1987) and are not a signature of an actual second component. Only in cases where the second component is clearly seen as a second peak in the LOSVD it is safe to assume that actually two distinct components contribute.

## 4.7 Summary

In this paper we present kinematic profiles for the major axis of 46 intermediate type galaxies. Our survey differs from other similar surveys in that we are able to resolve lower velocity dispersions which allows us to study kinematic features in cold systems like disks and pseudobulges. We combine these data with bulge to disk decompositions of the stellar light.

We find that bulges that have increased rotational support, as measured by larger values of  $\langle v^2 \rangle / \langle \sigma^2 \rangle$ , are likely to have lower Sérsic indices and show disk-like morphology.

Classical bulges on average tend to have higher central velocity dispersions than pseudobulges. In our sample the lowest central velocity dispersion in a galaxy with evidence for a classical bulge through a Sérsic index of 3.5 is  $\sigma_{r_e/10} = 85 \pm 2 \text{ kms}^{-1}$  (NGC7743).

We observe a correlation between the shape of the velocity dispersion profile and the bulge type as indicated by the Sérsic index and/or morphology. Classical bulges have centrally peaked velocity dispersion profiles, in general pseudobulges have flat dispersion profiles and even at times show drops in the central velocity dispersion. We observe that the disk regions of some of our galaxies have not always a low velocity dispersion. In some galaxies the velocity dispersion remains above ( $100 \text{ kms}^{-1}$ ) well into the region where the disk dominates the light.

We confirm the previously described multicomponent nature of NGC3521 (Zeilinger et al., 2001), NGC7217 Merrifield & Kuijken (1994) and NGC7331 (Prada et al., 1996) and find two additional systems — namely NGC3945 and NGC4736 — with signatures

of multiple kinematic components. They become apparent through a secondary peak or pronounced shoulder in the full line of sight velocity distributions (LOSVD) as derived from the kinematic fitting procedure. We present double Gaussian decompositions for all those systems.

As in elliptical galaxies (Bender et al., 1994), we find a correlation of  $h_3$  and  $v/\sigma$ , both locally as well as in the bulge averaged quantities. We observe no correlation of the higher moments with bulge luminosity, however we find a weak correlation between the average values of  $h_4$  and  $v/\sigma$ .

Through examination of the figures in Appendix A it is clear that the kinematic profiles of bulge-disk galaxies commonly contain substructure. Furthermore non-axisymmetric features in the stellar structure such as bars make understanding the kinematics of these galaxies more difficult. Future progress in understanding the kinematics of bulges will require 2D-methods capable of resolving low velocity dispersions commonly found in pseudobulges. We are currently executing such a survey using the VIRUS-W spectrograph (Fabricius et al., 2008).

## Acknowledgments

We would like to thank Luca Ciotti for providing velocity dispersion profiles for the isotropic models presented in his 1991 paper. We wish to thank Jesus Falcon Barroso of the SAURON collaboration who made kinematic maps of a number of the galaxies available to us in various formats which allowed for a detailed comparison of our data. We also wish to acknowledge the help of Gaelle Dumas who provided SAURON data from his 2007 paper. We thank Peter Erwin for many fruitful discussions and his valuable comments. We would also like to express our gratefulness to the efforts of the observing staff at the Hobby-Eberly Telescope (HET). Over the years of the duration of this survey they have constantly provided high quality data, give very valuable background information and have always been very helpful and approachable concerning technical aspects of the data. The Hobby-Eberly Telescope (HET) is a joint project of the University of Texas at Austin, the Pennsylvania State University, Stanford University, Ludwig-Maximilians-Universitaet Muenchen, and Georg-August-Universitaet Goettingen. The HET is named in honor of its principal benefactors, William P. Hobby and Robert E. Eberly. The Marcario Low Resolution Spectrograph is named for Mike Marcario of High Lonesome Optics who fabricated several optics for the instrument but died before its completion. The LRS is a joint project of the Hobby-Eberly Telescope partnership and the Instituto de Astronomia de la Universidad Nacional Autonoma de Mexico. The grism E2 used for these observations has been bought through the DFG grant BE1091/9-1. This work was supported by the SFB-Transregio 33 *The Dark Universe* by the Deutsche Forschungsgemeinschaft (DFG). This research has made use of the NASA/IPAC Extragalactic Database (NED) which is operated by the Jet Propulsion Laboratory, California Institute of Technology, under contract with the National Aeronautics and Space Administration. Some/all of the data presented in this paper were obtained from the Multimission Archive at the Space

Telescope Science Institute (MAST). STScI is operated by the Association of Universities for Research in Astronomy, Inc., under NASA contract NAS5-26555. Support for MAST for non-HST data is provided by the NASA Office of Space Science via grant NAG5-7584 and by other grants and contracts. We acknowledge the usage of the HyperLeda database (<http://leda.univ-lyon1.fr>) (Paturel et al., 2003).

# Chapter 5

## Summary & Conclusions

### VIRUS-W

We discuss the construction and commissioning of a fiber based integral field unit (IFU) spectrograph named VIRUS-W. The development of this instrument was originally initiated as part of the instrumentation efforts for the new 2 m Fraunhofer telescope on the mountain Wendelstein in the Bavarian Alps. As this instrument was completed before the telescope, we commissioned VIRUS-W for a temporary stay at the 2.7 m Harlan J. Smith telescope of the McDonald Observatory in Texas.

The instrument is specifically designed for the study of stellar and gaseous kinematics in local disk galaxies. Its IFU offers a relatively large field of view with  $105'' \times 55''$  on sky and the spectral resolution lies at  $R \simeq 8700$ . At this resolution velocity dispersions down to  $15 \text{ km s}^{-1}$  can be resolved. This approaches the regime at which stars are thought to form in gaseous disks. This stellar dynamics mode is optimized for throughput in the Mg-triplet region and the spectral coverage reaches from  $4850 \text{ \AA}$  to  $5480 \text{ \AA}$ , whilst with a strong drop-off of throughput at the ends of this range.

An additional lower resolution mode ( $R \simeq 3300$ ) aimed at the study of stellar populations gives access to a larger wavelength range of  $4340 \text{ \AA}$  to  $6040 \text{ \AA}$ . This covers a larger number of absorption features — most importantly  $\text{H}_\beta$  at large throughput — sufficient to determine age, metallicity and over-abundances.

The individual fiber cores have a diameter of  $150 \mu\text{m}$  which translates to  $2.3''$  on sky at a 2.7 m aperture and a beam of  $f/3.65$ . The fibers are sparsely packed with a fill factor of  $1/3$ . The large fiber apertures significantly undersample the typical seeing disks. But, as they integrate over larger amounts of signal, they result in high sensitivity, giving access to low surface brightness regimes and the coarse sampling is generally acceptable for the science cases which this instrument is intended for.

We commissioned VIRUS-W in November and December 2010. We were able to verify the instrumental resolution using spectral calibration lines and actual stellar spectra. Through observations of spectrophotometric standards we determine the throughput of both resolution modes. Our measurements indicate that the throughput of the stellar

dynamics mode reaches a peak of 37% which is somewhat larger than the value that we expect from the propagation of the efficiency of the individual optical elements. Reasons may lie in a slight overfilling of the IFU, stray light, limited accuracy of the CCD electronics gain estimate, and — most likely — too pessimistic assumptions for the individual element efficiencies. However the difference is small with 7%.

The low resolution mode's efficiency falls with 40% about 10% short of the expectation. We strongly suspect that this is due to an inaccurate setting of the grating angle which will have to be verified in a future run.

During the commissioning we observed a library of 18 stellar spectra, 12 of which are giant stars and are suitable for the derivation of stellar kinematics in multiple-template fitting algorithms. All stars are contained in the Lick/IDS library. We derive index strengths for all stars and compare them to the Lick values. We show that — after the usual linear corrections — we are able to put our measurements on the Lick system and hence are able to compare those values to the predictions from stellar population synthesis codes.

Finally, we obtained data for several galaxies including the spiral galaxy NGC2903, the elliptical NGC3091, and the dwarf galaxy NGC205. For those objects we derive line of sight velocities, velocity dispersions and the Gauss-Hermite moments  $h_3$  and  $h_4$  as a function of position. Through comparison with literature values we show that we are able to reproduce the low velocity dispersion of  $20 \text{ km s}^{-1}$  in the nucleus of NGC205 accurately.

NGC3091 was observed with the stellar population mode of VIRUS-W. In addition to the LOSVDs, we measure the strength of the Lick absorption line indices that fall into the covered wavelength range. A tentative comparison of a single stellar population fit assuming a Kroupa initial mass function with results from three-integral dynamical modelling shows a reasonable agreement in the recovered stellar mass-to-light ratio.

## HET Longslit Kinematic Survey

The light concentrations that are often seen in the centers of lenticular and spirals galaxies are often referred to as bulges. This is largely motivated by the observation that in many highly inclined or edge-on disks contain a central stellar component that protrudes far out above the disk. Candidate processes for the formation of these components merging events which — while keeping the out disk regions intact — destroy the inner regions and result in spherical, high dispersion components, and clump coalescence — the sinking of gas clumps into the central regions during the early evolutionary phases (Elmegreen et al., 2008).

Pseudobulges however, are thought to be much more disk-like. They are still apparent as *extra light* above the inwards extrapolation of the outer exponential disk profile, however they are thought to be flattened systems that are primarily supported by rotation. Many central regions of galaxies do show disk-features such as nuclear bars, rings, patchy star formation and spiral structure. Fisher & Drory (2008, 2010) showed that the Sérsic index differentiates between classical bulges and pseudobulges. Pseudobulges have Sérsic indices that are smaller than two and therefore light distributions that are more similar to that of an exponential disk. Kormendy & Kennicutt (2004) suggested that pseudobulges are most

likely secularly evolved systems.

We discuss and present results of a longslit kinematic survey of local spiral bulges that we conducted using the LRS spectrograph at the Hobby-Eberly-Telescope at the McDonald Observatory. We present major axis data for 46 S0 to Sc type galaxies and minor axis data for a subset of 28 galaxies. We systematically investigate whether the morphological and structural differences that are seen between classical and pseudobulges are reflected in their kinematics as well.

The variety that we observed in the kinematic profiles is large. We find however that pseudobulges generally have flatter slopes of the velocity dispersion profiles as measured by the logarithmic derivative of dispersion as function of radius. We find agreement between the Sérsic index and the dispersion slope as such that flat dispersion profiles occur preferentially in systems with low Sérsic indices and vice versa. We also find that pseudobulges occur preferentially in galaxies with low central velocity dispersions, and show lower averaged ratios of rotational velocity to velocity dispersion indicating a larger degree of rotational support.

However, we do see as well that bars seem to disturb this general picture. It is conceivable that through resonances and buckling instabilities, bars may increase the vertical dispersion of a disk and therefore destroy the signatures seen in the dispersion slope. It would be very interesting to investigate whether a systematic difference in velocity dispersions for regions inside bars and outside bars exists.

Major and minor slit observations however will necessarily cut at an arbitrary angle through bars. It is then unclear whether a rise that is observed in dispersion is due to the bar or the bulge. The additional occurrence of substructure complicates the interpretation of one-dimensional data. This motivates the construction of a dedicated instrument that is able to recover low velocity dispersions in two spatial dimensions.

## Outlook

During the first year after the successful commissioning of VIRUS-W proposals using this instrument were already awarded with a total of 70 nights by the McDonald Observatory time allocation committee. Projects concern themselves with the dynamics in almost all types of galaxies. We have collected data on elliptical and lenticular galaxies that will augment adaptive optics assisted SINFONI observations by our group, which try to determine the mass of the central black hole. Other projects study the kinematics of individual stars in dwarf galaxies, and the integrated stellar kinematics in low surface brightness galaxies to constrain the central slope of their dark matter halo.

We seek to continue the study of stellar and gaseous dynamics in disk galaxies. Our longslit survey showed that massive spirals exist where the dispersion in the disk region reaches values comparable to, or is lower than the instrumental dispersion of the LRS spectrograph (e.g. NGC4826). VIRUS-W will likely be able to resolve these low dispersions. We also saw that reliable measurements of the asymmetric deviations of the LOSVDs require even larger instrumental resolutions. VIRUS-W will be able to measure  $h_3$  and  $h_4$

moments in systems that we could not address before.

Datasets that were obtained since the commissioning run already contain several galaxies with bars. Based on those we can study the variation of the LOSVDs across these features and in the radial ranges of the expected resonances. The data may also lead to a measurement of the pattern speeds in these galaxies — the first such measurement based on stellar kinematics obtained with an IFU instrument.

Only a handful of systems are known to host counter rotating stellar components so far. The low number of known systems however, is probably primarily caused by the difficulty of their detection. However, their frequency and phase space structure may have strong implications for the understanding of disk formation. We have collected data on several galaxies for which previous studies established counter-rotating stellar components. Those works — including our own — were limited to the major axis in those systems. Double gaussian decompositions had no independent estimate of the width of the dispersion. The second spatial dimension will put a much firmer constraint on the fitted parameters and increase the detectability of such a second component.

The VENGA project (PI: Guillermo Blanc) has been observing 32 spiral galaxies with the sister instrument VIRUS-P. While, with a spectral resolution of  $R = 800$ , VIRUS-P will not resolve the dispersions in most of those objects, this additional dataset adds large spectral coverage which will give firm constraints on the composing stellar population. VIRUS-W is already following up those observations and will add kinematic information to that survey.

# Appendix A

## Kinematic profiles

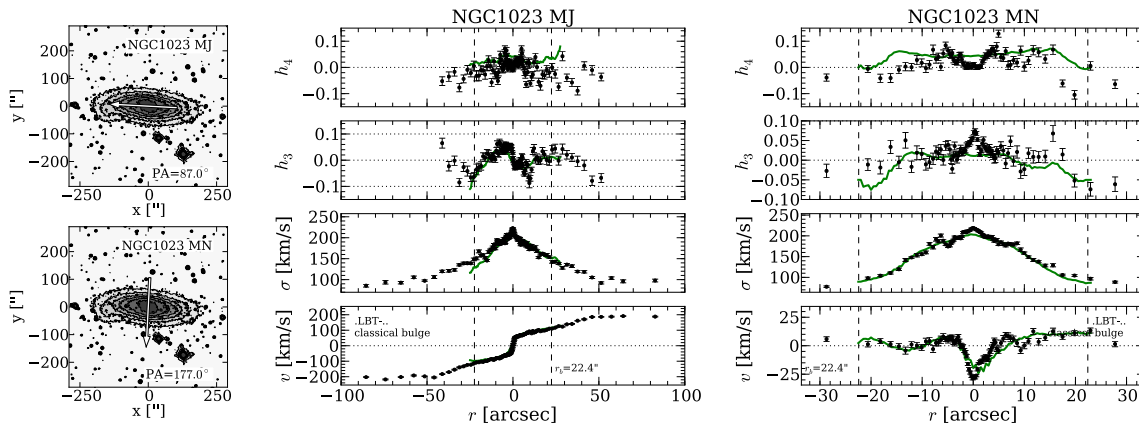


Figure A.16 Major and minor axis kinematic profiles for NGC1023. The slit position is indicated as arrow on a Digital Sky Survey image on the left. Positive radii are east of the galaxy center. We plot from bottom to top the rotational velocity, velocity dispersion,  $h_3$  and  $h_4$  moments. Vertical lines indicate the bulge radius. We plot SAURON results of Emsellem et al. (2004) in green. We matched our minor axis velocities to the SAURON velocity map by allowing an offset of the slit position. A 2 arcseconds offset to the west yielded the smallest residuals between the SAURON velocities and ours.

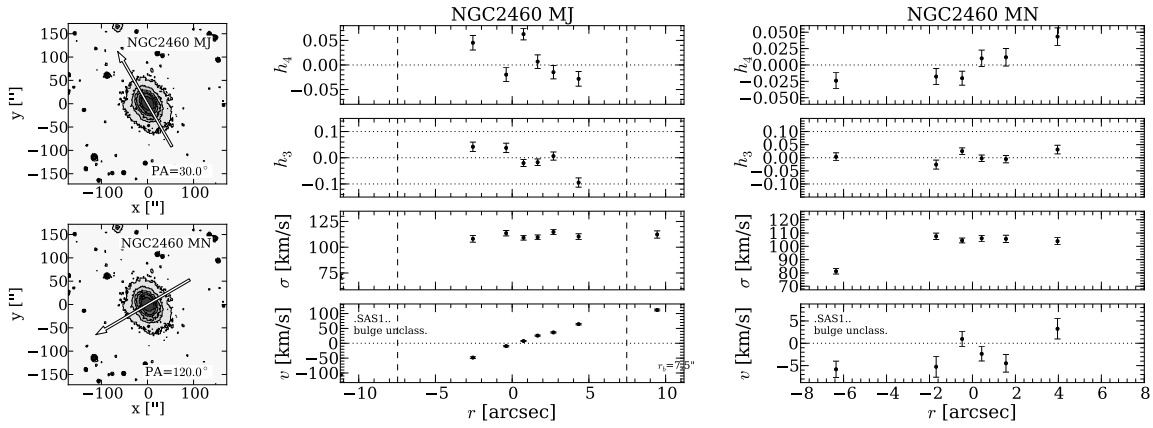


Figure A.16 *continued* – Major and minor axis kinematic profiles for NGC2460.

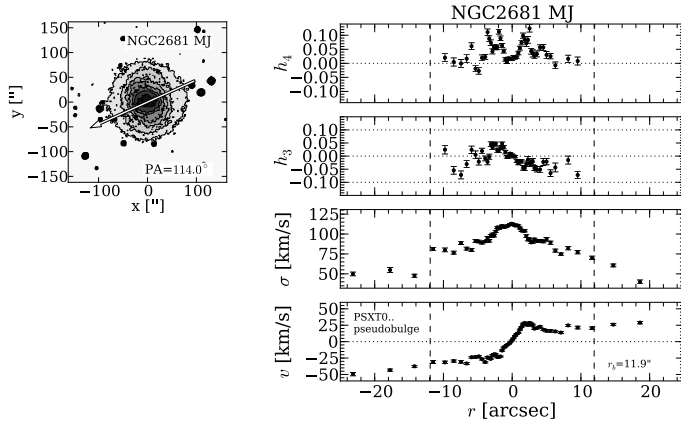


Figure A.16 *continued* – Major axis kinematic profile for NGC2681.

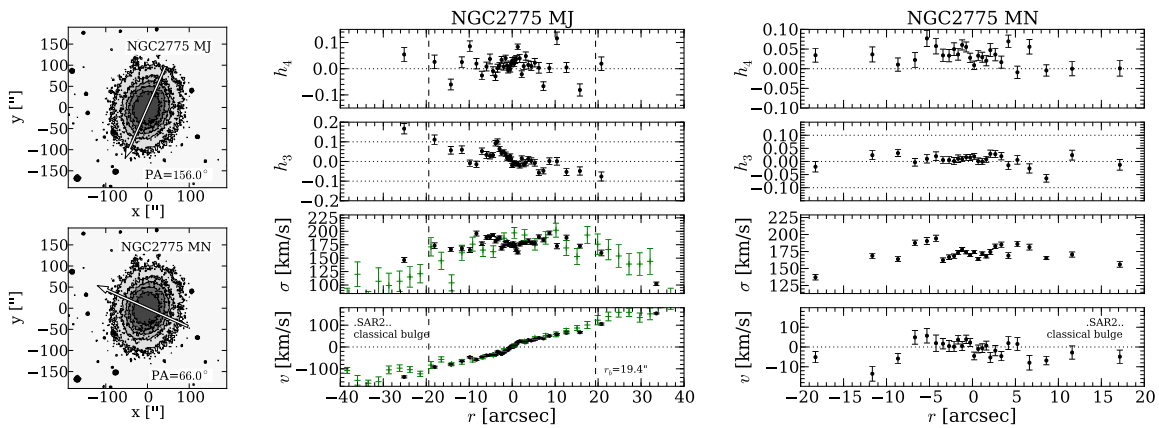


Figure A.16 *continued* – Major and minor axis kinematic profiles for NGC2775. We plot results of Corsini et al. (1999) in green.

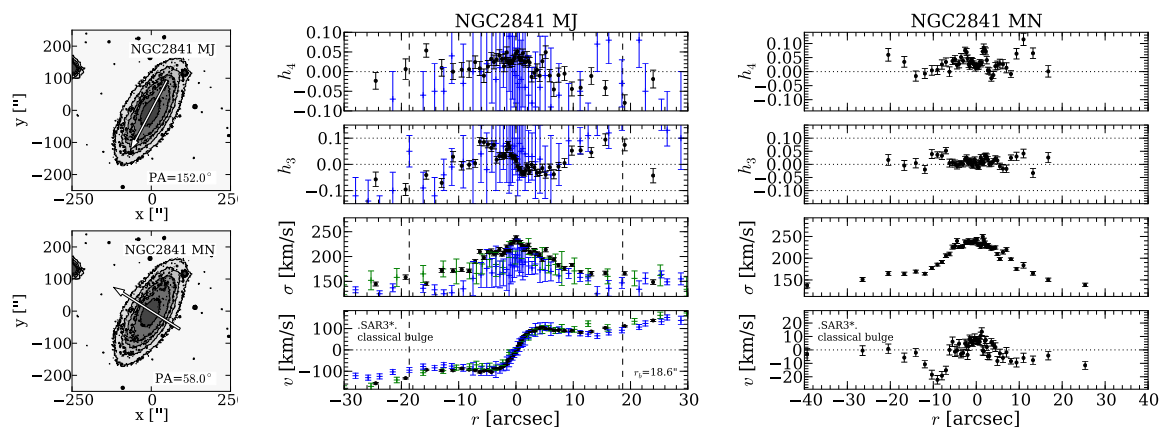


Figure A.16 *continued* – Major and minor axis kinematic profiles for NGC2841. We plot results of Héraudeau & Simien (1998) in green and those of Vega Beltrán et al. (2001) in blue.

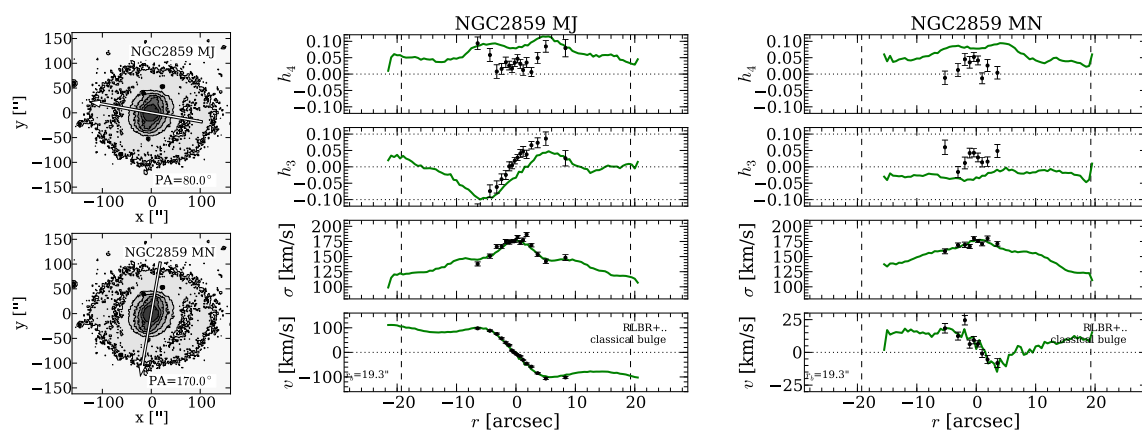


Figure A.16 *continued* – Major and minor axis kinematic profiles for NGC2859. We plot the SAURON results (de Lorenzo-Cáceres et al., 2008) in green.

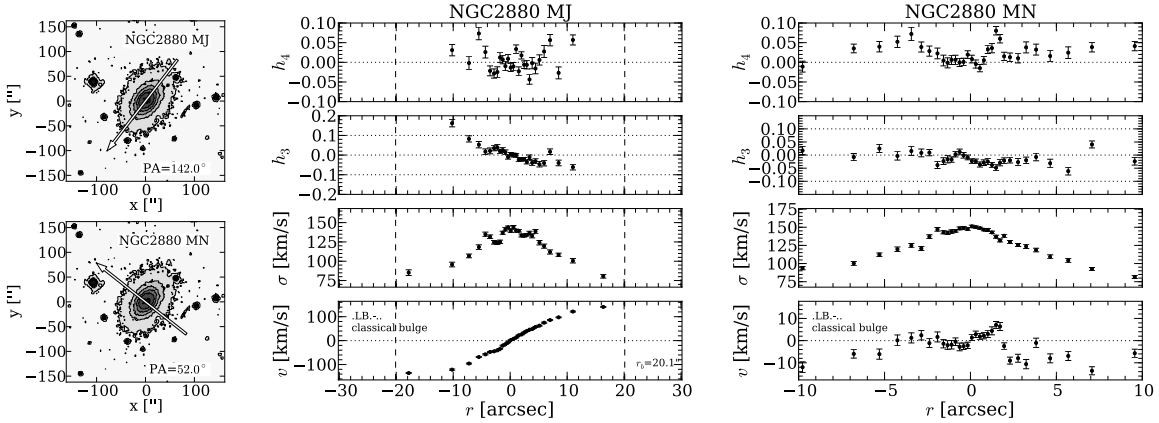


Figure A.16 *continued* – Major and minor axis kinematic profiles for NGC2880.

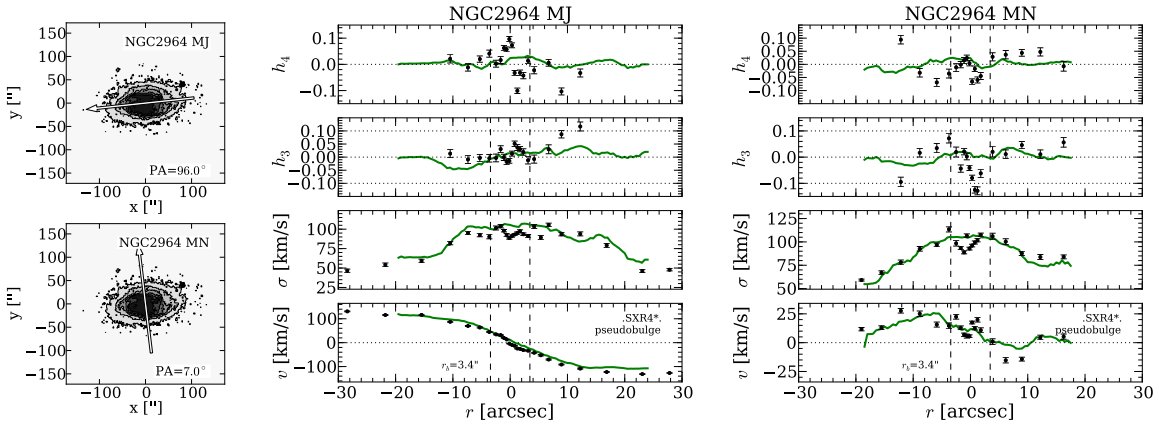


Figure A.16 *continued* – Major and minor axis kinematic profiles for NGC2964. We plot the SAURON results (Ganda et al., 2006) in green.

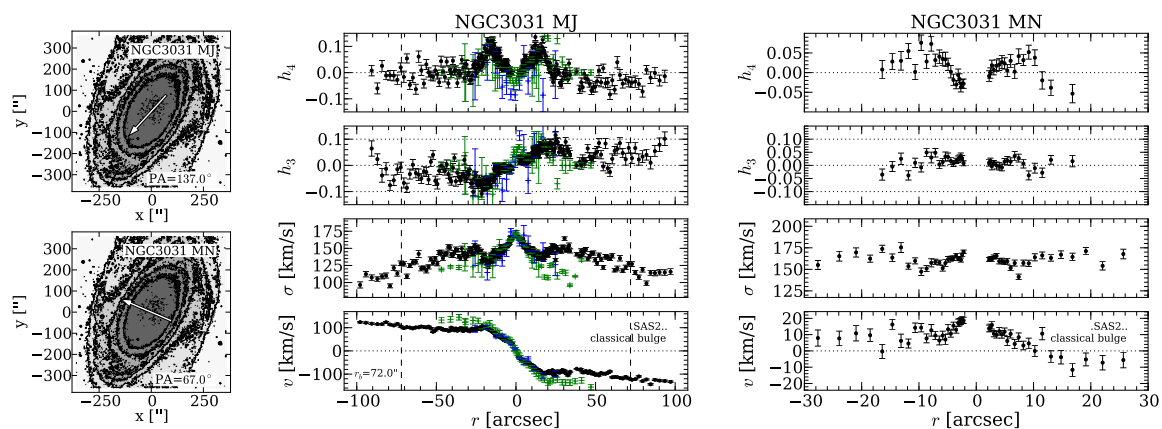


Figure A.16 *continued* – Major and minor axis kinematic profiles for NGC3031. Prominent central emission features connected to a liner type activity prevent us from deriving the central kinematics ( $r \pm 2$  arcseconds) reliably. We do not publish moments within the affected radius. We plot results of Vega Beltrán et al. (2001) in green and those of Bender et al. (1994) in blue. The data of Vega Beltrán et al. (2001) were taken with a slit position angle of  $157^\circ$  whereas we observed at a position angle of  $137^\circ$  which is responsible for the offset seen in velocity.

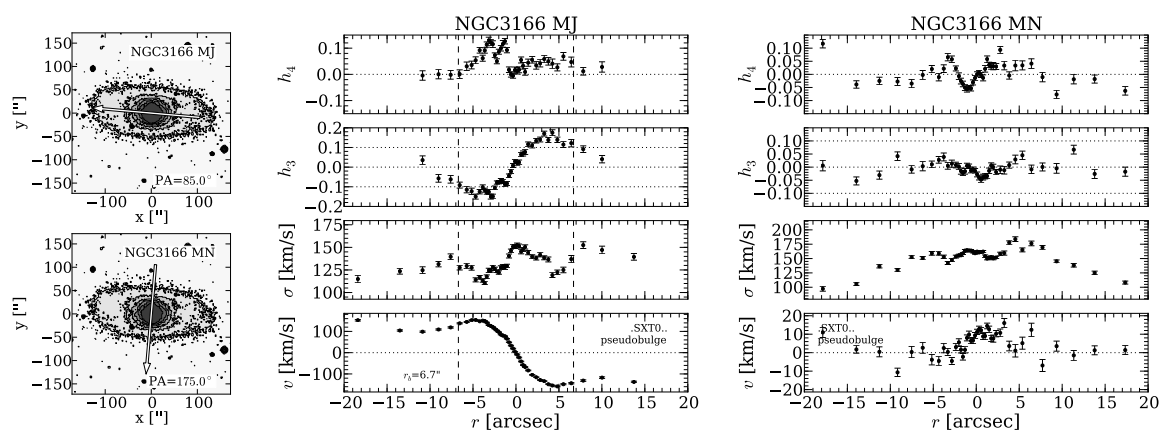


Figure A.16 *continued* – Major and minor axis kinematic profiles for NGC3166.

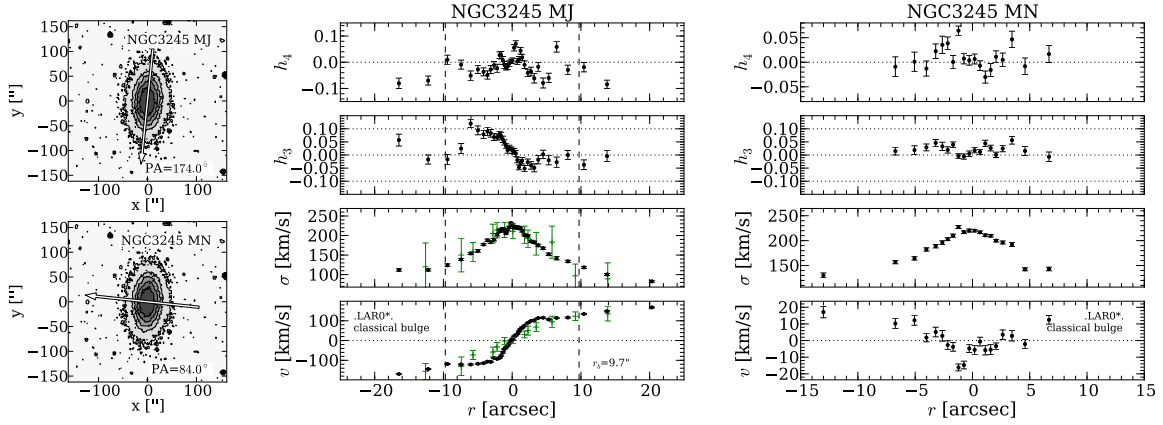


Figure A.16 *continued* – Major and minor axis kinematic profiles for NGC3245. We plot results of Simien & Prugniel (1998) in green.

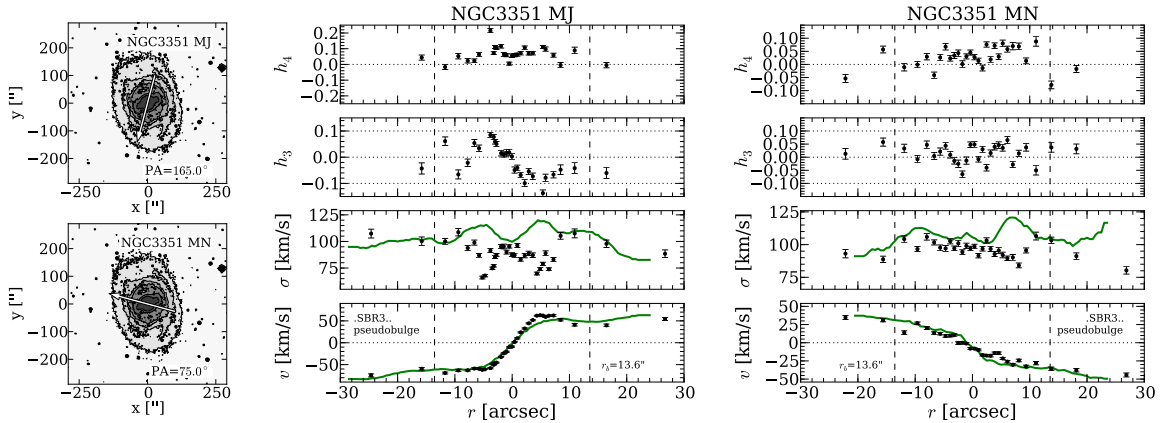


Figure A.16 *continued* – Major and minor axis kinematic profiles for NGC3351. We plot SAURON results of Dumas et al. (2007) in green.

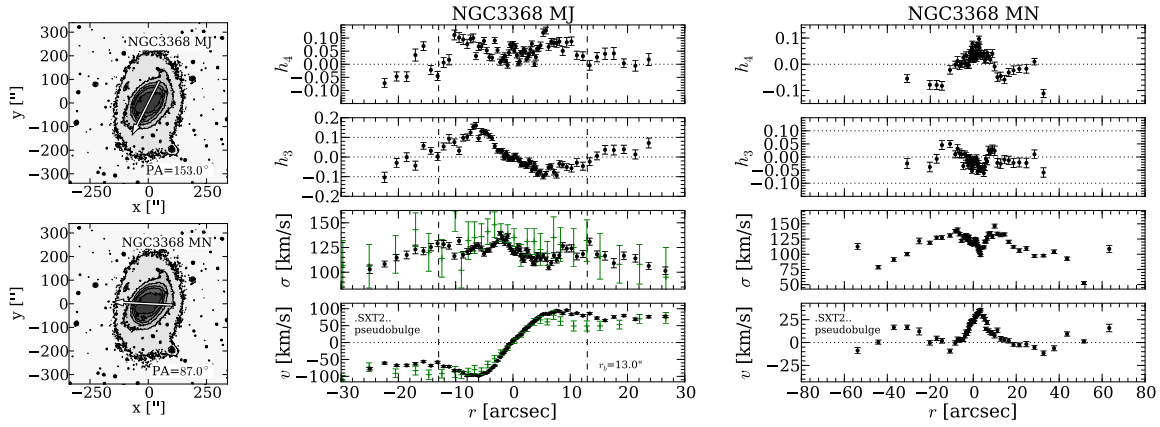


Figure A.16 *continued* – Major and minor axis kinematic profiles for NGC3368. We plot data from Héraudeau et al. (1999) in green.

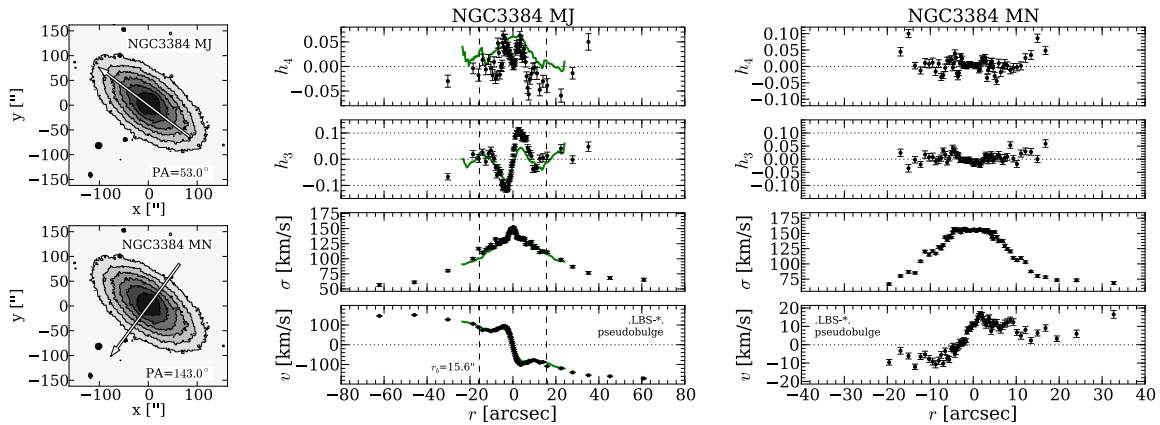


Figure A.16 *continued* – Major and minor axis kinematic profiles for NGC3384. We plot SAURON results of Emsellem et al. (2004) in green.

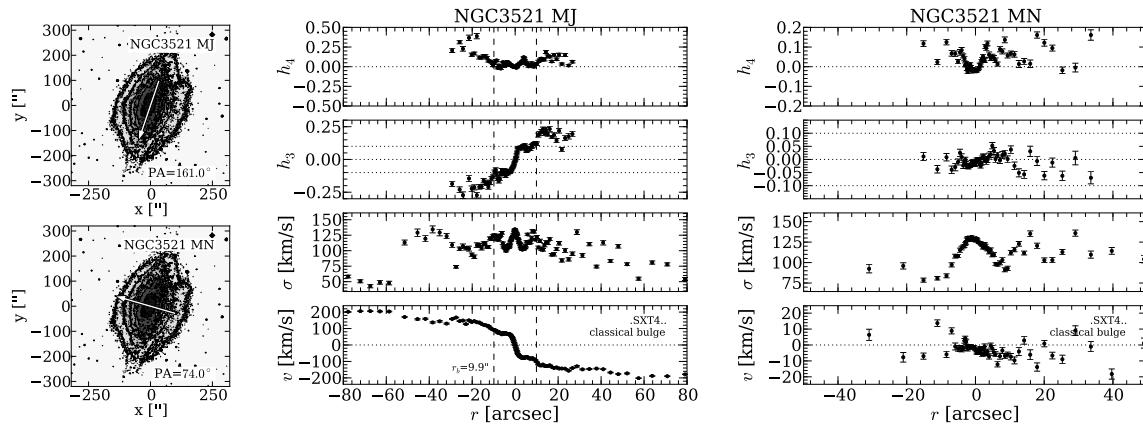


Figure A.16 *continued* – Major and minor axis kinematic profiles for NGC3521, see also figures 4.12 and 4.11.

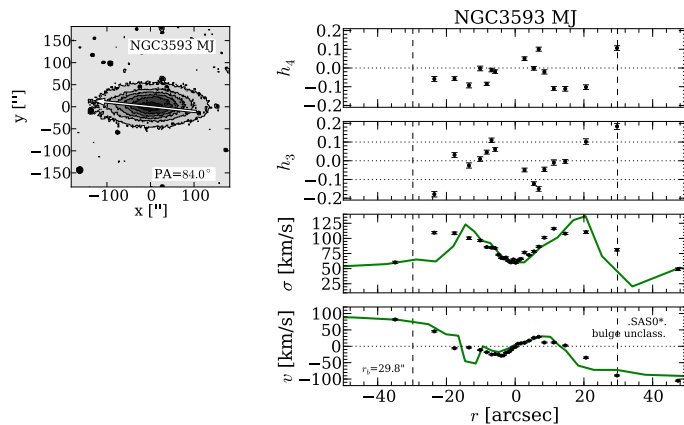


Figure A.16 Major axis kinematic profile for NGC3593, we plot the results of Bertola et al. (1996) in green.

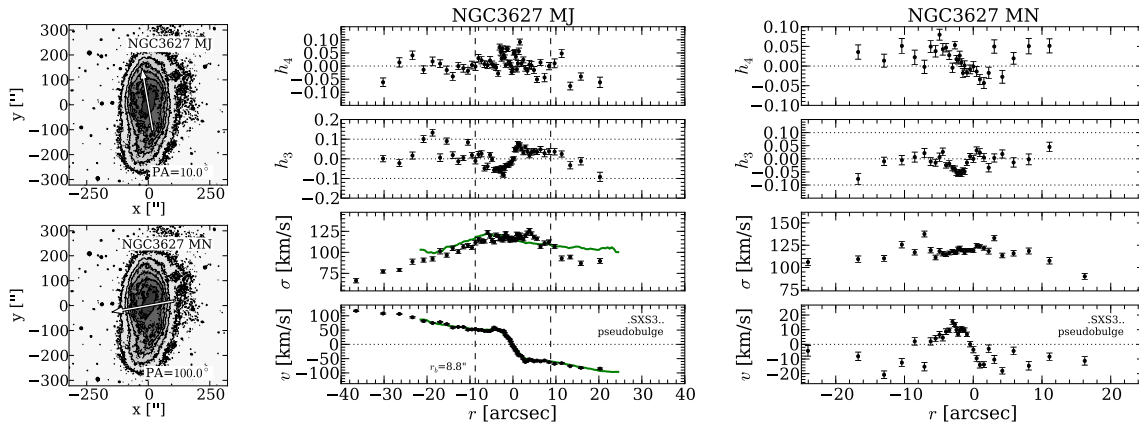


Figure A.16 *continued* – Major and minor axis kinematic profiles for NGC3627. We plot data of Héraudeau & Simien (1998) in green. Note: Their data were taken at a slit position angle of  $173^\circ$  whereas our adopted value for the major axis position angle is  $10^\circ$ .

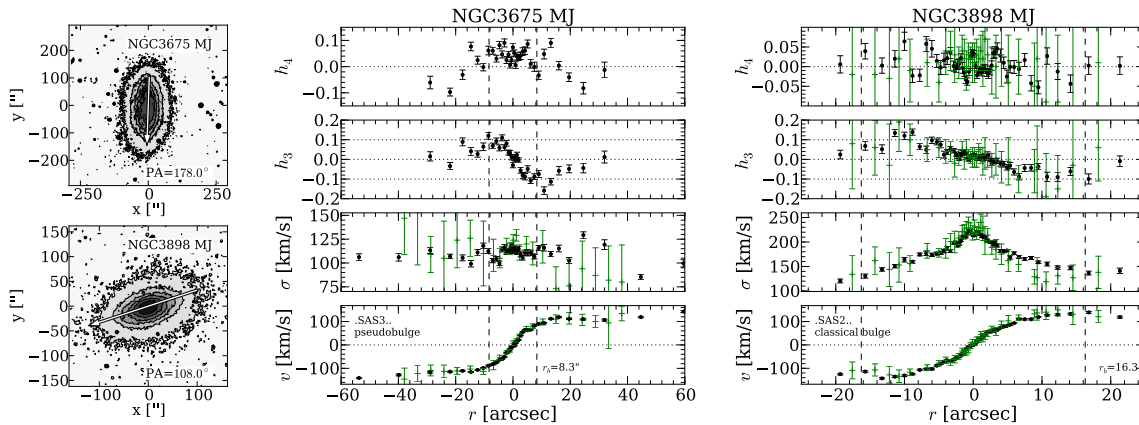


Figure A.16 *continued* – Major axis kinematic profiles for NGC3675 and NGC3898 we plot the results of Héraudeau & Simien (1998) and Pignatelli et al. (2001) in green.

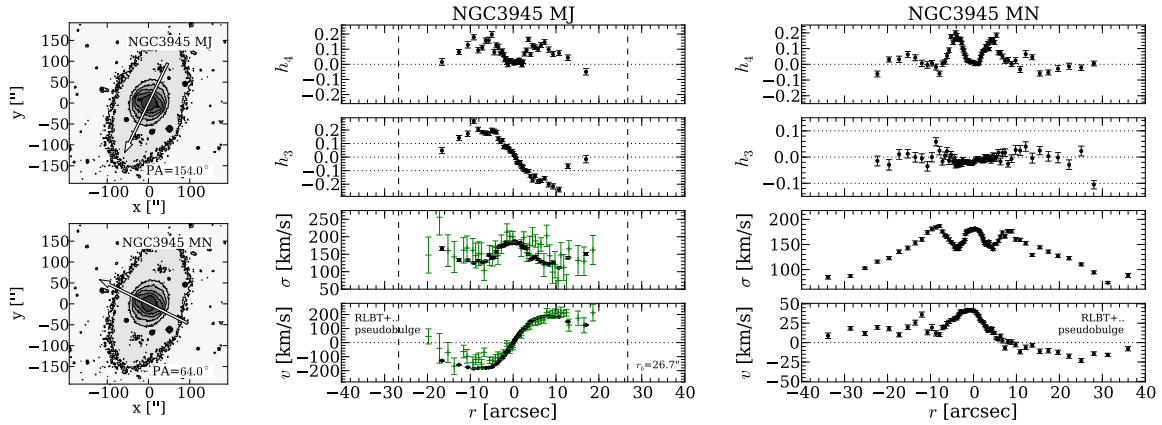


Figure A.16 *continued* – Major and minor axis kinematic profiles for NGC3945, see also Fig. 4.11. We plot data from Bertola et al. (1995) in green.

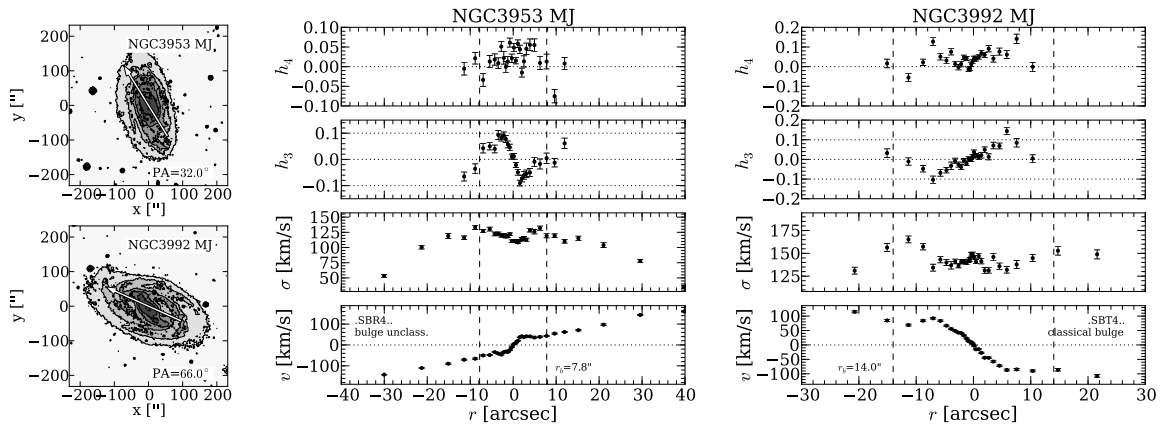


Figure A.16 *continued* – Major axis kinematic profiles for NGC3953 and NGC3992.

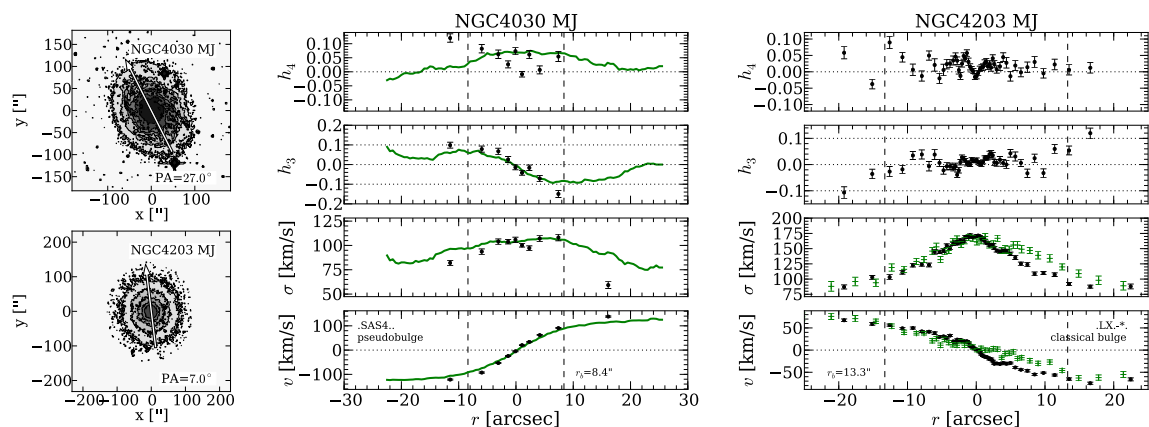


Figure A.16 Major axis kinematic profiles for NGC4030 and NGC4203. For NGC4030 plot the SAURON results of Ganda et al. (2006), and for NGC4203 the results of Simien & Prugniel (2002) in green. The latter were taken at a position angle of  $30^\circ$  which is quite different from our adopted value for the major axis position angle of  $7^\circ$ . The difference in velocity and dispersion seen on the east side is probably explained by this.

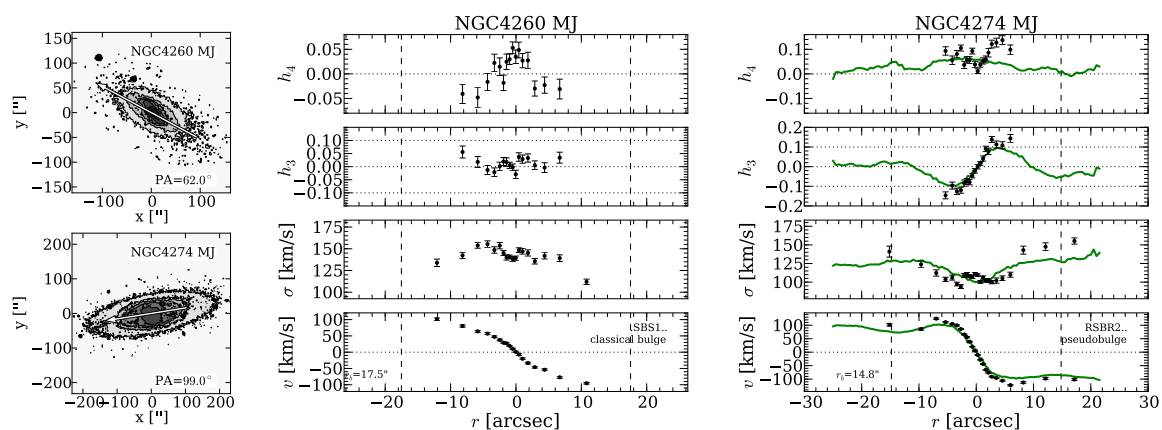


Figure A.16 *continued* – Major axis kinematic profiles for NGC4260 and NGC4274. For NGC4274 we plot the SAURON results (Falcón-Barroso et al., 2006) in green.

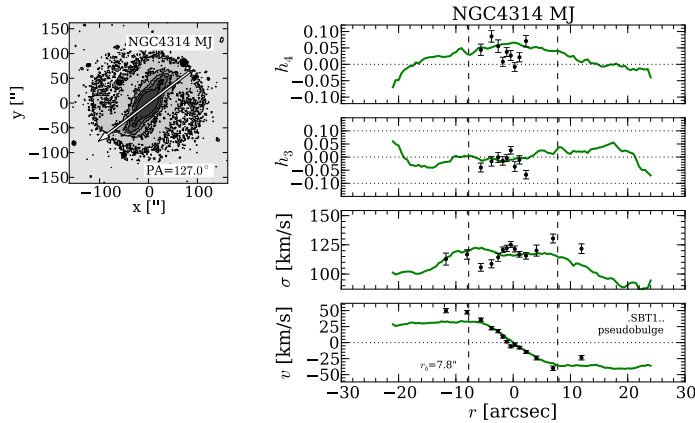


Figure A.16 *continued* – Major axis kinematic profile for NGC4314. We plot the SAURON results (Falc3n-Barroso et al., 2006) in green.

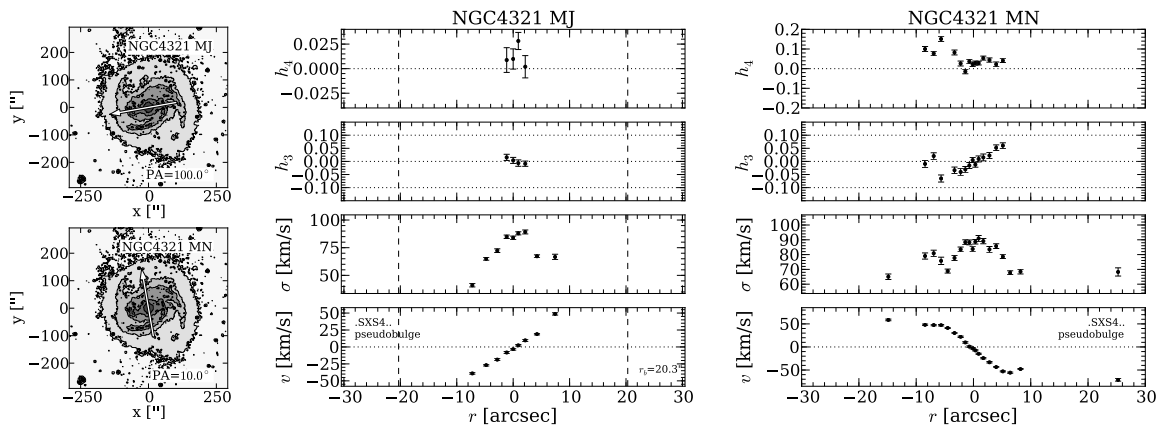


Figure A.16 *continued* – Major and minor axis kinematic profiles for NGC4321.

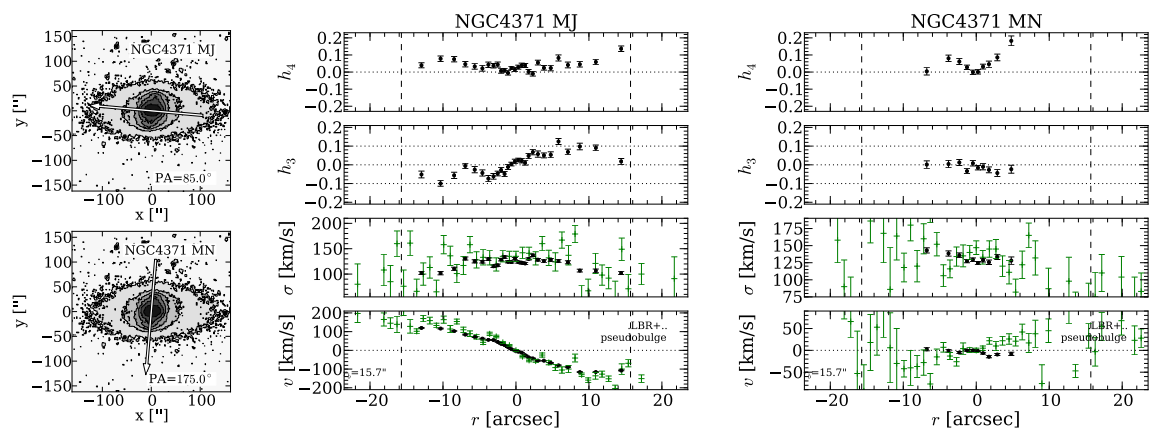


Figure A.16 *continued* – Major and minor axis kinematic profiles for NGC4371. We plot the PA=95° data from Bettoni & Galletta (1997) on our major axis data and their PA=175° on our minor axis data in green.

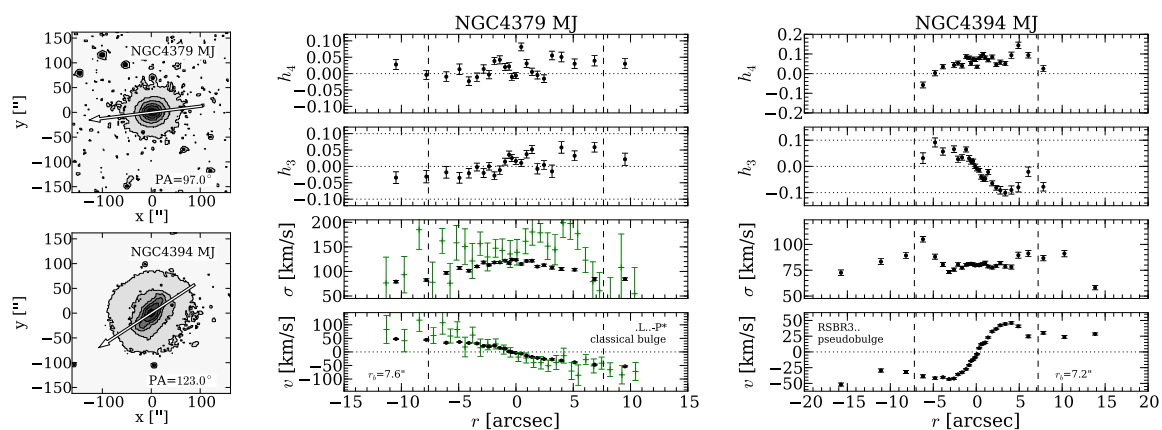


Figure A.16 *continued* – Major axis kinematic profiles for NGC4379 and NGC4394. For NGC4379 we plot the results of Bertola et al. (1995) in green.

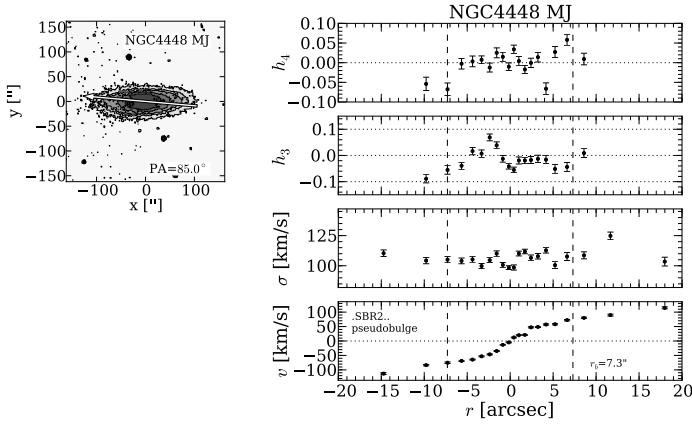


Figure A.16 *continued* – Major axis kinematic profile for NGC4448, reproduced from Fig. 4.6.

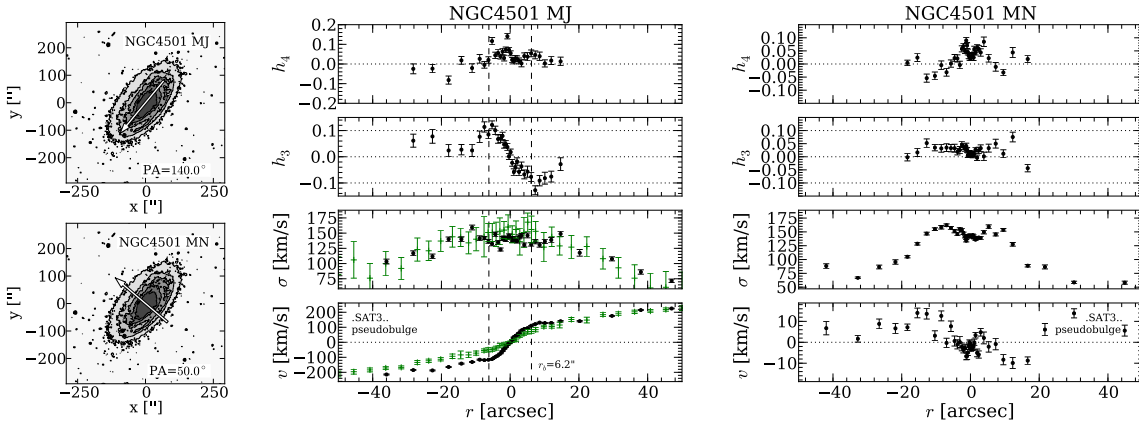


Figure A.16 *continued* – Major and minor axis kinematic profiles for NGC4501. We plot data from Héraudeau & Simien (1998) in green.

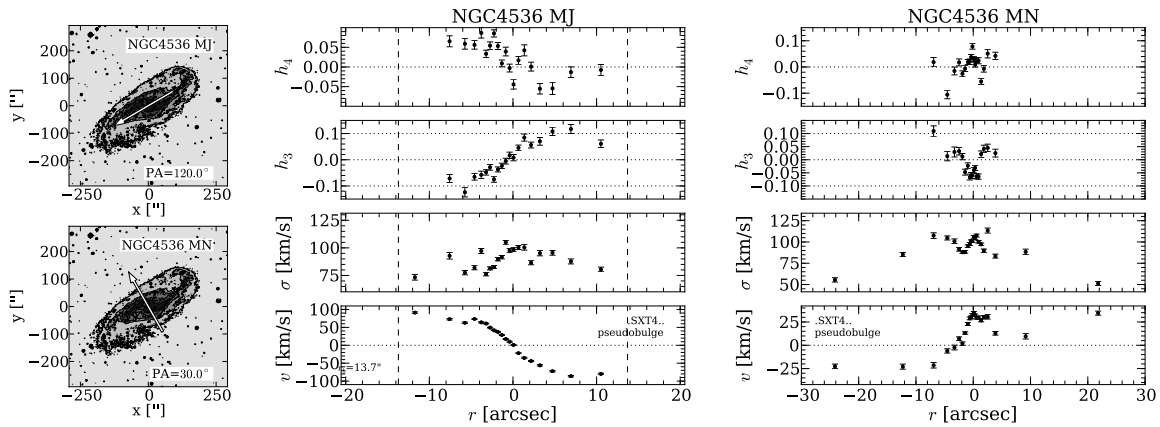


Figure A.16 *continued* – Major and minor axis kinematic profiles for NGC4536.

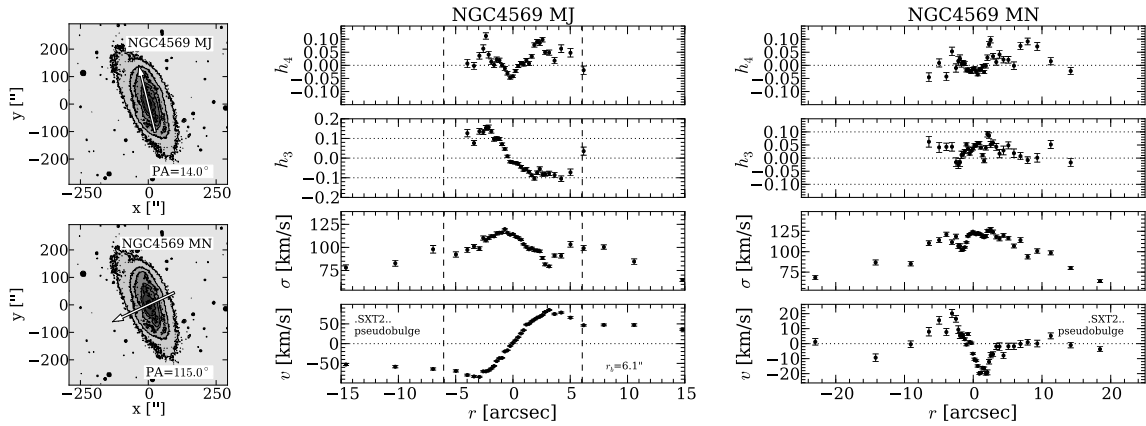


Figure A.16 *continued* – Major and minor axis kinematic profiles for NGC4569.

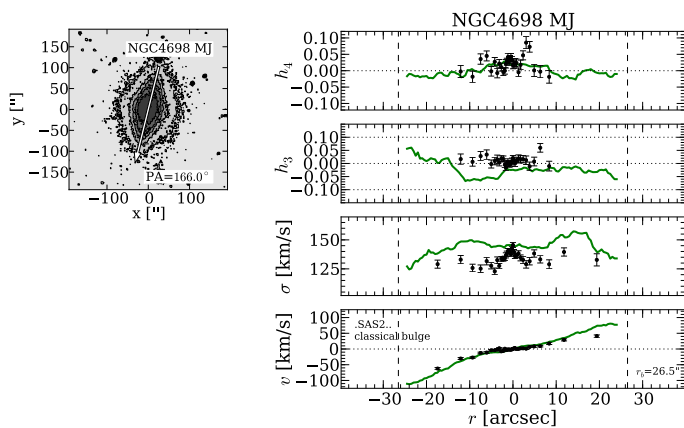


Figure A.16 *continued* – Major axis kinematic profile for NGC4698. We plot the SAURON results (Falc3n-Barroso et al., 2006) in green.

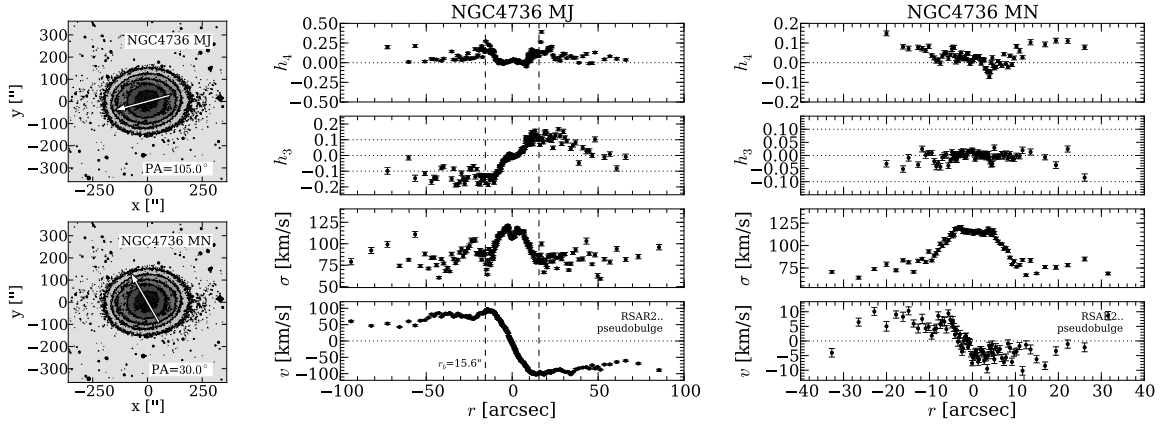


Figure A.16 *continued* – Major and minor axis kinematic profiles for NGC4736, see also Fig. 4.11.

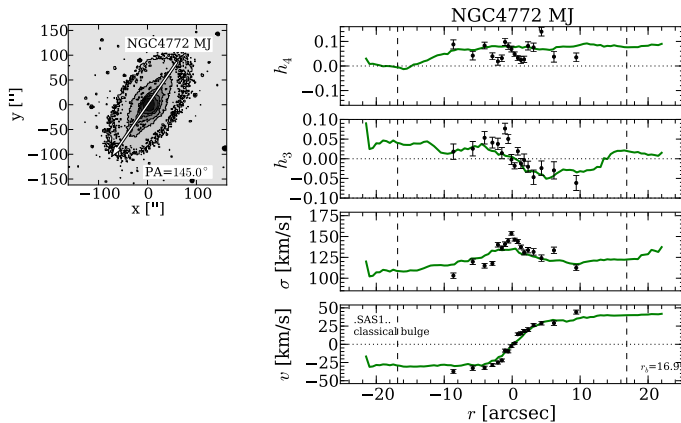


Figure A.16 *continued* – Major axis kinematic profile for NGC4772. We plot the SAURON results (Falcón-Barroso et al., 2006) in green.

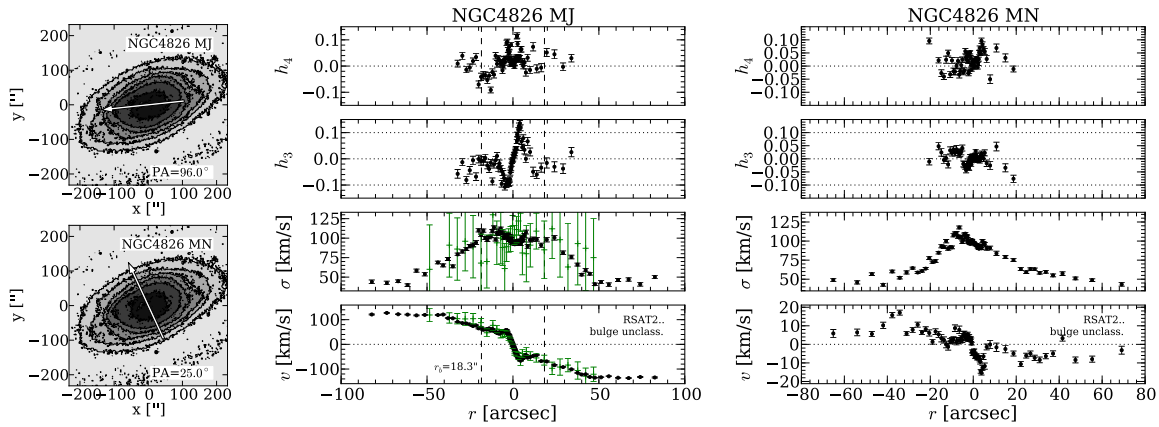


Figure A.16 *continued* – Major and minor axis kinematic profiles for NGC4826. We plot results of Héraudeau & Simien (1998) in green. Note: Their data were observed at a slit position angle of  $115^\circ$  whereas our adopted value for the major axis position angle is  $96^\circ$ .

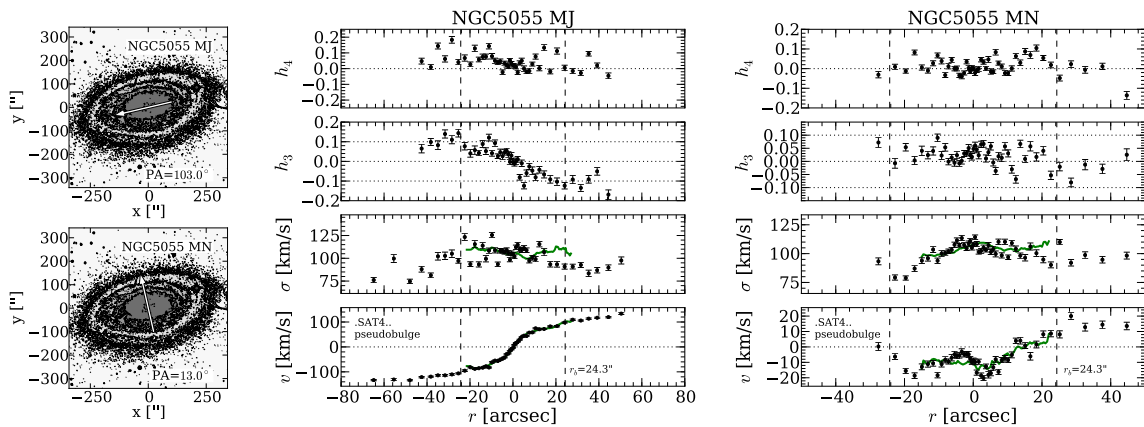


Figure A.16 *continued* – Major and minor axis kinematic profiles for NGC5055. We plot SAURON results from Dumas et al. (2007) in green.

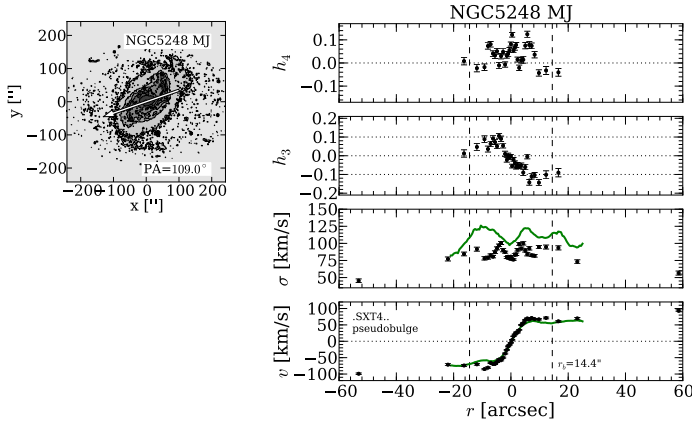


Figure A.16 *continued* – Major axis kinematic profile for NGC5248. We plot results from Dumas et al. (2007).

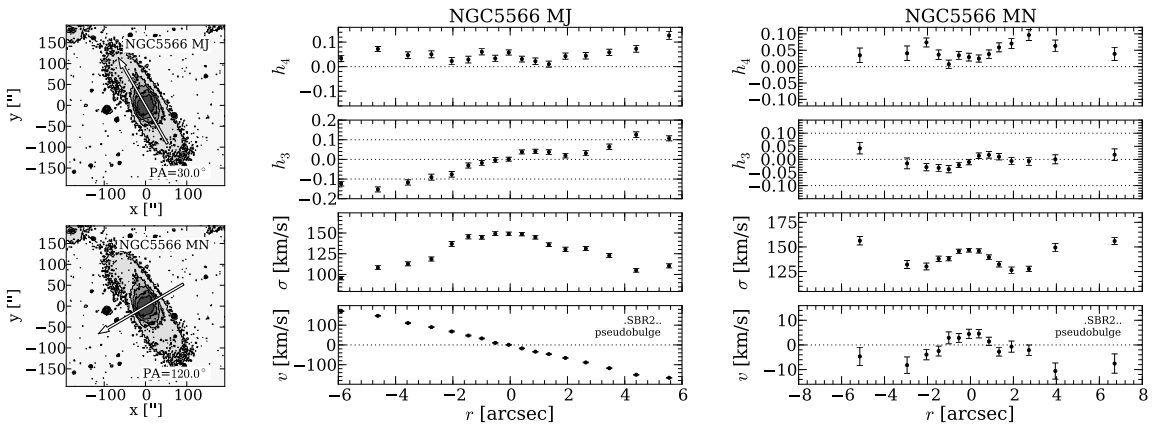


Figure A.16 *continued* – Major and minor axis kinematic profiles for NGC5566.

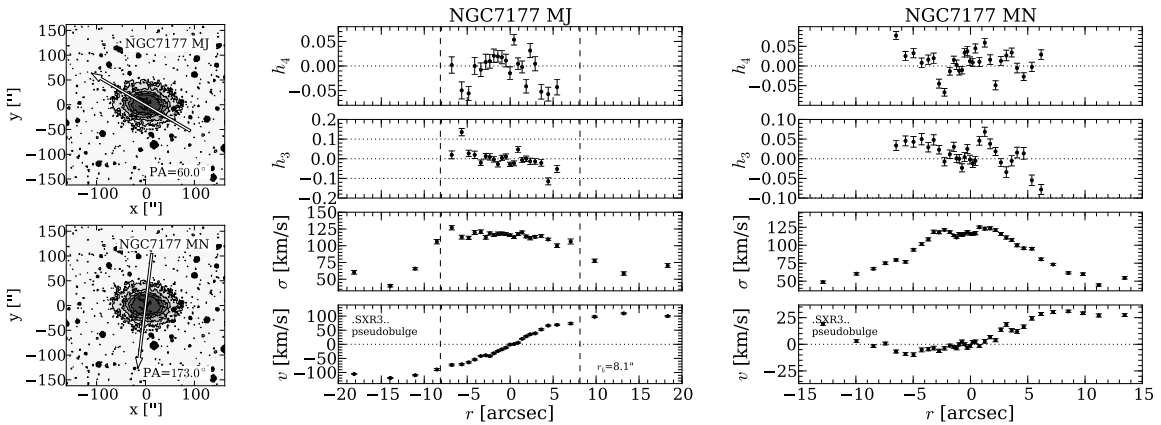


Figure A.16 *continued* – Major and minor axis kinematic profiles for NGC7177.

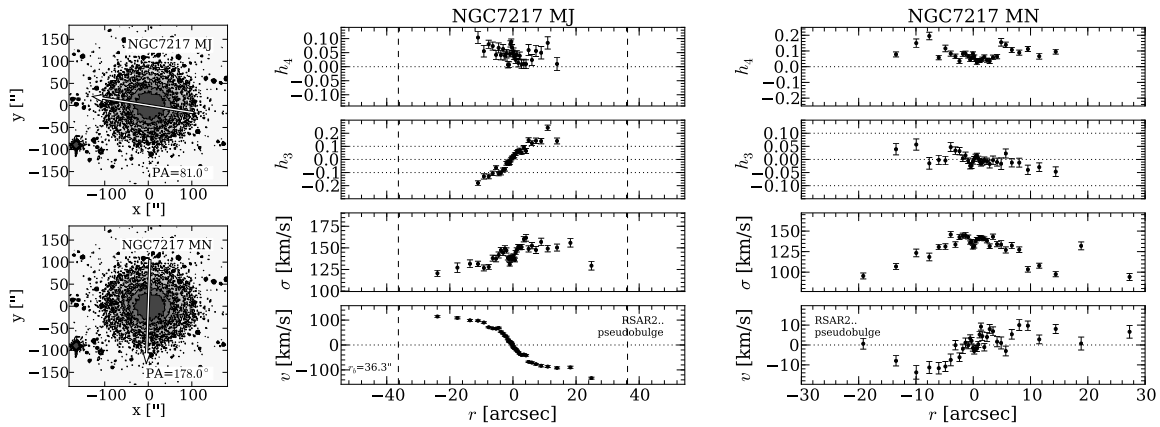


Figure A.16 *continued* – Major and minor axis kinematic profiles for NGC7217, see also Fig. 4.11.

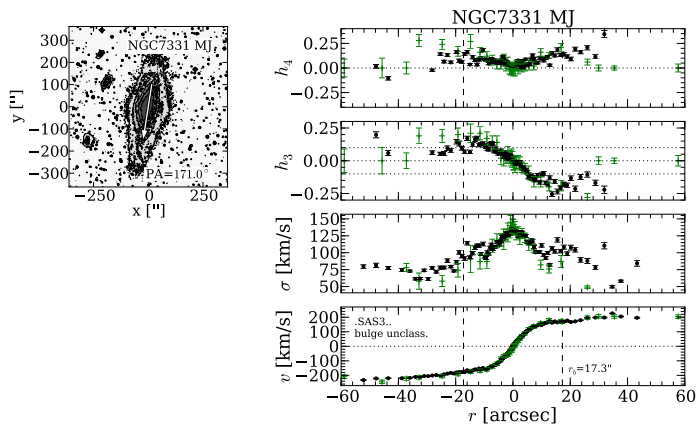


Figure A.16 *continued* – Major axis kinematic profile for NGC7331, see also Fig. 4.11. We plot results from Vega Beltrán et al. (2001) for NGC7331 in green.

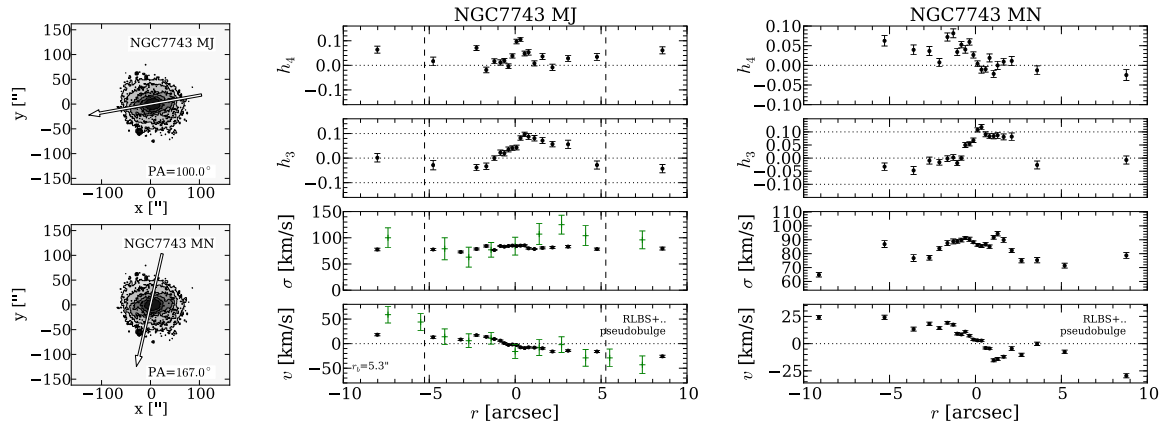


Figure A.16 *continued* – Major and minor axis kinematic profiles for NGC7743. We plot results from Kormendy (1982a) in green.

# Appendix B

## Notes on individual galaxies

### B.1 Classical Bulges

**NGC1023** .LBT-.. — Clean classical morphology in HST F555W. The rotation curve steps rapidly from  $\simeq +60 \text{ kms}^{-1}$  to  $\simeq -60 \text{ kms}^{-1}$  in the central two arcseconds and rises then gradually to a value of  $\simeq 200 \text{ kms}^{-1}$  at 50 arcseconds. The  $h_3$  profile shows an equally fast change with in the inner  $\simeq 2$  arcseconds from -0.03 to 0.03 with opposite sign. Like Emsellem et al. (2004) we see that the  $v/h_3$  anti-correlation turns into a correlation outwards of  $\simeq 10$  arcseconds. The velocity dispersion profile rises all the way to the centre. Outside of 50 arcseconds the velocity dispersion profile flattens out at about  $100 \text{ kms}^{-1}$  which coincides with a flattening in the rotation curve. This is significantly beyond the bulge radius of  $\simeq 22.4$  arcseconds. The minor axis rotation curve is mostly close to zero at larger radii but becomes negative inwards of 4 arcseconds ( $\simeq -25 \text{ kms}^{-1}$  at the centre). The acquisition image does not show an obvious offset of the minor axis slit but we note that due to the rapid rise of major axis rotation in the central arcseconds already a small offset of ( $\simeq 0.5$  arcsecond) to the west suffices to explain the observed behaviour. The  $h_3$  moments become positive in the same radial range, which is expected if the velocity offset is due to actual rotation. The minor axis  $h_4$  moments show a double peak at  $\pm 7$  arcseconds with maximum values of  $h_4 \simeq 0.04$ . The continuously centrally rising velocity dispersion of the major axis is reproduced on the minor axis.

**NGC2775** .SAR2.. — The HST F606W image shows a very clear classical morphology, the F450W image shows very little amounts of dust in the central region. Fisher & Drory (2008) find a Sérsic index of  $3.80 \pm 0.39$  for the photometric bulge in agreement with their classification as a classical bulge. We see a depression in the velocity dispersion profile inwards of 5 arcseconds in the major axis profile as well as in the minor axis profile which coincides with a steeper part in the rotation curve. Eskridge et al. (2002b) describe a large, slightly elliptical bulge which contains a bright nuclear point source. The Spitzer MIPS  $24 \mu\text{m}$  image shows a resolved nuclear source of emission which clearly stands out from a region of low emission which again in size roughly corresponds to the bulge radius. This

may hint at a cold nuclear component with active star formation which dominates the kinematics. We exclude the data inwards of 5 arcseconds from our analysis but note the this choice does significantly affect the position of NGC2775 in the plane of Sérsic index versus velocity dispersion slope.

**NGC2841** .SAR3\*. — The HST F438 image shows a weak nuclear dust spiral that is misaligned with the outer disc. The larger scale bulge morphology is smooth and shows little sign of dust and no spiral pattern. The  $h_3$  profile is anti-correlated with the rotation curve inwards of 4 arcseconds but then changes sign and becomes correlated with the velocity until about 20 arcseconds. The velocity dispersion profile is centrally rising and may show a little shelf inwards of  $\simeq 5$  arcseconds. The minor axis rotation curve shows an offset within the bulge radius.

**NGC2859** RLBR+.. — Prominent outer ring galaxy. This galaxy has no close-to V-band HST image available. The bulge morphology in HST F814W and in the acquisition images is generally smooth and classical with few weak dust lanes. Our long slit data do not cover the full bulge region ( $r_b = 19.3$  arcsec). Still the rotation curve starts flattening out at our outermost data point at  $r \simeq 8$  arcseconds. Within this region the velocity dispersion profile rises centrally to from about  $125 \text{ kms}^{-1}$  at  $\pm 6$  arcseconds to  $175 \text{ kms}^{-1}$  in the centre. The  $h_3$  moments are clearly anti-correlated with velocity. The  $h_4$  moments show indication of the double peak signature at  $r \simeq \pm 5$  arcseconds. The minor axis kinematic data only reach out to 6 arcseconds with little rotation along the minor axis (less than  $25 \text{ kms}^{-1}$ ). The coverage of the dispersion profile is insufficient to judge whether the central rise seen along the major axis is reproduced. The minor axis  $h_3$  and  $h_4$  moments are somewhat noisy but do not exceed values of 0.05 and show no significant trends.

**NGC2880** .LB-.. — The bulge morphology is classical in HST F555W. Erwin (2004) finds indication of a weak inner disk but acknowledges that this is the weakest case in his sample. The velocity dispersion profile rises centrally with a weak non-symmetric shelf-like structure inwards of  $\simeq 4$  arcseconds. The  $h_3$  moments are anti-correlated with velocity within the bulge.

**NGC3031** .SAS2.. — M81, interacting with the M81 group. Prominent central emission features connected to a liner type activity prevent us from deriving the central kinematics ( $r \pm 2$  arcseconds) reliably. This galaxy exhibits an interesting shape of its velocity dispersion profile. The profile first rises gradually until  $\simeq 150 \text{ kms}^{-1}$  at radius of about 25 arcseconds. It then drops quickly to a minimum of about  $130 \text{ kms}^{-1}$  at 18 arcseconds and rises then again to  $\simeq 160 \text{ kms}^{-1}$  at the centre. The drop around 18 arcseconds is accompanied by a rapid change of slope of the rotational velocity which stays relatively flat outwards of this radius and a strengthening of the  $h_3$  moments. Also the otherwise vanishing  $h_4$  moments rise to positive values ( $\simeq 0.1$ ) at  $r \simeq 15$  arcseconds where they form the most prominent double peak feature of our sample. The minor axis profile shows

similar local minima in the dispersion profile that are accompanied by local maxima in the  $h_4$  moments at radii of about 9 arcseconds. Given the inclination of  $59^\circ$  this points to a flattened structure within the bulge.

**NGC3245** .LAR0\*. — The HST F547M image reveals a nuclear dust disk while the larger scale bulge morphology is classical. This galaxy potentially hosts a lens (de Vaucouleurs & de Vaucouleurs, 1964). The rotational velocity exhibits a shelf reaching from about 3 arcseconds out to the bulge radius at 15 arcseconds. The velocity dispersion profile rises steadily towards the centre. The  $h_3$  moments are anti-correlated with velocity inwards of 5 arcseconds. At 5 arcseconds they reach a maximum and then drop to zero towards the bulge radius. The  $h_4$  are compatible with zero at the bulge radius but with decreasing radius briefly drop to about  $-0.05$  at  $\pm 5$  arcseconds. Finally inside of 2. arcseconds they become compatible with zero.

**NGC3521** .SXT4.. — The latest Hubble type with classical bulge in our sample. In HST F606W the classical bulge morphology stands in strong contrast to the strong outer disk spiral structure with a sudden transition of those two morphologies at  $r \simeq 10$  arcseconds. The rotation curve forms a shelf at about the bulge radius of 7 arcseconds but rises again slightly towards larger radii and starts to flatten out at 16 arcseconds. The velocity dispersion reaches a local maximum of  $\simeq 115 \text{ km s}^{-1}$  at the bulge radius but then strongly drops with decreasing radius and reaches a local minimum of  $\simeq 100 \text{ km s}^{-1}$  at 4 arcseconds. Further inwards the dispersion is centrally peaked. Outside the bulge region the dispersion shows another local maximum around 40 arcseconds which also corresponds to a slight secondary shelf on the rotational velocity. The  $h_3$  moments are anti-correlated with velocity and form a shelf at about the same radii where the inner shelf in rotational velocity is seen. Outside the bulge  $h_3$  becomes rather strong (up to 0.22) which is accompanied by strong, positive  $h_4$  moments of up to 0.15. These large moments are a consequence of the double-peak structure of the LOSVDs which has been previously reported by Zeilinger et al. (2001) caused by a secondary kinematic component (see §4.5.7). The minor axis velocity dispersion profile does not show the strong local minima that the major axis profile shows but is similarly disturbed outside the bulge.

**NGC3898** .SAS2.. — Outer disk dust spiral transitions into weak dust lanes over a smooth and classical bulge morphology in HST F606W. The rotation curve rises slowly out to  $r \simeq 10$  arcseconds but flattens well before reaching the bulge radius of  $\simeq 35$  arcseconds. The velocity dispersion profile is strongly centrally peaked and rises smoothly from  $\simeq 140 \text{ km s}^{-1}$  to  $\simeq 220 \text{ km s}^{-1}$  in the centre. The  $h_3$  moments are anti-correlated with velocity and reach local maximum at  $r \simeq 10$  arcseconds, the same radius where the flattening of the rotation curve sets in.

**NGC3992** .SBT4.. — This galaxy is prominently barred. While the bulge morphology generally appears classical it exhibits a few randomly distributed dust lanes in the only

available optical HST image in F547M. With increasing radius the velocity profile reaches a first plateau at  $r \simeq 7$  arcseconds but outside the bulge radius of 19.5 arcseconds it starts rising again slowly. The velocity dispersion profile is significantly depressed within the bulge region. The  $h_3$  moments are strongly anti-correlated with velocity inwards of 7 arcseconds but become weaker further out. The  $h_4$  moments show double peak feature around 8 arcseconds.

**NGC4203** .LX.-\*. — This galaxy represents a borderline case in the morphological bulge classification. The bulge has a few dust lanes in HST F555W superimposed on a generally smooth morphology. Fisher & Drory (2008) classify the bulge as classical and find a Sérsic index of  $2.34 \pm 0.54$ . The major axis velocity profile flattens out at about the bulge radius of 13.3 arcseconds. The velocity dispersion profile shows a prominent rise from about  $105 \text{ km s}^{-1}$  at the bulge radius to  $175 \text{ km s}^{-1}$  in the centre. The  $h_3$  moments are mostly compatible with zero in the bulge region. The  $h_4$  moments are noisy and show no significant trend within the covered region.

**NGC4260** .SBS1.. — Strongly barred. The bulge morphology is generally smooth. Martini et al. (2003) acknowledge the presence of dust structures in the central region but claim that they do not imply a sense of rotation. The bulge is classified as a classical bulge by Fisher & Drory (2008) with a Sérsic index of  $3.21 \pm 0.66$ . The velocity dispersion profile is somewhat irregular and S-shaped within the bulge region. The  $h_3$  moments are small and mostly compatible with zero, The  $h_4$  moments show a gradual drop from a central value of zero to about  $-0.06$  at about 10 arcseconds.

**NGC4379** .L.-P\* — Exhibits a very smooth and featureless central morphology in HST F555W. Fisher & Drory (2008) find a Sérsic index of  $3.48 \pm 0.22$ . The bulge radius is 7.6 arcseconds. The inset of the flattening of the rotational velocity occurs already at 8-10 arcseconds. The velocity dispersion profile is centrally peaked, rising from  $\simeq 90 \text{ km s}^{-1}$  at 10 arcseconds to  $\simeq 120 \text{ km s}^{-1}$  in the centre. The  $h_3$  moments are generally small (within the errors mostly compatible with zero) but an overall trend points to anti-correlation with velocity. The  $h_4$  values are are noisy but mostly compatible with zero.

**NGC4698** .SAS2.. — HST F606W shows some weak dust lanes in the central region which however do not show any sense of rotation. Classified as classical bulge by Fisher & Drory (2010), they find a Sérsic index of  $3.19 \pm 0.29$ . The major axis rotational velocity is relatively slowly rising. The velocity dispersion profile is mostly flat within the bulge region ( $r_b = 26.5$  arcseconds) with a weak central peak. In the small radial range that our data cover the  $h_3$  and  $h_4$  moments are mostly compatible with zero.

**NGC4772** .SAS1.. — The bulge morphology is smooth and featureless in HST F606W, the bulge is consequently classified as classical by Fisher & Drory (2008) and they find a Sérsic index of  $3.20 \pm 0.57$ . We did decompose this bulge in the H-band as well, our H-band

decomposition yields a bulge radius of 23.4 arcseconds. This value seems too large as the flattening of the velocity profile already sets in around 10 arcseconds. We therefore adopt the V-band decomposition of Fisher & Drory (2008) with a bulge radius of 16.9 arcseconds. Our data virtually only cover the bulge region. The velocity dispersion profile is generally noisy with values between  $100 \text{ km s}^{-1}$  and  $150 \text{ km s}^{-1}$  but features a clear central peak. The  $h_3$  moments are anti-correlated with velocity and reach values of up to about  $\pm 0.07$ .  $h_4$  moments scatter around values of 0.05 at all radii.

## B.2 Pseudobulges

**NGC2681** PSXT0.. — Possibly a triple barred system (Erwin & Sparke, 1999). In HST F555W a dust spiral is seen, which extends all the way into the centre. The rotational velocity curve shows a shelf between  $\simeq 2$  and  $\simeq 12$  arcseconds. The outer radius of the shelf region coincides with the bulge radius ( $r_b = 12$  arcseconds). Inwards of 2 arcseconds the rotation curve drops quickly to zero. With decreasing radius, the velocity dispersion rises from about  $50 \text{ km s}^{-1}$  to a value of  $\simeq 75 \text{ km s}^{-1}$  at the bulge radius. Towards smaller radii it first stays relatively constant but then shows a step at about 5 arcseconds and rises again inwards of 2 arcseconds. The  $h_3$  moments are anti-correlated with velocity in the region of the fast velocity rise but become correlated in the velocity shelf region. The  $h_4$  moments show a double peak feature in the radial range of 2-4 arcseconds.

**NGC2964** .SXR4\*. — High contrast dust spiral in HST F606W. The bulge is small ( $r_b = 3.4$  arcseconds) and we do not sufficiently resolve it to include this galaxy in any of our structural plots. Here we publish the kinematic profiles. The velocity dispersion rises from values of about  $40 \text{ km s}^{-1}$  in the disk to  $\simeq 106 \text{ km s}^{-1}$  at the bulge radius and exhibits a depression within the bulge.  $h_3$  and  $h_4$  moments scatter strongly within values of  $\pm 0.1$  which is possibly a consequence of the dust.

**NGC3166** .SXT0.. — The HST F547M image shows strong dust features and a dust spiral which extends all the way into the centre. Laurikainen et al. (2004) describe this galaxy as strongly barred. We did attempt a photometric bulge-to-disk decomposition for this galaxy using public available  $3.6 \mu\text{m}$  data. Our IR decomposition yields a bulge radius of 48.2 arcseconds which is vastly different from the V-band value of 6.7 arcseconds from Fisher & Drory (2008). Since the rotational velocity already reaches a local maximum at about 5 arcseconds, we adopt the V-band values here. The velocity dispersion profile shows a strong depression at  $\simeq 4.5$  arcseconds which is accompanied by relatively strong  $h_3$  moments of  $\pm 0.17$  and positive  $h_4$  moments and a local maximum in the rotation curve. The minor axis shows small but significant rotation within the bulge region ( $\simeq \pm 10 \text{ km s}^{-1}$ ) while the  $h_3$  moments are largely compatible with zero. The depression of the velocity dispersion is also seen on the minor axis whilst not as strong.

**NGC3351** .SBR3.. — The bulge hosts a clear spiral structure and a nuclear ring (Fisher & Drory, 2010) and shows signs of active star formation. The velocity dispersion profile shows a depression within the bulge region — most strongly at  $r \simeq 5$  arcseconds down to a value of  $70 \text{ kms}^{-1}$  — and rises again centrally to  $\simeq 90 \text{ kms}^{-1}$  which is still below the values of about  $100 \text{ kms}^{-1}$  seen just outside of the bulge radius. The  $h_3$  moments are clearly anti-correlated with velocity. The minor axis profile shows significant rotation ( $v_{max} \simeq 50 \text{ kms}^{-1}$ ) indicative of a slit misalignment, in fact there is a  $25^\circ$  difference between our major axis slit position of  $165^\circ$  and the Hyperleđa published value of  $9.9^\circ$ .

**NGC3368** .SXT2.. — Complex morphology with a number of stellar components (Erwin, 2004; Nowak et al., 2010). This galaxy is possibly double-barred (Jungwiert et al., 1997). The bulge hosts a strong nuclear spiral and an inner disk (Erwin, 2004) and is classified as pseudobulge by Fisher & Drory (2010) with a Sérsic index of  $1.6 \pm 0.18$ . The bulge radius is 30.6 arcseconds. The complex morphology is reflected in the kinematic structure. The rotational velocity reaches a local maximum at about 7 arcseconds. This is accompanied by local minimum in the velocity dispersion profile that has been rising inwards until  $\simeq 13$  arcseconds. Inwards of 7 arcseconds the dispersion rises again, but asymmetrically about the centre, see also Nowak et al. (2010). The local maximum in velocity and local minimum in dispersion coincide with strengthened  $h_3$  moments.  $h_3$  is anti-correlated with velocity inwards of 15 arcseconds but correlated outside. The  $h_4$  moments are close to zero at the bulge radius but become positive and reach a local maximum at about the same radii where the local maxima in velocity are observed and the drops in velocity dispersion and strengthening of  $h_3$  moments occur. The minor axis profile shows similar depressions in velocity dispersion. The minor axis velocity profile shows a central peak of about  $30 \text{ kms}^{-1}$ . Visual inspection of the pre-acquisition images reveals that a minor offset of the slit position ( $\simeq 1$  arcsec) to the west is responsible for the peak.

**NGC3384** .LBS-\*. — Contains a nuclear bar (Fisher & Drory, 2010) and a rapidly rotation disk described by Busarello et al. (1996); Fisher (1997) and Emsellem et al. (2004) already find strong  $h_3$  moments in anti-correlation with velocity. The velocity dispersion profile flattens inside the bulge radius but then has a pronounced peak inwards of 3 arcseconds that is accompanied by a dip (as seen by Fisher (1997); Emsellem et al. (2004) as well) in the  $h_4$  moments that become positive just outside of this region.

**NGC3627** .SXS3.. — Prominently barred galaxy with wide, open arms, interacting with the Leo group. High contrast dust lanes that extend to the very centre are seen in HST F606W and let Fisher & Drory (2008) classify this as a pseudobulge. They find a Sérsic index of  $2.9 \pm 0.83$ . After a fast rise the rotational velocity forms a shelf between 3 arcseconds and the bulge radius of about 13 arcseconds. Towards larger radii the velocity rises again. The velocity dispersion rises inwards, starting already far outside the bulge radius. At  $\simeq 4$  arcseconds it flattens out and stays virtually constant. The  $h_3$  moments are anti-correlated with velocity inside of 9 arcseconds but change sign at larger radii and

become correlated with velocity. While the minor axis rotation is compatible with zero at larger radii it exhibits significant rotation inwards of about 7 arcseconds that is also seen in anti-correlated  $h_3$  moments.

**NGC3675** .SAS3.. — The HST F606W image clearly shows a high contrast flocculent spiral that extends all the way into the centre. The velocity dispersion reaches a maximum of about  $110 \text{ km s}^{-1}$  at  $\simeq 40$  arcseconds and stays rather constant inside of this radius. The  $h_3$  moments are anti-correlated with velocity within the bulge and reach maximum values of about 0.1 at the bulge radius of 8.3 arcseconds.

**NGC3945** RLBT+.. — Double barred (Kormendy, 1979, 1982a; Wozniak et al., 1995; Erwin & Sparke, 1999, 2003; Erwin, 2004) galaxy with prominent outer ring. Exhibits complicated kinematic structure. The rotational velocity has local minima around 18 arcseconds, rises then towards smaller radii and reaches a local maximum around 8 arcseconds before it falls off to the centre. The dispersion profile has very strong local minima — drops from  $\simeq 150 \text{ km s}^{-1}$  to  $\simeq 110 \text{ km s}^{-1}$  — at  $r \simeq 8$  arcseconds but then rises again towards the centre. This galaxy shows exceptionally strong  $h_3$  moments of up to  $\simeq 0.25$  which are anti-correlated with velocity in the inner region but become positively correlated at about 20 arcseconds. The  $h_4$  moments are similarly strong (up to 0.2) with significant central depression. The LOSVDs do show significant low velocity shoulders at radii between  $2'' < \|r\| < 10''$  which is indicative of a kinematic distinct component (see Sec. 4.5.7). The minor axis profile also shows a local depression in velocity dispersion but at  $r \simeq 3.5$  arcseconds, the central dip in  $h_4$  is seen as well. We measure slight rotation along the observed position angle of  $64^\circ$  ( $i \simeq \pm 25 \text{ km s}^{-1}$ ) and a significant central offset of the velocity ( $\simeq 40 \text{ km s}^{-1}$ ). The major axis velocity profile shows that a slit position offset of one arcsecond is sufficient to explain the central velocity peak. A visual inspection of the pre-acquisition image confirmed that such an offset was indeed present (about 0.6 arcseconds).

**NGC4030** .SAS4.. — The flocculent spiral structure — easily seen in HST F606W — extends all the way to the centre with star-forming knots in the inner disk (Eskridge et al., 2002b). Fisher & Drory (2008) classify it as pseudobulge and find a Sérsic of  $1.75 \pm 0.08$ . The major axis rotational velocity reaches  $\simeq 100 \text{ km s}^{-1}$  at about the bulge radius of 8.4 arcseconds. The velocity dispersion stays moderately flat within the bulge region and drops off outside. The  $h_3$  moments are clearly anti-correlated with velocity and reach a values of up to 0.1 at a radius of about 7 arcseconds.  $h_4$  moments are compatible with zero at all radii that are covered by our data.

**NGC4274** RSB2.. — Classified as pseudobulge with a Sérsic index of  $1.60 \pm 0.35$  by (Fisher & Drory, 2010). The bulge hosts a prominent nuclear spiral including strong dust lanes and possibly a nuclear ring. The major axis rotational velocity rises quickly with increasing radius and starts flattening out at about 4 arcseconds, well with the bulge

radius of 14.8 arcseconds. The velocity dispersion profile shows a strong depression inside the bulge with values of about  $100 \text{ km s}^{-1}$ . Outside the bulge the dispersion rises to values exceeding  $130 \text{ km s}^{-1}$ . The  $h_3$  moments are well anti-correlated with velocity in the radial range that is covered by our data. They reach values of up to  $\pm 0.14$  at about the same radius where the rotational velocity starts to flatten out. This is accompanied by peaks in the  $h_4$  moments with values of up to 0.14.

**NGC4314** .SBT1.. — Strongly barred galaxy with prominent nuclear ring. It is consequently classified as pseudobulge by Fisher & Drory (2008). The rotational velocity starts to flatten at the bulge radius of 7.8 arcseconds. The velocity dispersion profile is asymmetric but relatively flat, it varies between values of  $105 \text{ km s}^{-1}$  and  $130 \text{ km s}^{-1}$ . The  $S/N$  only allows us to derive  $h_3$  and  $h_4$  moments inside a radius of 6 arcseconds. The  $h_3$  moments are mostly compatible with zero, the  $h_4$  moments rise from zero in the centre to values around 0.05 at 4 arcseconds.

**NGC4321** .SXS4.. — Double-barred galaxy (Erwin, 2004) with strong spiral structure, dust and star forming regions extends well into the bulge region. Consequently Fisher & Drory (2010) classify this as a pseudobulge and find a Sérsic index of  $1.20 \pm 0.19$ . Our major axis data cover only about a third of bulge region, we therefore exclude this galaxy from our structural analysis. The bulge radius is 20.3 arcseconds. The velocity dispersion rises inwards to a central value of  $\simeq 90 \text{ km s}^{-1}$ . The  $h_3$  and  $h_4$  moments are compatible with zero within the small radial range that is covered by our data.

**NGC4371** .LBR+.. — Strongly barred galaxy. Erwin & Sparke (1999) find a bright stellar ring that is notable by adjusting the contrast of the e.g. the HST F606W image carefully or through unsharp masking. Decompositions in  $3.6 \mu\text{m}$  (Fisher & Drory, 2010) and in the visible (Fisher & Drory, 2008) yield quite different values for the bulge radius (15.7 arcseconds in V vs. 42.5 arcseconds in  $3.6 \mu\text{m}$ ). Since the flattening of the rotational velocity profile sets in at 10 arcseconds we deem the value of the IR decomposition to be probably too large and use the V-band decomposition here. While free of obvious dust or spiral structures the ring with a radius of about 5 arcseconds falls within the bulge radius which lets (Fisher & Drory, 2010) classify this as a pseudobulge but they find a Sérsic index of  $3.92 \pm 0.31$ . The major axis rotational velocity starts to flatten out at a radius of 8 arcseconds with a weak shelf around 3-8 arcseconds. The velocity dispersion rises from about  $105 \text{ km s}^{-1}$  at the bulge radius to about  $130 \text{ km s}^{-1}$  at 7 arcseconds. Inside of 7 arcseconds the velocity dispersion stays relatively constant. The  $h_3$  moments are somewhat asymmetric but generally anti-correlated with velocity within the bulge. The  $h_4$  moments are compatible with zero in the centre but rise gradually to values of about 0.05 at 10 arcseconds. The minor axis velocity dispersion stays mostly constant within the covered radial range. The minor axis  $h_3$  moments remain compatible with zero while the  $h_4$  moments rise from zero at the centre to values of about 0.05 at  $\pm 9$  arcseconds.

**NGC4394** .RSBR3.. — Strongly barred galaxy with a face-on spiral in the central  $r \simeq 5$  arcseconds. This galaxy has a V-band decomposition available from Fisher & Drory (2008) and a  $3.6 \mu\text{m}$  decomposition available from Fisher & Drory (2010). The latter yields a bulge radius of 16.4 arcseconds. This value seems too large as the flattening of the velocity profile already sets in at about 4 arcseconds. We therefore adopt the V-band value of 7.2 arcseconds for the bulge radius. Fisher & Drory (2008) classify it as a pseudobulge and find a Sérsic index of  $1.65 \pm 0.5$ . The major axis velocity profile rises quickly to about  $50 \text{ km s}^{-1}$  at 3 arcseconds. The velocity dispersion exhibits two prominent maxima around the bulge radius. The maxima reach values of about  $105 \text{ km s}^{-1}$  but drop quickly to about  $80 \text{ km s}^{-1}$  just inside of the bulge and stay relatively constant towards smaller radii from there on. The  $h_3$  moments are anti-correlated with velocity inside the bulge. The  $h_4$  values are asymmetric and somewhat large within the bulge with values of up to 0.07 but we note that with dispersion values around  $80 \text{ km s}^{-1}$  we reach the limit of our ability to resolve those values properly.

**NGC4448** .SBR2.. — Fisher & Drory (2010) note a mild spiral structure that extends into the centre and find a Sérsic index of  $1.19 \pm 0.45$ . The major axis rotational velocity starts to flatten out at about 5 arcseconds — just inside of the bulge radius of 7.3 arcseconds. Outside of 5 arcseconds the velocity profile exhibits a weak shelf. The velocity dispersion is mostly constant at a value of  $\simeq 115 \text{ km s}^{-1}$  at all radii covered by our data. The  $h_3$  moments are somewhat asymmetric, close to zero at positive radii but vary strongly at negative radii. The  $h_4$  moments scatter about zero in the bulge region with a few outliers at -0.05.

**NGC4501** .SAT3.. — A nuclear spiral extends all the way to the centre in HST F606W. Fisher & Drory (2010) classify the bulge as pseudobulge and find a Sérsic index of  $0.89 \pm 0.65$ . The major axis velocity profile rises quickly from the centre to the bulge radius of 6.2 arcseconds but then flattens out at the bulge radius and forms a shelf out to about 20 arcseconds. The velocity dispersion rises from  $75 \text{ km s}^{-1}$  in the disk to about  $150 \text{ km s}^{-1}$  at 15 arcseconds. The  $h_3$  moments are strongly anti-correlated with velocity inside the bulge and reach values of  $\pm 0.1$  at the bulge radius.  $h_4$  moments are mostly compatible with zero at all radii. The minor axis velocity dispersion profile starts rising with decreasing radius inwards of 30 arcseconds and reaches a maximum of  $\simeq 155 \text{ km s}^{-1}$  at  $r = 10$  arcseconds. The minor axis velocity dispersion exhibits a central depression of about  $15 \text{ km s}^{-1}$ . The minor axis velocity,  $h_3$  and  $h_4$  moments are mostly compatible with zero.

**NGC4536** .SXT4.. — A strong dust spiral extends into the very centre. Fisher & Drory (2008) classify the bulge as pseudobulge and find a Sérsic index of  $1.88 \pm 0.35$ . The bulge radius is 13.7 arcseconds. The major axis rotational velocity flattens well inside bulge radius at around 2 arcseconds. The velocity dispersion profile is slightly asymmetric but mostly constant within the bulge region. The  $h_3$  moments are anti-correlated with velocity inside the bulge region and reach values of about 0.1. The  $h_4$  profile is asymmetric. The

minor axis velocities show slight asymmetric rotation ( $\simeq 25 \text{ km s}^{-1}$ ). The velocity dispersion profile rises centrally but stays relatively flat within  $\pm 10$  arcseconds. The minor axis  $h_3$  moments are somewhat noisy but seem to show a central depression.

**NGC4569** .SXT2.. — A nuclear spiral extends all the way to the centre. The bulge was classified as pseudobulge by Fisher & Drory (2010). They find a Sérsic index of  $1.97 \pm 0.38$ . The major axis rotational velocity rises with increasing radius to a local maximum of about  $80 \text{ km s}^{-1}$  at  $\pm 3$  arcseconds. The bulge radius is  $r_b = 6''$ . The velocity then drops to about  $50 \text{ km s}^{-1}$  at the maximum radius covered by our data. The velocity dispersion rises inwards to about  $100 \text{ km s}^{-1}$  at the bulge radius and then drops and reaches a local minimum around 3 arcseconds, roughly coinciding with the locations of the local maxima in the velocity profile. The  $h_3$  moments are anti-correlated with velocity inside the bulge. Their absolute values reach up to 0.15. The  $h_4$  moments show a strong double peak feature at about 3 arcseconds and fall off to zero at the bulge radius. The minor axis profile shows rotation in the bulge region. While somewhat asymmetric, the minor axis dispersion profile does not show the same complicated structure of the major axis profile. The  $h_3$  moments on the minor axis are mostly compatible with zero. The  $h_4$  moments are generally noisy but the double peak feature of the major axis is reproduced.

**NGC4736** RSAR2.. — Hosts a nuclear bar (Sakamoto et al., 1999) and prominent nuclear spiral which extends all the way into the centre in HST F555W. The bulge is classified as pseudobulge by Fisher & Drory (2010), they find a Sérsic index of  $1.30 \pm 0.20$ . The obtained kinematic data extend well into the disk. The rotational velocity flattens out abruptly at about the bulge radius of 15.6 arcseconds and shows a shallow negative gradient out to about 70 arcseconds where our data points start to become sparse. The velocity dispersion rises abruptly from about  $75 \text{ km s}^{-1}$  to  $115 \text{ km s}^{-1}$  at about the bulge radius. Well within the disk at radii larger than 50 arcseconds we see again a gradual increase of velocity dispersion. Inside of 2.5 arcseconds the velocity dispersion shows a drop. The  $h_3$  moments are anti-correlated with velocity but show s-shape around the centre. They reach exceptionally large values of  $\pm 0.2$  at the bulge radius. The  $h_4$  moments are compatible with zero in the inner bulge but reach pronounced local maxima of values as large as 0.17 at about the bulge radius. They fall off to zero at  $r \simeq 35$  arcseconds. These strong higher moments are a consequence of the multi-component structure of the LOSVDs at the respective radii (see Sec. 4.5.7). The minor axis profile reflects the rich structure seen in the major axis profile. The velocity dispersion rises significantly inwards of 10 arcseconds. The  $h_3$  moments are mostly compatible with zero at all radii,  $h_4$  moments are zero inside of 10 arcseconds but rise to about 0.1 at 20 arcseconds.

**NGC5055** .SAT4.. — The HST F606W image shows that the outer disk flocculent spiral extends into the very centre. Consequently this galaxy is classified as pseudobulge by Fisher & Drory (2010), they find a Sérsic index of  $1.33 \pm 0.68$ . The velocity dispersion profile remains flat inside the bulge radius of 24.3 arcseconds. The  $h_3$  moments are anti-

correlated with velocity inside the bulge and reach absolute values of up to 0.1 just outside of the bulge radius. The  $h_4$  moments are compatible with zero inwards of 10 arcseconds, they become noisy further out but show a weak tendency towards more positive values towards the bulge radius. The minor axis velocities appear somewhat irregular but small ( $< 20 \text{ km s}^{-1}$ ). The minor axis  $h_3$  moments are noisy but mostly scatter close to zero. Again the  $h_4$  moments are mostly compatible with zero inwards 10 arcseconds but show a weak increase further out but only on the east side.

**NGC5248** .SXT4.. — Has a prominent nuclear spiral clearly visible in HST F814W. The bulge was classified as pseudobulge by Fisher & Drory (2010), they find a Sérsic index of  $0.69 \pm 0.27$ . The rotational velocity starts to flatten at about 6 arcseconds — well inside the bulge radius of 14.4 arcseconds. The velocity profile shows a shelf between  $\simeq 10$  arcseconds and  $\simeq 40$  arcseconds. The velocity dispersion profile is mostly flat at about  $80 \text{ km s}^{-1}$  with two small peaks at  $r \simeq \pm 4$  arcseconds. The  $h_3$  moments are anti-correlated with velocity and reach values of up to  $\pm 0.1$ . The  $h_4$  moments scatter around values of 0.05.

**NGC5566** .SBR2.. — Shows a nuclear spiral in HST F606W. The surface brightness profile does not resemble a traditional bulge plus disk structure. We do not include this galaxy in any of the structural plots and publish only the kinematic profile here. The rotational velocity starts to flatten at 6 arcseconds. The velocity dispersion profile rises towards the centre and peaks at a value of about  $150 \text{ km s}^{-1}$ . The  $h_3$  moments are anti-correlated with velocity and reach values of up to 0.15. The  $h_4$  moments are small in the central arcseconds but rise to values of about 1.1 at  $\simeq \pm 5$  arcseconds.

**NGC7177** .SXR3.. — A nuclear bar extends out to about  $r = 10$  arcseconds. The bulge is classified as pseudobulge by Fisher & Drory (2010), they find a Sérsic index of  $1.79 \pm 0.22$ . The flattening of the major axis rotational velocity coincides with bulge radius of  $r_b = 8.1$  arcseconds. The velocity dispersion rises from about  $50 \text{ km s}^{-1}$  in the disk to values of  $\simeq 115 \text{ km s}^{-1}$  inside the bulge but remains relatively flat inside the bulge radius. The  $h_3$  moments are weakly anti-correlated with velocity but remain small. The  $h_4$  moments drop to values of -0.05 at  $\simeq \pm 5$  arcseconds. The minor axis shows an asymmetric velocity profile with values of up to  $\pm 25 \text{ km s}^{-1}$ . The minor axis velocity dispersion again rises from about  $50 \text{ km s}^{-1}$  in the disk to values of about  $115 \text{ km s}^{-1}$  at 2.5 arcseconds and remains flat inside. The  $h_3$  moments are anti-correlated with velocity. The  $h_4$  moments are noisy and scatter around zero.

**NGC7217** RSAR2.. — Fisher & Drory (2010) point out a sudden break in morphology at a radius of about 8 arcseconds where the outer spiral transitions onto a relatively smooth morphology with little dust. They consequently label this bulge as classical. However, the bulge radius from the decomposition is significantly larger with 36 arcseconds and contains significant parts of the inner spiral. We therefore restore the classification as a pseudobulge from Fisher & Drory (2008). The rotational velocity profile starts to flatten out at about

10 arcseconds. The major axis dispersion profile is asymmetric with higher values on the east side of the centre. Within the central  $\pm 2$  arcseconds the velocity dispersion shows a mild depression of about  $20 \text{ km s}^{-1}$ . The  $h_3$  moments are well anti-correlated with velocity. The  $h_4$  moments scatter around values of 0.05. We observe mild rotation on the minor axis (of the order of  $\pm 10 \text{ km s}^{-1}$ ) indicative of a slight slit misalignment. The minor axis velocity dispersion is symmetric and rises towards the centre from values of about  $100 \text{ km s}^{-1}$  at radii of  $\pm 20$  arcseconds to  $145 \text{ km s}^{-1}$  at 2 arcseconds. Within the central arcseconds the mild depression which is seen on the major axis is reproduced on the minor axis. The minor axis  $h_3$  moments mostly scatter around zero while  $h_4$  moments fall closer to 0.05 with a few relatively large outliers at radii around 6-10 arcseconds. Merrifield & Kuijken (1994) found the 20%-30% of the light is captured in a counterrotating component. We confirm this and present a kinematic decomposition in §4.5.7.

**NGC7743** RLBS+.. — The central region exhibits some weak dust lanes overlaid on a generally (Martini et al., 2003) smooth light distribution. The bulge is classified as classical bulge by Fisher & Drory (2008). The amplitude of the rotation is small at about  $\pm 25 \text{ km s}^{-1}$  due to the low inclination. We find rotation of similar value along the minor axis slit due to a misplacement of the slit ( $166^\circ$  rather than  $10^\circ$ ). The velocity dispersion is flat for both position angles and takes values of about  $80 \text{ km s}^{-1}$ . Both, major axis and *minor axis*  $h_3$  moments are anti-correlated with velocity and become compatible with zero at the bulge radius. The  $h_4$  moments are very noisy, probably due to the low velocity dispersion of this object.

### B.3 Bulges Without Classification

**NGC2460** .SAS1.. — Mixed type morphology in HST F606W with a weak asymmetric dust structure in the bulge region ( $r_b = 7.5$  arcsec) that is overlaid on an otherwise smooth light distribution. We label this bulge as unclassified. The decomposition gave a value of  $3.70 \pm 0.36$  for the Sérsic index and 7.5 arcseconds for the bulge radius. Our kinematic datapoints only extend out to about 5 arcseconds. Within this region the velocity dispersion profile is flat and  $h_3$  and  $h_4$  moments scatter around zero.

**NGC3593** .SAS0\*. — Peculiar bulge structure with prominent spiral visible even in NIC F160W classified a pseudobulge by Fisher & Drory (2010). We label it as *non-classified* because its high inclination inhibits an unperturbed view into the bulge region. This is the only example in our sample where counter rotation is readily seen in the velocity profile (this was found also by Bertola et al., 1996). The counter rotation within the bulge radius is reflected in the anti-correlated  $h_3$  moments. The velocity dispersion drops dramatically from  $\simeq 115 \text{ km s}^{-1}$  at the bulge radius to  $\simeq 60 \text{ km s}^{-1}$  in the centre.

**NGC3953** .SBR4.. — Fisher & Drory (2010) classify this bulge as pseudobulge but recognize that there is no optical HST image available. They find a Sérsic index of  $1.5 \pm 0.14$ .

Here we label it as *non-classified*. The rotational velocity profile first reaches a weak local maximum at  $r \simeq 2.5$  arcseconds before it starts rising again at the bulge radius ( $r_b = 7.8$  arcseconds). The disk velocity dispersion rises centrally from values of  $\simeq 50 \text{ km s}^{-1}$  at  $\pm 30$  arcseconds to  $\simeq 130 \text{ km s}^{-1}$  at  $\simeq 8$  arcseconds. Within the bulge it then falls toward a central value of  $\simeq 110 \text{ km s}^{-1}$ . The fast central increase of velocity is accompanied by strong anti-correlated  $h_3$  moments with values of up to  $\pm 0.1$  at  $r \simeq 6$  arcseconds. At the bulge radius the anti-correlation turns into a correlation. The  $h_4$  moments are generally noisy in the bulge region and scatter between zero and 0.05.

**NGC4826** RSAT2.. — Also named the *black eye* galaxy. An extreme dust spiral in the central 50 arcseconds stands in strong contrast to a virtually dust free outer disk. The central dust content leads to a classification as pseudobulge in Fisher & Drory (2008) and they find a Sérsic index of  $3.94 \pm 0.68$ . The major axis kinematic profile is rich in structure. The rotational velocity rises quickly from the centre to a value of  $\simeq 50 \text{ km s}^{-1}$  at  $r = 4$  arcseconds. It then forms a shallow trough around 8 arcseconds and then rises again — more slowly — out to 50 arcseconds where it finally flattens out. The velocity dispersion in the disk is  $\simeq 60 \text{ km s}^{-1}$ , it shows a distinct central increase inwards of 50 arcseconds. The dispersion reaches values of up to  $110 \text{ km s}^{-1}$  inside of 17 arcseconds. Inside the bulge radius ( $r_b = 18.3$  arcseconds) the velocity dispersion then shows a central depression down to  $90 \text{ km s}^{-1}$ . The  $h_3$  moments are strongly anti-correlated with velocity inside the bulge radius and reach absolute values of up to 0.15. The  $h_4$  moments show two peaks at about  $\pm 3$  arcseconds. We find weak rotation along the minor axis ( $\simeq \pm 10 \text{ km s}^{-1}$ ). The central increase in velocity dispersion is also seen along the minor axis, the increase sets in at a radius of about 25 arcseconds. This is much closer to the centre than in the case of the major axis and points to a flattened structure. The centre of the velocity dispersion profile is asymmetric which may be a consequence of the strong dust. The minor axis  $h_3$  and  $h_4$  moments are compatible with zero. The fact that the final flattening of the rotational velocity and the inset of the dispersion increase at 50 arcseconds falls together with the sudden appearance of the strong dust structure is intriguing and lets one suspect that the actual bulge radius falls closer to 50 arcseconds. The much smaller bulge radius from the decomposition may be a consequence of the strong dust content in the central regions (see also discussion in §4.5.4).

**NGC7331** .SAS3.. — The HST F555W image shows several dust lanes in the bulge region. However these do not imply any sense of rotation and seem to be overlaid on a generally smooth light distribution. Fisher & Drory (2008) admit that the high inclination leaves the classification as classical bulge questionable. Here we label it as *non-classified*. The rotational velocity profile is already flattened at the bulge radius of  $r_b = 17.3$  arcseconds. The velocity dispersion rises from about  $75 \text{ km s}^{-1}$  in the disk to  $125 \text{ km s}^{-1}$  in the centre. The dispersion profile has two steps or shoulders at  $\simeq \pm 20$  arcseconds. The  $h_3$  moments are generally anti-correlated with velocity and reach a local maximum of about 0.15 at the bulge radius. Also the  $h_4$  moments reach local maxima at the bulge radius with

values of up to 0.15. These large moments are a consequence of the double-peak structure of the LOSVDs caused by a counterrotating kinematic component discovered by Prada et al. (1996) (see §4.5.7).

# Bibliography

- Abraham, R. G., Merrifield, M. R., Ellis, R. S., Tanvir, N. R., & Brinchmann, J. 1999, MNRAS, 308, 569
- Adams, J. J., Blanc, G. A., Hill, G. J., Gebhardt, K., Drory, N., Hao, L., Bender, R., Byun, J., Ciardullo, R., Cornell, M. E., Finkelstein, S. L., Fry, A., Gawiser, E., Gronwall, C., Hopp, U., Jeong, D., Kelz, A., Kelzenberg, R., Komatsu, E., MacQueen, P. J., Murphy, J., Odoms, P. S., Roth, M., Schneider, D. P., Tufts, J. R., & Wilkinson, C. P. 2011, ApJS, 192, 5
- Athanassoula, E. 2003, MNRAS, 341, 1179
- . 2005, MNRAS, 358, 1477
- Athanassoula, E. & Misiriotis, A. 2002, MNRAS, 330, 35
- Baade, W. 1944, ApJ, 100, 137
- Bacon, R., Adam, G., Baranne, A., Courtes, G., Dubet, D., Dubois, J. P., Emsellem, E., Ferruit, P., Georgelin, Y., Monnet, G., Pecontal, E., Rousset, A., & Say, F. 1995, A&AS, 113, 347
- Bacon, R., Copin, Y., Monnet, G., Miller, B. W., Allington-Smith, J. R., Bureau, M., Carollo, C. M., Davies, R. L., Emsellem, E., Kuntschner, H., Peletier, R. F., Verolme, E. K., & de Zeeuw, P. T. 2001, MNRAS, 326, 23
- Baldry, I. K., Bland-Hawthorn, J., & Robertson, J. G. 2004, PASP, 116, 403
- Barden, S. C., Sawyer, D. G., & Honeycutt, R. K. 1998, in Society of Photo-Optical Instrumentation Engineers (SPIE) Conference Series, Vol. 3355, Society of Photo-Optical Instrumentation Engineers (SPIE) Conference Series, ed. S. D'Odorico, 892–899
- Barnes, S., Cottrell, P. L., Albrow, M. D., Frost, N., Graham, G., Kershaw, G., Ritchie, R., Jones, D. J., Sharples, R. M., Bramall, D. G., Clark, P., Luke, P., Schmoll, J., & Tyas, L. M. G. 2008, in Ground-based and Airborne Instrumentation for Astronomy II Conference - Proceedings of SPIE Volume 7014 Paper 7014-152 (2008), Presented at the Society of Photo-Optical Instrumentation Engineers (SPIE) Conference

- Bell, E. F., Baugh, C. M., Cole, S., Frenk, C. S., & Lacey, C. G. 2003, *MNRAS*, 343, 367
- Bender, P. L., Currie, D. G., Dicke, R. H., Eckhardt, D. H., Faller, J. E., Kaula, W. M., Mulholland, J. D., Plotkin, H. H., Poultney, S. K., Silverberg, E. C., Wilkinson, D. T., Williams, J. G., & Alley, C. O. 1973, *Science*, 182, 229
- Bender, R. 1990, *A&A*, 229, 441
- Bender, R., Doebereiner, S., & Moellenhoff, C. 1988, *A&AS*, 74, 385
- Bender, R. & Moellenhoff, C. 1987, *A&A*, 177, 71
- Bender, R. & Paquet, A. 1995, in *IAU Symposium*, Vol. 164, *Stellar Populations*, ed. P. C. van der Kruit & G. Gilmore, 259
- Bender, R., Paquet, A., & Nieto, J.-L. 1991, *A&A*, 246, 349
- Bender, R., Saglia, R. P., & Gerhard, O. E. 1994, *MNRAS*, 269, 785
- Bertin, E. & Arnouts, S. 1996, *A&AS*, 117, 393
- Bertola, F., Cinzano, P., Corsini, E. M., Pizzella, A., Persic, M., & Salucci, P. 1996, *ApJL*, 458, L67+
- Bertola, F., Cinzano, P., Corsini, E. M., Rix, H.-W., & Zeilinger, W. W. 1995, *ApJL*, 448, L13+
- Bertola, F. & Corsini, E. M. 1999, in *IAU Symposium*, Vol. 186, *Galaxy Interactions at Low and High Redshift*, ed. J. E. Barnes & D. B. Sanders, 149–+
- Bertola, F., Corsini, E. M., Vega Beltrán, J. C., Pizzella, A., Sarzi, M., Cappellari, M., & Funes, J. G. 1999, *ApJL*, 519, L127
- Bettoni, D. & Galletta, G. 1997, *A&AS*, 124, 61
- Beuing, J., Bender, R., Mendes de Oliveira, C., Thomas, D., & Maraston, C. 2002, *A&A*, 395, 431
- Binney, J. 2005, *MNRAS*, 363, 937
- Binney, J. & Tremaine, S. 1987, *Galactic dynamics*
- Blakeslee, J. P., Jordán, A., Mei, S., Côté, P., Ferrarese, L., Infante, L., Peng, E. W., Tonry, J. L., & West, M. J. 2009, *ApJ*, 694, 556
- Blanc, G. A., Adams, J., Gebhardt, K., Hill, G. J., Drory, N., Hao, L., Bender, R., Ciardullo, R., Finkelstein, S. L., Gawiser, E., Gronwall, C., Hopp, U., Jeong, D., Kelzenberg, R., Komatsu, E., MacQueen, P., Murphy, J. D., Roth, M. M., Schneider, D. P., & Tufts, J. 2010a, *ArXiv e-prints*

- Blanc, G. A., Gebhardt, K., Heiderman, A., Evans, II, N. J., Jogee, S., van den Bosch, R., Marinova, I., Weinzirl, T., Yoachim, P., Drory, N., Fabricius, M., Fisher, D., Hao, L., MacQueen, P. J., Shen, J., Hill, G. J., & Kormendy, J. 2010b, in *Astronomical Society of the Pacific Conference Series*, Vol. 432, *New Horizons in Astronomy: Frank N. Bash Symposium 2009*, ed. L. M. Stanford, J. D. Green, L. Hao, & Y. Mao, 180–+
- Blanc, G. A., Heiderman, A., Gebhardt, K., Evans, II, N. J., & Adams, J. 2009, *ApJ*, 704, 842
- Block, D. L., Puerari, I., Knapen, J. H., Elmegreen, B. G., Buta, R., Stedman, S., & Elmegreen, D. M. 2001, *A&A*, 375, 761
- Block, D. L. & Wainscoat, R. J. 1991, , 353, 48
- Bonatto, C., Bica, E., & Alloin, D. 1989, *A&A*, 226, 23
- Bonnet, H., Conzelmann, R., Delabre, B., Donaldson, R., Fedrigo, E., Hubin, N. N., Kissler-Patig, M., Lizon, J.-L., Paufigue, J., Rossi, S., Stroebele, S., & Tordo, S. 2004, in *Society of Photo-Optical Instrumentation Engineers (SPIE) Conference Series*, Vol. 5490, *Society of Photo-Optical Instrumentation Engineers (SPIE) Conference Series*, ed. D. Bonaccini Calia, B. L. Ellerbroek, & R. Ragazzoni, 130–138
- Bottema, R. 1993, *A&A*, 275, 16
- Boulesteix, J., Georgelin, Y., Marcelin, M., & Monnet, G. 1984, in *Presented at the Society of Photo-Optical Instrumentation Engineers (SPIE) Conference*, Vol. 445, *Society of Photo-Optical Instrumentation Engineers (SPIE) Conference Series*, ed. A. Boksenberg & D. L. Crawford, 37–41
- Brault, J. W. & White, O. R. 1971, *A&A*, 13, 169
- Braun, R., Walterbos, R. A. M., & Kennicutt, Jr., R. C. 1992, , 360, 442
- Braun, R., Walterbos, R. A. M., Kennicutt, Jr., R. C., & Tacconi, L. J. 1994, *ApJ*, 420, 558
- Bruzual, G. & Charlot, S. 2003, *MNRAS*, 344, 1000
- Buckley, D. A. H., Cottrell, P. L., Nordsieck, K. H., O'Donoghue, D. E., & Williams, T. B. 2004, in *Society of Photo-Optical Instrumentation Engineers (SPIE) Conference Series*, Vol. 5492, *Society of Photo-Optical Instrumentation Engineers (SPIE) Conference Series*, ed. A. F. M. Moorwood & M. Iye, 60–74
- Bureau, M. & Athanassoula, E. 2005, *ApJ*, 626, 159
- Bureau, M. & Freeman, K. C. 1999a, *AJ*, 118, 126
- . 1999b, *AJ*, 118, 126

- Burgh, E. B., Bershady, M. A., Westfall, K. B., & Nordsieck, K. H. 2007, *PASP*, 119, 1069
- Burkert, A. 1995, *ApJL*, 447, L25
- Busarello, G., Capaccioli, M., D'Onofrio, M., Longo, G., Richter, G., & Zaggia, S. 1996, *A&A*, 314, 32
- Buta, R. & Combes, F. 1996, *FCPH*, 17, 95
- Caon, N., Capaccioli, M., & D'Onofrio, M. 1993, *MNRAS*, 265, 1013
- Cappellari, M., Bertola, F., Burstein, D., Buson, L. M., Greggio, L., & Renzini, A. 1999, *ApJL*, 515, L17
- Cappellari, M. & Emsellem, E. 2004, *PASP*, 116, 138
- Carignan, C. & Freeman, K. C. 1985, *ApJ*, 294, 494
- Carlberg, R. G. 1984, *ApJ*, 286, 403
- Carollo, C. M. 1999, *ApJ*, 523, 566
- Carollo, C. M., Stiavelli, M., de Zeeuw, P. T., & Mack, J. 1997, *AJ*, 114, 2366
- Carollo, C. M., Stiavelli, M., & Mack, J. 1998, *AJ*, 116, 68
- Choi, P. I., Guhathakurta, P., & Johnston, K. V. 2002, *AJ*, 124, 310
- Chung, A. & Bureau, M. 2004, *AJ*, 127, 3192
- Ciotti, L. 1991, *A&A*, 249, 99
- Cole, S., Aragon-Salamanca, A., Frenk, C. S., Navarro, J. F., & Zepf, S. E. 1994, *MNRAS*, 271, 781
- Combes, F., Debbasch, F., Friedli, D., & Pfenniger, D. 1990, *A&A*, 233, 82
- Combes, F. & Sanders, R. H. 1981, *A&A*, 96, 164
- Conselice, C. J., Bershady, M. A., Dickinson, M., & Papovich, C. 2003, *AJ*, 126, 1183
- Copin, Y., Bacon, R., Emsellem, E., Bureau, M., Miller, B. W., Verolme, E., de Zeeuw, P. T., Davies, R., Peletier, R. F., Carollo, M. C., & Monnet, G. 2000, in *Astronomical Society of the Pacific Conference Series*, Vol. 197, *Dynamics of Galaxies: from the Early Universe to the Present*, ed. F. Combes, G. A. Mamon, & V. Charmandaris, 249–+
- Corsini, E. M., Pizzella, A., Sarzi, M., Cinzano, P., Vega Beltrán, J. C., Funes, J. G., Bertola, F., Persic, M., & Salucci, P. 1999, *A&A*, 342, 671
- Davidge, T. J. 2003, *ApJ*, 597, 289

- de Blok, W. J. G. 2010, *Advances in Astronomy*, 2010
- de Blok, W. J. G., van der Hulst, J. M., & Bothun, G. D. 1995, *MNRAS*, 274, 235
- de Blok, W. J. G., Walter, F., Brinks, E., Trachternach, C., Oh, S.-H., & Kennicutt, Jr., R. C. 2008, *AJ*, 136, 2648
- de Lorenzo-Cáceres, A., Falcón-Barroso, J., Vazdekis, A., & Martínez-Valpuesta, I. 2008, *ApJL*, 684, L83
- De Lucia, G., Fontanot, F., Wilman, D., & Monaco, P. 2011, *MNRAS*, 414, 1439
- De Lucia, G., Springel, V., White, S. D. M., Croton, D., & Kauffmann, G. 2006, *MNRAS*, 366, 499
- De Rijcke, S., Prugniel, P., Simien, F., & Dejonghe, H. 2006, *MNRAS*, 369, 1321
- de Vaucouleurs, G. & de Vaucouleurs, A. 1964, *Reference catalogue of bright galaxies*, ed. de Vaucouleurs, G. & de Vaucouleurs, A.
- de Vaucouleurs, G., de Vaucouleurs, A., Corwin, Jr., H. G., Buta, R. J., Paturel, G., & Fouque, P. 1991, *Third Reference Catalogue of Bright Galaxies*, ed. de Vaucouleurs, G., de Vaucouleurs, A., Corwin, H. G., Jr., Buta, R. J., Paturel, G., & Fouque, P.
- de Zeeuw, P. T., Bureau, M., Emsellem, E., Bacon, R., Carollo, C. M., Copin, Y., Davies, R. L., Kuntschner, H., Miller, B. W., Monnet, G., Peletier, R. F., & Verolme, E. K. 2002, *MNRAS*, 329, 513
- Debattista, V. P., Carollo, C. M., Mayer, L., & Moore, B. 2005, *ApJ*, 628, 678
- Debattista, V. P. & Sellwood, J. A. 2000, *ApJ*, 543, 704
- Dekel, A., Birnboim, Y., Engel, G., Freundlich, J., Goerdt, T., Mumcuoglu, M., Neistein, E., Pichon, C., Teyssier, R., & Zinger, E. 2009, , 457, 451
- Deul, E., Kuijken, K., & Valentijn, E. A. 2002, in *Presented at the Society of Photo-Optical Instrumentation Engineers (SPIE) Conference*, Vol. 4836, *Society of Photo-Optical Instrumentation Engineers (SPIE) Conference Series*, ed. J. A. Tyson & S. Wolff, 189–198
- Drozdovsky, I. O. & Karachentsev, I. D. 2000, *A&AS*, 142, 425
- Dumas, G., Mundell, C. G., Emsellem, E., & Nagar, N. M. 2007, *MNRAS*, 379, 1249
- Edvardsson, B., Andersen, J., Gustafsson, B., Lambert, D. L., Nissen, P. E., & Tomkin, J. 1993, *A&A*, 275, 101
- Efstathiou, G., Frenk, C. S., White, S. D. M., & Davis, M. 1988, *MNRAS*, 235, 715
- Eggen, O. J., Lynden-Bell, D., & Sandage, A. R. 1962, *ApJ*, 136, 748

- Eisenhauer, F., Abuter, R., Bickert, K., Biancat-Marchet, F., Bonnet, H., Brynnel, J., Conzelmann, R. D., Delabre, B., Donaldson, R., Farinato, J., Fedrigo, E., Genzel, R., Hubin, N. N., Iserlohe, C., Kasper, M. E., Kissler-Patig, M., Monnet, G. J., Roehrl, C., Schreiber, J., Stroebele, S., Tecza, M., Thatte, N. A., & Weisz, H. 2003a, in Presented at the Society of Photo-Optical Instrumentation Engineers (SPIE) Conference, Vol. 4841, Society of Photo-Optical Instrumentation Engineers (SPIE) Conference Series, ed. M. Iye & A. F. M. Moorwood, 1548–1561
- Eisenhauer, F., Tecza, M., Thatte, N., Genzel, R., Abuter, R., Iserlohe, C., Schreiber, J., Huber, S., Roehrl, C., Horrobin, M., Schegerer, A., Baker, A. J., Bender, R., Davies, R., Lehnert, M., Lutz, D., Nesvadba, N., Ott, T., Seitz, S., Schoedel, R., Tacconi, L. J., Bonnet, H., Castillo, R., Conzelmann, R., Donaldson, R., Finger, G., Gillet, G., Hubin, N., Kissler-Patig, M., Lizon, J.-L., Monnet, G., & Stroebele, S. 2003b, *The Messenger*, 113, 17
- Ekholm, T., Lanoix, P., Teerikorpi, P., Fouqué, P., & Paturel, G. 2000, *A&A*, 355, 835
- Elmegreen, B. G., Bournaud, F., & Elmegreen, D. M. 2008, *ApJ*, 688, 67
- Emsellem, E., Cappellari, M., Peletier, R. F., McDermid, R. M., Bacon, R., Bureau, M., Copin, Y., Davies, R. L., Krajnović, D., Kuntschner, H., Miller, B. W., & de Zeeuw, P. T. 2004, *MNRAS*, 352, 721
- Erwin, P. 2004, *A&A*, 415, 941
- Erwin, P. & Sparke, L. S. 1999, *ApJL*, 521, L37
- . 2002, *AJ*, 124, 65
- . 2003, *ApJS*, 146, 299
- Eskridge, P. B., Frogel, J. A., Pogge, R. W., Quillen, A. C., Berlind, A. A., Davies, R. L., DePoy, D. L., Gilbert, K. M., Houdashelt, M. L., Kuchinski, L. E., Ramírez, S. V., Sellgren, K., Stutz, A., Terndrup, D. M., & Tiede, G. P. 2002a, *ApJS*, 143, 73
- . 2002b, *ApJS*, 143, 73
- Eskridge, P. B., Frogel, J. A., Pogge, R. W., Quillen, A. C., Davies, R. L., DePoy, D. L., Houdashelt, M. L., Kuchinski, L. E., Ramírez, S. V., Sellgren, K., Terndrup, D. M., & Tiede, G. P. 2000, *AJ*, 119, 536
- Faber, S. M. & Jackson, R. E. 1976, *ApJ*, 204, 668
- Fabricius, M. H., Barnes, S., Bender, R., Drory, N., Grupp, F., Hill, G. J., Hopp, U., & MacQueen, P. J. 2008, in Society of Photo-Optical Instrumentation Engineers (SPIE) Conference Series, Vol. 7014, Society of Photo-Optical Instrumentation Engineers (SPIE) Conference Series

- Fabricius, M. H., Saglia, R. P., Fisher, D. B., Drory, N., Bender, R., & Hopp, U. 2011, ApJ
- Falcón-Barroso, J., Bacon, R., Bureau, M., Cappellari, M., Davies, R. L., de Zeeuw, P. T., Emsellem, E., Fathi, K., Krajnović, D., Kuntschner, H., McDermid, R. M., Peletier, R. F., & Sarzi, M. 2006, MNRAS, 369, 529
- Finkelstein, S. L., Hill, G. J., Gebhardt, K., Adams, J., Blanc, G. A., Papovich, C., Ciardullo, R., Drory, N., Gawiser, E., Gronwall, C., Schneider, D. P., & Tran, K.-V. 2011, ApJ, 729, 140
- Fisher, D. 1997, AJ, 113, 950
- Fisher, D., Franx, M., & Illingworth, G. 1996, ApJ, 459, 110
- Fisher, D. B. 2006, ApJL, 642, L17
- Fisher, D. B. & Drory, N. 2008, AJ, 136, 773
- . 2010, ApJ, 716, 942
- . 2011, ApJL, 733, L47+
- Fontanot, F., De Lucia, G., Wilman, D., & Monaco, P. 2011, ArXiv e-prints
- Förster Schreiber, N. M., Genzel, R., Lehnert, M. D., Bouché, N., Verma, A., Erb, D. K., Shapley, A. E., Steidel, C. C., Davies, R., Lutz, D., Nesvadba, N., Tacconi, L. J., Eisenhauer, F., Abuter, R., Gilbert, A., Gillessen, S., & Sternberg, A. 2006, ApJ, 645, 1062
- Freeman, K. C. 1970, ApJ, 160, 811
- Frenk, C. S., White, S. D. M., Efstathiou, G., & Davis, M. 1985, , 317, 595
- Gadotti, D. A. & de Souza, R. E. 2005, ApJ, 629, 797
- Gadotti, D. A. & dos Anjos, S. 2001, AJ, 122, 1298
- Ganda, K., Falcón-Barroso, J., Peletier, R. F., Cappellari, M., Emsellem, E., McDermid, R. M., de Zeeuw, P. T., & Carollo, C. M. 2006, MNRAS, 367, 46
- Gebhardt, K., Richstone, D., Kormendy, J., Lauer, T. R., Ajhar, E. A., Bender, R., Dressler, A., Faber, S. M., Grillmair, C., Magorrian, J., & Tremaine, S. 2000, AJ, 119, 1157
- Gebhardt, K., Richstone, D., Tremaine, S., Lauer, T. R., Bender, R., Bower, G., Dressler, A., Faber, S. M., Filippenko, A. V., Green, R., Grillmair, C., Ho, L. C., Kormendy, J., Magorrian, J., & Pinkney, J. 2003, ApJ, 583, 92

- Gebhardt, K. & Thomas, J. 2009, *ApJ*, 700, 1690
- Geha, M., Guhathakurta, P., Rich, R. M., & Cooper, M. C. 2006, *AJ*, 131, 332
- Gerhard, O. E. 1993, *MNRAS*, 265, 213
- Gerssen, J., Kuijken, K., & Merrifield, M. R. 1999, *MNRAS*, 306, 926
- . 2003, *MNRAS*, 345, 261
- Gössl, C. A. & Riffeser, A. 2002, *A&A*, 381, 1095
- Graham, A. & Colless, M. 1997, *MNRAS*, 287, 221
- Grupp, F. 2006, *NewAR*, 50, 323
- Grupp, F., Lang, F., & Hopp, U. 2008, in *Ground-based and Airborne Instrumentation for Astronomy II Conference - Proceedings of SPIE Volume 7014 Paper 7014-281 (2008)*, Presented at the Society of Photo-Optical Instrumentation Engineers (SPIE) Conference
- Gultekin, K., Richstone, D. O., Gebhardt, K., Lauer, T. R., Tremaine, S., Aller, M. C., Bender, R., Dressler, A., Faber, S. M., Filippenko, A. V., Green, R., Ho, L. C., Kormendy, J., Magorrian, J., Pinkney, J., & Siopis, C. 2009, *ArXiv e-prints*
- Hasan, H. & Norman, C. 1990, *ApJ*, 361, 69
- Hastings, W. K. 1970, *Biometrika*, 57, 97
- Héraudeau, P. & Simien, F. 1998, *A&AS*, 133, 317
- Héraudeau, P., Simien, F., Maubon, G., & Prugniel, P. 1999, *A&AS*, 136, 509
- Hill, G. J., Gebhardt, K., Komatsu, E., Drory, N., MacQueen, P. J., Adams, J., Blanc, G. A., Koehler, R., Rafal, M., Roth, M. M., Kelz, A., Gronwall, C., Ciardullo, R., & Schneider, D. P. 2008a, in *Astronomical Society of the Pacific Conference Series, Vol. 399, Panoramic Views of Galaxy Formation and Evolution*, ed. T. Kodama, T. Yamada, & K. Aoki, 115–+
- Hill, G. J., Gebhardt, K., Komatsu, E., & MacQueen, P. J. 2004, in *American Institute of Physics Conference Series, Vol. 743, The New Cosmology: Conference on Strings and Cosmology*, ed. R. E. Allen, D. V. Nanopoulos, & C. N. Pope, 224–233
- Hill, G. J., Lee, H., Vattiat, B. L., Adams, J. J., Marshall, J. L., Drory, N., Depoy, D. L., Blanc, G., Bender, R., Booth, J. A., Chonis, T., Cornell, M. E., Gebhardt, K., Good, J., Grupp, F., Haynes, R., Kelz, A., MacQueen, P. J., Mollison, N., Murphy, J. D., Rafal, M. D., Rambold, W. N., Roth, M. M., Savage, R., & Smith, M. P. 2010, in *Society of Photo-Optical Instrumentation Engineers (SPIE) Conference Series, Vol. 7735, Society of Photo-Optical Instrumentation Engineers (SPIE) Conference Series*

- Hill, G. J., MacQueen, P. J., Smith, M. P., Tufts, J. R., Roth, M. M., Kelz, A., Adams, J. J., Drory, N., Grupp, F., Barnes, S. I., Blanc, G. A., Murphy, J. D., Altmann, W., Wesley, G. L., Segura, P. R., Good, J. M., Booth, J. A., Bauer, S.-M., Popow, E., Goertz, J. A., Edmonston, R. D., & Wilkinson, C. P. 2008b, in Society of Photo-Optical Instrumentation Engineers (SPIE) Conference Series, Vol. 7014, Society of Photo-Optical Instrumentation Engineers (SPIE) Conference Series
- Hill, G. J., MacQueen, P. J., Tufts, J. R., Kelz, A., Roth, M. M., Altmann, W., Segura, P., Gebhardt, K., & Palunas, P. 2006, in Presented at the Society of Photo-Optical Instrumentation Engineers (SPIE) Conference, Vol. 6269, Ground-based and Airborne Instrumentation for Astronomy. Edited by McLean, Ian S.; Iye, Masanori. Proceedings of the SPIE, Volume 6269, pp. 62692J (2006).
- Hill, G. J., Nicklas, H. E., MacQueen, P. J., Mitsch, W., Wellem, W., Altmann, W., Wesley, G. L., & Ray, F. B. 1998, in Presented at the Society of Photo-Optical Instrumentation Engineers (SPIE) Conference, Vol. 3355, Society of Photo-Optical Instrumentation Engineers (SPIE) Conference Series, ed. S. D'Odorico, 433–443
- Hodge, P. W. 1973, *ApJ*, 182, 671
- Hopp, U., Goessl, C. A., Grupp, F., Lang, F., Mitsch, W., Relke, H., Ries, C., Wilke, S., & Bender, R. 2008, in Observatory Operations: Strategies, Processes, and Systems Conference - Proceedings of SPIE Volume 7016 Paper 7016-65 (2008), Presented at the Society of Photo-Optical Instrumentation Engineers (SPIE) Conference
- Hubble, E. 1929, *Proceedings of the National Academy of Science*, 15, 168
- Illingworth, G. 1977, *ApJL*, 218, L43
- Jablonka, P., Martin, P., & Arimoto, N. 1996, *AJ*, 112, 1415
- Jensen, J. B., Tonry, J. L., Barris, B. J., Thompson, R. I., Liu, M. C., Rieke, M. J., Ajhar, E. A., & Blakeslee, J. P. 2003, *ApJ*, 583, 712
- Jungwiert, B., Combes, F., & Axon, D. J. 1997, *A&AS*, 125, 479
- Kaufmann, T., Mayer, L., Wadsley, J., Stadel, J., & Moore, B. 2007, *MNRAS*, 375, 53
- Kelz, A., Bauer, S. M., Grupp, F., Hill, G. J., Popow, E., Palunas, P., Roth, M. M., MacQueen, P. J., & Tripphahn, U. 2006, in Society of Photo-Optical Instrumentation Engineers (SPIE) Conference Series, Vol. 6273, Society of Photo-Optical Instrumentation Engineers (SPIE) Conference Series
- Kennicutt, Jr., R. C. 1998, *ApJ*, 498, 541
- Kent, S. M. 1987, *AJ*, 93, 1062

- Kinney, A. L., Bohlin, R. C., Calzetti, D., Panagia, N., & Wyse, R. F. G. 1993, *ApJS*, 86, 5
- Knapen, J. H., Shlosman, I., & Peletier, R. F. 2000, *ApJ*, 529, 93
- Kormendy, J. 1979, *ApJ*, 227, 714
- Kormendy, J. 1982a, in *Saas-Fee Advanced Course 12: Morphology and Dynamics of Galaxies*, ed. L. Martinet & M. Mayor, 113–288
- . 1982b, *ApJ*, 257, 75
- Kormendy, J. 1993, in *IAU Symposium, Vol. 153, Galactic Bulges*, ed. H. Dejonghe & H. J. Habing, 209–+
- Kormendy, J. & Barentine, J. C. 2010, *ApJL*, 715, L176
- Kormendy, J., Drory, N., Bender, R., & Cornell, M. E. 2010, *ApJ*, 723, 54
- Kormendy, J. & Fisher, D. B. 2008, in *Astronomical Society of the Pacific Conference Series, Vol. 396, Astronomical Society of the Pacific Conference Series*, ed. J. G. Funes & E. M. Corsini, 297–+
- Kormendy, J., Fisher, D. B., Cornell, M. E., & Bender, R. 2008, *ArXiv e-prints*
- Kormendy, J. & Kennicutt, Jr., R. C. 2004, *ARAA*, 42, 603
- Krajnović, D., McDermid, R. M., Cappellari, M., & Davies, R. L. 2009, *MNRAS*, 399, 1839
- Kroupa, P. 2001, *MNRAS*, 322, 231
- Kuntschner, H., Emsellem, E., Bacon, R., Bureau, M., Cappellari, M., Davies, R. L., de Zeeuw, P. T., Falcón-Barroso, J., Krajnović, D., McDermid, R. M., Peletier, R. F., & Sarzi, M. 2006, *MNRAS*, 369, 497
- Kuzio de Naray, R., McGaugh, S. S., & de Blok, W. J. G. 2008, *ApJ*, 676, 920
- Larson, R. B. 1974, *MNRAS*, 166, 585
- Lauer, T. R. 1985, *ApJ*, 292, 104
- Laurikainen, E. & Salo, H. 2002, *MNRAS*, 337, 1118
- Laurikainen, E., Salo, H., Buta, R., & Vasylyev, S. 2004, *MNRAS*, 355, 1251
- Le Borgne, D., Rocca-Volmerange, B., Prugniel, P., Lançon, A., Fioc, M., & Soubiran, C. 2004, *A&A*, 425, 881

- Lee, M. G. 1996, *AJ*, 112, 1438
- MacArthur, L. A., González, J. J., & Courteau, S. 2009, *MNRAS*, 395, 28
- Maillard, J. P. 1995, in *Astronomical Society of the Pacific Conference Series*, Vol. 71, IAU Colloq. 149: Tridimensional Optical Spectroscopic Methods in Astrophysics, ed. G. Comte & M. Marcelin, 316–+
- Maraston, C. 1998, *MNRAS*, 300, 872
- . 2005, *MNRAS*, 362, 799
- Martinez-Valpuesta, I., Shlosman, I., & Heller, C. 2006, *ApJ*, 637, 214
- Martini, P., Regan, M. W., Mulchaey, J. S., & Pogge, R. W. 2003, *ApJS*, 146, 353
- Massey, P., Strobel, K., Barnes, J. V., & Anderson, E. 1988, *ApJ*, 328, 315
- Mehlert, D., Saglia, R. P., Bender, R., & Wegner, G. 2000, *A&AS*, 141, 449
- Méndez-Abreu, J., Corsini, E. M., Debattista, V. P., De Rijcke, S., Aguerri, J. A. L., & Pizzella, A. 2008, *ApJL*, 679, L73
- Merrifield, M. R. & Kuijken, K. 1994, *ApJ*, 432, 575
- Merrifield, M. R. 1996, in *Astronomical Society of the Pacific Conference Series*, Vol. 91, IAU Colloq. 157: Barred Galaxies, ed. R. Buta, D. A. Crocker, & B. G. Elmegreen, 179
- Mulchaey, J. S. & Regan, M. W. 1997, *ApJL*, 482, L135
- Mulchaey, J. S., Regan, M. W., & Kundu, A. 1997, *ApJS*, 110, 299
- Murphy, J. D., Gebhardt, K., & Adams, J. J. 2011, *ApJ*, 729, 129
- Murphy, J. D., MacQueen, P. J., Hill, G. J., Grupp, F., Kelz, A., Palunas, P., Roth, M., & Fry, A. 2008, in *Presented at the Society of Photo-Optical Instrumentation Engineers (SPIE) Conference*, Vol. 7018, *Society of Photo-Optical Instrumentation Engineers (SPIE) Conference Series*
- Navarro, J. F., Frenk, C. S., & White, S. D. M. 1996, *ApJ*, 462, 563
- Navarro, J. F., Ludlow, A., Springel, V., Wang, J., Vogelsberger, M., White, S. D. M., Jenkins, A., Frenk, C. S., & Helmi, A. 2010, *MNRAS*, 402, 21
- Newton, I. 1672, *Philosophical Transactions of the Royal Society*, 3075
- Norman, C. A., Sellwood, J. A., & Hasan, H. 1996, *ApJ*, 462, 114
- Nowak, N., Saglia, R. P., Thomas, J., Bender, R., Davies, R. I., & Gebhardt, K. 2008, *MNRAS*, 391, 1629

- Nowak, N., Saglia, R. P., Thomas, J., Bender, R., Pannella, M., Gebhardt, K., & Davies, R. I. 2007, *MNRAS*, 379, 909
- Nowak, N., Thomas, J., Erwin, P., Saglia, R. P., Bender, R., & Davies, R. I. 2010, *MNRAS*, 403, 646
- Oh, S.-H., de Blok, W. J. G., Brinks, E., Walter, F., & Kennicutt, Jr., R. C. 2011, *AJ*, 141, 193
- Oke, J. B. 1990, *AJ*, 99, 1621
- Patton, D. R., Pritchett, C. J., Carlberg, R. G., Marzke, R. O., Yee, H. K. C., Hall, P. B., Lin, H., Morris, S. L., Sawicki, M., Shepherd, C. W., & Wirth, G. D. 2002, *ApJ*, 565, 208
- Paturel, G., Petit, C., Prugniel, P., Theureau, G., Rousseau, J., Brouty, M., Dubois, P., & Cambr esy, L. 2003, *A&A*, 412, 45
- Pedrotti, F. L. & Pedrotti, L. S. 1993, *Introduction to Optics* (New Jersey: Prentice Hall)
- Peletier, R. F. 1993, *A&A*, 271, 51
- Peletier, R. F., Falc on-Barroso, J., Bacon, R., Cappellari, M., Davies, R. L., de Zeeuw, P. T., Emsellem, E., Ganda, K., Krajnovi c, D., Kuntschner, H., McDermid, R. M., Sarzi, M., & van de Ven, G. 2007, *MNRAS*, 379, 445
- Pfenniger, D. 1984, *A&A*, 134, 373
- . 1985, *A&A*, 150, 112
- Pfenniger, D. & Norman, C. 1990, *ApJ*, 363, 391
- Pignatelli, E., Corsini, E. M., Vega Beltr an, J. C., Scarlata, C., Pizzella, A., Funes, J. G., Zeilinger, W. W., Beckman, J. E., & Bertola, F. 2001, *MNRAS*, 323, 188
- Pizzella, A., Corsini, E. M., Vega Beltr an, J. C., & Bertola, F. 2004, *A&A*, 424, 447
- Prada, F., Gutierrez, C. M., Peletier, R. F., & McKeith, C. D. 1996, *ApJL*, 463, L9+
- Press, W. H. 2002, *Numerical recipes in C++ : the art of scientific computing*, ed. Press, W. H.
- Press, W. H., Teukolsky, S. A., Vetterling, W. T., & Flannery, B. P. 2007, *Numerical Recipes 3rd Edition: The Art of Scientific Computing*, 3rd edn. (Cambridge University Press)
- Raha, N., Sellwood, J. A., James, R. A., & Kahn, F. D. 1991, , 352, 411

- Ramsey, L. W., Adams, M. T., Barnes, T. G., Booth, J. A., Cornell, M. E., Fowler, J. R., Gaffney, N. I., Glaspey, J. W., Good, J. M., Hill, G. J., Kelton, P. W., Krabbendam, V. L., Long, L., MacQueen, P. J., Ray, F. B., Ricklefs, R. L., Sage, J., Sebring, T. A., Spiesman, W. J., & Steiner, M. 1998a, in *Society of Photo-Optical Instrumentation Engineers (SPIE) Conference Series*, Vol. 3352, *Society of Photo-Optical Instrumentation Engineers (SPIE) Conference Series*, ed. L. M. Stepp, 34–42
- Ramsey, L. W., Adams, M. T., Barnes, T. G., Booth, J. A., Cornell, M. E., Fowler, J. R., Gaffney, N. I., Glaspey, J. W., Good, J. M., Hill, G. J., Kelton, P. W., Krabbendam, V. L., Long, L., MacQueen, P. J., Ray, F. B., Ricklefs, R. L., Sage, J., Sebring, T. A., Spiesman, W. J., & Steiner, M. 1998b, in *Presented at the Society of Photo-Optical Instrumentation Engineers (SPIE) Conference*, Vol. 3352, *Society of Photo-Optical Instrumentation Engineers (SPIE) Conference Series*, ed. L. M. Stepp, 34–42
- Renzini, A. 1999, in *The Formation of Galactic Bulges*, ed. C. M. Carollo, H. C. Ferguson, & R. F. G. Wyse, 9
- Riess, A. G., Macri, L., Casertano, S., Sosey, M., Lampeitl, H., Ferguson, H. C., Filippenko, A. V., Jha, S. W., Li, W., Chornock, R., & Sarkar, D. 2009, *ApJ*, 699, 539
- Roškar, R., Debattista, V. P., Stinson, G. S., Quinn, T. R., Kaufmann, T., & Wadsley, J. 2008, *ApJL*, 675, L65
- Rubin, V. C., Burstein, D., Ford, Jr., W. K., & Thonnard, N. 1985, *ApJ*, 289, 81
- Rusli, S. P. 2012
- Rusli, S. P., Thomas, J., Erwin, P., Saglia, R. P., Nowak, N., & Bender, R. 2011, *MNRAS*, 410, 1223
- Saglia, R. P., Bender, R., & Dressler, A. 1993, *A&A*, 279, 75
- Saglia, R. P., Fabricius, M., Bender, R., Montalto, M., Lee, C.-H., Riffeser, A., Seitz, S., Morganti, L., Gerhard, O., & Hopp, U. 2010, *A&A*, 509, A61+
- Saha, A., Thim, F., Tammann, G. A., Reindl, B., & Sandage, A. 2006, *ApJS*, 165, 108
- Saha, K., Tseng, Y., & Taam, R. E. 2010, *ApJ*, 721, 1878
- Sakamoto, K., Okumura, S. K., Ishizuki, S., & Scoville, N. Z. 1999, *ApJS*, 124, 403
- Salpeter, E. E. 1955, *ApJ*, 121, 161
- Sarzi, M., Falcón-Barroso, J., Davies, R. L., Bacon, R., Bureau, M., Cappellari, M., de Zeeuw, P. T., Emsellem, E., Fathi, K., Krajnović, D., Kuntschner, H., McDermid, R. M., & Peletier, R. F. 2006, *MNRAS*, 366, 1151

- Savage, R., Booth, J., Cornell, M., Good, J., Hill, G. J., Lee, H., MacQueen, P., Rafal, M., Vattiat, B., Gebhardt, K., Beno, J., Zierer, J., Perry, D., Rafferty, T., Ramiller, C., Taylor, III, C., Beets, T., Hayes, R., Heisler, J., Hinze, S., Soukup, I., Jackson, J., Mock, J., Worthington, M., Mollison, N., Molina, O., South, B., Wardell, D., & Wedeking, G. 2010, in Society of Photo-Optical Instrumentation Engineers (SPIE) Conference Series, Vol. 7733, Society of Photo-Optical Instrumentation Engineers (SPIE) Conference Series
- Schiavon, R. P. 2007, *ApJS*, 171, 146
- Schulze, A. & Gebhardt, K. 2011, *ApJ*, 729, 21
- Schwarzschild, M. 1979, *ApJ*, 232, 236
- Scorza, C. & Bender, R. 1995, *A&A*, 293, 20
- Seigar, M. S. & James, P. A. 1998, *MNRAS*, 299, 672
- Sellwood, J. A. & Binney, J. J. 2002, *MNRAS*, 336, 785
- Sellwood, J. A. & Wilkinson, A. 1993, *Reports on Progress in Physics*, 56, 173
- Shen, J. & Sellwood, J. A. 2004, *Coevolution of Black Holes and Galaxies*
- Simien, F. & Prugniel, P. 1998, *A&AS*, 131, 287
- . 2002, *A&A*, 384, 371
- Simkin, S. M. 1974, *A&A*, 31, 129
- Siopis, C., Gebhardt, K., Lauer, T. R., Kormendy, J., Pinkney, J., Richstone, D., Faber, S. M., Tremaine, S., Aller, M. C., Bender, R., Bower, G., Dressler, A., Filippenko, A. V., Green, R., Ho, L. C., & Magorrian, J. 2009, *ApJ*, 693, 946
- Smirnov, N. V. 1939, *Bulletin Moscow University*, 2, 3
- Song, M. in prep 2012
- Soubiran, C., Bienaymé, O., Mishenina, T. V., & Kovtyukh, V. V. 2008, *A&A*, 480, 91
- Springob, C. M., Masters, K. L., Haynes, M. P., Giovanelli, R., & Marinoni, C. 2009, *ApJS*, 182, 474
- Stone, R. P. S. 1977, *ApJ*, 218, 767
- Storchi-Bergmann, T., Dors, Jr., O. L., Riffel, R. A., Fathi, K., Axon, D. J., Robinson, A., Marconi, A., & Östlin, G. 2007, *ApJ*, 670, 959
- Subbarao, M., Choi, T. S., & Nikzad, A. 1993, *Optical Engineering*, 32, 2824

- Tamburro, D., Rix, H.-W., Leroy, A. K., Mac Low, M.-M., Walter, F., Kennicutt, R. C., Brinks, E., & de Blok, W. J. G. 2009, *AJ*, 137, 4424
- Taylor, K. & Atherton, P. D. 1980, *MNRAS*, 191, 675
- Terndrup, D. M. 1993, in *Astronomical Society of the Pacific Conference Series*, Vol. 39, *The Minnesota Lectures on the Structure and Dynamics of the Milky Way*, ed. R. M. Humphreys, 9
- Thomas, D., Greggio, L., & Bender, R. 1999, *MNRAS*, 302, 537
- Thomas, D., Maraston, C., & Bender, R. 2002, , 281, 371
- . 2003, *MNRAS*, 339, 897
- Tonry, J. L., Dressler, A., Blakeslee, J. P., Ajhar, E. A., Fletcher, A. B., Luppino, G. A., Metzger, M. R., & Moore, C. B. 2001, *ApJ*, 546, 681
- Toomre, A. 1977, in *Evolution of Galaxies and Stellar Populations*, ed. B. M. Tinsley & R. B. G. Larson D. Campbell, 401
- Trager, S. C., Worthey, G., Faber, S. M., Burstein, D., & Gonzalez, J. J. 1998, *ApJS*, 116, 1
- Treuthardt, P., Buta, R., Salo, H., & Laurikainen, E. 2007, *AJ*, 134, 1195
- Tully, R. B. & Fisher, J. R. 1988, *Catalog of Nearby Galaxies*, ed. Tully, R. B. & Fisher, J. R.
- Tully, R. B., Rizzi, L., Shaya, E. J., Courtois, H. M., Makarov, D. I., & Jacobs, B. A. 2009, *AJ*, 138, 323
- Valluri, M., Ferrarese, L., Merritt, D., & Joseph, C. L. 2005, *ApJ*, 628, 137
- van Albada, T. S. 1982, *MNRAS*, 201, 939
- van den Bergh, S., Abraham, R. G., Whyte, L. F., Merrifield, M. R., Eskridge, P. B., Frogel, J. A., & Pogge, R. 2002, *AJ*, 123, 2913
- van der Marel, R. P. & Franx, M. 1993, *ApJ*, 407, 525
- Vanderriest, C. 1980, *PASP*, 92, 858
- Vazdekis, A. 1999, *ApJ*, 513, 224
- Vazdekis, A., Sánchez-Blázquez, P., Falcón-Barroso, J., Cenarro, A. J., Beasley, M. A., Cardiel, N., Gorgas, J., & Peletier, R. F. 2010, *MNRAS*, 404, 1639

- Vega Beltrán, J. C., Pizzella, A., Corsini, E. M., Funes, J. G., Zeilinger, W. W., Beckman, J. E., & Bertola, F. 2001, *A&A*, 374, 394
- Weinberg, M. D. 1985, *MNRAS*, 213, 451
- Weiss, A., Peletier, R. F., & Matteucci, F. 1995, *A&A*, 296, 73
- White, S. D. M. & Frenk, C. S. 1991, *ApJ*, 379, 52
- White, S. D. M. & Rees, M. J. 1978a, *MNRAS*, 183, 341
- . 1978b, *MNRAS*, 183, 341
- Wilkinson, A., Sharples, R. M., Fosbury, R. A. E., & Wallace, P. T. 1986, *MNRAS*, 218, 297
- Worthey, G., Faber, S. M., & Gonzalez, J. J. 1992, *ApJ*, 398, 69
- Worthey, G., Faber, S. M., Gonzalez, J. J., & Burstein, D. 1994, *ApJS*, 94, 687
- Wozniak, H., Friedli, D., Martinet, L., Martin, P., & Bratschi, P. 1995, *A&AS*, 111, 115
- Yoachim, P., Roškar, R., & Debattista, V. P. 2010, *ApJL*, 716, L4
- Zacharias, N., Monet, D. G., Levine, S. E., Urban, S. E., Gaume, R., & Wycoff, G. L. 2005, *VizieR Online Data Catalog*, 1297, 0
- Zeilinger, W. W., Vega Beltrán, J. C., Rozas, M., Beckman, J. E., Pizzella, A., Corsini, E. M., & Bertola, F. 2001, , 276, 643

# Acknowledgements

First of all I wish to thank the Max-Planck Institute for Extraterrestrial Physics (MPE) and the University Observatory Munich and especially Ralf Bender and Ulrich Hopp for giving me this unique opportunity to construct an instrument in this thesis. Such an endeavour naturally includes a significant risk and I am grateful for the trust, the responsibility, and all the support that was given to me. They both provided tremendous amounts of advise and willingness to discuss many of the questions, details and problems which naturally occur during such a thesis.

I would like to thank Roberto Saglia to whom I owe all my wisdom concerning the extraction of accurate kinematics out of stellar spectra. He also provided the largest part of the raw data for the science part. The success of this thesis is largely owed to him and his advise. I would like to thank Niv Drory for the rich amount of advise, for the many long discussions, the introduction to astronomical observations and all the support during my work.

I want to especially acknowledge the contribution of Frank Group who — as the designer of the instrument — provided the backbone of the instrumentation part. He is largely responsible for the great success of the construction VIRUS-W. I wish to thank David Fisher who provided a large amount of the data that is included in the science part of this thesis. He added raw data as well as detailed surface brightness decompositions. Further, he provided input in many valuable discussions over the years.

I wish to express my gratefulness to all members of the Wendelstein instrumentation team. VIRUS-W really is the result of a team effort, in many meetings, emails, private communications they all contributed significantly to the great success of VIRUS-W. I would like to point out especially the help of Florian Lang who constructed many of the parts for VIRUS-W and was always approachable for questions concerning the mechanical design. I would also like to thank Claus Gössl who provided many comments and suggestions that added greatly to the accomplishment of this instrumentation effort. I would like to thank Wolfgang Mitch who as part of the instrumentation team provided many helpful suggestions and support around the electronic design.

Philipp Wullstein, Jan Snigula and Guillermo Blanc participated in the commissioning run of VIRUS-W, supported the assembly, the integration of the software into the telescope system and helped conducting the first observing run. The surprisingly smooth commissioning and the fact that we obtained science quality data literally from the first minute on, is largely owed to their great efforts.

I would also like to express my gratitude for all the help and support by the McDonald Observatory and its Staff. David Doss, Earl Green, Brian Roman, Terry Wilemon, Kevin Meyer, Darrin Crook have been extremely helpful both in preparations but also on site. We very much enjoyed the hospitality at the Astronomer Lodge. The staff has always made even extended stays a very enjoyable time. We thank the McDonald TAC and directorate for allowing us to bring VIRUS-W and their willingness to accept the inconvenience that comes with such endeavours.

With the design of the VIRUS-P instrument Philipp MacQueen and Gary Hill provided the soul of VIRUS-W. Both were always very open and willing to discuss the many questions around the detail of the design and the manufacturing of really each of the individual parts of VIRUS-W. Without question, the construction of VIRUS-W during the duration of this thesis would have been impossible. I further wish to express my appreciation for the design contributions of Stuart Barnes and Bernard Delabre who provided the raw design of the camera of VIRUS-W.

The construction of any astronomical instrument brings along the necessity for custom mechanical engineering and machining. In hundreds of hours Peter Well, Franz Mittermayer and Adolf Karasz of the machine shop at the University Observatory created the over one hundred custom parts the VIRUS-W needed. They did so with great amount of patience and experience and always with an exceptional degree of quality. I want to thank Toni Mittermayer who helped greatly with many aspects of the logistics and the handling of large parts. I also want to thank the head of the MPE machine shop Stephan Czempel for many fruitful discussions on the details of the mechanical design and his willingness to produce very critical parts at the MPE.

I wish to thank the many manufacturers who provided high quality optics and electronics. VIRUS-W functions so well because it is a sum of parts that all individually were produced to highest standards. I wish to point out the manufacturer of the camera cryostat Spectral Instruments and especially the help and support by Kevin Toerne. Further, I further wish to thank Präzisions Optik Gera (POG) for the production of the camera lens which in its optical quality exceeded all our expectations. I especially want to thank their executive director Aleksander Wlodarski, who personally lead the efforts of the construction of the lens. I also want to thank Manfred Groth who led the production of the large optical prisms at POG. Their optical quality is outstanding. We are greatly sorry that Manfred Groth did not live to see the completion and the success of VIRUS-W.

I wish to thank greatly Kaiser Optical System who, in a tremendous effort, produced one of the largest and highest resolution holographic gratings in existence and with the low resolution mode grating one of the most efficient gratings of any optical instrument. Here I want to thank especially Jim Arns who, over the years of this project, provided many important suggestions and critical improvements to the final design. With his endless effort to push the enhancements of the process to achieve the highest efficiency grating VIRUS-W owe a great amount of its brilliance to him.

I want to thank Peter Erwin for many very fruitful discussions. He has been a constant source of tremendous insight and detailed knowledge of the structural details of virtually all local galaxies. Also, I would like to thank Stephanie Rusli for making early results of

her dynamical modelling of NGC 3091 available before publication.

This work was supported by the SFB-Transregio 33 *The Dark Universe* by the Deutsche Forschungsgemeinschaft (DFG).

And finally and most importantly I wish to express my deepest gratitude to the support of my wife Wenjing Zhang. She had to carry large parts of the burdens that result from a thesis like this. Her patience over countless lost evenings and weekends and my extended trips to observing runs and conferences, her acceptance of my devotion of great amounts of time to this project really made this all possible. Thank you!

## CURRICULUM VITAE

## EDUCATION

**Max Planck Institute for Extraterrestrial Physics**, Munich, Germany

PhD, Astronomy

- Thesis Topic: Kinematics Across Bulge Types A Longslit Kinematic Survey and Dedicated Instrumentation
- Advisor: Professor Ralf Bender
- Area of Study: Galaxy evolution and instrumentation

**Technische Universität Berlin**, Berlin, Germany

Diploma, Physics, October 2006

- Thesis Topic: Quantum Efficiency Characterization of Fully Depleted back side illuminated CCD's
- Advisors: Armin Karcher and Professor Susanna Orlic
- Specializations: Quantum Optics and General Relativity

B.S. (equiv.), Computer Science, June 2004

- Specialization: (Software engineering and database development)

**Summerschools**

- Astronomical Instrumentation, Heidelberg, Sept. 2008
- Black Holes and Galaxy Evolution, Bad Honnef, Germany, August 2008
- pre-IAU Symposium Formation and Evolution of Galaxy Bulges, Oxford, UK, Jul. 2007
- Plasma physics: confinement, transport and collective effects, Greifswald, Germany, August 2008

**Hermann-Hesse-Oberschule, Berlin, Germany**

- High school diploma (Abitur), May 28-th, 1997

## PREVIOUS WORK EXPERIENCE

**Max Planck Institute for Extraterrestrial Physics**, Munich, Germany*PhD in the OPINAS group,***Since October 2006**

- Principle Investigator of the VIRUS-W Integral Field Unit spectrograph. Full responsibility for optical design, purchase of subcomponents, monitoring of manufacturing process, mechanical engineering, integration and commissioning of the instrument.

- Conducted programs to study stellar masses, star formation rates, stellar populations and black hole scaling relations of bulges in local spiral galaxies.
- Lead multi-year long-slit spectroscopic survey of bulges at the Hobblerly Elberly Telescope.

**Lawrence Berkeley National Laboratory, Berkeley, USA,**

*Master theses' work within the SNAP group* **April 2005 to May 2006**

- Responsible for the further implementation and automation of the quantum efficiency testing setup.
- Design of hard- and software and implementation of a device to measure the surface reflectivity of CCDs.
- Improvements of algorithms to measure various CCD characteristics such as quantum efficiency, gain and read noise.

*Internship, CCD testing, within the SNAP group* **March 2004 to Sept. 2004**

- Improved and added functionality to existing CCD readout software.
- Further development and implementation of various Charge-Coupled Devices (CCD) testing procedures such as *Pocket Pumping*, *EPER*.
- Development of software for ASIC (CRIC-chip) tests.

**University Hospital Carité Berlin, Department for Infection Prevention, Berlin, Germany**

*Civil Servant* **May 2000 to May, 2001**

- Endotoxins in air conditioning systems: In-field collection of samples to study the concentration of endotoxins in air – possibly responsible for the sick building syndromes
- Evaluation of databases on cross-infections in hospital environments.

*Student research assistant* **May 2001 to May 1st, 2002**

- KISS project, Implementation of databases and interfaces to collect, store, organize and analyze statistical data on nosocomial infection in more than 100 participating hospitals.
- Support and training of participating clinic personnel.
- Development of database and interface for data collection on infections with highly resistant pathogens such as MRSA and VRE.

CONFERENCES

- Tautenburg Conference, Big Science with Small Telescopes, Jena, Germany, 2010
- SPIE Astronomical Instrumentation, San Diego, USA, 2010

- Detectors for Astronomy 2009 (member of LOC), Garching, Germany, 2009
- Deciphering the Universe through Spectroscopy, Potsdam, Germany, 2009
- Hunting for the Dak, Malta, 2009
- SPIE Astronomical Instrumentation, Marseille, France, 2007
- ESO 3D2008, Garching, Germany, 2008
- IAU 245, Formation and Evolution of Galaxy Bulges, Oxford, UK, 2007
- SPIE Electronic Imaging, San Jose, California, USA, 2006

## PUBLICATIONS

M. H. Fabricius, R. P. Saglia, D. B. Fisher, N. Drory, R. Bender, and U. Hopp. Kinematic Signatures of Bulges Correlate with Bulge Morphologies and Sérsic Index. *submitted to ApJ*, 2011.

J. J. Adams, K. Gebhardt, G. A. Blanc, M. H. Fabricius, G. J. Hill, J. D. Murphy, R. C. E. van den Bosch, and G. van de Ven. The central dark matter distribution of NGC 2976. *ArXiv e-prints*, October 2011.

D. B. Fisher, N. Drory, and M. H. Fabricius. Bulges of Nearby Galaxies with Spitzer: The Growth of Pseudobulges in Disk Galaxies and its Connection to Outer Disks. *ApJ*, 697:630–650, May 2009.

S. B. Pu, R. P. Saglia, M. H. Fabricius, J. Thomas, R. Bender, and Z. Han. Radially extended kinematics and stellar populations of the massive ellipticals NGC 1600, NGC 4125, and NGC 7619 . Constraints on the outer dark halo density profile. *A&A*, 516:A4, June 2010.

N. A. Roe, C. J. Bebek, K. S. Dawson, J. H. Emes, M. H. Fabricius, J. A. Fairfield, D. E. Groom, S. E. Holland, A. Karcher, W. F. Kolbe, N. P. Palaio, and G. Wang. Radiation-tolerant, red-sensitive CCDs for dark energy investigations. *Nuclear Instruments and Methods in Physics Research A*, 572:526–527, March 2007.

R. P. Saglia, M. Fabricius, R. Bender, M. Montalto, C.-H. Lee, A. Riffeser, S. Seitz, L. Morganti, O. Gerhard, and U. Hopp. The old and heavy bulge of M 31 . I. Kinematics and stellar populations. *A&A*, 509:A61+, January 2010.

## CONFERENCE PUBLICATIONS

N. Drory, D. B. Fisher, and M. H. Fabricius. Bulges of Nearby Galaxies-What Are the Structures We See in the Centers of Disk Galaxies? In V. P. Debattista & C. C. Popescu, editor, *American Institute of Physics Conference Series*, volume 1240 of *American Institute of Physics Conference Series*, pages 195–198, June 2010.

- M. Fabricius, R. Saglia, N. Drory, D. Fisher, R. Bender, and U. Hopp. Velocity Dispersions Across Bulge Types. In V. P. Debattista & C. C. Popescu, editor, *American Institute of Physics Conference Series*, volume 1240 of *American Institute of Physics Conference Series*, pages 239–240, June 2010.
- M. H. Fabricius, S. Barnes, R. Bender, N. Drory, F. Grupp, G. J. Hill, U. Hopp, and P. J. MacQueen. VIRUS-W: an integral field unit spectrograph dedicated to the study of spiral galaxy bulges. In *Society of Photo-Optical Instrumentation Engineers (SPIE) Conference Series*, volume 7014 of *Society of Photo-Optical Instrumentation Engineers (SPIE) Conference Series*, August 2008.
- M. H. Fabricius, R. Bender, N. Drory, F. Grupp, G. J. Hill, and U. Hopp. VIRUS-W A fiber based integral field unit spectrograph for the study of galaxy bulges. In M. Bureau, E. Athanassoula, and B. Barbuy, editors, *IAU Symposium*, volume 245 of *IAU Symposium*, pages 417–418, July 2008.
- M. Fabricius, M. Bebek, C. J., D. E. Groom, A. Karcher, and N. A. Roe. Quantum efficiency characterization of LBNL CCD's: Part II. Reflectivity Measurements. In M. M. Blouke, editor, *Society of Photo-Optical Instrumentation Engineers (SPIE) Conference Series*, volume 6068 of *Society of Photo-Optical Instrumentation Engineers (SPIE) Conference Series*, pages 133–143, February 2006.
- D. E. Groom, C. J. Bebek, M. Fabricius, J. A. Fairfield, A. Karcher, W. F. Kolbe, N. A. Roe, and J. Steckert. Characterization of LBNL SNAP CCD's: Quantum efficiency, reflectivity, and point-spread function. In *American Astronomical Society Meeting Abstracts*, volume 38 of *Bulletin of the American Astronomical Society*, page 1038, December 2006.
- D. E. Groom, C. J. Bebek, M. Fabricius, A. Karcher, W. F. Kolbe, N. A. Roe, and J. Steckert. Quantum efficiency characterization of LBNL CCD's: Part I. The quantum efficiency machine. In M. M. Blouke, editor, *Society of Photo-Optical Instrumentation Engineers (SPIE) Conference Series*, volume 6068 of *Society of Photo-Optical Instrumentation Engineers (SPIE) Conference Series*, pages 133–143, February 2006.
- S. E. Holland, C. J. Bebek, K. S. Dawson, J. H. Emes, M. H. Fabricius, J. A. Fairfield, D. E. Groom, A. Karcher, W. F. Kolbe, N. P. Palaio, N. A. Roe, and G. Wang. High-voltage-compatible fully depleted CCDs. In *Society of Photo-Optical Instrumentation Engineers (SPIE) Conference Series*, volume 6276 of *Society of Photo-Optical Instrumentation Engineers (SPIE) Conference Series*, July 2006.
- A. Karcher, C. J. Bebek, M. Fabricius, B. Krieger, H. von der Lippe, M. Redelstap, and J. P. Walder. Integrating Signal Processing and A/D CONVERSION in One Focal Plane Mounted ASIC. In J. E. Beletic, J. W. Beletic, & P. Amico, editor, *Scientific Detectors for Astronomy 2005*, page 691, March 2006.